



February 4, 2022

Conceptual design of the Spin Physics Detector

Version 1.1

The SPD collaboration*

*Contact person: A. Guskov (JINR), Alexey.Guskov@cern.ch

Contents

1	Executive summary	7
2	Physics case	10
1	Gluons in proton and deuteron	10
1.1	Gluon probes at NICA SPD	11
1.2	Gluons at large x	15
1.3	Tests of TMD factorization with gluon probes	17
1.4	Linearly polarized gluons in unpolarized nucleon	18
1.5	Hadron structure and heavy charmonia production mechanisms	19
1.6	Non-nucleonic degrees of freedom in deuteron	21
1.7	Gluon polarization Δg with longitudinally polarized beams	22
1.8	Gluon-related TMD and twist-3 effects with transversely polarized beams	25
1.9	Gluon transversity in deuteron	27
1.10	Deuteron tensor polarization and shear forces	29
1.11	Summary	30
2	Quarks in proton and deuteron	31
2.1	Single-transverse spin asymmetries in the production of light mesons	31
2.2	Drell-Yan pair production	33
2.3	Generalized parton distributions	33
2.4	Polarized fragmentation functions	35
3	Tests of the QCD basics at low energies	36
3.1	Elastic scattering	36
3.2	Single-spin asymmetries at low energies	39
3.3	Exclusive hard processes with deuterons	40
3.4	Scaling behavior of exclusive reactions with the lightest nuclei and spin observables	41

3.5	Vector mesons and the open charm near the threshold	42
3.6	Central nucleon-nucleon collisions	45
3.7	Onset of deconfinement in p - p and d - d central collisions	46
3.8	Study of the lightest neutral hypernuclei with strangeness -1 and -2	47
3.9	Multiquark correlations and exotic state production	48
3.10	Yield of antiprotons in hadronic collisions for astrophysical dark matter search .	49
3	Polarized beams	51
1	Available species and types of collisions	51
2	Beam structure, intensity, and luminosity	51
3	Polarization control and monitoring	53
3.1	Transportation of polarized ions in the accelerator complex	53
3.2	Spin dynamic modes in the NICA collider	53
3.3	Specifications to the polarized beams in the collider	54
3.4	Polarization control in the NICA collider without snakes in the ST-mode	54
3.5	Ion polarization control in the ST-mode by means of two snakes	56
3.6	Stability of spin motion	57
3.7	Spin flipping system	57
3.8	Online control of the polarization in the collider	57
3.9	Polarized beams dynamics in the Nuclotron	57
3.10	Operation modes of the NICA collider with polarized beams	59
3.11	Conclusion	59
4	Detector layout	61
1	General design	61
2	Magnetic system	63
3	Beam pipe	65
4	Vertex detector	66
4.1	General overview	66
4.2	Double-sided silicon detectors	70
4.3	Mechanical layout	70
4.4	MAPS option	71
4.5	Cost estimate	72
5	Straw tracker	72

5.1	Straw technology	73
5.2	General layout of the ST	73
5.3	Front-end electronics	74
5.4	Cost estimate	76
6	Electromagnetic calorimeter	76
6.1	Overview of the SPD calorimeter	77
6.2	Design of the calorimeter module prototype	79
6.3	Multi-pixel photodiodes	80
6.4	MPPC readout and the high-voltage control	81
6.5	Readout electronics	81
6.6	Cosmic ray test results	82
6.7	Dependence of the calorimeter response on the number of photoelectrons	83
6.8	Long-term stability	84
6.9	Cost estimate	85
7	Range (muon) system	86
7.1	General description	86
7.2	System layout	86
7.3	Mini drift tubes detector	87
7.4	Front-end electronics	88
7.5	Performance figures	91
7.6	Cost estimate	92
8	Particle identification system	92
8.1	Time-of-flight system	93
8.2	Aerogel counters	98
9	Beam-beam counters	99
9.1	Inner part of the BBC: MCP	100
9.2	Outer part of the BBC: scintillation tiles	101
10	Zero degree calorimeter	103
5	Local polarimetry	107
1	Asymmetry in inclusive production of charged particles	107
2	Inclusive π^0 production	107
3	Single transverse spin asymmetry for very forward neutron production	109

6	Detector control system	111
1	DCS concept	111
2	DCS architecture	113
3	SCADA for the DCS	114
7	Data acquisition system	116
1	Introduction	116
2	DAQ structure	117
3	Data format	118
4	Cost estimate	122
8	Computing and offline software	123
1	SPD computing model	123
2	Online filter	124
3	Computing system	125
3.1	Computing model	125
3.2	Computing services	126
4	Offline software	127
5	Resource estimate	128
9	Physics performance	129
1	General performance of the SPD setup	129
1.1	Minimum bias events	129
1.2	Tracking	131
1.3	Vertex reconstruction	132
1.4	Particle identification	133
1.5	Calorimetry	135
2	Accuracies of the asymmetries measurement	138
2.1	Charmonia production	139
2.2	Prompt photon production	142
2.3	Open charm production	145
10	Integration and services	147
1	Experimental building of SPD	147
2	Auxiliary equipment and services	148

11 Beam test facilities	150
1 Test zone with extracted Nuclotron beams	150
2 Tests at the SPD straight section of the collider	151
12 Running strategy	153
1 Accelerator	153
2 Spin Physics Detector	154
13 Cost estimate	156
14 Participating institutions and author list	157
15 Conclusion	161
16 List of abbreviations	162

Preface

According to the astrophysical and cosmological data, the relative contribution of visible baryonic matter, the properties of which are determined by strong and electromagnetic interactions, is about 5% of the Universe mass. With respect to two other components, dark matter and dark energy, baryonic matter seems to be a well-studied subject. In fact, despite the great advances in quantum chromodynamics made in describing the interaction of quarks and gluons within the framework of the perturbative approach, the question of why nucleons are exactly like we see them, remains open. Understanding the structure and the fundamental properties of the nucleon directly from the dynamics of its quarks and gluons based on the first principles is one of the main unsolved problems of QCD.

The nucleon behaves like a spinning top with a spin of $\hbar/2$. This spin is responsible for such fundamental properties of Nature as the nucleon magnetic moment, different phases of matter at low temperatures, the properties of neutron stars, and the stability of the known Universe. That is why the study of the spin structure of the nucleon is of particular importance. The naive quark model has successfully predicted most of the gross properties of hadrons, such as charge, parity, isospin and symmetry properties and their relations. Some of the dynamics of particle interactions can be qualitatively understood in terms of this model as well. However, it falls short in explaining the spin properties of hadrons in terms of their constituents. Since the famous "spin crisis" that began in 1987, the problem of the nucleon spin structure remains one of the most intriguing puzzles in the contemporary high-energy physics. The central problem, for many years attracting both enormous theoretical and experimental efforts, is the problem of how the spin of the nucleon is built up from spins and orbital momenta of its constituents – the valence and sea quarks and gluons. A full description can be given in terms of the so-called transverse-momentum dependent parton distribution functions.

Over the last 25 years, both polarized deep inelastic scattering experiments (CERN, DESY, JLab, SLAC) and high-energy polarized proton-proton collisions (RHIC at BNL) have been the major providers of information about spin-dependent structure functions of the nucleon. Nevertheless, our knowledge of the internal structure of the nucleon is still limited. This is especially true of the gluon contribution. New facilities for spin physics, such as the Electron-Ion Collider at BNL and the fixed-target experiments at CERN LHC are planned to be built in the near future to get the missing information.

The Spin Physics Detector, a universal facility for studying the nucleon spin structure and other spin-related phenomena with polarized proton and deuteron beams, is proposed to be placed in one of the two interaction points of the NICA collider that is under construction at the Joint Institute for Nuclear Research (Dubna, Russia). At the heart of the project there is huge experience with polarized beams at JINR. The main objective of the proposed experiment is the comprehensive study of the unpolarized and polarized gluon content of the nucleon. Spin measurements at the Spin Physics Detector at the NICA collider have bright perspectives to make a unique contribution and challenge our understanding of the spin structure of the nucleon.

In this document the Conceptual Design of the Spin Physics Detector is presented.

Chapter 1

Executive summary

The Spin Physics Detector (proto-)collaboration proposes to install a universal detector in the second interaction point of the NICA collider under construction (JINR, Dubna) to study the spin structure of the proton and deuteron and the other spin-related phenomena with polarized proton and deuteron beams at a collision energy up to 27 GeV and a luminosity up to $10^{32} \text{ cm}^{-2} \text{ s}^{-1}$. In the polarized proton-proton collisions, the SPD experiment [1] at NICA will cover the kinematic gap between the low-energy measurements at ANKE-COSY and SATURNE and the high-energy measurements at the Relativistic Heavy Ion Collider, as well as the planned fixed-target experiments at the LHC (see Fig. 1.1). The possibility for NICA to operate with polarized deuteron beams at such energies is unique.

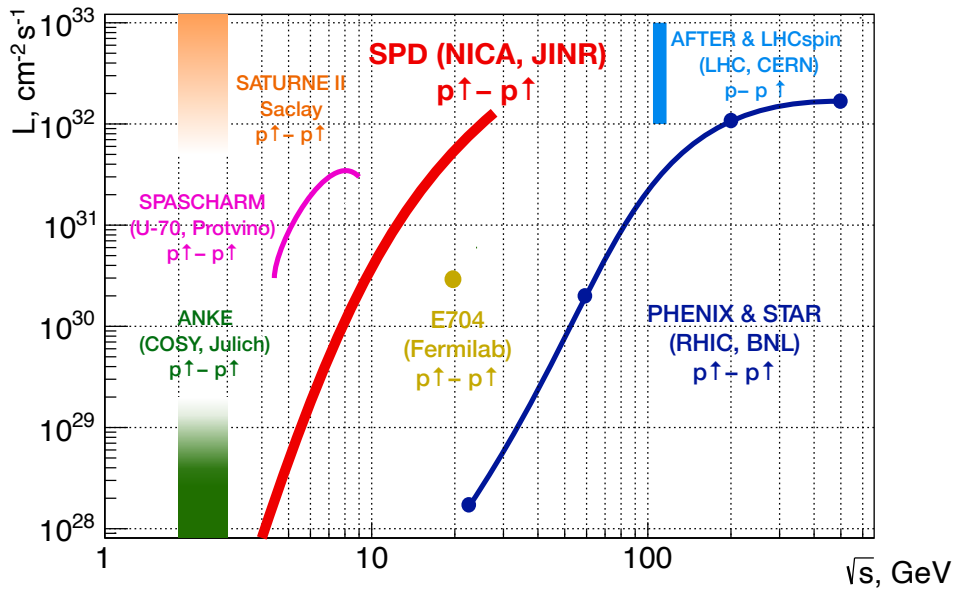


Figure 1.1: NICA SPD and the other past, present, and future experiments with polarized protons.

SPD is planned to operate as a universal facility for comprehensive study of the unpolarized and polarized gluon content of the nucleon at large Bjorken- x , using different complementary probes such as: charmonia, open charm, and prompt photon production processes. The experiment aims at providing access to the gluon helicity, gluon Sivers, and Boer-Mulders functions in the nucleon, as well as the gluon transversity distribution and tensor PDFs in the deuteron, via the measurement of specific single

and double spin asymmetries (see Tab. 1.1). The results expected to be obtained by SPD will play an important role in the general understanding of the nucleon gluon content and will serve as a complementary input to the ongoing and planned studies at RHIC, and future measurements at the EIC (BNL) and fixed-target facilities at the LHC (CERN). Simultaneous measurement of the same quantities using different processes at the same experimental setup is of key importance for minimization of possible systematic effects. Other polarized and unpolarized physics is possible, especially at the first stage of NICA operation with reduced luminosity and collision energy of the proton and ion beams.

Table 1.1: Gluon TMD PDFs at twist-2. The columns represent gluon polarization, while the rows represent hadron polarization. The PDFs planned to be addressed at SPD are highlighted in red.

	Unpolarized	Circular	Linear
Unpolarized	$g(x)$ density		$h_1^{\perp g}(x, k_T)$ Boer-Mulders function
Longitudinal		$\Delta g(x)$ helicity	Kotzinian-Mulders function
Transverse	$\Delta_N^g(x, k_T)$ Sivers function	Worm-gear function	$\Delta_T g(x)$ transversity (deuteron only), pretzelosity

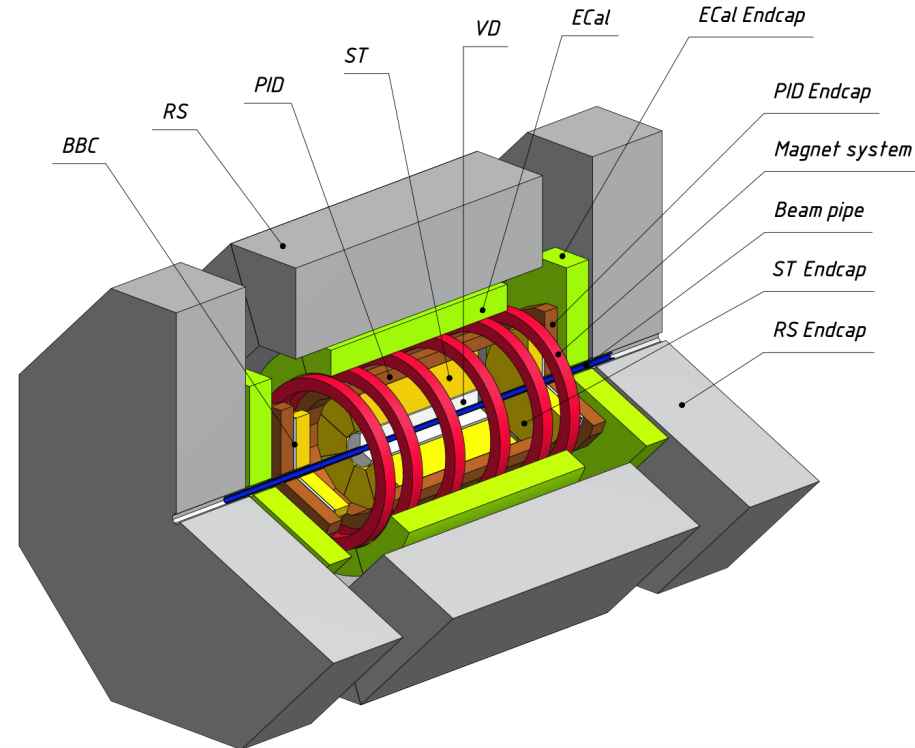


Figure 1.2: General layout of the SPD setup.

The physics goals dictate the layout of the detector. The SPD experimental setup is being designed as a universal 4π detector with advanced tracking and particle identification capabilities based on modern technologies. The silicon vertex detector (VD) will provide resolution for the vertex position on the level of below $100 \mu\text{m}$ needed for reconstruction of secondary vertices of D -meson decays. The straw

tube-based tracking system (ST) placed within a solenoidal magnetic field of up to 1 T at the detector axis should provide the transverse momentum resolution $\sigma_{p_T}/p_T \approx 2\%$ for a particle momentum of 1 GeV/c . The time-of-flight system (PID) with a time resolution of about 60 ps will provide $3\sigma \pi/K$ and K/p separation of up to about 1.2 GeV/c and 2.2 GeV/c , respectively. Possible use of the aerogel-based Cherenkov detector could extend this range. Detection of photons will be provided by the sampling electromagnetic calorimeter (ECal) with the energy resolution $\sim 5\%/\sqrt{E}$. To minimize multiple scattering and photon conversion effects for photons, the detector material will be kept to a minimum throughout the internal part of the detector. The muon (range) system (RS) is planned for muon identification. It can also act as a rough hadron calorimeter. The pair of beam-beam counters (BBC) and zero-degree calorimeters will be responsible for the local polarimetry and luminosity control. To minimize possible systematic effects, SPD will be equipped with a triggerless DAQ system. A high collision rate (up to 4 MHz) and a few hundred thousand detector channels pose a significant challenge to the DAQ, online monitoring, offline computing system, and data processing software.

The proposed physics program covers at least 5 years of the SPD running.

The estimated cost of the Spin Physics Detector at current prices is about 96 M\$. This value does not cover the R&D expenses and the construction of the SPD Test zone. Any expenses related to the development and construction of the infrastructure for polarized beams at NICA are also out of this estimation.

Chapter 2

Physics case

1 Gluons in proton and deuteron

Gluons, together with quarks, are the fundamental constituents of the nucleon. They play a key role in generation of its mass and carry about half of its momentum in hard (semi)inclusive processes. The spin of the nucleon is also built up from the intrinsic spin of the valence and sea quarks (spin-1/2), gluons (spin-1), and their orbital angular momenta. Notwithstanding the progress achieved during the last decades in the understanding of the quark contribution to the nucleon spin, the gluon sector is much less developed. One of the difficulties is the lack of the direct probes to access gluon content in high-energy processes. While the quark contribution to the nucleon spin was determined quite precisely in semi-inclusive deep-inelastic scattering (SIDIS) experiments like EMC, HERMES, and COMPASS, the gluon contribution is still not well-constrained even so it is expected to be significant.

In recent years, the three-dimensional partonic structure of the nucleon became a subject of a careful study. Precise mapping of three-dimensional structure of the nucleon is crucial for our understanding of Quantum Chromodynamics (QCD). One of the ways to go beyond the usual collinear approximation is to describe nucleon content in the momentum space employing the so-called Transverse-Momentum-Dependent Parton Distribution Functions (TMD PDFs) [2–7].

The most powerful tools to study TMD PDFs are the measurements of the nucleon spin (in)dependent azimuthal asymmetries in SIDIS [2, 5, 6, 8] and Drell–Yan processes [9, 10]. Complementary information on TMD fragmentation process, necessary for the interpretation of SIDIS data, is obtained from e^+e^- measurements [11]. Being an actively developing field, TMD physics triggers a lot of experimental and theoretical interest all over the world, stimulating new measurements and developments in TMD extraction techniques oriented on existing and future data from lepton-nucleon, electron-positron and hadron-hadron facilities at BNL, CERN, DESY, FNAL, JLab, and KEK. For recent reviews on experimental and theoretical advances on TMDs see Refs. [12–16]. While a lot of experimental measurements were performed (and are planned) and theoretical understanding was achieved for Leading Order (LO) (twist-2) TMD PDFs such as Sivers, transversity and Boer-Mulders functions of quarks, only few data relevant for the study of gluon TMD PDFs are available [17–22].

The simplest model of the deuteron is a weakly-bound state of a proton and a neutron mainly in the S-wave with a small admixture of the D-wave state. This approach is not much helpful in the description of the deuteron structure at large Q^2 ¹. Possible non-nucleonic degrees of freedom in deuteron could play an important role in the understanding of the nuclear modification of PDFs (the EMC ef-

¹We use Q^2 (or μ^2) as a generic notation for the hard scale of a reaction: the invariant mass square of lepton pairs in Drell–Yan processes, Q^2 , transverse momentum square p_T^2 of produced hadron or its mass square M^2 .

fect). Since the gluon transversity operator requires two-unit helicity-flip it does not exist for spin-1/2 nucleons [23]. Therefore, proton and neutron gluon transversity functions can not contribute directly to the gluon transversity of the deuteron. A non-zero deuteron transversity could be an indication of a non-nucleonic component or some other exotic hadronic mechanisms within the deuteron.

Most of the existing experimental results on spin-dependent gluon distributions in nucleon are obtained in the experiments at DESY (HERMES), CERN (COMPASS), and BNL (STAR and PHENIX). Study of polarized gluon content of the proton and nuclei is an important part of future projects in Europe and the United States such as AFTER@LHC and LHCSpin at CERN, and EIC at BNL [24–26]. Notwithstanding the gluons in nucleon were successfully probed in SIDIS measurements, hadronic collisions have an important advantage since they probe the gluons at the Born-level without involving the EM couplings.

1.1 Gluon probes at NICA SPD

The polarized gluon content of proton and deuteron at intermediate and high values of the Bjorken x will be investigated using three complementary probes: inclusive production of charmonia, open charm, and prompt photons. Study of these processes is complementary to such proven approaches to access the partonic structure of the nucleon in hadronic collisions as the inclusive production of hadrons with high transverse momentum and the Drell-Yan process. Unfortunately, the latter one is unlikely to be accessible at SPD due to the small cross-section and unfavourable background conditions. For effective registration of each aforementioned gluon probes, the SPD setup is planned to be equipped with a range (muon) system, an electromagnetic calorimeter, a time-of-flight system, straw tracker, and a silicon vertex detector. Nearly a 4π coverage of the setup and a low material budget in the inner part of the setup should provide a large acceptance for the detection of the desired final states. In Fig. 2.1(a) the kinematic phase-space in x and Q^2 to be accessed by the SPD is compared to the corresponding ranges of previous, present and future experiments. Parameters of the experimental facilities planning to contribute to gluon physics with polarized beams are listed in Tab. 2.1. Figure 2.1(b) illustrates the behavior of the cross-sections for the inclusive production of J/ψ , $\psi(2S)$, D -mesons and high- p_T prompt photons in p - p collisions as a function of \sqrt{s} .

We do not discuss separately such gluon probe as inclusive production of neutral and charged pions and other light mesons, for which the $qg \rightarrow qg$ hard process dominates in a certain kinematic region. They have been successfully used to access the polarized gluon content of the proton at the RHIC experiments and can of course be used at SPD for this purpose. Registration of these processes does not impose additional specific requirements on the experimental setup and can be performed in parallel with the aforementioned main probes.

1.1.1 Charmonia production

From the experimental point of view, for considered energies, hadronic production of charmonia seems to be particularly suited to access gluon content in hadrons. Production of prompt J/ψ -mesons looks most attractive, since large data set of $J/\psi \rightarrow \mu^+ \mu^-$ (the branching fraction BF is 0.06 [31]) events is accumulated in beam-dump experiments with proton and pion beams at \sqrt{s} close to 20 GeV. However J/ψ -meson is not the cleanest probe of the proton structure, since a significant fraction (about 20% [32]) of J/ψ -mesons observed in hadronic collisions is produced indirectly through decays of χ_{cJ} and $\psi(2S)$ (the so-called feed-down contribution), and modeling of this contribution introduces additional uncertainties in theoretical calculations. Hence, to provide additional constraints to production models, it is important to study the production of χ_{cJ} and $\psi(2S)$ separately, through their decays $\chi_{cJ} \rightarrow \gamma J/\psi$ ($BF = 0.014, 0.343$ and 0.19 for $J = 0, 1, 2$ [31]) and $\psi(2S) \rightarrow J/\psi \pi^+ \pi^-$ ($BF = 0.347$ [31]). The latter state is of special interest, because it is essentially free from feed-down contamination from higher charmonium states, due to the proximity of $D^0 \bar{D}^0$ -threshold. However, the separation of the $\chi_{c0,1,2}$ signals

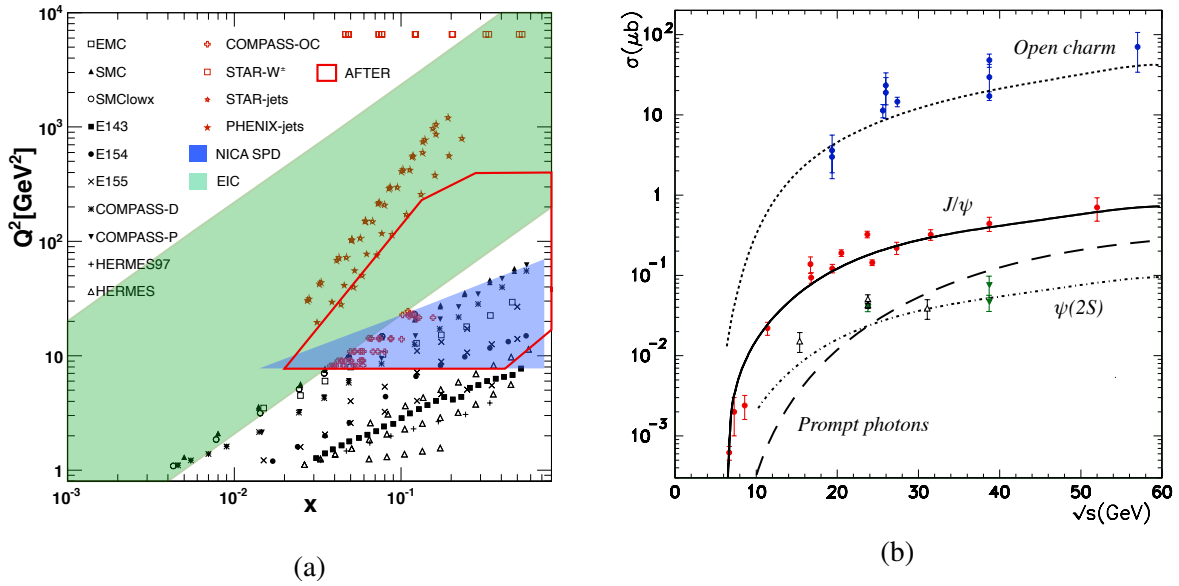


Figure 2.1: (a) The kinematic coverage, in the (x, Q^2) plane, of the hadronic cross-section data for the processes commonly included in global QCD analyses of polarized quark (black) and gluon (red) PDFs [27]. The kinematic domain expected to be covered by NICA SPD by charmonia, open charm and prompt-photon production is shown in blue. (b) Cross-section for the processes of open charm, J/ψ , $\psi(2S)$ and prompt photons ($p_T > 3$ GeV) production as a function of center-of-mass energy (based on [28]).

Table 2.1: Main present and future actors in gluon spin physics.

Experimental facility	SPD @NICA [30]	RHIC [29]	EIC [26]	AFTER @LHC [24]	SpinLHC [25]
Scientific center	JINR	BNL	BNL	CERN	CERN
Operation mode	collider	collider	collider	fixed target	fixed target
Colliding particles & polarization	p^\uparrow - p^\uparrow d^\uparrow - d^\uparrow p^\uparrow - d , p - d^\uparrow	p^\uparrow - p^\uparrow	e^\uparrow - p^\uparrow , d^\uparrow , $^3\text{He}^\uparrow$	p - p^\uparrow , d^\uparrow	p - p^\uparrow
Center-of-mass energy $\sqrt{s_{NN}}$, GeV	≤ 27 (p - p) ≤ 13.5 (d - d) ≤ 19 (p - d)	63, 200, 500	20-140 (e - p)	115	115
Max. luminosity, $10^{32} \text{ cm}^{-2} \text{ s}^{-1}$	~ 1 (p - p) ~ 0.1 (d - d)	2	1000	up to ~ 10 (p - p)	4.7
Physics run	>2025	running	>2030	>2025	>2025

is a challenging experimental task due to the small mass difference between the states and low energy resolution of the electromagnetic calorimeters for soft photons.

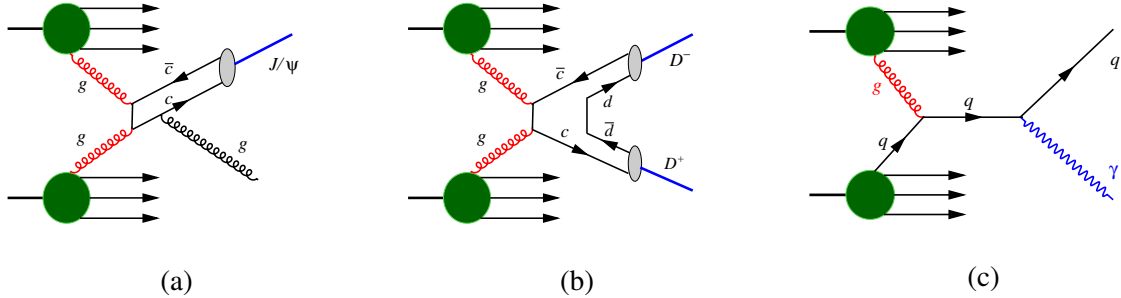


Figure 2.2: Diagrams illustrating three probes to access the gluon content of proton and deuteron in polarized collisions at NICA SPD: production of (a) charmonium, (b) open charm, and (c) prompt photons.

Besides, from the theoretical point of view the task of accessing gluon distributions using heavy quarkonia is rather challenging. The heavy quark-antiquark pair couples directly to gluons from initial-state hadrons (Fig. 2.2(a)) and its production can be calculated perturbatively, because the hard scale of the process is limited from below by the heavy quark mass, providing direct access to polarized and unpolarized gluon distributions. However, the process of transition of the heavy quark-antiquark pair into a physical bound-state is not well understood at present and can become a source of significant theoretical uncertainties. We review the modern status of the theory of quarkonium production in more detail in Sec. 1.5 to explain the latter point.

Therefore, quarkonium production can be used to study the structure of hadrons only with a great caution and only if results consistent with other probes will eventually emerge. The studies of hadronic structure and heavy quarkonium production mechanism should become complementary. But for now the most reasonable phenomenological strategy for measurements at SPD concerning quarkonia is to study yields and polarization of different quarkonium states in a wide kinematic range, at various energies, and in polarized as well as unpolarized hadronic collisions, to constrain the theoretical models. When the theory of production of heavy quarkonia is firmly established – it will become an invaluable tool to study the details of hadronic structure.

1.1.2 Open charm production

It is well-known that heavy flavor production offers direct probes of the gluon distributions in hadrons. The basic mechanism responsible for charm pair production in pp collisions is the gluon fusion (GF, see Fig. 2.2(b)). In the framework of pQCD, the GF contributes to the hadron cross-section as $\mathcal{L}_{gg} \otimes \hat{\sigma}_{c\bar{c}}$, where the gluon luminosity \mathcal{L}_{gg} is a convolution of the gluon densities in different protons, $\mathcal{L}_{gg} = g \otimes g$. At leading order in pQCD, $\mathcal{O}(\alpha_s^2)$, the partonic cross-section $\hat{\sigma}_{c\bar{c}}$ describes the process $gg \rightarrow c\bar{c}$.

The GF contribution to the charmonia production in pp collisions has the form $\mathcal{L}_{gg} \otimes \hat{\sigma}_{(c\bar{c})+X} \otimes W_{c\bar{c}}$. At the Born level, the partonic cross-section $\hat{\sigma}_{(c\bar{c})+X}$ is of the order of α_s^3 because its basic subprocess is $gg \rightarrow (c\bar{c}) + g$. Moreover, the quantity $W_{c\bar{c}}$, describing the probability for the charm pair to form a charmonium, imposes strong restrictions on the phase space of the final state.² For these two reasons, the α_s -suppression and phase space limitation, the cross-sections for charmonia production are almost two orders of magnitude smaller than the corresponding ones for open charm, see Figs. 2.1 (b).

To analyze the kinematics of a $D\bar{D}$ pair, each D -meson has to be reconstructed. The decay modes $D^+ \rightarrow \pi^+ K^- \pi^+$ (BF=0.094) and $D^0 \rightarrow K^- \pi^+$ (BF=0.04) can be used for that. To suppress a combinatorial background SPD plans to use the search for a secondary vertex of a D -meson decay that is about $100 \mu\text{m}$ far from the interaction point (the $c\tau$ values are 312 and $123 \mu\text{m}$ for the charged and neutral D -mesons,

²To form a charmonium, the momenta of the produced quark and antiquark should be sufficiently close to each other.

respectively). The identification of a charged kaon in the final state by the time-of-flight system would also help to do that. The production and decay of D^* -mesons could be used as additional tags for open-charm events. Single-reconstructed D -mesons also carry reduced but still essential information about gluon distribution that is especially important in the low-energy region lacking statistics.

1.1.3 *Prompt photon production*

Photons emerging from the hard parton scattering subprocess, the so-called prompt photons, serve as a sensitive tool to access the gluon structure of hadrons and hadron-hadron collisions. Inclusive direct photon production proceeds without fragmentation, i.e. the photon carries the information directly from the hard scattering process. Hence this process measures a combination of initial k_T effects and hard scattering twist-3 processes. There are two main hard processes for the production of direct photons: gluon Compton scattering, $gq(\bar{q}) \rightarrow \gamma q(\bar{q})$ (Fig. 2.2(c)), which dominates, and quark-antiquark annihilation, $q\bar{q} \rightarrow \gamma g$. Contribution of the latter process to the total cross-section is small.

Theoretical predictions for inclusive prompt photon production are shown in Fig. 2.3(a) as transverse momentum spectrum at the energy $\sqrt{s} = 27$ GeV. Calculations are performed in LO and NLO approximations of the Collinear Parton Model (CPM), as well as in the Parton Reggeization Approach (PRA), which is a QCD and QED gauge-invariant version of k_T -factorization. They include direct and fragmentation contributions, the latter one is about 15-30 %. The K-factor between LO and NLO calculations in the CPM slightly depends on $p_{T\gamma}$ and equals about 1.8 [33]. LO prediction of PRA coincides with the result of NLO CPM calculation at moderate transverse momenta ($p_T < 4$ GeV) while at higher p_T PRA predicts somewhat harder p_T -spectrum.

In experiments prompt photons are detected alongside with a much larger number of photons from decays of secondary π^0 and η mesons (minimum-bias photons). The main challenge is to subtract these decay contributions to obtain the photons directly emitted from hard collisions. This kind of background is especially important at small transverse momenta of produced photons (p_T) and gives the lower limit of the accessible p_T range. Therefore the prompt-photon contribution with $p_T \leq 2 - 3$ GeV is usually unreachable in the experiment [34]. Figure 2.3(b) [35] presents the comparison of the p_T spectra ($x_T = 2p_T/\sqrt{s}$) measured in a wide kinematic range of \sqrt{s} in different fixed-target and collider experiments and the theoretical NLO calculations performed within the JETPHOX package [36]. While high-energy collider results exhibit rather good agreement with expectations, situation at high- x_T is not pretty good. The results of the E706 ($\sqrt{s} = 31.6$ and 38.8 GeV) [37] and R806 ($\sqrt{s} = 63$ GeV) [38] experiments break out the trend and demonstrate some "slope". It could be an indication of possible systematic effects that have not been yet fully understood.

A pair of prompt photons can be produced in hadronic interactions in $q\bar{q}$ annihilation, quark-gluon scattering, and gluon-gluon fusion hard processes (at the leading, next-to-leading, and next-to-next-leading orders, respectively). The double prompt photon production in nucleon interactions at low energies is not yet well-studied experimentally. The production cross-section for proton-carbon interaction at $\sqrt{s} = 19.4$ GeV/c has been measured by the CERN NA3 experiment [39]. Based on this result we can expect the cross-section of the double photon production with $p_T > 2$ GeV/c for each photon on the level of about 0.5 nb.

Estimations of the expected event rates are evaluated for p - p collisions at $\sqrt{s} = 27$ and 13.5 GeV for the projected integrated luminosity 1.0 and 0.1 fb^{-1} , respectively that corresponds effectively to one year of data taking (10^7 s). The results are listed in Tab. 2.2.

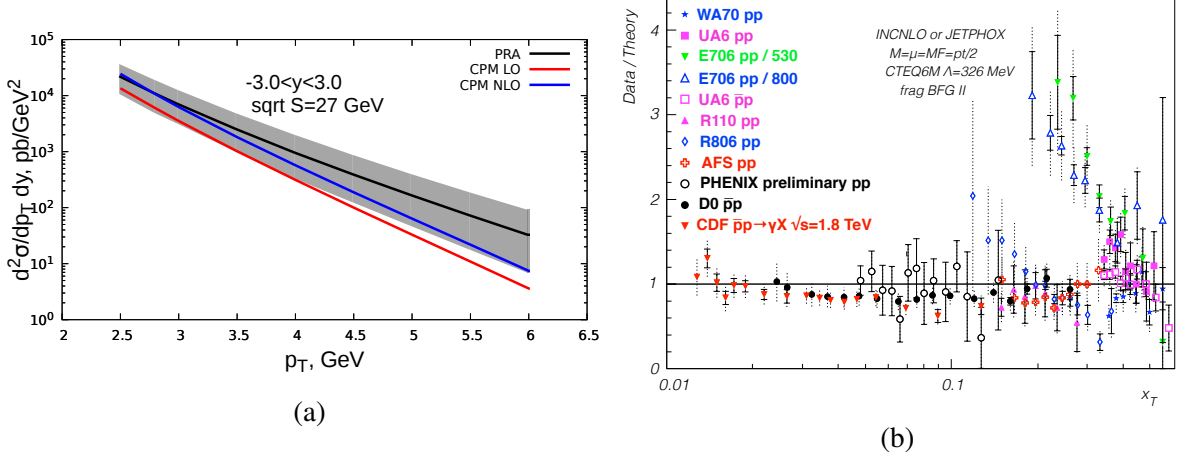


Figure 2.3: (a) Prediction for prompt photon transverse momentum spectrum at $\sqrt{s} = 27$ GeV obtained in LO (red line) and NLO (blue line) approximations of CPM and LO of PRA (black line). Uncertainty bands for PRA predictions are due to factorization/renormalization scale variation only. (b) Data-to-theory ratio for the fixed-target and collider experiments [35].

Table 2.2: Expected cross-section and counts for each of the gluon probes per one effective year of SPD running (10^7 s). Detector acceptance and reconstruction efficiency are not taken into account.

Probe	$\sigma_{27 \text{ GeV}}$, nb ($\times \text{BF}$)	$\sigma_{13.5 \text{ GeV}}$, nb ($\times \text{BF}$)	$N_{27 \text{ GeV}}$, 10^6	$N_{13.5 \text{ GeV}}$, 10^6
Prompt- γ ($p_T > 3$ GeV/c)	35	2	35	0.2
J/ψ $\rightarrow \mu^+ \mu^-$	200	60		
	12	3.6	12	0.36
$\psi(2S)$ $\rightarrow J/\psi \pi^+ \pi^- \rightarrow \mu^+ \mu^- \pi^+ \pi^-$	25	5		
	0.5	0.1	0.5	0.01
	0.2	0.04	0.2	0.004
$\chi_{c1} + \chi_{c2}$ $\rightarrow \gamma J/\psi \rightarrow \gamma \mu^+ \mu^-$	200			
	2.4		2.4	
n_c $\rightarrow p\bar{p}$	400			
	0.6		0.6	
Open charm: $D\bar{D}$ pairs	14000	1300		
Single D -mesons				
$D^+ \rightarrow K^- 2\pi^+$ ($D^- \rightarrow K^+ 2\pi^-$)	520	48	520	4.8
$D^0 \rightarrow K^- \pi^+$ ($\bar{D}^0 \rightarrow K^+ \pi^-$)	360	33	360	3.3

1.2 Gluons at large x

The gluon PDF is one of the less known parton distributions in the proton because the available data constrain weakly the quantity $g(x, Q^2)$, particularly for x greater than 0.5 [42, 43]. In the high- x region, the gluon density is usually parameterized as $g(x, Q^2) \sim (1 - x)^L$, and values of L extracted from global

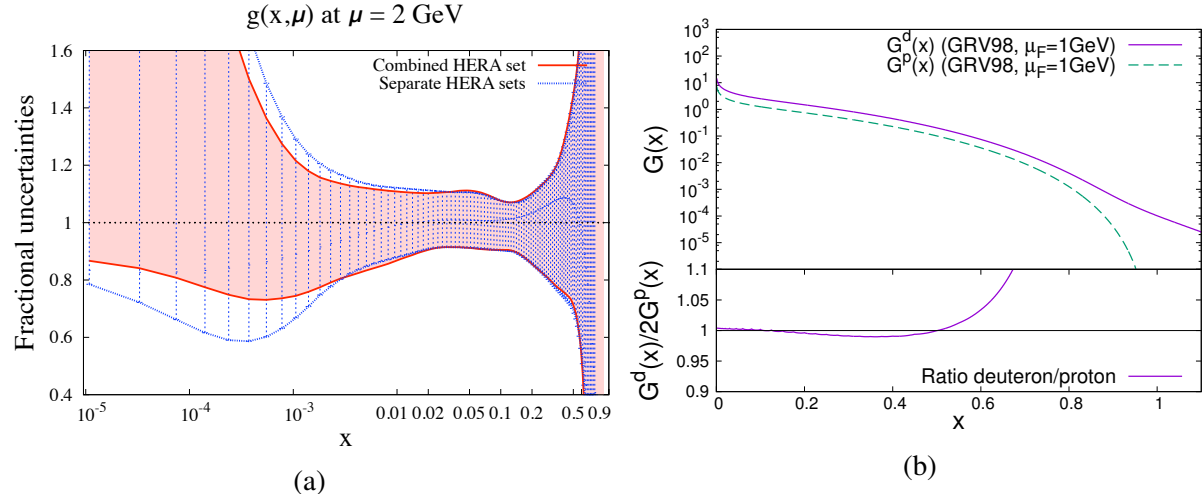


Figure 2.4: (a) Uncertainty of unpolarized gluon PDF based on HERA data ($\mu = 2$ GeV) [40]. (b) Gluon PDF in the deuteron in comparison with the nucleon [41].

fits differ considerably from each other. In particular, obtained results for L vary from 3 to 11 at $Q^2 = 1.9$ GeV² [44].

To improve the situation with large x , one needs precise data on the heavy flavor production at energies not so far from the production threshold. Concerning the open charm production in pp collisions, the corresponding cross-sections are poorly known for $\sqrt{s} < 27$ GeV [45, 46].³ Presently, the only available measurements for this region were performed by the E769 experiment, which corresponds to three hundred events collected in pA collisions [47]. Unfortunately, the E769 results have large uncertainties, which is enough to estimate only the order of magnitude for the $pp \rightarrow c\bar{c}X$ cross-section at $\sqrt{s} \approx 20$ GeV. For this reason, future studies of the open charm production at SPD in pp and dd collisions for $\sqrt{s} \leq 27$ GeV are of special interest. In particular, they will allow to reduce significantly the present uncertainties in the gluon density (and α_s) at a GeV scale, especially for high x .

Detailed information on the gluon distribution at large x is very important for various phenomenological applications. For instance, it is of current interest to estimate the $b\bar{b}$ pair production cross-section at NICA energies. Such predictions, however, are not presently reliable due to their strong dependence on the exponent L which is poorly known. Another example is the DGLAP evolution of the PDFs. Using precise data on $g(x, Q^2)$ (and α_s) at $Q^2 \sim m_c^2$ (m_c is the mass of the c-quark) as boundary conditions in the DGLAP equations, one could reduce essentially the uncertainties in evolution of PDFs for higher values of Q .

From the theoretical point of view, the threshold behavior of cross-sections is closely related to the so-called infrared renormalon problem. It is well known that radiative corrections to the production cross-sections contain the mass (or threshold) logarithms whose contribution is expected to be sizable near the threshold. These logarithms are usually taken into account within the soft gluon resummation (SGR) formalism [48–52]. Formally resummed cross-sections are, however, ill-defined due to the Landau pole contribution, and few prescriptions have been proposed to avoid the renormalon ambiguities [53–56]. Unfortunately, numerical predictions for heavy quark production cross-sections may significantly depend on the choice of resummation prescription. Undoubtedly, anticipated data from SPD on the charm production not so far from the production threshold will provide an excellent test for these prescriptions.

Another interesting problem that could be addressed at NICA SPD is to probe the intrinsic charm (IC)

³On the contrary, few data exist for the J/ψ production cross-section down to threshold, see Fig. 2.1(b).

content of the proton [57, 58]. The IC contribution to open charm production is expected to be sizable near the threshold because its PDF, $c(x, Q^2)$, is predicted to be harder than the gluonic one. The IC could be also accessed via double J/ψ production. As a result, the IC density in the proton can be dominant at sufficiently large x independently of its overall normalization [59]. To visualize the IC component, one needs to collect enough events like $D\bar{D}$ pair produced in $pp \rightarrow D\bar{D}$ with a large overall x_F close to 1. Those events are predicted to be very rare within the gluon fusion mechanism and would directly indicate the five-quark component in the proton, $|uudcc\rangle$.

Investigation of the open charm production in p - p , p - d and d - d collisions might be one of the key points in the NICA SPD program. The motivation is twofold. On the one hand, production of D -mesons in p - p collisions is practically unmeasured at NICA energies. On the other hand, these presently unavailable data on open charm production rates are strongly necessary for determination of the gluon density $g(x, \mu)$ at large x where this PDF is practically unknown.

Moreover, anticipated results on the open charm production are very important for many other current issues in particle physics: from infrared renormalon ambiguities in cross-sections to intrinsic charm content of the proton.

1.3 Tests of TMD factorization with gluon probes

The description of hard inclusive processes in hadron collisions is based on factorization theorems. The formulation of factorization theorems in terms of the TMD PDFs of quarks and gluons is the most important step towards studying the 3D structure of hadrons and the nature of their spins. The conventional TMD-approach [60] can be applied for study of the processes with colorless final states with transverse momenta much smaller than the relevant scale of hadron interactions, $q_T \ll Q$. In recent years a substantial success was achieved in the quark sector of TMD PDFs related with their correct theoretical definition and the connection with experimentally observed cross-sections within the framework of factorization theorems [7]. In the case of unpolarized hadron collisions, in the leading twist approximation the production cross-section is a function of two independent TMD PDFs, i.e. distribution functions of unpolarized quarks f_1^q and distribution functions of transversely polarized quarks $h_1^{\perp q}$ (referred to as Boer-Mulders function) in unpolarized nucleons. For description of cross-sections in collisions of polarized hadrons, the number of TMD PDFs increases.

However, the situation with gluon TMD PDFs is significantly different. Until recently, gluon TMD PDFs were used only within the framework of phenomenological models of the type of the Generalized Parton Model (GPM), in which the factorization formula of the Collinear Parton Model is applied if small (non-perturbative-origin) transverse momenta of gluons from colliding hadrons are available.

The proof of the factorization theorem for processes with gluon TMD PDFs, as well as the formulation of evolution equations for them, have been presented relatively recently in [61], where they were applied to describe the Higgs boson production with small transverse momenta. However, hard processes in which detailed information on gluon TMD PDFs can be obtained primarily, include the processes of production of heavy mesons (D, B) and heavy quarkonia ($J/\psi, \Upsilon, \eta_c, \eta_b, \dots$). In these processes, there are two non-perturbative mechanisms to be factorized: the emission of soft gluons in the initial state and the formation of a colorless hadron in the final state. Even in the case of heavy meson production with small transverse momenta when their spectrum is determined only by a non-perturbative q_T —distribution of initial gluons, for factorization of hard and soft interactions it is not enough to use the TMD PDFs formalism, the introduction of new non-perturbative process-dependent hadron observables, the so-called TMDShFs (TMD shape functions) [62, 63] is needed. Moreover, the differential cross-section for the

process of production of the state \mathcal{Q} in a collision of unpolarized hadrons is written as⁴

$$\frac{d\sigma}{dyd^2q_T} \sim f_1^g \otimes f_1^g \otimes S_{\mathcal{Q}} - w_{UU} \otimes h_1^{\perp g} \otimes h_1^{\perp g} \otimes S_{\mathcal{Q}}, \quad (2.1)$$

where $S_{\mathcal{Q}}$ is the polarization-independent TMDShFs of this process and w_{UU} is the universal contribution weight function of linearly polarized TMD PDFs.

The factorization theorem contains three or more non-perturbative hadronic quantities at low transverse momenta: gluon TMD PDFs and TMDShFs. Thus, the phenomenological extraction of gluon TMDs from quarkonium production processes is still possible, i.e., a robust factorization theorem can potentially be obtained in any particular case of heavy meson production. However one also needs to model and extract the involved TMDShFs.

1.4 Linearly polarized gluons in unpolarized nucleon

The search for the polarized quarks and gluons in unpolarized hadrons is of special interest in the studies of the spin-orbit couplings of partons and understanding of the proton spin decomposition. The corresponding intrinsic transverse momentum \vec{k}_T dependent distributions of the transversely polarized quarks, $h_1^{\perp q}(x, \vec{k}_T^2)$, and linearly polarized gluons, $h_1^{\perp g}(x, \vec{k}_T^2)$, in an unpolarized nucleon have been introduced in Refs. [4] and [64]. Contrary to its quark version $h_1^{\perp q}$ the TMD density $h_1^{\perp g}$ is T - and chiral-even, and thus can directly be probed in certain experiments.

Azimuthal correlations in heavy quark pair production in unpolarized ep and pp collisions as probes of the density $h_1^{\perp g}$ have been considered in Refs. [65, 66]. For the case of DIS, the complete angular structure of the pair production cross-section has been obtained in terms of seven azimuthal modulations. However, only two of those modulations are really independent; they can be chosen as the $\cos\varphi$ and $\cos 2\varphi$ distributions, where φ is the heavy quark (or anti-quark) azimuthal angle [67, 68].⁵

To probe the TMD distributions, the momenta of both heavy quark and anti-quark, \vec{p}_Q and $\vec{p}_{\bar{Q}}$, in the process $pp \rightarrow Q\bar{Q}X$ should be measured (reconstructed). For further analysis, the sum and difference of the transverse heavy quark momenta are introduced,

$$\vec{K}_\perp = \frac{1}{2} (\vec{p}_{Q\perp} - \vec{p}_{\bar{Q}\perp}), \quad \vec{q}_T = \vec{p}_{Q\perp} + \vec{p}_{\bar{Q}\perp}, \quad (2.2)$$

in the plane orthogonal to the collision axis. The azimuthal angles of \vec{K}_\perp and \vec{q}_T are denoted as ϕ_\perp and ϕ_T , respectively.

The angular structure of the $pp \rightarrow Q\bar{Q}X$ cross-section has the following form:

$$d\sigma_{pp} \propto A(q_T^2) + B(q_T^2)q_T^2 \cos 2(\phi_\perp - \phi_T) + C(q_T^2)q_T^4 \cos 4(\phi_\perp - \phi_T). \quad (2.3)$$

Assuming factorization for the TMD distributions, the terms A , B and C can schematically be written as the following convolutions [66]:

$$\begin{aligned} A &\propto f_1^q \otimes f_1^{\bar{q}} \otimes A_q + f_1^g \otimes f_1^g \otimes A_g + h_1^{\perp q} \otimes h_1^{\perp g} \otimes A_g^\perp, \\ B &\propto h_1^{\perp q} \otimes h_1^{\perp \bar{q}} \otimes B_q + f_1^g \otimes h_1^{\perp g} \otimes B_g, \\ C &\propto h_1^{\perp g} \otimes h_1^{\perp g} \otimes C_g. \end{aligned} \quad (2.4)$$

⁴Here $f_1^g(x) \equiv g(x)$.

⁵The function $h_1^{\perp g}$ can also be determined from measurements of the Callan-Gross ratio in DIS [69].

The order α_s^2 predictions for the coefficients A_i , B_i and C_i ($i = q, g$) in Eqs.(2.4) are presented in Ref.[66]. Using these results, one can, in principle, extract the densities $h_1^{\perp q}(x, \vec{k}_T^2)$ and $h_1^{\perp g}(x, \vec{k}_T^2)$ from azimuthal distributions of the $D\bar{D}$ pairs produced in pp collisions.

Another processes proposed to probe the linearly polarized gluons in unpolarized proton are: pseudoscalar C -even quarkonia (such as η_c and χ_c) [70], di-gamma ($pp \rightarrow \gamma\gamma X$) [71] and J/ψ - pair ($pp \rightarrow J/\psi J/\psi X$) [72] production. These reactions are however strongly suppressed in comparison with $pp \rightarrow D\bar{D}X$.

1.5 Hadron structure and heavy charmonia production mechanisms

In this section we give a short review of modern status of the theory of heavy quarkonium production with an emphasis on possible applications of heavy quarkonium measurements for studies of the gluon content of hadrons.

Production of heavy quarkonia proceeds in two stages: first, a heavy quark-antiquark pair is produced at short distances, predominantly via gluon-gluon fusion but also with a non-negligible contribution of $q\bar{q}$ and qg -initiated subprocesses. The second stage is hadronization of quark-antiquark pair into a physical quarkonium state, which happens at large distances (low scales) and is accompanied by a complicated rearrangement of color via exchanges of soft gluons between the heavy quark-antiquark pair and other colored partons produced in the collision. Existing approaches, aimed to describe hadronization stage, such as Non-Relativistic QCD factorization (NRQCD-factorization) [73] and (Improved-) Color-Evaporation Model (CEM) [74–77] are currently facing serious phenomenological challenges (see e.g. recent reviews [78, 79]). NRQCD-factorization is challenged by the long-standing “polarization puzzle” [80, 81] and violation of Heavy-Quark Spin Symmetry relations between Long-Distance Matrix Elements (LDMEs) of η_c and J/ψ [82], while CEM usually rather poorly reproduces the detailed shapes of inclusive p_T -spectra of charmonia and bottomonia and, unlike NRQCD-factorization [83, 84], significantly under-predicts bulk of cross-section for pair hadroproduction of J/ψ even at NLO in α_s [85]. Presently, the study of the heavy-quarkonium production mechanism is an active field of research, with new approaches, such as subleading-power fragmentation [86] and Soft-Gluon Factorization [87–89], being proposed recently.

Due to the above-mentioned problems and the multitude of competing theoretical approaches and the models available on the market, our lack of quantitative understanding of the mechanism of hadronization can become a source of significant theoretical uncertainties if quarkonium production is to be used as a tool to study the proton structure. The Fig. 2.5 provides an insight on this situation at NICA SPD. In this figure, predictions of three models for the p_T -spectrum (Fig. 2.5(a)) and p_T -dependence of the polarization parameter λ_θ (Fig. 2.5(b)) are compared. The first one relies on the NLO calculation in Collinear Parton Model (with LO being $O(\alpha_s^3)$, see Fig. 2.2(a)) to describe short-distance part of the cross-section and uses the NRQCD-factorization formalism for the long-distance part, with LDMEs of the latter tuned to charmonium production data in hadronic collisions, DIS and e^+e^- -annihilation [80, 81, 90, 91]. In the second prediction, the short-distance part of the cross-section is calculated in the LO ($O(\alpha_s^2)$ for color-octet and P -wave contributions and $O(\alpha_s^3)$ for color-singlet S -wave ones) of PRA [92], while LDMEs in this calculation had been fitted to the charmonium hadroproduction data from RHIC, Tevatron and LHC [93, 94]. The third prediction is performed in the LO ($O(\alpha_s^2)$) of PRA with the same unintegrated PDFs as for the second one, but interfaced with an improved Color-Evaporation Model (ICEM) of Ref. [95] for description of hadronization. Non-perturbative parameters of the ICEM had been taken from the Ref. [95] where they had been fitted to charmonium hadroproduction data at Tevatron and LHC energies. Predictions of all three models for inclusive J/ψ p_T -spectrum at NICA SPD appear to be consistent within their uncertainty bands. However, the structure of these predictions is significantly different, with NRQCD-based predictions being dominated by gluon-gluon fusion subprocess, while

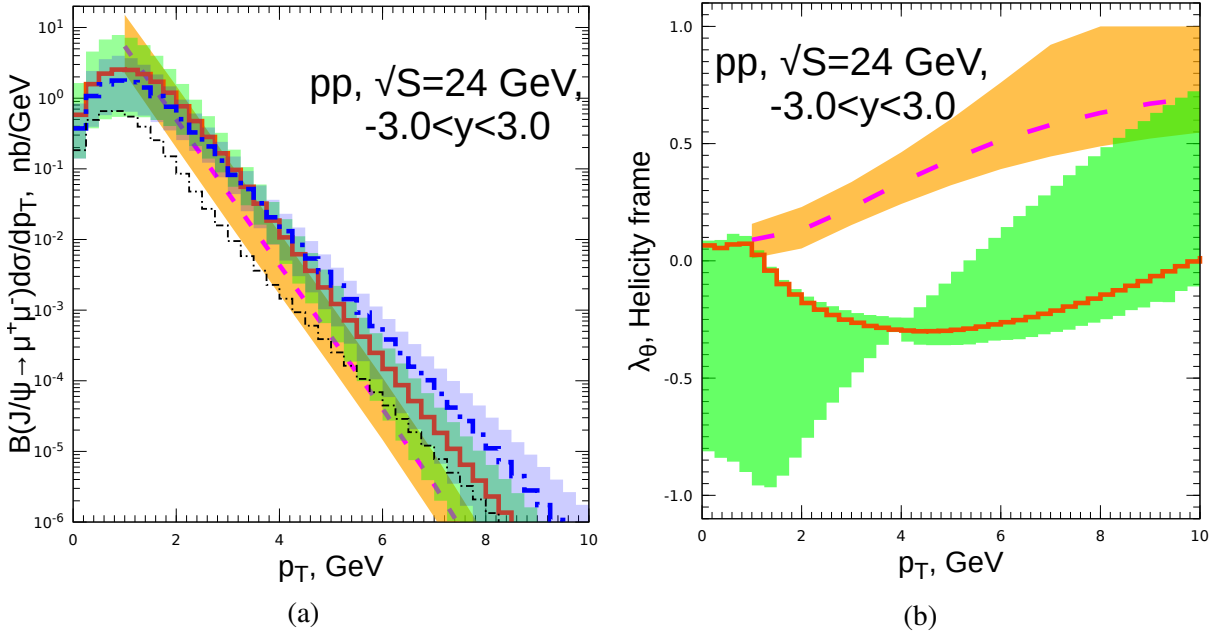


Figure 2.5: Theoretical predictions for inclusive J/ψ p_T -spectrum (a) and p_T -dependence of polarization parameter λ_θ (b) in various models: NLO of Collinear Parton Model + NRQCD-factorization (thick dashed line with orange uncertainty band) [90, 91], LO of PRA [92] + NRQCD-factorization (thick solid histogram with a green uncertainty band) [93, 94], and LO PRA [92] + Improved Color Evaporation Model (thick dash-dotted histogram with blue uncertainty band) [95]. The contribution of $q\bar{q}$ -annihilation channel to the central ICEM prediction is depicted by the thin dash-dotted histogram. Uncertainty bands are due to factorization/renormalization scale variation only.

ICEM prediction containing significant contamination from $q\bar{q}$ -annihilation (thin dash-dotted histogram in the Fig. 2.5(a)), which reaches up to 50% at low $p_T < 1$ GeV/c and contributes up to 10% at higher $p_T > 3$ GeV/c. Also ICEM tends to predict significantly harder p_T -spectrum at $p_T > 5$ GeV/c, than NRQCD-based PRA prediction which was performed with the same unintegrated PDFs.

The discussion above shows, that the J/ψ p_T -spectrum can be reliably predicted only in a limited range of transverse momenta, approximately from 3 to 6 GeV at $\sqrt{s} = 24$ GeV. At higher p_T the shape of the spectrum becomes highly model-dependent and at lower $p_T < M_{J/\psi}$ the TMD-factorization effects (including possible violation of factorization, see [62, 63]) come into the game and the contribution of $q\bar{q}$ -annihilation subprocess becomes uncertain. Nevertheless, predictions and measurements of rapidity or x_F -differential cross-sections even in this limited p_T -range could help to further constrain the gluon PDF, e.g. to rule-out the extreme values of L in the $x \rightarrow 1$ asymptotics of the PDF $\sim (1-x)^L$.

Predictions of NLO CPM and LO of PRA for polarization parameter λ_θ (see the Fig. 2.5(b)) are significantly different, with PRA predicting mostly un-polarized production ($\lambda_\theta \simeq 0$) while CPM predicts transverse polarization ($\lambda_\theta = +1$) at high p_T . Disagreement of the predictions for polarization parameters mostly reflects the difference of LDMEs obtained in two fits and their large uncertainty bands are due to significant uncertainties of LDMEs. Measurements of heavy quarkonium polarization at NICA energies will provide additional constraints on models, however due to well-known problems with description of polarization at high energies [80, 81] constraints coming from polarization measurements should be interpreted with great care and one should try to disentangle conclusions for gluon PDF from the results related to heavy quarkonium polarization.

We would like to emphasise here also, that studies of η_c -production at NICA SPD will be instrumental for better understanding of its production mechanism. If the color singlet mechanism dominated NRQCD prediction turns out to be correct, then η_c production becomes a unique instrument to study the gluon content of the proton without introducing additional free-parameters, such as the color octet LDMEs, to the analysis.

1.6 Non-nucleonic degrees of freedom in deuteron

The naive model describes the deuteron as a weakly-bound state of a proton and a neutron mainly in S-state with a small admixture of the D-state. However, such a simplified picture failed to describe the HERMES experimental results on the b_1 structure function of the deuteron [96]. Modern models treat the deuteron as a six-quark state with the wave function

$$|6q\rangle = c_1|NN\rangle + c_2|\Delta\Delta\rangle + c_3|CC\rangle, \quad (2.5)$$

that contains such terms as the nucleon $|NN\rangle$, Δ -resonance $|\Delta\Delta\rangle$ and the so-called hidden color component $|CC\rangle$ in which two color-octet baryons combine to form a color singlet [97]. Such configurations can be generated, for example, if two nucleons exchange a single gluon. The relative contribution of the hidden-color term varies from about 0.1% to 80% in different models [98]. The components other than $|NN\rangle$ should manifest themselves in the high- Q^2 limit. Possible contributions of the Fock states with a valent gluon like $|uuudddg\rangle$ could also be discussed [41, 99].

The unpolarized gluon PDF of the deuteron in the light-front quantization was calculated in the Ref. [41] under the approximation where the input nuclear wave function is obtained by solving the nonrelativistic Schrödinger equation with the phenomenological Argonne v18 nuclear potential as an input. Gluon PDFs calculated per nucleon are very similar for the proton one in the range of small and intermediate x values while for $x > 0.6$ the difference becomes large due to the Fermi motion (see Fig. 2.14(a)). A similar work was performed in Ref. [100] for determination of the spatial gluon distribution in the deuteron for low- x that could be tested in the J/ψ production at EIC. Today the gluon content of deuteron and light nuclei

becomes the matter of interest for the lattice QCD studies [101]. Apart from the general understanding of the gluon EMC effect, the measurement of the gluon PDF at high- x for deuteron could provide a useful input for high-energy astrophysical calculation [41].

SPD can perform an explicit comparison of the differential inclusive production cross-sections $d\sigma/dx_F$ for all three gluon probes: charmonia, open charm, and prompt photons using p - p and d - d collisions at $\sqrt{s_{NN}} = 13.5$ GeV and possibly below. Such results could be treated in terms of the difference of unpolarized gluon PDFs in deuteron and nucleon.

1.7 Gluon polarization Δg with longitudinally polarized beams

The gluon helicity distribution function $\Delta g(x)$ is a fundamental quantity characterizing the inner structure of the nucleon. It describes the difference of probabilities to find in the longitudinally polarized nucleon a gluon with the same and opposite spin orientations. The integral $\Delta G = \int \Delta g(x) dx$ can be interpreted as the gluon spin contribution to the nucleon spin. After the EMC experiment discovered that only a small part of proton spin is carried by the quarks [102], the gluon spin was assumed to be another significant contributor. So ΔG is a key ingredient of the nucleon helicity sum rule

$$\frac{1}{2} = \frac{1}{2} \Delta \Sigma + \Delta G + L_q + L_g, \quad (2.6)$$

where $\Delta \Sigma \approx 0.25$ [16] is the net contribution from the quark spin and L_q, L_g represent the contributions of the orbital angular momenta of quarks and gluons, respectively.

The first attempt to measure the gluon polarization in the nucleon was made by the FNAL E581/704 Collaboration using a 200 GeV polarized proton beam and a polarized proton target [103]. They measured the longitudinal double-spin asymmetries A_{LL} for inclusive multi- γ and $\pi^0\pi^0$ production to be consistent with zero within their sensitivities. In the following years a set of SIDIS measurements was performed by the HERMES [104], SMC [105] and COMPASS [106–110] experiments. The production of hadron pairs with high transverse momenta and the production of the open charm where the photon-gluon fusion mechanism dominates were studied. It was figured out that with a large uncertainty the value of ΔG is close to zero. Nevertheless, for gluons carrying a large fraction x of the nucleon momentum, an evidence of a positive polarization has been observed, see Fig. 2.6(a). New input for ΔG estimation was obtained from the measurement of the A_{LL} asymmetries in the inclusive production of high- p_T neutral [111–114] and charged pions [115], η -mesons [111], jets [116], di-jets [117, 118], heavy flavors [119], and, recently, J/ψ -mesons [120] in polarized p - p collisions at RHIC. The new data in general are in agreement with SIDIS measurements, which demonstrates the universality of the helicity-dependent parton densities and QCD factorization.

At the moment the most recent sets of polarized PDFs extracted in the NLO approximation are LSS15 [121], DSSV14 [122, 123], NNPDF-pol1.1 [27], and JAM17 [124]. To obtain them, different approaches, parameterizations, and sets of experimental data were used, see Ref. [125] for more details. Fit results for $\Delta g(x)$ from DSSV14 and NNPDF-pol1.1 are presented in Fig. 2.6(b) [123]. The RHIC p - p data put a strong constraint on the size of $\Delta g(x)$ in the range $0.05 < x < 0.2$ while a constraint on its sign is weaker as soon as in some processes only Δg squared is probed (see details below). The small x region remains still largely unconstrained and could be covered in future by measurements at EIC [26]. The region of high x is covered at the moment only by SIDIS measurements which still lack a proper NLO description [126]. The uncertainty of the contribution to Δg from the kinematic range $0.001 < x < 0.05$ vs. the corresponding contribution from the range $x > 0.05$ for the DSSV global fits is shown in Fig. 2.7(a) [122].

In case of the longitudinally polarized p - p collisions the asymmetry A_{LL} is defined as

$$A_{LL} = \frac{\sigma^{++} - \sigma^{+-}}{\sigma^{++} + \sigma^{+-}}, \quad (2.7)$$

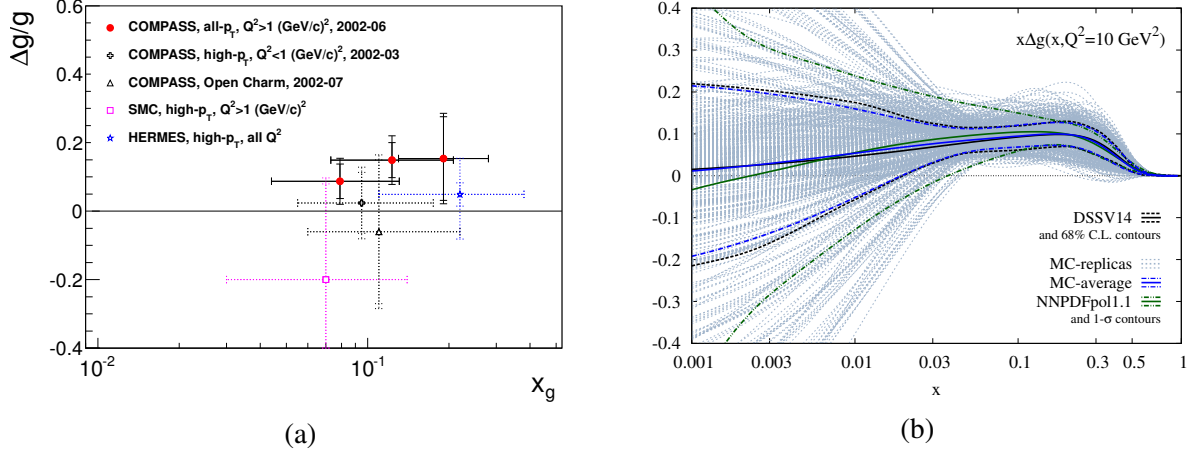


Figure 2.6: (a) SIDIS data on $\Delta g(x)/g(x)$ extracted in LO [110]. (b) Global fit results for the gluon helicity distribution $\Delta g(x)$ [123].

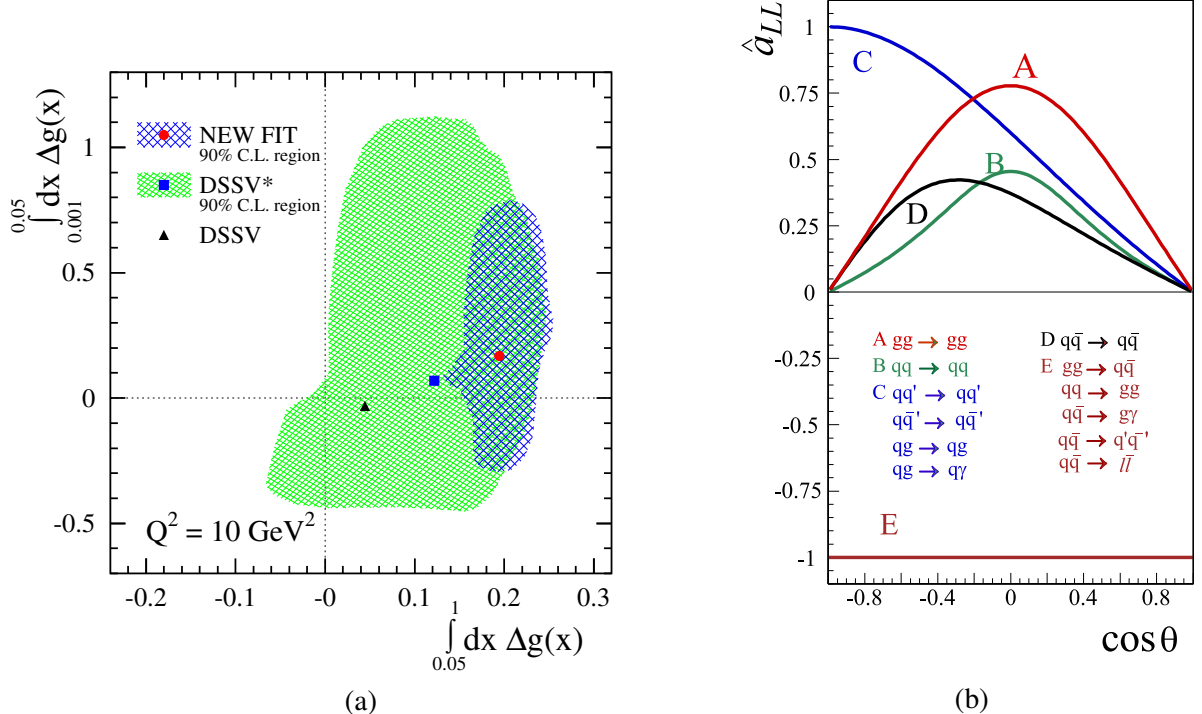


Figure 2.7: (a) Estimates of contributions of low- x and high- x kinematic ranges into ΔG for the DSSV series of the global fit. The 90% C.L. areas are shown [122]. (b) Partonic longitudinal double-spin asymmetries A_{LL} for different hard processes as a function of center-of-mass scattering angle [127].

where σ^{++} and σ^{+-} denote the cross-sections with the same and opposite proton helicity combinations, respectively. For the prompt photons produced via the gluon Compton scattering

$$A_{LL}^\gamma \approx \frac{\Delta g(x_1)}{g(x_1)} \otimes A_{1p}(x_2) \otimes \hat{a}_{LL}^{gq(\bar{q}) \rightarrow \gamma q(\bar{q})} + (1 \leftrightarrow 2). \quad (2.8)$$

Here $A_{1p}(x)$ is the asymmetry well-measured in a wide range of x and $\hat{a}_{LL}^{gq(\bar{q}) \rightarrow \gamma q(\bar{q})}$ is the asymmetry of the corresponding hard process. The Fig. 2.7(b) shows the behavior of \hat{a}_{LL} for different hard processes

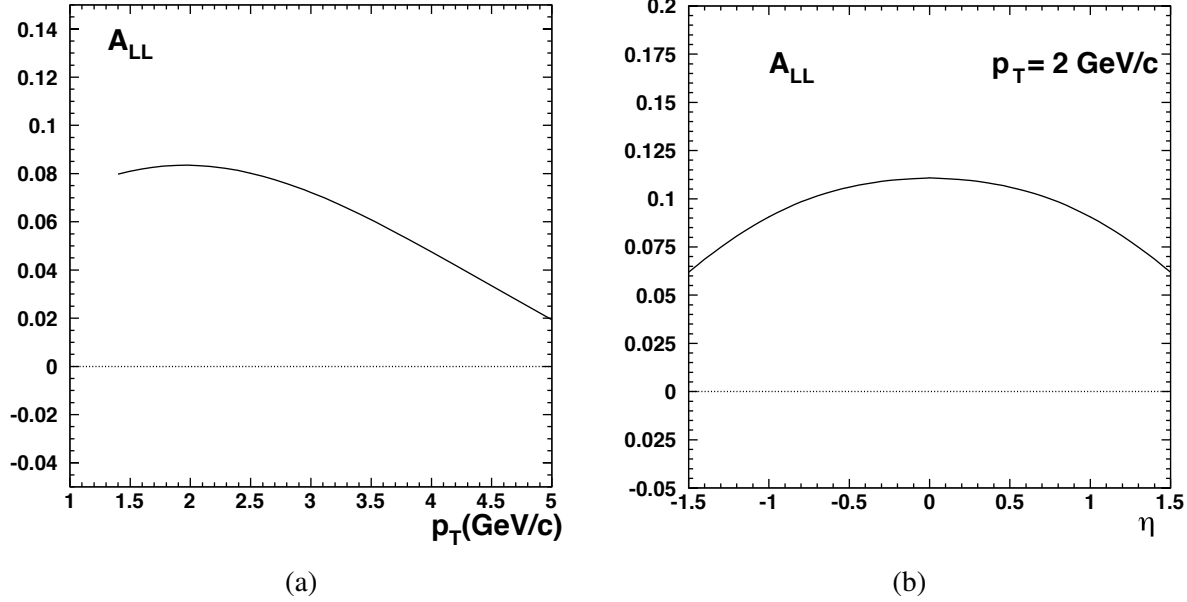


Figure 2.8: Longitudinal double spin asymmetry A_{LL} for inclusive J/ψ production calculated for p - p collisions at $\sqrt{s} = 39$ GeV in the LO approximation as a function of a) transverse momentum p_T and b) pseudorapidity η [128].

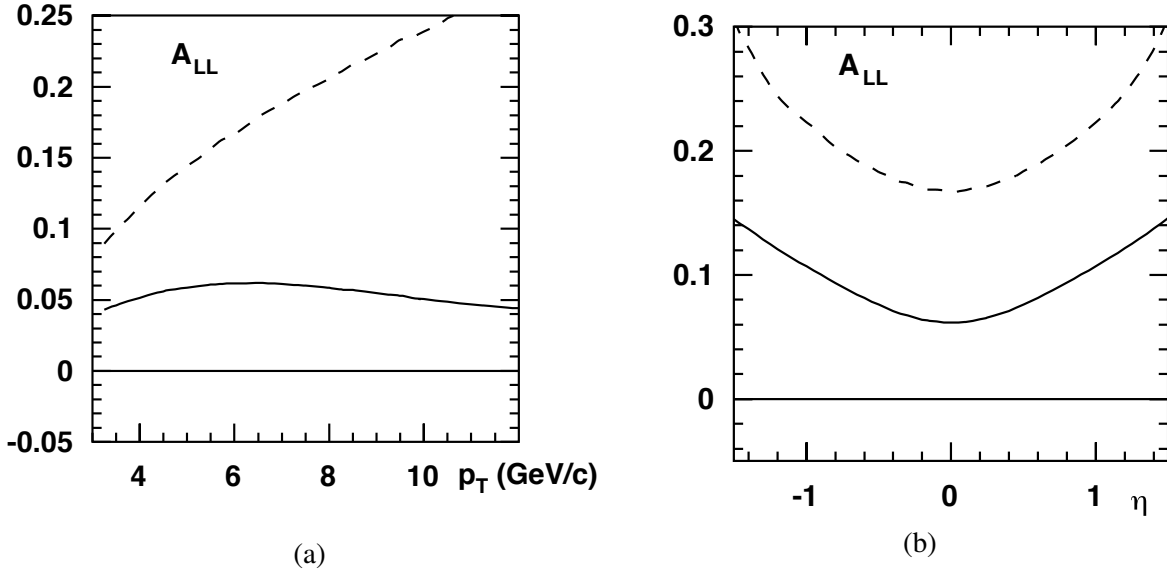


Figure 2.9: Longitudinal double spin asymmetry A_{LL} for inclusive prompt-photon production calculated for p - p collisions at $\sqrt{s} = 39$ GeV in the LO approximation as a function of a) transverse momentum p_T and b) rapidity η ($p_T = 6$ GeV/c) [128].

as a function of the center-of-mass scattering angle. For charmonia and open charm production via the gluon-gluon fusion process the expression for the corresponding asymmetry reads

$$A_{LL}^{c\bar{c}} \approx \frac{\Delta g(x_1)}{g(x_1)} \otimes \frac{\Delta g(x_2)}{g(x_2)} \otimes \hat{a}_{LL}^{gg \rightarrow c\bar{c}X}. \quad (2.9)$$

This asymmetry on the one hand is more sensitive to the gluon polarization than the corresponding one for the prompt photons due to the quadratic dependence on Δg . On the other hand the sign of the Δg

value can not be determined from it. So the measurements with prompt photons and heavy-quark states are complementary. The contribution of $q\bar{q}$ annihilation processes to the above-mentioned asymmetries is negligible despite $\hat{a}_{LL} = -1$ because of the smallness of the sea-quark polarization in the nucleon.

It is important to emphasise that a sizable systematic uncertainty of A_{LL} measurements in the inclusive J/ψ production comes from our limited knowledge of charmonia production mechanisms including the feed-down contribution. Each of them has different partonic asymmetries \hat{a}_{LL} [129]. For the Δg estimation in Ref. [120] the value of $\hat{a}_{LL}^{J/\psi}$ has been forced to -1 . The SPD setup will have the possibility to reconstruct χ_{cJ} states via their radiative decays and resolve J/ψ and $\psi(2S)$ signals in a wide kinematic range and disentangle contributions of different production mechanisms. The quality of the Δg estimation could be significantly improved by measuring A_{LL} separately for each charmonium state.

Predictions for the longitudinal double-spin asymmetries A_{LL} in p - p collisions can be found in Refs. [130] (J/ψ) and [131] (prompt photons). They mostly cover the kinematic range of the RHIC experiments. Some estimates for A_{LL} in charmonia [128] and prompt-photon [128, 132, 133] production at $\sqrt{s} = 39$ GeV (see Figs. 2.8 and 2.9, respectively) have been done in preparation of the unrealized HERA- \vec{N} project.

The authors of the Ref. [134] proposed to extract information about the gluon helicity Δg via the study of the production of high- p_T prompt photons accompanied by Σ^+ hyperons. To do that, the single longitudinal spin asymmetry A_L^{Σ} and the polarization of the produced Σ^+ hyperons should be measured. However, further elaboration of this method is needed.

1.8 Gluon-related TMD and twist-3 effects with transversely polarized beams

One of the promising ways to investigate the spin structure of the nucleon is the study of transverse single-spin asymmetries (SSAs) in the inclusive production of different final states in high-energy interactions. The SSA A_N is defined as

$$A_N = \frac{\sigma^\uparrow - \sigma^\downarrow}{\sigma^\uparrow + \sigma^\downarrow}, \quad (2.10)$$

where σ^\uparrow and σ^\downarrow denote the inclusive production cross-sections with opposite transverse polarization of one of the colliding particles. At the moment, more than forty years after the transverse spin phenomena were discovered, a wealth of experimental data indicating non-zero A_N in the lepton-nucleon and nucleon-nucleon interactions was collected. However, our understanding of the SSA phenomenon is not yet conclusive.

Theoretically two dual approaches are used to explain the transverse single-spin asymmetries: the collinear twist-3 formalism and the transverse momentum dependent (TMD) factorization approach. In the first one at large transverse momenta $p_T \gg \Lambda_{QCD}$ of a produced particle, the collinear factorization involving twist-3 contributions for three-parton (Efremov-Teryaev-Qiu-Sterman) correlations [135–138] is used. Here $\Lambda_{QCD} \approx 200$ MeV is the QCD scale. An alternative approach assumes the TMD factorization, valid for $p_T \ll Q$, where the SSAs come from the initial-state quark and gluon Sivers functions or the final-state Collins fragmentation functions. The Sivers function $f_{1T}^{\perp, q(g)}(x, k_T)$ is a TMD PDF that describes the left-right asymmetry in the distribution of the partons w.r.t. to the plane defined by the nucleon spin and momentum vectors. Originating from the correlation between the spin of the nucleon and the orbital motion of partons, it is an important detail of the three-dimensional picture of the nucleon. This function is responsible for the so-called Sivers effect (for both quarks and gluons) that was first suggested in [139] as an explanation for the large single transverse spin asymmetries A_N in the inclusive production of the nucleon. More on the theoretical and experimental status of the transverse spin structure of the nucleon can be found in Refs. [14, 140]. The first attempt to access the gluon Sivers function (GSF) studying azimuthal asymmetries in high- p_T hadron pair production in SIDIS of transversely polarised

deuterons and protons, was performed by COMPASS [21]. Using neural network techniques the contribution originating from Photon–Gluon Fusion (PGF) subprocess has been separated from the leading-order virtual-photon absorption and QCD Compton scattering subprocesses. The measured combined proton-deuteron PGF-asymmetry was found to be negative and more than two standard deviations below zero, which supports the possible existence of a non-zero Sivers function. In the meantime, COMPASS did not see any signal for the PGF Collins asymmetry, which can analogously be related to the gluon transversity distribution. COMPASS studied GSF also through Sivers asymmetry in the J/ψ -production channel [22], again obtaining an indication of a negative asymmetry.

Recently, in Ref. [141] a first estimate of the GSF was obtained using the midrapidity data on the A_N SSA, measured in π^0 production at RHIC [17]. The extraction was performed within the GPM framework using GRV98-LO set for the unpolarized PDF and available parameterizations for the quark Sivers functions (SIDIS1 from Ref. [142] and SIDIS2 from Ref. [143]). The two parameterizations were obtained using different options for fragmentation functions, namely Kretzer [144] and DSS07 [145] sets, which give significantly different results for gluons. The latter point has a strong impact on the extracted GSF especially in low- x region. First k_T -moments of the GSF $\Delta_N^{q(g)}(x, k_T)$ for the SIDIS1 and SIDIS2 sets are shown in Fig. 2.10 (a) and (b), respectively.

The gluon Sivers function is expected to satisfy the positivity bound defined as two time the unpolarized TMD gluon distribution. However, some theoretical expectations are that the gluon Sivers function at relatively high x is about 1/3 of the quark one [140].

Several inclusive processes were proposed to access the gluon-induced spin effects in transversely polarized p - p collisions. Single spin asymmetries for production of charmonia [146] (RHIC, AFTER), open charm [147–150] (RHIC) [150] (AFTER), and prompt photons [137, 151] (E704), [152] (RHIC) were estimated using both approaches for the experimental conditions of the past, present, and future experiments.

The SSA $A_N^{J/\psi}$ in the J/ψ production was measured by PHENIX in the p - p and p - A collisions at $\sqrt{s_{NN}} = 200$ GeV/c [18, 19]. The obtained values for $A_N^{J/\psi}$ are consistent with zero for negative and positive x_F . The consistent with zero result for SSA A_N^{γ} with isolated direct photons in midrapidity region was obtained recently by PHENIX [153].

Theoretical predictions [146] based on the Color Evaporation Model with TMD approach and the gluon Sivers function from Ref. [154] for different center-of-mass energies are shown in Fig. 2.11(a) as functions of rapidity y . Since the J/ψ production mechanism is not well understood, the measurement of the $A_N^{J/\psi}$ may bring a valuable input to that matter as well. Predictions for $A_N^{J/\psi}$ in proton-proton collisions at NICA energy $\sqrt{s} = 27$ GeV, obtained in GPM + NRQCD approach, as function of x_F and p_T are shown in the Figure (2.12). For comparison, results are presented for SIDIS1 [142] and D’Alesio et al. [155, 156] parameterizations of proton Sivers function.

A measurement with open-heavy hadrons (both D - and B -mesons) was performed at RHIC (PHENIX, $\sqrt{s} = 200$ GeV) [20] using high- p_T muons from their semileptonic decays. The obtained results are affected by relatively large statistical uncertainties and do not exhibit any significant non-zero asymmetry. Nevertheless, the results do not contradict the predictions of the twist-3 approach from Ref. [148]. The Sivers effect contribution to the A_N^D asymmetry calculated within the Generalized Parton Model for $\sqrt{s} = 27$ GeV is presented in Fig. 2.11(b).

The measurement of the A_N^{γ} SSA with prompt photons provides a unique opportunity to study the Sivers PDF and twist-3 correlation functions, since the corresponding hard process does not involve fragmentation in the final state and thus is exempt from the Collins effect. The first attempt to measure A_N^{γ} at $\sqrt{s} = 19.4$ GeV was performed at the fixed target experiment E704 at Fermilab in the kinematic range

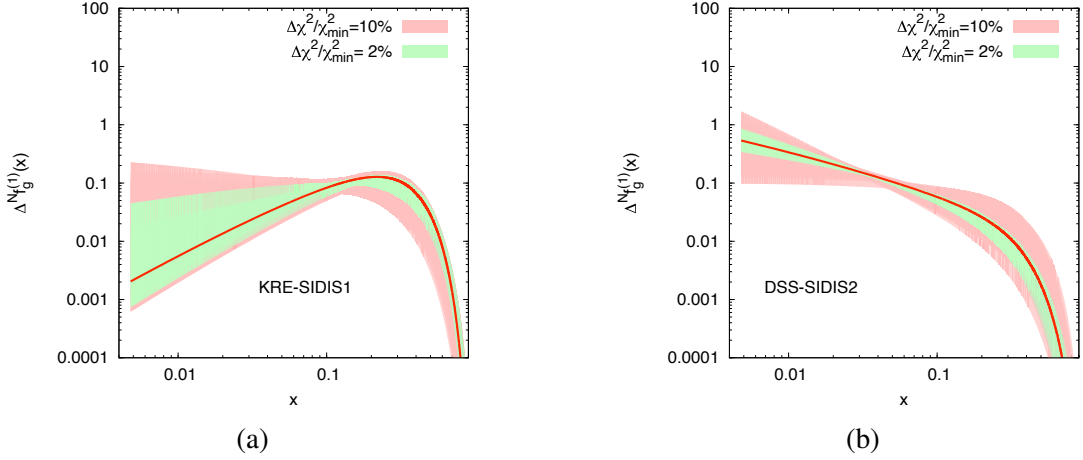


Figure 2.10: The first k_T -moment of the gluon Sivers function for SIDIS1 [142] and SIDIS2 [143] extractions of the quark Sivers functions [141].

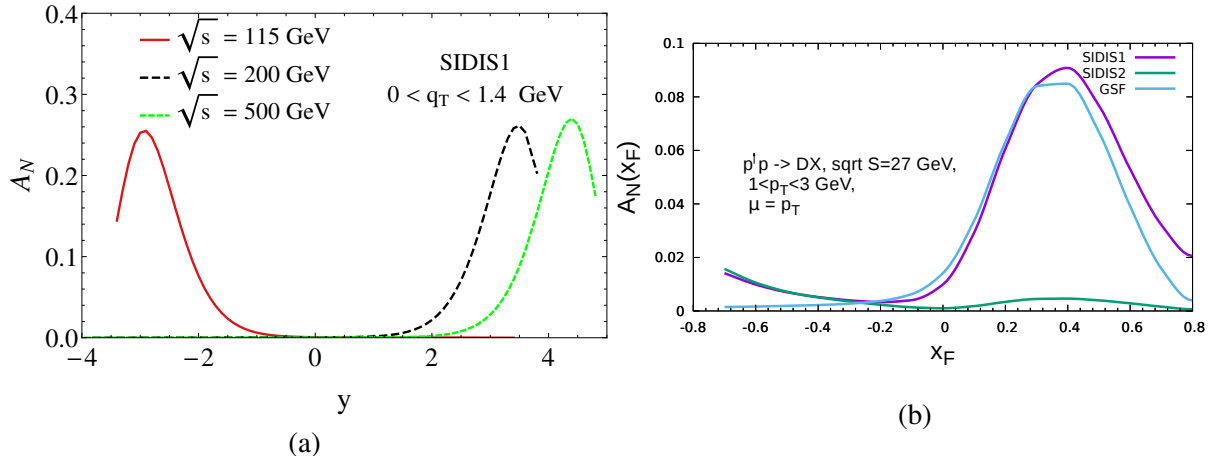


Figure 2.11: (a) Predictions for $A_N^{J/\psi}$ for $\sqrt{s} = 115$ GeV (AFTER), 200 GeV and 500 GeV (RHIC) as a function of rapidity y [146]. (b) Sivers effect contribution to the A_N^D asymmetry calculated within the Generalized Parton Model.

$-0.15 < x_F < 0.15$ and $2.5 \text{ GeV}/c < p_T < 3.1 \text{ GeV}/c$. The results were consistent with zero within large statistical and systematic uncertainties [157]. Figure 2.13(a) shows the expected A_N^γ asymmetry as a function of x_F for $\sqrt{s} = 27$ GeV based on the SIDIS1 extraction of the gluon Sivers function. Quark and gluon contributions from the gluon Compton scattering, dominating at positive and negative values of x_F , respectively, are shown separately. The $q\bar{q}$ annihilation contribution is also presented. Dashed lines illustrate the twist-3 predictions for $\sqrt{s} = 30$ GeV and $p_T = 4 \text{ GeV}/c$ for negative [151] and positive [137] values of x_F . The p_T dependence of the A_N^γ asymmetry at $x_F = -0.5$ is shown for different values of \sqrt{s} in Fig. 2.13(b).

1.9 Gluon transversity in deuteron

The transversity function $\Delta_T q(x)$ is defined for partons as the difference of probabilities to find in a transversely polarized nucleon a parton with the same and opposite spin orientations. In spite of the definition is similar to the helicity function $\Delta q(x)$, the transversity describes a completely different aspect of the nucleon spin structure. This function is known quite well after a series of SIDIS and Drell-Yan experiments. As soon as the transversity is related with the spin flip, for the spin-1/2 nucleon only a

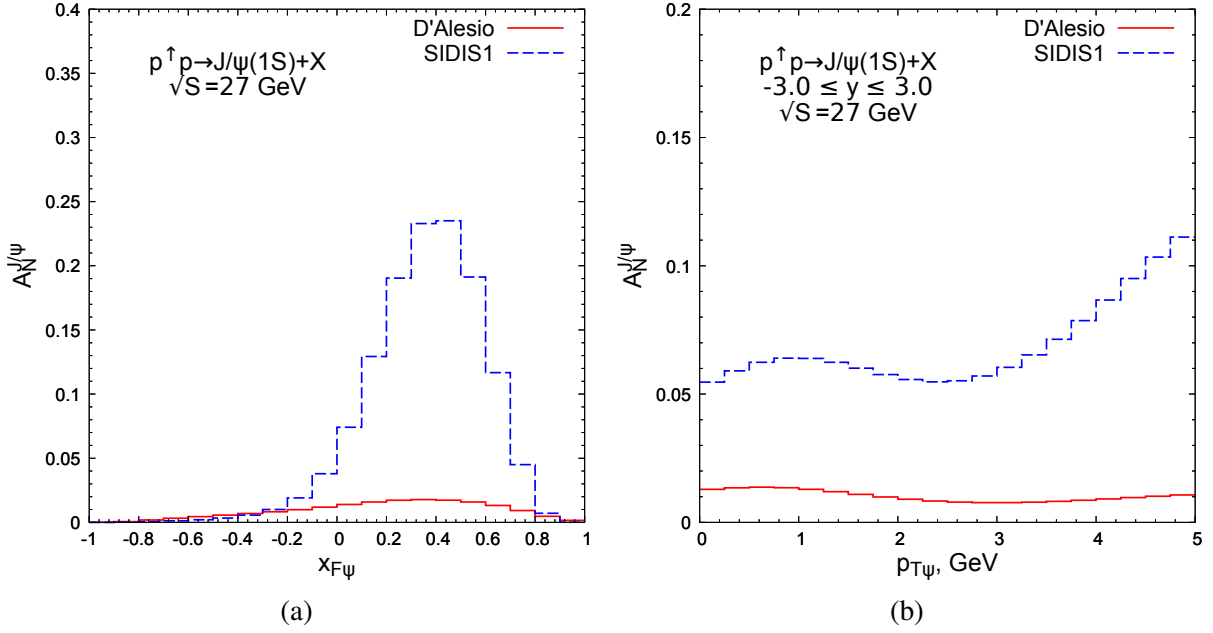


Figure 2.12: Predictions for $A_N^{J/\psi}$ as function of x_F (b) and p_T (b) in p - p collisions at the energy $\sqrt{s} = 27$ GeV obtained in GPM + NRQCD approach.

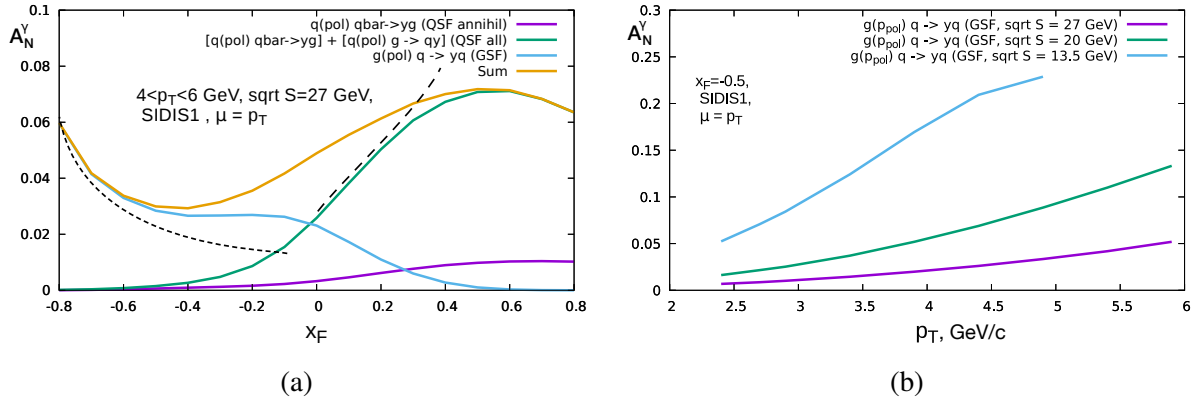


Figure 2.13: (a) x_F -dependence of the asymmetry A_N^γ calculated basing on the SIDIS1 Sivers function for $\sqrt{s} = 27$ GeV and $4 < p_T < 6$ GeV/c. Gluon and quark contributions are shown separately by color solid lines. Dashed lines illustrate the twist-3 predictions for $\sqrt{s} = 30$ GeV and $p_T = 4$ GeV/c for negative [151] and positive [137] values of x_F . (b) p_T -dependence of the A_N^γ asymmetry for different values of \sqrt{s} at $x_F = -0.5$.

quark contribution ($\Delta s = 1$) is possible while $\Delta s = 2$ for the spin-1 gluons is forbidden in the twist-2. Nevertheless, a tiny nonzero gluon transversity is allowed due to higher-twist effects and possible physics beyond the Standard model like electric dipole moment of the neutron [158]. The transverse double spin asymmetry A_{TT} defined for interaction of transversely polarized hadrons by the similar manner as A_{LL} is a way to access the transversity. But due to the absence of a gluonic contribution in the leading order in the case of the nucleon interactions $A_{TT} \ll A_{LL}$. As an example, the asymmetry A_{TT}^γ for the prompt-photon production at 200 and 500 GeV coming from the $q\bar{q}$ annihilation process calculated in LO [159] and NLO [160] is shown in Fig. 2.14.

The situation changes [161] for the spin-1 deuteron where a gluon component not embedded into the

nucleons is possible. So in the collision of transversely polarized deuterons a nonzero contribution of the gluon transversity $\Delta_T g(x)$ to A_{TT} asymmetries is possible already in the twist-2. At the moment there is no experimental data on the gluon transversity in the deuteron. So, a measurement of the double transverse spin asymmetries A_{TT} in the gluon-induced processes at polarized d - d collisions at NICA SPD could be a way to access the $\Delta_T g(x)$.

The gluon-induced (NLO) Drell-Yan process $qg \rightarrow q\gamma^* \rightarrow q\mu^+\mu^-$ was proposed in Ref. [158] as a way to access it in the collisions of linearly polarized deuterons and unpolarized protons at the SpinQuest experiment at Fermilab ($\sqrt{s_{NN}} = 15$ GeV). Under assumption that $\Delta_T g(x) = \Delta g(x)$, the asymmetry

$$A_{E_{xy}} = \frac{d\sigma(E_x) - d\sigma(E_y)}{d\sigma(E_x) + d\sigma(E_y)} \quad (2.11)$$

could reach the level of a few percent as it is shown in Fig. 2.14 (b). At NICA SPD, the J/ψ , open charm and prompt-photon production in p - d and d - d collisions with a linearly polarized deuteron can be used to access the gluon transversity. The asymmetry $A_{E_{xy}}$ in these processes is expected to be of the same order of magnitude.

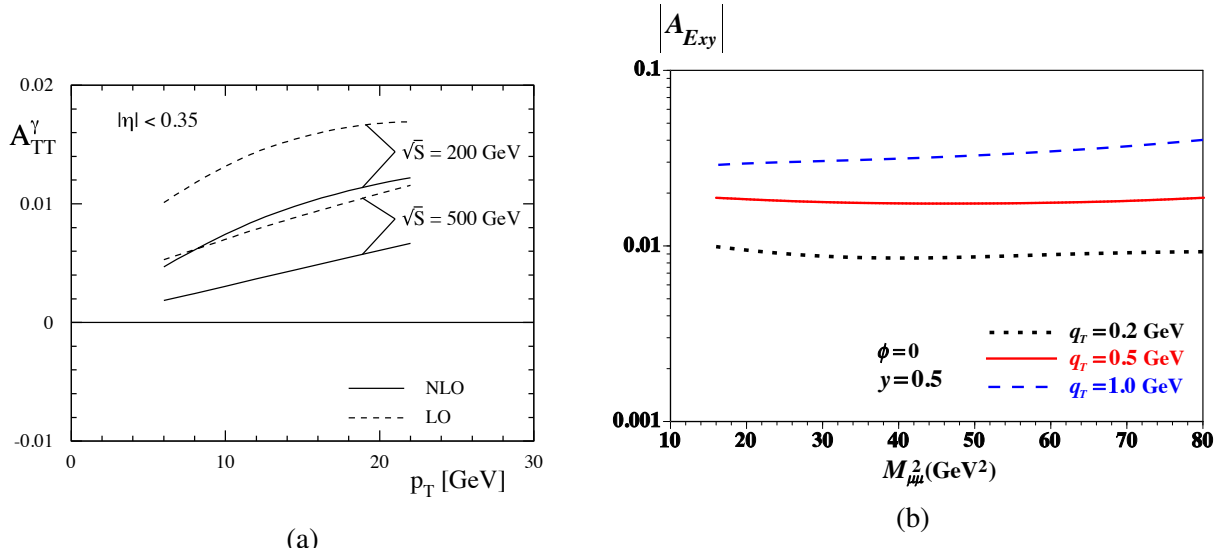


Figure 2.14: (a) A_{TT}^γ asymmetry for the prompt-photon production at 200 and 500 GeV coming from the $q\bar{q}$ annihilation process calculated in LO [159] and NLO [160]. (b) Spin asymmetries $|A_{E_{xy}}|$ for the proton-deuteron Drell-Yan process as a function of the dimuon mass squared for the dimuon rapidity $y = 0.5$ and different transverse momenta q_T [158].

1.10 Deuteron tensor polarization and shear forces

The availability of tensor polarized deuteron beam opens a possibility to study shear forces generated by quarks and gluons [162]. The natural way to get the traceless part of the energy-momentum tensor related to shear is provided just by tensor polarization, as the relevant tensor $S^{\mu\nu}$ is a traceless one by construction. The contribution of the "tensor polarized" parton distribution C^T [163, 164] (introduced as an "aligned" one [165]) is constrained by the zero sum rule [165] for its second moment (complementing the Close-Kumano sum rule [164]) which may be decomposed into quark and gluon components [166]:

$$\sum_{i=q,\bar{q}} \int_0^1 C_i^T(x) x dx = \delta_T(Q^2), \quad (2.12)$$

$$\int_0^1 C_G^T(x) x dx = -\delta_T(Q^2). \quad (2.13)$$

As a result, the matrix elements of energy momentum tensors of quarks and gluons look like

$$\sum_i \langle P, S | T_i^{\mu\nu} | P, S \rangle_{Q^2} = 2P^\mu P^\nu (1 - \delta(Q^2)) + 2M^2 S^{\mu\nu} \delta_T(Q^2) \quad (2.14)$$

$$\langle P, S | T_g^{\mu\nu} | P, S \rangle_{\mu^2} = 2P^\mu P^\nu \delta(Q^2) - 2M^2 S^{\mu\nu} \delta_T(Q^2), \quad (2.15)$$

where the second terms describe the average (integrated over transverse distance) shear force. Here M is the nucleon mass.

The zero sum rules (2.12) were later interpreted [167] as yet another manifestation of Equivalence Principle (EP), as it was done earlier [168] for Ji sum rules. In turn, the smallness of δ_T , compatible with the existing HERMES data, was suggested [167] to be the new manifestation of Extended Equivalence Principle (ExEP) [169–171] valid separately for quarks and gluons in non-perturbative QCD due to the confinement and chiral symmetry violation. It was originally suggested for anomalous gravitomagnetic moments [169, 171]. In particular, it provides the rotation of spin in the terrestrial experiment with the angular velocity of Earth rotation. Let us stress, that it may seem trivial if spin is considered just as a vector. However, it becomes highly non-trivial if the measurement of spin by the device rotating together with Earth is taken into account. This is a particular example of the practical importance of the quantum theory of measurement. Another example may be represented by the Unruh radiation in heavy-ion collisions [172], which implies that the particles production may be also considered as a quantum-mechanical measurement in the non-inertial hadronic medium.

Recently, ExEP was also discovered for the pressure [173].

To check ExEP for shear force one may use future studies of DIS at JLab and of Drell-Yan process with tensor polarized deuterons [174]⁶.

Note that tensor polarized parton distribution may be also measured in *any* hard process with the relevant combination of deuteron polarizations, in particular, for large p_T pions production, providing much better statistics. The correspondent quantity can be the P-even Single Spin asymmetry

$$A_T = \frac{d\sigma(+) + d\sigma(-) - 2d\sigma(0)}{d\sigma(+) + d\sigma(-) + d\sigma(0)} \sim \frac{\sum_{i=q,\bar{q},g} \int d\hat{\sigma}_i C_i^T(x)}{\sum_{i=q,\bar{q},g} \int d\hat{\sigma}_i q_i(x)}, \quad (2.16)$$

where the differential cross-section with definite polarization of deuteron appears.

Note that due to the tensor polarization tensor being traceless the sum rule for the three mutually orthogonal orientations of coordinate frame is valid [165]:

$$\sum_i S_{zz}^i = 0. \quad (2.17)$$

As a result, the leading twist kinematically dominant "longitudinal" tensor polarization can be obtained by accelerating *transverse* polarized deuterons which will be accessible at NICA.

1.11 Summary

The proposed measurements at SPD will be carried out performing high-luminosity p - p , p - d and d - d collisions at the center-of-mass energy up to 27 GeV using longitudinally or transversely polarized proton and vector- or tensor-polarized deuteron beams. The SPD experiment will have a unique possibility to

⁶Complementary probes are provided by vector mesons [170].

probe gluon content employing simultaneously three gluon-induced processes: the inclusive production of charmonia (J/ψ and higher states), open charm production, and production of the prompt photons. The kinematic region to be covered by SPD is unique and has never been accessed purposefully in polarized hadronic collisions. The data are expected to provide inputs for gluon physics, mostly in the region around $x \sim 0.1$ and above. The expected event rates for all three aforementioned production channels are sizable in the discussed kinematic range and the experimental setup is being designed to increase the registration efficiency for the final states of interest.

The main proposed measurements to be carried out at SPD are summarized in Table 2.3. More detailed review of the possible polarized gluon physics at NICA SPD could be found at [175].

Table 2.3: Study of the gluon content in proton and deuteron at SPD.

Physics goal	Observable	Experimental conditions
Gluon helicity $\Delta g(x)$	A_{LL} asymmetries	$p_L-p_L, \sqrt{s} = 27 \text{ GeV}$
Gluon Sivers PDF $\Delta_N^g(x, k_T)$, Gluon Boer-Mulders PDF $h_1^{\perp g}(x, k_T)$	A_N asymmetries, Azimuthal asymmetries	$p_T-p, \sqrt{s} = 27 \text{ GeV}$ $p-p, \sqrt{s} = 27 \text{ GeV}$
TMD-factorization test	Diff. cross-sections, A_N asymmetries	p_T-p , energy scan
Unpolarized gluon density $g(x)$ in deuteron Unpolarized gluon density $g(x)$ in proton	Differential cross-sections	$d-d, p-p, p-d$ $\sqrt{s_{NN}} = 13.5 \text{ GeV}$ $p-p, \sqrt{s} \leq 20 \text{ GeV}$
Gluon transversity $\Delta g_T(x)$ "Tensor polarized" PDF $C_G^T(x)$	Double vector/tensor asymmetries Single vector/tensor asymmetries	$d_{tensor}-d_{tensor}, \sqrt{s_{NN}} = 13.5 \text{ GeV}$ $d_{tensor}-d, p-d_{tensor}$

The study of the gluon content in the proton and deuteron at NICA SPD will serve as an important contribution to our general understanding of the spin structure of hadrons and QCD fundamentals. The expected inputs from the SPD will be highly complementary to the ongoing and planned measurements at RHIC, future facilities such as EIC at BNL and fixed-target LHC projects at CERN.

2 Quarks in proton and deuteron

2.1 Single-transverse spin asymmetries in the production of light mesons

The single-transverse spin asymmetries (STSA) in the inclusive production of light mesons are the simplest spin observables in hadronic scattering and also related with the Sivers, Collins, and Boer-Mulders transverse momentum dependent functions discussed in the previous section. But unlike the case of charmonia, open charm and prompt photon production, quarks are the main contributors to the corresponding asymmetries. The first result for A_N was reported by the E704 collaboration for the production of the charged and neutral pions in $p^\uparrow-p$ and $\bar{p}^\uparrow-p$ collisions at $\sqrt{s} = 19.4 \text{ GeV}$, which is up to 30% in the forward direction [176–179]. Similar values were reported by the RHIC experiments for higher energies [180–184].

Understanding of STSAs in the light mesons production is possible basing on the QCD factorization approach that separates the cross-sections into perturbatively calculable partonic-level cross-section and non-perturbative physics encoded in parton distribution functions (PDFs) and fragmentation functions (FFs). Being included into the global analysis together with other available data they are the important source of information about quark TMD functions. The JAM20 [185] is a recent example of such global QCD analysis where the available data for p - p collisions have been combined with SSA data in SIDIS, Drell-Yan pair production, and e^+e^- annihilation.

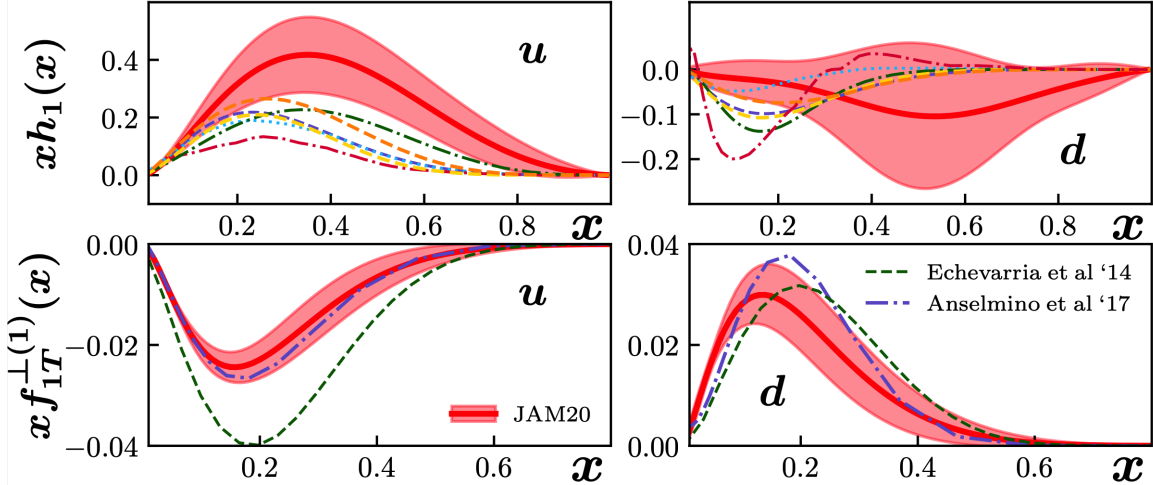


Figure 2.15: The extracted from the global analysis JAM20 (JAM collaboration) [185] functions $h_1(x)$ and $f_{1T}^{\perp(1)}(x)$ at $Q^2 = 4$ (GeV/c) 2 together with the corresponding results of other groups.

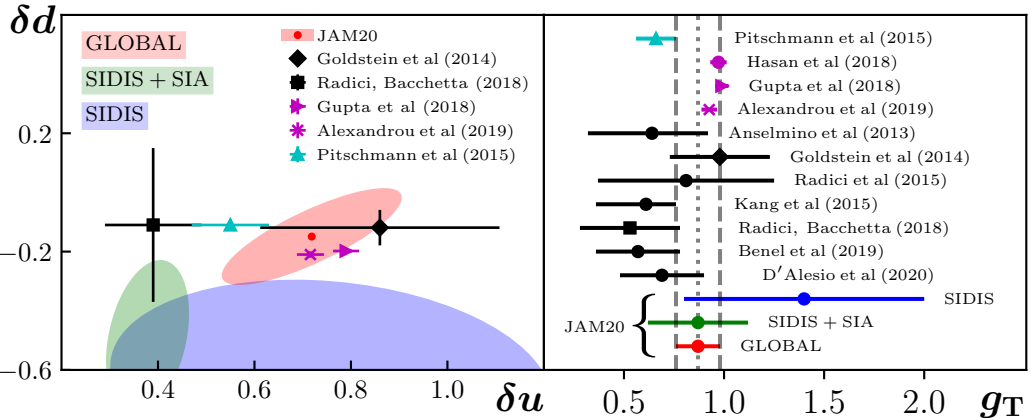


Figure 2.16: The results of the global analysis JAM20 (JAM collaboration) [185] along with others from phenomenology (black), lattice QCD (purple), and Dyson-Schwinger (cyan) for the tensor charges δu , δd and $g_T = \delta u - \delta d$ at $Q^2 = 4$ (GeV/c) 2 .

The first momenta $h_1(x)$ and $f_{1T}^{\perp(1)}(x)$ of the TMD pretzelosity $h_1(x, k_T)$ and Sivers $f_{1T}^{\perp(1)}(x, k_T)$ functions obtained from the global analysis JAM20 together with 1σ uncertainties at $Q^2 = 4$ (GeV/c) 2 are presented in Fig. 2.15. The so-called tensor charges

$$\delta q = \int_0^1 (h_1^q(x) - h_1^{\bar{q}}(x)) dx \quad (2.18)$$

for u and d quarks and $g_T = \delta u - \delta d$ are shown in Fig. 2.16. New data on the STSA in the light mesons production in the SPD energy range (and especially high- p_T data) are very much in demand for such kind of global analyses [186].

2.2 Drell-Yan pair production

Production of Drell-Yan (DY) pairs in polarized hadronic collisions $pp \rightarrow \gamma^* \rightarrow \mu^+ \mu^-$ is a promising way to touch the TMD PDFs of valence quarks and sea antiquarks by measuring the azimuthal asymmetries. A tiny DY cross-section and a huge combinatorial background coming from decays of secondary pions and kaons into muons make this task rather difficult. A typical detector configuration for such kind of studies at $\sqrt{s} \sim 20$ GeV is a fixed-target beam-dump setup where due to the Lorentz boost most of secondary pions and kaons are stopped in a thick absorber before decaying. At the moment only the COMPASS experiment at CERN has presented the results for the three azimuthal asymmetries measured in pion-induced polarized DY [187, 188]. The observed glimpse of the sign change in the Sivers asymmetries is found to be consistent with the fundamental prediction of QCD that the Sivers TMD PDF extracted from the DY has a sign opposite to the one extracted from the SIDIS data. Unique results for the Sivers functions of \bar{u} and \bar{d} are expected from the SpinQuest experiment at Fermilab [189, 190].

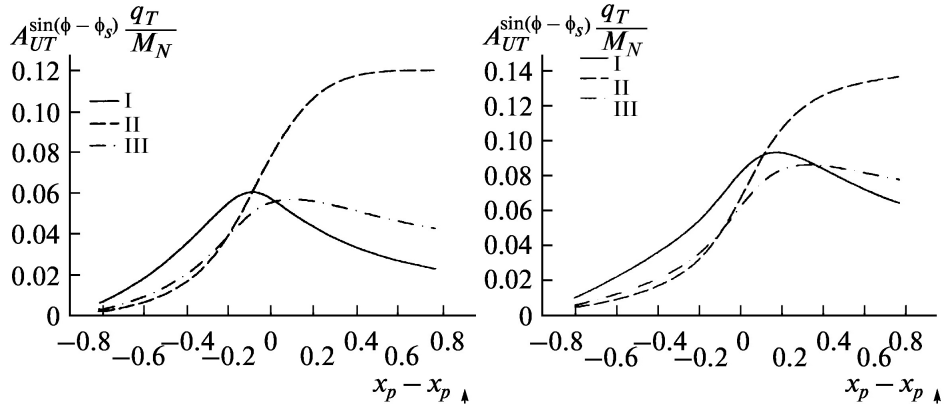


Figure 2.17: Estimated Sivers asymmetries for the NICA conditions $s = 20$ GeV, $Q^2 = 4$ GeV 2 (left) and $s = 20$ GeV, $Q^2 = 15$ GeV 2 (right). Fits for the Sivers functions are taken from [191].

Unfortunately, the Spin Physics Detector cannot use the advantage of fixed-target beam-dump setups and the expected background conditions for the Drell-Yan measurements are rather untoward. However, further improvement of the experimental techniques and analysis procedures could give a chance to access polarized DY at SPD. The estimated Sivers and Boer-Mulders asymmetries for the SPD conditions are presented in Fig. 2.17 and 2.18, respectively.

2.3 Generalized parton distributions

The concept of Generalized Parton Distributions (GPDs) is a complementary to the TMD PDFs approach to describe the three-dimensional structure of hadrons. Study of the deeply virtual meson production (DVMP) is one of the proven ways to access GPDs. This process has been investigated at HERMES [192], COMPASS [193, 194], CLAS [195] using electron and muon beams. An exclusive electromagnetic process $pp \rightarrow ppM$ shown in Fig. 2.19(a), where the first proton radiates a photon with low virtuality that interacts with the other proton and produces a meson, could be used to access the Generalized Parton Distributions at SPD. At the SPD energies, the meson photoproduction amplitude can

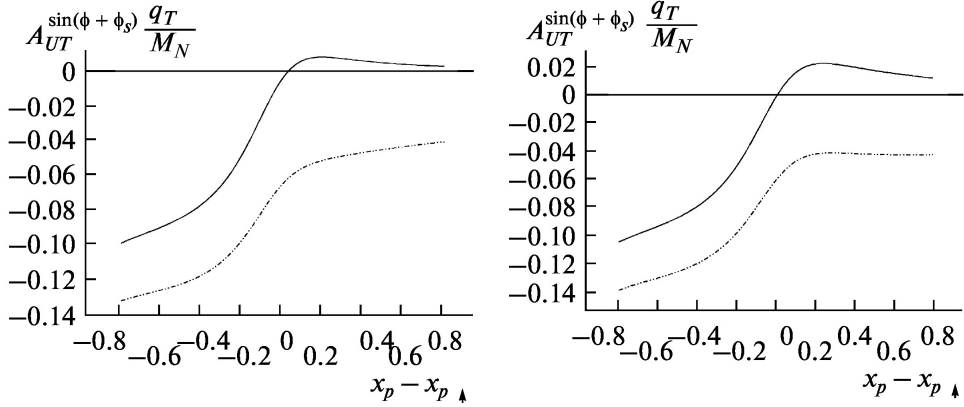


Figure 2.18: Estimated Boer-Mulders asymmetries for the NICA conditions.

be presented in a factorized form as a convolution of the hard scattering part which can be calculated perturbatively and the GPDs [196, 197]. In the case of vector mesons production, the odderon exchange (that could be described as an exchange by at least 3 gluons) is also possible and the interference of these two channels is a matter of special interest. Ultraperipheral p - A collisions at SPD, which enhance the photoproduction contribution by several orders of magnitude could also be considered. In addition, ultraperipheral processes could be used to test the most general non-perturbative concept of the Generalized Transverse Momentum dependent Distributions (GTMD). This possibility was explored for high energies in Ref. [198] but the approach could be extended down to the SPD energies.

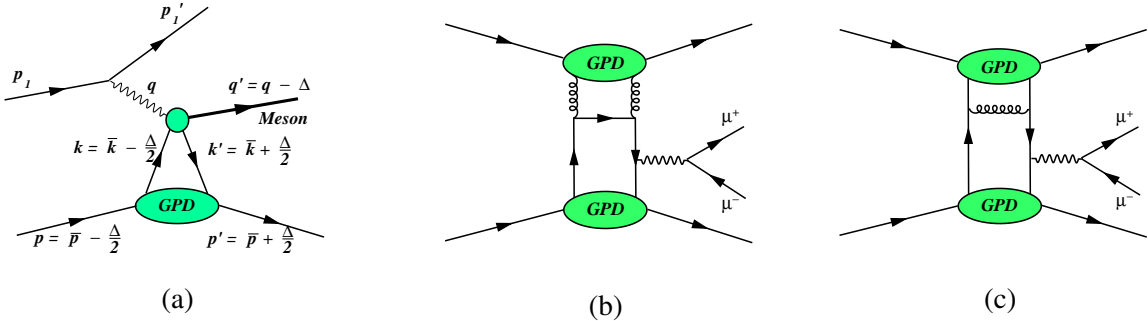


Figure 2.19: (a) Vector meson production at NICA via photoproduction mechanism or odderon exchange. (b, c) Drell-Yan process with gluon and quark GPDs.

The exclusive production of the J/ψ meson can be studied at SPD at energies $W = \sqrt{(q+p)^2} \sim 5 \div 15$ GeV. Here q and p are the 4-momenta of a virtual photon (odderon) and a proton, respectively. The large meson mass makes it possible to perform perturbative calculations at sufficiently low Q^2 , where the photon exchange should dominate. The corresponding cross-section is estimated to be of about $\sigma_{J/\psi} \sim 10$ nb. The main contribution to the cross-section is coming from the gluon GPDs.

The exclusive Drell-Yan (exDY) process was proposed for the study of GPDs in p - p collisions in Ref. [199]. The kinematics of this process is defined by convolution of two GPDs. Both quark and gluon GPDs contribute to the exDY cross-section via the diagrams shown schematically in Fig. 2.19(b, c).

Investigation of the cross-section determined by two-GPDs effects is in progress now [200]. It is shown that the gluon and sea quark GPDs lead to the cross-section which does not decrease with the growth of energy. The exDY cross-section $d\sigma/dQ^2$ at the NICA kinematics $\sqrt{s} = 24$ GeV and $Q^2 = 5$ (GeV/c) 2

is estimated as $5 \text{ pb}/(\text{GeV}/c)^2$ which is much smaller with respect to the inclusive Drell-Yan cross-section. Nevertheless, the exclusivity requirement applied in the analysis of the future SPD dimuon data could increase the signal-to-background ratio. It should be mentioned that J/ψ could also be produced exclusively in a similar way.

2.4 Polarized fragmentation functions

The information on the polarization of produced partons can be transmitted to the asymmetries of final state hadrons. This process is controlled by the polarized fragmentation functions.

JINR played the pioneering role in that activity started with the notion of jet handedness [201, 202] which was explored in Z_0 decays [203]. To measure this quantity one should explore the P-odd mixed products of hadron (usually pions) momenta in the jets and compare the number of these products with different signs indicating the right and left triples:

$$A = \frac{N_L - N_R}{N_L + N_R}. \quad (2.19)$$

In the case of transverse quark polarization the triple may contain its direction as well as that of jet momentum, so that only the pion momentum is varying. This is the case of Collins function [204] revealed in the specific angular modulations. The Collins functions are systematically studied in e^+e^- annihilation, SIDIS and hadronic processes.

Another opportunity to form the P-odd combination of momenta is the dihadron and interference fragmentation functions [205]. The dihadron fragmentation function was effectively used for transversity measurement [206].

The polarized fragmentation functions for both helicity and transversity quark distributions can be used also in the case of Λ -hyperon production [207].

The polarized quark and gluon fragmentation functions may be explored in the production to tensor polarized vector mesons [208].

The gluon fragmentation to the transverse polarized quarkonium [209] may be also considered as polarized fragmentation function. It is known to produce the dominant transverse polarization of colour-octet states.

The exploration of polarized fragmentation function in hadronic processes should involve the measurement of rapidity dependence of the hard process, which should be essential in separation of various partonic subprocesses.

2.4.1 Λ -polarization

The Λ -hyperon is an ideal testing ground for spin studies since it has a rather simple spin structure in the naive quark parton model. Furthermore, its self-analyzing decay makes polarization measurements experimentally feasible. Measurements of the Λ polarization in hadronic collisions can provide a clear answer to the question of whether polarized u and d quarks can transfer polarization to the final state Λ . Polarization of the Λ was the subject to close study in the polarized lepton production (COMPASS [210, 211], HERMES [212], E665 [213]), and p - p collisions (E704 [214, 215], STAR [216], PHENIX [217]).

There is a well known experimental fact that the hyperons produced in the unpolarized p - p collisions are polarized transversely to the production plane [218]. That is the result of higher-twist effects. Polarization measurement of the Λ -hyperons produced inclusively in p - p collisions with one of the protons

longitudinally polarized,

$$p^\uparrow p \rightarrow \Lambda^\uparrow X, \quad (2.20)$$

could provide information about the spin-dependent fragmentation function $D_{q,g \rightarrow \Lambda}(z)$ that describes fragmentation of quarks and gluons into the Λ .

The E704 measurement [215] of the parameter D_{NN} , characterizing the fraction of incident (polarized) proton polarization transferred to the inclusively produced Λ , was performed at $\sqrt{s} = 19.4$ GeV. The unexpectedly large value, up to about 30%, was found for the large p_T . The obtained result can not be treated easily within the existing models.

3 Tests of the QCD basics at low energies

Quantum chromodynamics has a remarkable success in describing the high-energy and large-momentum transfer processes, where partons in hadrons behave, to some extent, as free particles and, therefore, the perturbative QCD approach can be used. Cross-section of a process in QCD is factorized into two parts: the process-dependent perturbatively-calculable short-distance partonic cross-section (the hard part) and universal long-distance functions, PDFs and FFs (the soft part). Nevertheless, a largest fraction of hadronic interactions involves low-momentum transfer processes in which the effective strong coupling constant is large and the description within a perturbative approach is not adequate. A number of (semi-)phenomenological approaches have been developed through the years to describe strong interaction in the non-perturbative domain starting from the very basic principles. They successfully describe such crucial phenomena, as the nuclear properties and interactions, hadronic spectra, deconfinement, various polarized and unpolarized effects in hadronic interaction, etc. The transition between the perturbative and non-perturbative QCD is also a subject of special attention. In spite of a large set of experimental data and huge experience in few-GeV region with fixed-target experiments worldwide, this energy range still attracts both experimentalists and theoreticians. In addition, the low-energy physics at SPD is some kind of a bridge to the physics program of MPD, another experiment at NICA [219–221]. In this Section, we discuss certain problems that could be addressed at the initial stage of SPD operation with a reduced collision energy and luminosity, realizing, however, that this list is not exhaustive.

3.1 Elastic scattering

3.1.1 Large-angle p - N elastic scattering

The p - p and p - n elastic scattering at high energy $\sqrt{s} = 5 \div 7$ GeV and large transferred momentum $-t = 5 \div 10$ GeV² is powered by the short-range properties of N - N interactions corresponding to a small separation between nucleons $r_{NN} \sim \hbar/\sqrt{-t} \leq 0.1$ fm. There are three following aspects of QCD dynamics in these processes. (i) First, the differential cross-section $d\sigma^{pp}/dt(s, \theta_{cm})$ at a fixed angle $\theta_{cm} \sim 90^\circ$ on the whole follows the pQCD constituent counting rules $d\sigma^{pp}/dt(s, \theta_{cm}) \sim s^{-10}$ [222–225]. However, a clear deviation from this prediction in the form of oscillations with an increasing energy is observed in the region $s = 10 \div 40$ GeV² [222–225]. The irregularity in the energy dependence is at the level of $\sim 50\%$ in the region, where the magnitude of the p - p elastic cross-section falls down by 8 orders of magnitude. (ii) Second, anomalous polarization asymmetries were observed in hard p - N scattering at $p_{lab} = 11.75$ GeV/c [226–228]. The elastic p - p -cross-section with spins of protons parallel and normal to the scattering plane is almost four times larger than the cross-section with antiparallel spins. The challenge is that in order to generate such a large polarization effect, one needs to have a large contribution from the double spin-flip helicity amplitude ϕ_2 or a negligible contribution from the helicity conserving ϕ_1 amplitude. However, in pQCD, in contrast, ϕ_2 is the most suppressed and ϕ_1 is the largest [229]. Predicted within the pQCD (quark-interchange model), the double spin asymmetry $A_{NN} = 1/3$ does not depend on energy [230], [231], whereas the measured asymmetry demonstrates

”oscillating“ energy dependence. (iii) The third QCD aspect of hard NN scattering is related to the Color Transparency phenom (CT), that is, a reduction of the absorption in the nuclear medium of hard produced hadrons, both mesons and baryons [232], [233]. The initial and final hadrons participating in hard process in point-like configurations dictated by mechanism of high momentum transfer, have small color dipole momenta and, therefore, small interaction cross-section with the nuclear medium. These expectations resulted in huge theoretical and experimental activities in the 90’s. While the CT effect is observed for the hard production of the $q\bar{q}$ systems, the similar effect for qqq is elusive. The data [234, 235] on the reaction $p+A \rightarrow pp+X$ on the ^{12}C and ^{27}Al show an ”oscillatory“ effect again, i.e. the transparency increases with an increasing momentum up to $p_{lb} = 9 \text{ GeV}/c$, and then decreases below the Glauber calculation predictions at $14 \text{ GeV}/c$. An attempt to connect all the three above-mentioned aspects together into one approach was undertaken in Ref. [236] and, recently, in [229]. However, the recent measurement of the cross-section of the reaction $e^{12}\text{C} \rightarrow epX$ at $Q^2 = 8 \div 14 \text{ (GeV}/c)^2$ [237] shows no CT effect and this fact raises new questions to the analysis made in [229]. Nevertheless, according to [236], the observed large variations in spin correlations of p - p elastic scattering are consistent with formation in the s-channel of the ”octoquark“ resonances $uuds\bar{s}uud$ and $uudc\bar{c}uud$ near the strangeness and charm production thresholds, respectively. The variations with an increasing energy are explained as a result of interference of the pQCD background amplitude with non-perturbative resonant amplitudes. Furthermore, the model [236] provides a description of the oscillations in the unpolarized differential p - p elastic cross-section. One should mention, however, that another explanation of the oscillation effect in the $d\sigma^{pp}/dt(s, \theta_{cm})$ was suggested in Ref. [238].

A different spin-isospin structure of the transition matrix elements for the near threshold J/ψ production in p - n and p - p collisions [239] means that spin observables in p - n elastic scattering can give independent information on the considered dynamics. Data on these observables are almost absent in the considered energy region. A task to get such data from the $p^\uparrow d^\uparrow \rightarrow pnp$ reaction is accessible for NICA SPD.

3.1.2 Polarized p - d elastic scattering within the Glauber model and p N spin amplitudes

Nucleon-nucleon elastic scattering contains fundamental information on the dynamics of the NN interaction and constitutes a basic process in the physics of atomic nuclei and hadrons. Full information about the spin amplitudes of p - p and p - n elastic scattering can be obtained, in principle, from a complete polarization experiment, which, however, requires to measure dozens of independent observables at a given collision energy and constitutes a too complicated experimental task. A systematic reconstruction of these amplitudes from the scattering data is provided by the SAID data base [240] and covers laboratory energies up to 3 GeV ($p_{lab} \approx 3.8 \text{ GeV}/c$) for pp and 1.2 GeV ($p_{lab} \approx 1.9 \text{ GeV}/c$) for p - n scattering. At higher energies there are only non-complete data on p - p scattering, whereas the information about the p - n system is very scarce. In the literature there are several models and corresponding parametrizations for p - N amplitudes. Some of them are obtained in the eikonal approach for the lab momentum of $6 \text{ GeV}/c$ [241] and for the LHC energies [242]. Within the Regge phenomenology, a parametrization is obtained for $3\text{-}50 \text{ GeV}/c$ (corresponding to $2.77 < \sqrt{s} < 10 \text{ GeV}$) [243] and for the values of s above 6 GeV^2 ($p_{lab} \geq 2.2 \text{ GeV}/c$) in Ref. [244]. A possible way to check the existing parametrizations is to study the spin effects in proton-deuteron (p - d) and deuteron-deuteron (d - d) elastic and quasi-elastic scattering. At high energies and small four-momentum transfer t , p - d scattering can be described by the Glauber diffraction theory of multistep scattering, which involves on-shell p - N elastic scattering amplitudes as input data. Applications of this theory with spin-dependent effects included [245] indicate a good agreement with the p - d scattering data at energies of about 1 GeV , if the SAID data on p - N scattering amplitudes are used as input for the calculations [246–248].

The spin-dependent Glauber theory [245, 246] has been recently applied [249] to calculate the spin observables of p - d elastic scattering at $3 \div 50 \text{ GeV}/c$, utilizing the pp elastic scattering amplitudes f_{pp} established and parametrized in Ref. [243] within the Regge formalism. The Regge approach allows one

to construct $p - n$, f_{pn} , (and $\bar{p} - n$, $f_{\bar{p}n}$) amplitudes together with $p - p$ amplitudes at small $-t$ and large s . This feature allows one to perform a test of a broad set of p - N amplitudes and applicability of the Regge model itself to p - N elastic scattering. However, in view of the scarce experimental information about the spin-dependent p - n amplitudes and taking into account that the spin-independent parts of the p - p and p - n amplitudes at high energies are approximately the same, it was assumed in [249], as a first approximation, that $f_{pn} = f_{pp}$. The unpolarized differential cross-section, vector (A_y^p, A_y^d) and tensor (A_{xx}, A_{yy}) analyzing powers and some spin correlation parameters ($C_{x,x}, C_{y,y}, C_{xx,y}, C_{yy,y}$)⁷ of pd elastic scattering were calculated at $p_l = 4.85 \text{ GeV}/c$ and $45 \text{ GeV}/c$ at $0 < -t < 2 \text{ GeV}^2$, using p - N amplitudes from [243]. As shown in Ref. [249] the available data on p - d elastic differential cross-section in the forward hemisphere are well described by this model. Most sensitive to the spin-dependent p - N amplitudes are the vector analyzing powers A_y and the spin correlation parameters $C_{x,x}$ and $C_{y,y}$. Thus, even the measurement of the ratio A_y^d/A_y^p at low t gives valuable information on the transverse spin-spin term in NN-amplitudes [251]. In contrast, the tensor analyzing powers A_{xx} and A_{yy} are very weakly sensitive to those amplitudes and weakly change with increasing energy. The polarization observables calculated in [249] can be measured at NICA SPD and will provide a test of the used p - N amplitudes. The corresponding differential cross-section is rather large in the considered region $p_{lab} = 3 \div 50 \text{ GeV}/c$ and $|t| = 0 \div 2 \text{ GeV}^2$ being $d\sigma/dt > 0.1 \text{ mb}/\text{GeV}^2$. The expected counting rate N at $p_{lab} = 50 \text{ GeV}/c$ ($q_{pp}^{cm} = 5 \text{ GeV}/c$) for the luminosity $L = 5 \times 10^{30} \text{ cm}^{-2}\text{s}^{-1}$ and for the solid angle $\Delta\Omega = 0.03$ is $N \geq 10^2 \text{ s}^{-1}$.

The p - N helicity amplitudes ϕ_5 and $\phi_1 + \phi_3$, which can be tested in the above described procedure are necessary in the search for time-reversal invariance effects in double-polarized pd scattering [252, 253]. The data of the spin-correlation parameters on p - p elastic scattering being analyzed in the framework of the eikonal model [242] will allow one to obtain the space structure of the spin-dependent hadron forces [254].

3.1.3 Elastic d - d scattering.

The spin observables of d - d - elastic scattering in forward hemisphere also can be used to test spin-dependent amplitudes of p - N elastic scattering since the Glauber model can be applied to the description of these observables. Unpolarised differential cross-section of the d - d elastic scattering in forward hemisphere measured at energies $\sqrt{s} = 53 \div 63 \text{ GeV}$ [255] was well described by the modified Glauber theory including Gribov inelastic corrections. At lower energies corresponding to the SPD NICA region, one may expect that inelastic corrections are not important, that can be checked by direct calculation of unpolarised cross-section and subsequent comparison with the data. In this calculations the above considered spin dependent amplitudes of the pd elastic scattering [249] can be used as input for the Glauber calculations of the dd scattering.

At large scattering angles $\theta_{cm} \sim 90^\circ$ the $pd \rightarrow pd$ and $dd \rightarrow dd$ processes are sensitive to the short-range (six-quark) structure of the deuteron. Therefore, measurement of the differential cross-sections or spin observables of these processes at large θ_{cm} will be important to search for non-nucleonic degrees of freedom of the deuteron.

3.1.4 Elastic small-angle p - p scattering and periphery of the nucleon

The first evidence of the pion cloud effect in the diffractive scattering $|t| \sim 0.1 \text{ GeV}^2 \approx 4m_\pi^2$ has been found in the ISR measurements [256]. A theoretical study of the effect was provided by Anselm and Gribov [257] and recently in Refs. [258] and [259]). The oscillation effect observed at ISR was studied later on in Protvino and one more oscillation in the differential cross-section was found there at $|t| \sim 0.5 \text{ GeV}^2$ located at a higher t , it might be related to somewhat heavier mesons around the proton.

⁷We use here notations of Ref. [250]

The oscillation effect of the $p\bar{p}$ scattering amplitude at a small momentum transfer was found also in the analysis of the recent high-precision experimental data of the TOTEM collaboration at $\sqrt{s} = 13$ TeV [260]. The effect is related to the behavior of the hadron potential at large distances [261]. The SPD experiment [262] can provide new precise data on small-angle elastic $p\bar{p}$ -scattering to explore this phenomenon. For this purpose, measurements in the kinematic region of $|t| \sim 0.1 \div 0.8 \text{ GeV}^2$ will be performed. They will simultaneously detect in coincidence elastically scattered protons at angles $\theta \sim 3 \div 10^\circ$ with an accuracy of t determination higher than $\sim 0.02 \text{ GeV}^2$.

3.2 Single-spin asymmetries at low energies

A systematic study of such single-spin phenomena as the transverse single-spin polarization of hadrons (A_N) and the polarization of hyperons (P_N) in $p\bar{p}$, $d\bar{d}$, $C\bar{C}$, and $Ca\bar{Ca}$ collisions is proposed. A systematic study means a detailed study of the dependence of the observed A_N and P_N for dozens of reactions on variables, such as collision energy (\sqrt{s}), Feynman variable (x_F), transverse momentum (p_T), the atomic weights of the colliding particles (A_1 and A_2), the multiplicity of charged particles (N_{ch}) in the event, and the centrality of collisions. The study of a large number of reactions will reveal the dependence of A_N and P_N on the quantum numbers (spin, isospin, flavor, etc.) of the hadrons participating in the reaction. A systematic study also implies a global analysis of all available single-spin data within a certain model in order to identify general behavior and the mechanism of the origin of polarization phenomena.

One of such models is the chromomagnetic quark polarization (CPQ) model [263]. The CPQ model assumes the presence of an inhomogeneous circular transverse chromomagnetic field \mathbf{B}^a in the interaction region of colliding hadrons. The interaction of the chromomagnetic moments of test quarks, which later form the observed hadron, with the field \mathbf{B}^a leads, as a result of the Stern-Gerlach effect, to the appearance of spin effects (with non-zero A_N and P_N). The spin precession of test quarks leads to the phenomenon of oscillations $A_N(x_F)$ and $P_N(x_F)$ depending on the Feynman variable x_F , and the frequency of these oscillations depends on the number of spectator quarks, color charges of quarks and antiquarks, and the direction of their motion in the c.m. of reactions. The frequency of these oscillations is a linear function of the number of quarks and antiquarks - spectators interacting in pairs with each of the test quarks, taking into account the color state of the pair. The highest oscillation frequencies are expected in the case of antibaryon production in baryon collisions and in ion collisions.

The CPQ model also predicts for a number of reactions such a phenomenon as the resonance dependence of A_N and P_N on energy (\sqrt{s}), which occurs if the sign of the color charge of the test quark and spectators is opposite. The most interesting reaction in this respect is the production of anti-lambda in various initial states of the beams of the NICA collider, for which the resonance energy is close to 7 GeV in the center-of-mass system.

The threshold dependence of A_N on the hadron production angle in the center-of-mass system is also predicted. An example of the manifestation of the threshold dependence A_N is the reaction $p\uparrow p(A) \rightarrow \pi^- X$, for which the threshold angle is 74° , since the test quark is the d -quark, which is heavier than the u -quark.

An important advantage of hyperons is the ability to measure A_N and P_N through the angular distribution of their decay products, which allows the comparison of these observables with the model predictions.

The rate of pion production in $p\bar{p}$ collisions varies from $3 \times 10^7 \text{ s}^{-1}$ at 23 GeV to $2 \times 10^5 \text{ s}^{-1}$ at 7 GeV. In $C + C$ and $Ca + Ca$ collisions, it will be three orders of magnitude lower. The rate of production of hyperons is two orders of magnitude lower than that of pions. Antihyperons are produced 5 to 10 times less frequently than hyperons.

3.3 Exclusive hard processes with deuterons

Questions involved in the studies of the short-range nuclear structure and the understanding of the microscopic nucleon structure and dynamics of large-momentum transfer processes are delicately intertwined: the understanding of hard dynamics of two-body processes is also necessary for precision studies of the short-range nuclear structure. Exclusive large t reactions like a $dp \rightarrow ppn$ process can address many of these questions. The advantages of such a reaction are a good knowledge of the non-relativistic deuteron wave function and the ability to choose both kinematics sensitive to the dynamics of elastic N - N scattering and the kinematics sensitive to the short-range deuteron structure. The collider kinematics presents a number of advantages, as all particles in the considered reactions have large momenta and hence can be easily detected.

3.3.1 Probing dynamics of N - N interaction

The simplest kinematics is production of two approximately back-to-back nucleons with large transverse momenta and a spectator nucleon with a longitudinal momentum $p \sim p_d/2$ and a transverse momentum of ≥ 200 MeV/c [264, 265].

In the impulse approximation this process corresponds to elastic scattering of the projectile proton off the quasi-free nucleon of the target. In this kinematics soft rescatterings of the initial and final nucleons, which accompany the hard $pp(pn)$ reaction, are large. The eikonal approximation, which accounts for relativistic kinematics as dictated by the Feynman diagrams, reveals the important role played by the initial and final state interactions in the angular and momentum dependences of the differential cross-section in the well-defined kinematics. The condition for the applicability of the generalized eikonal approximation [266] is that the c.m. scattering angle and invariant mass of the two-nucleon system are large enough, so that $-t, -u \geq 2$ GeV 2 .

It was suggested in [232, 233] that nucleons in the elementary reaction interact in small-size configurations with a small cross-section – the color transparency phenomenon. This effect is suppressed by the space-time evolution of nucleon wave packets [267, 268]. However the effect of evolution is small for the deuteron, where typical distances between nucleons in the rescattering amplitude are ≤ 1.5 fm. Hence the discussed process allows one to measure the wave packet size of a nucleon practically right in the interaction point.

It was pointed out that the hard dynamics in p - p and p - n elastic scattering may be rather different [269]. Hence it would be instructive to compare the channels where pp and pn are produced with a large p_T .

Experiments with polarized beams would greatly add to this program: due to a better separation of kinematic domains where impulse approximation, double and triple scattering dominate, the studies of $p^{\uparrow}d^{\uparrow} \rightarrow pNN$ processes will allow one to investigate the spin structure of p - p and p - n elastic scattering at large t (the latter is practically not known). Also, it would be possible to find out whether the strong difference between the cross-sections of elastic scattering of protons with parallel and antiparallel spins [226] involves collisions of protons in configurations with sizes depending on the spin orientation.

Moreover, it would be possible to study the effects of coherence in the channels, where the exchange by gluons in the t-channel is not possible, for example, $pd \rightarrow \Delta NN$. In particular, it would be possible to test the effect of chiral transparency suggested in [270] – suppression of the pion field in the nucleons experiencing large $-t$ scattering.

3.3.2 Probing microscopic deuteron structure

It is established now that the dominant source of the short range correlations (SRC) in nuclei are proton-neutron correlations with the same quantum numbers as the deuteron and with a high-momentum tail

similar to that in the deuteron (see review in [271, 272]). Hence the deuteron serves as a kind of the hydrogen atom of the SRC physics. Only after it has been tested experimentally that the approximations currently used for the description of the p - d reaction work well, it will be possible to perform high-precision studies of the SRC in heavier nuclei.

It was demonstrated in Ref.[264, 265] that under specific kinematical conditions (in particular, low transverse momenta of slow nucleons in the deuteron rest frame) the effect of the initial and final state interactions can be accounted for by rescaling the cross-section calculated within the plane wave impulse approximation. In this kinematics it would be possible to check the universality of the wave function – in particular, its independence on the momentum transfer in the elementary reaction. Such factorization is expected to break down at sufficiently large $-t$ and $-u$, where scattering involves interaction of nucleons in the small-size configurations (the color transparency mode) since the small-size configurations are suppressed in bound nucleons with suppression growing with the nucleon off-shellness [268].

Studies of the non-nucleonic configurations in the deuteron as well as relativistic effects in the scattering off a polarized deuteron are a separate matter of interest. In particular, it would be possible to search for non-nucleonic degrees of freedom, like 6-quark, two Δ isobars via a production reaction $pd \rightarrow \Delta^{++} p \Delta^-$ with Δ^{++} and proton back to back and Δ^- being slow in the deuteron rest frame.

3.4 Scaling behavior of exclusive reactions with the lightest nuclei and spin observables

The structure of the lightest nuclei at short distances $r_{NN} < 0.5$ fm or high relative momenta ($q > \hbar/r_{NN} \sim 0.4$ GeV/c) constitutes a fundamental problem in nuclear physics. One of the most important questions is related to the search for the onset of a transition region from the meson-baryon to the quark-gluon picture on nuclei. A definite signature for transition to the valence quark region is given the constituent counting rules (CCR) [273, 274]. According the dimensional scaling, the differential cross-section of a binary reaction at a sufficiently high incident energy can be parametrized as $d\sigma/dt \sim s^{-(n-2)} f(t/s)$, where n is the sum of constituent quarks in all participants, s and t are the Mandelstam variables. Many hard processes with free hadrons are consistent with the CCR at energies of several GeV. The CCR properties of the reactions with the lightest nuclei were observed in photodisintegration of the deuteron $\gamma d \rightarrow pn$ at $E_\gamma = 1 \div 4$ GeV and ${}^3\text{He}$ nucleus $\gamma {}^3\text{He} \rightarrow ppn$, $\gamma {}^3\text{He} \rightarrow dp$. Earlier data on the reaction $dd \rightarrow tp$, $dd \rightarrow {}^3\text{He} n$ [275] and $pd \rightarrow pd$, as was shown in Ref.[276], also follow the CCR behavior s^{-22} and s^{-16} , respectively, at surprisingly low energies of 0.5 GeV. Recently, the CCR behavior of the reaction $pd \rightarrow pd$ was observed in [277, 278] at higher energies. On the other hand, the reaction with pion production $pp \rightarrow d\pi^+$ does not follow the CCR rule demonstrating the differential cross-section $\sim s^{-9}$ instead of s^{-12} . One possible way to explain this is a partial restoration of chiral symmetry at high enough excitation energy [279]. However, a systematic study of these properties of the reactions with the lightest nuclei are absent. Therefore, it is important to know whether the reaction $pn \rightarrow d\rho^0$ follows the CCR behavior and at what minimal energy there is a CCR onset. Assuming the model of the vector meson dominance and taking into account the observed CCR behavior of the $\gamma d \rightarrow pn$ reaction, one may expect the $\sim s^{-12}$ dependence of the cross-section of the reaction $pn \rightarrow d\rho^0$. Furthermore, a possible relation between the CCR behavior of the unpolarized cross-section and the spin observables of the same reaction are practically not known. The NICA SPD facility provides a good opportunity for this study, using polarized beams in p - p , d - d , and p - d collisions.

The tensor A_{yy} and vector A_y analyzing power in d - p - elastic scattering obtained at 60° , 70° , 80° and 90° in the center-of-mass system versus transverse momentum p_T [280, 281] demonstrates negative and positive asymptotics, respectively. Note that the negative sign of A_{yy} is observed also in the deuteron inclusive breakup at a large p_T [282],[283]. It would be interesting to extend the range of the measurements to a larger p_T , where the manifestation of non-nucleonic degrees of freedom is expected. New precise measurements with small statistical and systematic uncertainties at energies higher than $\sqrt{s} \geq 3.3$ GeV and

at different scattering angles are required to make a conclusion about the validity of the CCR [273, 274] in $d-p$ elastic scattering. We also propose to measure different vector and tensor analyzing powers in $d-p$ elastic scattering at the SPD energies.

The measurements of $d-p$ elastic scattering can be performed either with polarized deuterons and unpolarized protons, or with unpolarized deuterons and polarized deuterons. The $d-p$ elastic scattering events can be selected, using cuts on the azimuthal and polar scattering angles correlations. The vector A_y and tensor A_{yy} and A_{xx} analyzing powers will be measured simultaneously in the case of vertically polarized deuteron beams. The precision on the tensor $\Delta A_{yy} \sim 0.09$ and $\Delta A_{xx} \sim 0.09$ and on the vector $\Delta A_y \sim 0.03$ analyzing powers can be achieved for the scattering angle $\sim 90^\circ \pm 5^\circ$ at $\sqrt{s} \sim 4.5$ GeV ($p_T \sim 1.7$ GeV/c) for 30 days of the beam time at the luminosity $L \approx 10^{29} \text{ cm}^{-2} \text{ s}^{-1}$. We expect $\sim 70\%$ of the beam polarization from the ideal values of polarization for different spin modes. The counting rate has been estimated using the $d-p$ elastic scattering cross-section parameterization from Ref.[278]. The spin correlations can be obtained in quasi-free $d-p$ elastic scattering using $d-d$ collisions.

3.5 Vector mesons and the open charm near the threshold

The study of charm production (hidden and open) and backward vector meson production at SPD will take full advantage of the possibility of using polarized p , d beams (as well as heavier ions) in a kinematical region where the data on cross-sections are scarce and polarization effects are mostly unmeasured. In general, threshold meson production in $N-N$ collisions gives a deeper insight in the reaction mechanisms, as it is shown by the experimental programs at different proton accelerators, such as SATURNE and COSY.

3.5.1 Charm production

The production mechanisms for charmonium and D (D^*) mesons in nucleon-nucleon collisions is poorly understood. Charm quarks do not preexist in the nucleon as valence quarks: how they are formed and how they hadronize is an open question. To interpret the production and the propagation of charm in heavy-ion collisions as a probe of quark-gluon plasma (QGP), it is necessary to have a solid theoretical background based on the understanding of elementary processes.

Experimental data and theoretical studies of J/ψ production in different processes and of its decays exist: for a review, see [284], and for the most recent data collection – [285]. In the threshold region, the final particles are produced in the S -state and the spin structure of the matrix element is largely simplified. The effective proton size, which is responsible for charm creation, has to be small, $r_c \simeq 1/m_c \simeq 0.13$ fm, where m_c is the c -quark mass, selecting small impact parameters [286]. The S -wave picture can, therefore, be applied for $q \leq m_c$, where q is the norm of the J/ψ – three-momentum in the reaction center of mass (CMS). The momenta of the produced particles are small, but the mechanisms for the production of charmed quarks must involve large scales. In Ref. [239], the near-threshold J/ψ – production in nucleon-nucleon collisions was analyzed in the framework of the general model independent formalism, which can be applied to any reaction $NN \rightarrow NN V^0$, where $V^0 = \omega, \phi$, or J/ψ . Such reactions show large isotopic effects: a large difference for pp - and pn -collisions, which is due to the different spin structure of the corresponding matrix elements at the threshold: $\sigma(np \rightarrow npJ/\psi)/\sigma(pp \rightarrow ppJ/\psi) = 5$.

In Ref. [239] an estimation for the J/ψ production was suggested from the comparison of the cross-sections for the ϕ and J/ψ production in pp collisions. For the same value of the energy excess, $Q = \sqrt{s} - 2m - m_V$, taking into account the different phase space volumes, coupling constants for the decay $V \rightarrow \pi\rho$, monopole-like phenomenological form factor for the vertex $\pi^* \rho^* V$, with virtual π and ρ , one finds the following simple parameterization for the cross-section, holding in the near-threshold region only:

$$\sigma[nb] = 0.097(Q[\text{GeV}])^2. \quad (2.21)$$

In Ref. [287], a parameterization of the exponential form

$$\sigma[nb] = ae^{-bM_{J/\psi}/\sqrt{s}} \quad (2.22)$$

was suggested. The values $a = 1000$ [nb], and $b = 16.7$ GeV reproduce the experimental data above the threshold rather well.

In Fig. 2.20(a), the data for $pp \rightarrow J/\psi pp$ (red circles) and $pA \rightarrow J/\psi X$ (blue squares) are plotted from the recollections in Refs. [284] (filled symbols) and [285] (open symbols). Different symbols differentiate J/ψ production in pp or (extrapolated from) pA collisions. The data, mostly collected at CERN, are reconstructed from the measurement using models and/or assumptions, and the compiled total cross-section for J/ψ production may differ up to a factor of two. For example, the original reference for the measurement from Protvino at $\sqrt{s} = 11.5$ GeV [288] gives $\sigma(pp \rightarrow (J/\psi \rightarrow \mu^+ \mu^-)X) = 9.5 \pm 2.5$ nb, whereas the same experimental point is referenced as $\sigma = 11 \pm 3$ nb, in Ref. [284] and $\sigma = 20 \pm 5.2$ nb, in Ref. [285]. The cross-section from Ref. [239] is also plotted in Fig. 2.20(a) (solid line).

Taking the value of luminosity $L = 10^{30}$ cm $^{-2}$ s $^{-1}$, one expects 3 counts/hour for such a process with a cross-section of the order of 1 nb. This number is not corrected for the detector efficiency and reconstruction with identification, for example, in a missing mass. The reconstruction of J/ψ through its decay into a lepton pair, that is, the preferred mode, requires two additional orders of magnitude, as the branching ratio is ($\simeq 5.9 \pm 0.5$) 10 $^{-2}$.

In Ref. [239], it was shown that only one polarization observable, the J/ψ -polarization, is identical for $p-p$ and $p-n$ collisions: the J/ψ meson is transversely polarized, even in collisions of unpolarized nucleons.

Open charm production, $N N \rightarrow N \bar{D} \Lambda_C(\Sigma_C)$, gives information on scattering lengths, effective radius, hadronic form factors, and coupling constants and is also related to the dynamics of charm creation in $N-N$, $N-A$, $A-A^*$ collisions. The spin and isospin structure of the matrix element for the reactions

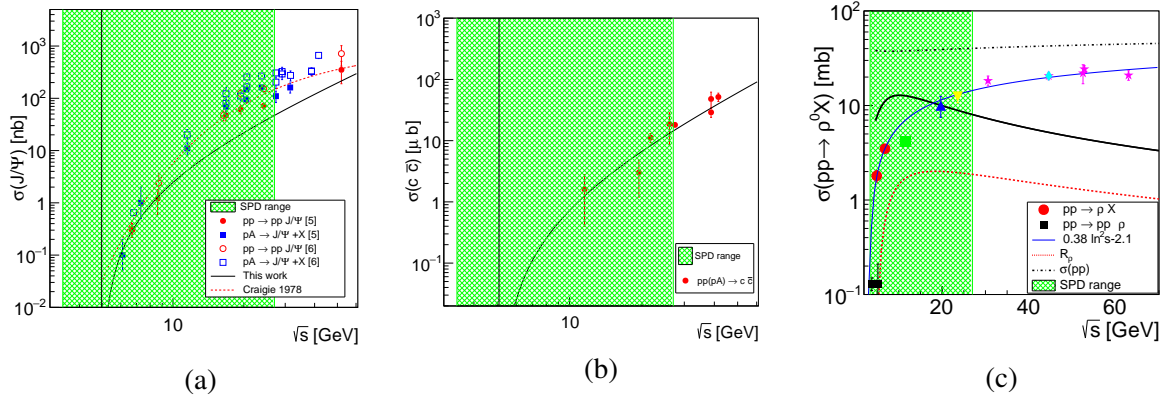


Figure 2.20: (a) Experimental data on J/ψ production in $p-p$ (red circles) and $p-A$ (blue squares) reactions, from the recollections in Refs. [284] (filled symbols) and [285] (open symbols). The solid line is the calculation from Ref. [239]. (b) Total charm production in $p-p$ and $p-A$ collisions. The data are from Ref. [289]. The line is a threshold parametrization (see text). (c) Cross-section for ρ -meson production in $p-p$ collisions: inclusive (different symbols and colors from different experiments) and exclusive data from $pp \rightarrow p p \rho$ (black squares). The calculation from Ref. [290] shown as a black line. The red dashed line is the renormalization factor. The black dash-dotted line is the total pp cross-section. The first red point is the inclusive measurement from Ref. [291]. The blue line is the parametrization from Ref. [292]. The green filled region represents the SPD range.

$N N \rightarrow \Lambda_C(\Sigma_C) \bar{D} N$ was derived for open charm in Ref. [293]. A detailed estimation of cross-sections and the expressions of the polarization observables can be found there. The existing information and estimations indicate that the near-threshold cross-section can be of the order of microbarns. The threshold cross-section normalized at the lowest existing value is plotted in Fig. 2.20(b), where the insert highlights the threshold region.

The charm production near threshold cross-section follows the behavior:

$$\sigma[\mu b] = 0.03(Q[\text{GeV}])^2. \quad (2.23)$$

It is plotted in Fig. 2.20(b) over a collection of data from Ref. [289] reanalyzed from several experiments on charm production in p - p and p - A collisions at different facilities. We stress that these are difficult measurements, with low counting rates and huge backgrounds, but even setting upper limits will be important, as no data at all are present in the threshold region.

The understanding of charm production (open or hidden) should unify different steps: parton-level hard process with production of $c\bar{c}$ pairs, after hadronization of $c\bar{c}$ into J/ψ or into charmed hadrons (mesons and baryons), including the final state interaction of the produced charmed hadrons with other particles. The relatively large transferred momenta involved in most processes of J/ψ production in hadron-hadron collisions allow one to treat the first step in the framework of perturbative QCD. But the applicability of QCD is not so straightforward for the description of the c -quark hadronization. In this respect, precise data collected in the SPD energy range will bring important information, especially if covering a wide range above the threshold.

3.5.2 Backward meson production

Larger counting rates are expected for light meson productions, since cross-sections are of the order of mb. The ρ^0 meson production in elementary collisions and on nuclei has been discussed, for example, in Ref. [294] and references therein. The ρ^0 inclusive cross-section has been measured at different accelerators since the 70's, mostly at CERN [295], and more recently by the HADES collaboration [291]. In Ref. [292], the following parametrization was suggested

$$\sigma(pp \rightarrow \rho^0 X) = (0.38 \pm 0.02) \ln^2 s - (2.1 \pm 0.4). \quad (2.24)$$

In Ref. [290], a specific kinematics, the backward light meson production in p - p or p - A collisions, was discussed in similarity to the "quasi-real electron method", where a hard photon is produced on the collision of electrons on any target [296]. Two important characteristics have been proved for the electron case: (i) the collinear emission probability has a logarithmic enhancement; (ii) the cross-section can be factorized in a term related to the probability of the meson emission with a given energy at a given angle from the beam particle, and a term related to the interaction of the beam remnant after emission on the target.

In hadron case, the cross-section can be written as:

$$\begin{aligned} d\sigma^{pT \rightarrow h_+ X}(s, x) &= \sigma^{nT \rightarrow X}(\bar{x}s) dW_{h_+}(x), \\ d\sigma^{pT \rightarrow h_0 X}(s, x) &= \sigma^{pT \rightarrow X}(\bar{x}s) dW_{h_0}(x), \end{aligned} \quad (2.25)$$

where h is a hadron, x ($\bar{x} = 1 - x$) is the energy fraction carried by the meson (the beam remnant). $dW_h(x)$ can be inferred using the QED result corrected by a renormalization factor in order to account for the emission of n real soft neutral pions escaping the detection.

The prediction of the model for backward ρ -meson production in p - p collisions is shown in Fig. 2.20(c) as a thick solid black line. The red dashed line is the renormalization factor, integrated over x . The total

p - p cross-section is the black dash-dotted line. The blue line is the parameterization of the inclusive ρ cross-section from Ref. [292]). The available data are also shown as different symbols and colors for inclusive measurements and as black squares for exclusive ρ production. Backward production can be of the order of several mb, and, therefore accessible at SPD even with the initial lower luminosity. Collecting precise, systematic data should help to refine the models and is of great interest for the collision on heavy targets as well. Backward kinematics could constitute an original contribution to the field, offering an alternative possibility to produce neutron beams.

3.6 Central nucleon-nucleon collisions

The main experimental basis for clarification of the non-perturbative QCD (NPQCD) baryon structure is the baryon spectroscopy and the short-range nucleon-nucleon interaction. The more the nucleons are overlapped during the collision, the higher sensitivity of the latter is to the NPQCD structure. The maximum sensitivity can be reached in conditions of overlapping of the quark core of nucleons and sufficiently long time of this overlapping. Unfortunately, these conditions are practically not met in the available nucleon-nucleon experimental data: at relatively low energies the effective momentum transfers are not sufficiently high, and at high energies the contents of colliding nucleons diverge too quickly. This circumstance explains why the region of the NN collisions at distances smaller than the radius of the nucleon core still remains unexplored. Access to this area is possible through the central collisions (CC) of the nucleons at adequate energies. The collisions are usually named central if the corresponding impact parameter R is small, $R < r_{core} \approx 0.4$ fm.

Overlapping of the nucleon cores can be achieved at the center-of-mass energies $\sqrt{s}_{min} = U_{rep}(0) + 2m_N$, where $U_{rep}(0)$ is the repulsive potential of the NN interaction at a zero distance, $U_{rep}(0) \approx 1$ GeV. Then the minimal energy of interest is $\sqrt{s}_{min} \approx 2.9$ GeV. At the energies less than 7.5 GeV (corresponding to the chiral symmetry breaking momentum $\Lambda_{\chi SB} \approx 1.2$ GeV/c [297, 298]) the resulting intermediate state is an excited $(6q)^*$ system of six chiral constituent quarks interacting via goldstone boson, gluon exchange and confinement potential. This interaction is supposed to be much more intensive than in the perturbative quark-gluon system, and provides therefore relatively long lifetime of the system, sufficient for manifestation of the NPQCD structure. Under certain conditions, it can even produce quasi-bound states, resonance dibaryons. It should be stressed that the $(6q)^*$ system under consideration is characterized by very high baryon and energy densities, since two baryons and the whole center-of-mass energy is concentrated in a small volume of about $4/3\pi(r_{core})^3$ size.

Decay of the $(6q)^*$ system leads to reconstruction of hadronic states in the form

$$pp \rightarrow (6q)^* \rightarrow N N \text{ Mesons}, \quad (2.26)$$

where *Mesons* denotes the system of light mesons, predominantly pions.

Peripheral N - N collisions proceed mainly via production of excited baryons N^* in the intermediate state

$$pp \rightarrow \{(NN^*) \text{ or } (N^*N^*)\} \rightarrow N N \text{ Mesons} \quad (2.27)$$

and have, in general, the final state similar to that in the central collisions (2.26). Therefore, in order to distinguish the central collision process (2.26) from the peripheral (2.27), one needs special centrality criteria. According to [299, 300], there are two such criteria: A) using of the reaction

$$NN \rightarrow d(90^\circ) \text{ Mesons}, \quad (2.28)$$

where $d(90^\circ)$ is a deuteron emitted at the angle close to 90° ⁸; B) smallness of the interaction region size $r_{int} < r_{core}$, where $r_{int} = 1/(-Q^2)^{1/2}$ with $Q = P_1 - D/2$. Here P_1 is the four-momentum of one of the initial nucleons and D is the four-momentum of the final joined nucleon pair.

⁸or reaction $NN \rightarrow \{pp\}_{S_0}(90^\circ) \text{ Mesons}$, where $\{pp\}_{S_0}$ is a proton pair in the 1S_0 state

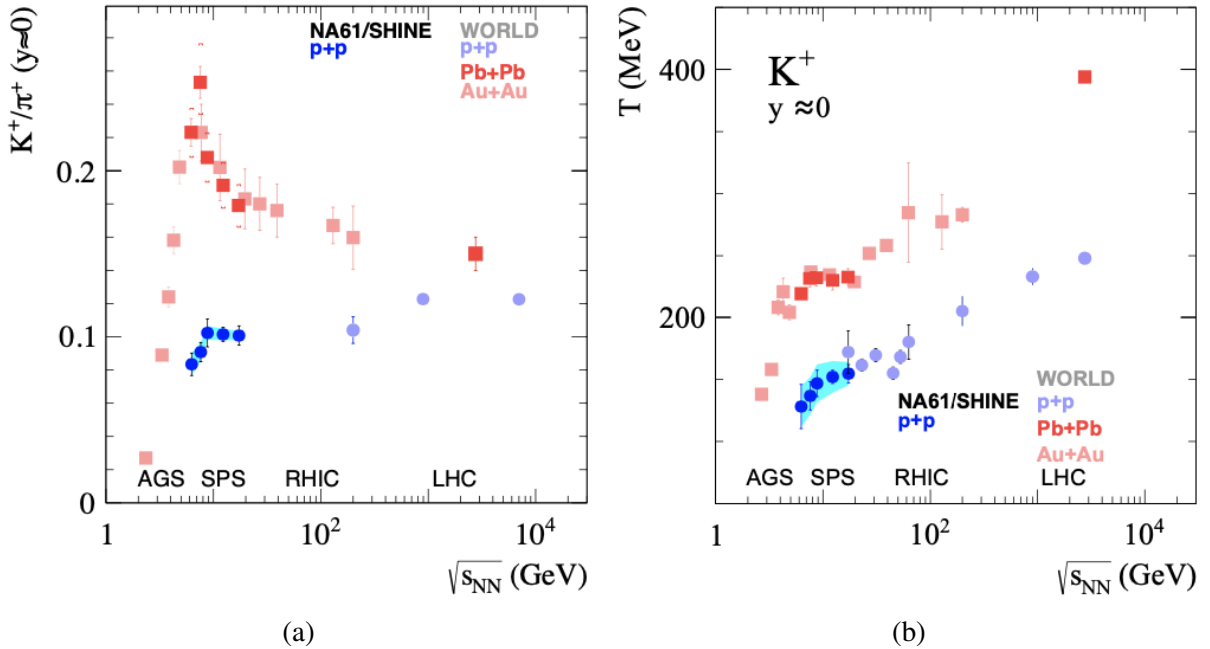


Figure 2.21: Energy dependence of the K^+/π^+ ratio (a) and the inverse slope parameter T of transverse mass spectra (b) at mid-rapidity. The NA61/SHINE results for inelastic p - p interactions are shown together with the world data [304].

Evaluation of feasibility of the experiments with the above centrality criteria shows [300] that at the expected luminosity [30] the event rate at SPD could be significant.

The following goals can be aimed at, in particular, in the experiments with central collisions:

- study of known and search for new dibaryon resonances in the region of $\sqrt{s} \approx 2.5 \div 7.5$ GeV;
- search for the predicted dominance of the σ -meson production [301];
- search for the expected effects caused by the chiral symmetry partial restoration (drop of mass and width of mesons) [302, 303];
- study of the energy dependence of the reaction (2.28) cross-section, which is sensitive to the strength of the confinement forces and the value of the chiral symmetry breaking momentum;
- first measurement of the analyzing power of the reaction (2.28) for transverse and longitudinal beam polarization.

It is worth to mention that experiments of this kind have never been carried out systematically. There exists a possibility of observing new unexpected effects that can induce new approaches in solving the fundamental problems of the non-perturbative QCD.

3.7 Onset of deconfinement in p - p and d - d central collisions

A study of the phase diagram of strongly interacting matter by varying interaction energy at central collisions of heavy ions is a primary goal of the NICA MPD experiment [219]. A structure in the energy dependence of several observables in the range of $\sqrt{s_{NN}} \approx 7 \div 12$ GeV was predicted for the transition to a deconfined phase. However, recently NA61/SHINE found intriguing similarities in p - p interactions, where no deconfinement transition is expected [304]. It can be interesting to study this effect in p - p and

d-d interactions in the first phase of SPD. These measurements can serve as an important crosscheck for the results of NA61/SHINE and, potentially, results of MPD.

The energy dependence of the K^+/π^+ ratio and inverse-slope parameters of transverse-mass spectra (the so-called effective temperature T) of kaons at mid-rapidity are shown in Fig. 2.21. The results for heavy ion collisions are plotted for comparison. The K^+/π^+ ratio in heavy ion collisions shows the so called horn structure. Following a fast rise the ratio has maximum at around 8 GeV and then settles to a plateau value at higher energies. Meanwhile, the collision energy dependence of the T parameter shows the so-called step structure at about the same value of $\sqrt{s_{NN}}$.

The K^+ yield is proportional to the overall strangeness production and pions can be associated with the total entropy produced in the reaction. Thus, the K^+/π^+ production ratio can be a good measure of strangeness-to-entropy ratio, which is different in the confined phase (hadrons) and the QGP (quarks, anti-quarks, and gluons). The K^+ is a proper observable for this measurement, because the anti-hyperon yield is small and the main carriers of anti-strange quarks are K^+ and K^0 with $\langle K^+ \rangle \approx \langle K^0 \rangle$ due to approximate isospin symmetry. Thus, the K^+ (or K^0) yield counts about half of all $s\bar{s}$ pairs produced in the collisions and contained in the reaction products. In contrast, the fraction of strange quarks carried by K^- (or \bar{K}^0) and hyperons is comparable, which makes the structure in the K^-/π^- distribution less pronounced.

A hydrodynamic expansion model of the strongly interacting matter is used for description of *A-A* collisions. This model is replaced in *p-p* collisions by excitation of resonances or strong fields between colour charges of quarks and diquarks (strings) [305] which makes them qualitatively different. However, the similarity of the transition energy in the central heavy ion collisions and the break energy in *p-p* interactions observed by NA61/SHINE provokes the question of whether there is a common physics origin of the two effects. This makes the precision measurement of the kaon-to-pion ratio in *p-p* and *d-d* interactions an interesting topic for the first phase of SPD, when the beam polarization is not available yet.

3.8 Study of the lightest neutral hypernuclei with strangeness -1 and -2

It is no doubt that the question of stability of the $A = 4$ double- Λ hypernuclei would be crucial for our understanding of the role played by hyperons in nuclear matter [306–308]. While it is still controversial for model calculations of such a four-body problem in the mode of weak binding [306, 309, 310], [311], [311, 312], we suggest that certain general properties arising from the weakly binding systems involving the 2-body and 3-body bound-state energies provide guidance for a possible stability of $_{\Lambda\Lambda}^4n$ [313, 314]. Meanwhile, we propose a sensitive reaction process for the search for $_{\Lambda\Lambda}^4n$ in deuteron-deuteron scatterings, i.e.

$$dd \rightarrow K^+ K^+ _{\Lambda\Lambda}^4n, \quad (2.29)$$

which is accessible at NICA. After all, it would rely on the experimental study to decide the dedicated dynamics for such an exotic system.

The quantum numbers of the ground state $_{\Lambda\Lambda}^4n$ will favor $J^P = 0^+$, where the neutron pair and Λ pair have spin 0, and namely, their spins are anti-parallel, respectively. At the same time, the total isospin is $I = 1$. Thus, the total wavefunction of the ground state is anti-symmetric under the interchange of the two nucleons or the two Λ .

The most ideal reaction for producing $_{\Lambda\Lambda}^4n$ should be $dd \rightarrow K^+ K^+ + T$, which is an extremely clean process, since the background processes involving the K^+K^- productions become irrelevant. Here T is a doubly-strange tetra-baryon system. It makes the measurement of the missing mass spectrum recoiling against the K^+K^+ pairs sensitive to the existence of any pole structure in the $nn\Lambda\Lambda$ system.

In Ref. [313], we have shown that the energy region above $E_{cm} \simeq 5.2$ GeV is favored to produce $_{\Lambda\Lambda}^4n$ with the total cross-section of about 2.5 nb. Here, based on the same analysis, we make a rough estimate of its production rate at the kinematics of SPD.

We estimate that the total cross-section at $E_{cm} = 6.7$ GeV, where the luminosity is $L = 10^{30} \text{ cm}^{-2} \text{ s}^{-1}$, will drop by about one order of magnitude compared with the peak value of about 2 nb. Thus, the events expected in effective one-year runtime (10^7 s) are

$$N = \sigma_{total} \times L \times t = 0.2 \text{ nb} \times 10^{30} \text{ cm}^{-2} \text{ s}^{-1} \times 10^7 \text{ s} \simeq 2000 , \quad (2.30)$$

which is sufficient for establishing the state. Even though the detection efficiency will reduce the events, there will be tens to hundreds of events to count.

Apart from the process of $dd \rightarrow K^+K^+$ (n, n, Λ, Λ), it is also interesting to look at the proton-proton collisions, $pp \rightarrow K^+K^+\Lambda\Lambda$, where the missing mass spectrum of K^+K^+ also provides a clean and direct way to search for the di-baryon $\Lambda\Lambda$, or to study the $\Lambda\Lambda$ interactions. For the proton-deuteron collisions, the double K^+ channel is $pd \rightarrow K^+K^+n\Lambda\Lambda$. The recoiled part of the double K^+ is $n\Lambda\Lambda$, which literally can produce the exotic H di-baryon. A direct measurement of such a system would provide rich information about both $\Lambda\Lambda$ and $n\Lambda$ interactions [315, 316], [317, 318], [319, 320]. Nevertheless, notice that the final states have access to the nK^+ invariant mass spectrum. The exclusive measurement of this process can also tell whether the light pentaquark state $\Theta^+(1540)$ exists or not.

3.9 Multiquark correlations and exotic state production

Multiquark correlations in the collisions of particles and nuclei play an important role in the understanding of QCD. Multiquark correlation phenomena may be divided into three classes. The first one can be related to parton distribution functions (PDFs) of the colliding hadrons and nuclei. In the leading twist approximation, in the nuclear PDFs there is a contribution at large $x > 1$, which is related with objects known as fluctons [321], or few-nucleon short-range correlations [268]. Beyond the leading twist, two- or three-quark correlations in parton distributions of hadron and nuclei are related with higher twist contributions. The second one is related to parton subprocesses. Namely, when multiparton scattering occurs, that is, e.g., when two partons from each colliding object scatter off each other simultaneously. The third class can be related to production of exotic multiquark resonance states, e.g., pentaquark and tetraquark states. Below one can find a brief possible outline for the studies at SPD, which can shed light on all the three classes of multiquark phenomena mentioned above.

3.9.1 Multiquark correlations: fluctons and diquarks

Nuclear fluctons consist of nucleons compressed in distances comparable with nucleon size, so that the flucton with five or six nucleons could be considered as a cold dense baryon matter since the effective nuclear density [322] would be as high as that in the core of neutron stars [271]. Fluctons are directly connected with cumulative hadron production in the nuclear fragmentation region [323, 324]. The flucton approach [325], which is based on hard QCD-factorization and EMC-ratio constraints, predicts an extra nuclear quark sea, which has a rather hard momentum distribution: the extra nuclear sea x -slope is equal to the x -slope of the valence quarks. It leads to "superscaling" for cumulative hadron production at $x > 1$ in the nuclear fragmentation region: the x -slope of all cumulative hadron distributions including the "sea" ones [325, 326] are the same. The superscaling phenomenon was experimentally confirmed by the ITEP group [327, 328]. In high- p_T cumulative processes at the central region, other contributions should be added to the contribution of the nuclear PDFs at $x > 1$, such as the contributions from the PDFs of the other colliding object and possible intranuclear rescattering effects [329, 330]. Therefore, beyond the nuclear fragmentation region, one should observe deviations from superscaling for cumulative production. Another aspect of multiquark correlations is two-quark correlations (diquark states) in baryons

[331]. This is an important source of high- p_T baryon production [332–334]. Being a higher-twist the diquark contribution can describe the strong scaling violation for baryon production in hard processes at SPD energies [333–335].

3.9.2 *Multiparton scattering*

Measuring a few-particle correlation at SPD, one can study multiparton scattering processes [335], which are related to 2D- and 3D- PDFs. It is also significant for production of multiquarks systems [335, 336].

3.9.3 *Multiquark exotic state production*

Multiparton scattering [336] provides a unique opportunity to study production of various multiquark states, such as, e.g., in Refs. [337–339] at the SPD energies. For multiquark systems with possible diquark structure [340, 341] it can be an issue of particular interest [335, 336].

Near the thresholds of heavy quarks production, where relative velocities of final particles vanish, formation of new type of resonances, such as J/ψ - N , is expected [342–345]. This question became especially interesting after pentaquark observations at LHCb [346, 347] in the decay $\Lambda_b^0 \rightarrow J/\psi p K^-$.

The enhancement effect was observed at the thresholds of the reactions $e^+e^- \rightarrow p\bar{p}$ and $e^+e^- \rightarrow \Lambda\bar{\Lambda}$ [348] and also in the decay $J/\psi \rightarrow p\bar{p}\gamma$ [349]. Furthermore, the double spin correlation A_{NN} measured in large angle ($\sim 90^\circ$) p - p elastic scattering [228] demonstrates an enhancement near the strange ($\sqrt{s} = 2.5$ GeV) and charm ($\sqrt{s} = 5$ GeV) thresholds, respectively, in the two-baryon system. According to [236], the observed strong spin correlations are consistent with formation of “octoquark” resonances $uuds\bar{s}uud$ and $uudcc\bar{u}ud$ in the s -channel. SPD has a possibility of searching for such states.

To summarize this section, SPD, together with the study of the inclusive particle production and few-particle correlations at different kinematic regions in p - p collisions, as well as in the cumulative processes with light nuclei, has a unique opportunity to test various aspects of multiquark correlations: from the cold dense baryon matter to the exotic multiquark resonance production.

3.10 Yield of antiprotons in hadronic collisions for astrophysical dark matter search

Dark matter (DM) is a long-standing mystery in cosmology. It makes up more than 26% of the Universe [350], yet we still do not know its identity. Evidence of DM is mostly gravitational, *e.g.* the rotation curves of spiral galaxies and the mass discrepancy in galaxy clusters [351]. The most favored candidate for DM is the Weakly Interacting Massive Particles [352]. Different search approaches are employed to search for DM, each with its own underlying paradigm. The main approaches are collider searches, direct detection, and indirect detection. The latter includes astrophysical searches that seek to detect potential anomalous signatures that are hypothetically produced via pair annihilation and decay of DM particles, in the cosmic ray (CR) spectrum [352]. Naturally, these experiments track different signal components. However, the chance of detection is thought to be higher for rare antimatter components, such as antiprotons. Recently, the AMS-02 experiment [353] has measured a cosmic antiproton flux with unprecedented precision over a wide energy range (from 1 to 450 GeV) [354]. However, we still cannot confirm or rule out an antiproton signature in these measurements due to several sources of uncertainties [355].

Secondary antiprotons are produced in collisions of primary CRs with the interstellar medium (ISM). To be able to detect any anomalous signal, we first need to subtract the flux of antiprotons produced by these CR-ISM collisions. Even though there are several sources of uncertainty standing in the way of pinpointing what this ordinary flux is—such as propagation parameters, solar modulation, and primary spectra slopes—the most significant uncertainty, which ranges from 20% to 50% according to the energy, comes from antiproton-production cross-sections [355]. Almost 70% of the secondary antiproton yield

is produced in p - p collisions. However, the existing datasets for this production channel are incredibly scarce, and mostly date back to before 1980. Moreover, all old datasets did not account for the hyperon decay or isospin effect [356]. As for other production channels, data are almost non-existent. Thus, if we were to catch up with the accuracy of AMS-02 measurements, we would have to perform a new precision measurements of antiproton-production cross-sections in p - p collisions, as well as other production channels (*e.g.* p - d , p - 3He , p - 4He , and 4He - 4He). It is also hoped to study the contribution of different production mechanisms, such as hyperon (namely, $\bar{\Lambda}$ and $\bar{\Sigma}^-$) and neutron decays. The kinematic range that needs to be covered to achieve that has already been outlined [357].

Preliminary MC studies [358, 359] show that at the SPD energy range, the production rate is $> 10^5 \text{ s}^{-1}$, which would minimize the statistical uncertainty. In addition, the 4π angular acceptance will allow SPD to access a wider kinematic range, in terms of transverse momenta, in comparison with fixed-target experiments operating at the same energy level. With a precise TOF (time-of-flight) system ($\sigma_{TOF} \sim 70 \text{ ps}$), K^-/\bar{p} separation can be achieved with a high purity of up to $\sim 3.5 \text{ GeV}/c$. SPD can also contribute to the measurement of hyperon-decay contribution via reconstruction of secondary vertices [359]. To summarize, the SPD detector can make a sizable contribution to the search for physics beyond the standard model in terms of the astrophysical search for DM.

Chapter 3

Polarized beams

1 Available species and types of collisions

The basic specification to the available polarization states and combinations is the following:

- protons (possibly helium-3 ions at the second stage): vector polarization, longitudinal and transverse direction in respect to the particle velocity;
- deuterons: vector and tensor polarization, vertical direction of polarization, longitudinal polarization up to about a $4 \text{ GeV}/c$ momentum, and longitudinal polarization at discrete momentum of about $13 \text{ GeV}/c$;
- possibility of colliding any available polarized particles: p - p with a luminosity up to $10^{32} \text{ cm}^{-2} \text{ s}^{-1}$ and d - d , p - d , p - ^3He , d - ^3He with a luminosity of $10^{30} \text{ cm}^{-2} \text{ s}^{-1}$ at the collision energy equivalent to p - p collisions;
- possibility of asymmetric collisions should be considered as an option for the future development of the facility;
- for essential reduction of a systematic uncertainty, a spin-flipping system is implemented, which allows one to rotate the polarization direction with a step of 90° simultaneously in all bunches within a minimal time period.

Feasibility of the technical implementation of the above-mentioned conditions is presented in Refs. [360–363].

2 Beam structure, intensity, and luminosity

The beam structure of polarized proton and deuteron beams at the first stage will correspond to the one optimized for the NICA heavy-ion mode. Some of the important for SPD operation parameters in the case of a bunched beam are the following: number of bunches – 22, bunch length $\sigma = 60 \text{ cm}$, collider orbit length – 503 m, bunch velocity $v \approx c = 3 \times 10^8 \text{ m/s}$, revolution time $\tau = 1.67 \times 10^{-6} \text{ s}$, bunch revolution frequency $f \approx 0.6 \text{ MHz}$, time gap between bunches $\Delta\tau = 76.0 \times 10^{-9} \text{ s}$, crossing angle at the SPD interaction point – 0° . The dependence of the p - p -collision luminosity on the energy and number of protons is presented in Fig. 3.1 [30].

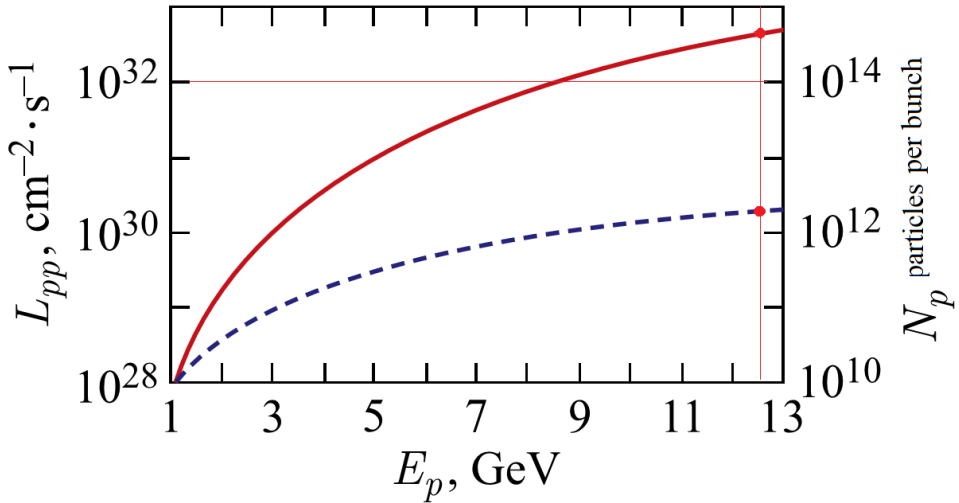


Figure 3.1: Normalized dependence of the luminosity L_{pp} (the red curve and the left scale) and the beam intensity N_p (the blue curve and the right scale) on the proton kinetic energy in the p - p -collision [30].

As it is clear from the calculations, the luminosity level of $1 \times 10^{30} \text{ cm}^{-2} \text{ s}^{-1}$ is reached at a bunch intensity of 10^{11} polarized protons, whereas to obtain the level of $1 \times 10^{32} \text{ cm}^{-2} \text{ s}^{-1}$ a multi-bunch storage mode should be used [364]. The average luminosity in this case is reduced due to the cycle time efficiency. Basic factors for that are presented in the Table 3.1.

The effectiveness (Figure of Merit, FOM) of a collider experiment with two polarized beams depends not only on the collision luminosity L , but also on the polarization degrees P_1 and P_2 of the colliding beams [365]:

$$FOM = LP_1^2 P_2^2. \quad (3.1)$$

The statistical uncertainty of a measurement is proportional to $1/\sqrt{FOM}$, so the FOM describes sensitivity of the experiment or resolution. The value of the FOM depends on a specific scheme applied for suppression of depolarizing effects in each element of the accelerator complex such as the ion source,

Table 3.1: Main parameters of the NICA operation cycle.

Parameter	Injected beam energy	
	2 GeV	7.5 GeV
Nuclotron dipole field ramp up/down, T/s	0.6/1	
Dipole magnetic field, T	0.42	1.22
Number of accelerated particles per pulse	7×10^{10}	
Number of cycles to store 2×10^{13} particles	2×285 (per both rings)	
Storage time, s	923.5	2291
Other time factors, s		~ 50
Luminosity lifetime (30% polarization degradation), s		5400
Beam deceleration to the new injection portion, s	~ 25	~ 12
Total cycle duration, s	~ 6500	~ 7850
Cycle time efficiency, %	83.1	69.8
Double polarized collision efficiency FOM, %		~ 0.5
Luminosity averaged over cycle, $10^{32} \text{ cm}^{-2} \text{ s}^{-1}$	2.9	2.45

beam transportation lines, the Nuclotron and collider rings. It also depends on the beam store procedure, needed to provide the specified luminosity and other conditions of the experiment as well. The strong dependence of the FOM on the polarization (the fourth power) requires a high level of attention to maintain the polarization degree at all stages of the operation.

3 Polarization control and monitoring

3.1 Transportation of polarized ions in the accelerator complex

Polarized protons and deuterons from the SPI are first accelerated in the linac LU-20M and afterwards are injected and accelerated in the Nuclotron to the specified energy and extracted to the collider via the long transfer line. The main tasks at this stage are the following: i) preservation of the beam polarization during acceleration in the Nuclotron (and in the collider as well) and ii) polarization control in the collider mode. Moreover, it is necessary to adjust the polarization direction in the transfer line and the other points of the collider orbit.

3.2 Spin dynamic modes in the NICA collider

From the spin dynamics point of view, the NICA collider can operate in two modes, namely: in a Distinct Spin mode (DS-mode) and in the Spin Transparency mode (ST-mode) [363, 366]. In the DS-mode periodic motion of the spin along the particle orbit is the only possible way, i.e. – stationary magnetic structure selects the only one stable direction of the polarization vector in any point of the particle orbit and the fractional part of the spin tune is not equal to zero. In the ST-mode the direction of the spin vector is reproduced in any point at every turn, i.e. the magnetic structure of the accelerator (or the storage ring) is transparent for the spin – the fractional part of the spin tune is equal to zero [367].

The main difference between the DS- and ST-mode can be observed while manipulating the spin direction during physics data taking. In the ST-mode, the spin motion is very sensitive to magnetic field changes, because particles move in the vicinity of the integer resonance. In the case use of the additional "weak" magnetic field, the rotating spin at small angles $\phi \ll 1$ provides the needed polarization direction at any specified point of the collider [368, 369]. It is possible to use a pair of solenoids with a field integral of $1 \text{ T} \times m$, which would introduce negligible distortions to the closed particle orbit in order to produce the necessary variation of the spin angle in the NICA collider over the momentum range up to $13.5 \text{ GeV}/c$. In the case of the DS-mode similar procedure will require spin rotators based on a strong field, rotating the spins at the angles of $\phi \sim 1$. Thus, in case of changing the polarization direction from the longitudinal to the transverse one, it would be necessary to apply the transverse field with the total integral of $20 \div 30 \text{ T} \times m$, which would result in strong distortions of the closed particle orbit. The amplitude of the distortions can reach tens of centimeters at low energies. Thus, efficient polarization control of ions, especially deuterons, by means of quasi-stationary weak fields is possible only if the ST-mode is used.

The configuration of the NICA collider with two solenoid snakes inserted into its straights allows one to operate with polarized proton and deuteron beams in the both DS- and ST-modes (see Fig. 3.2)

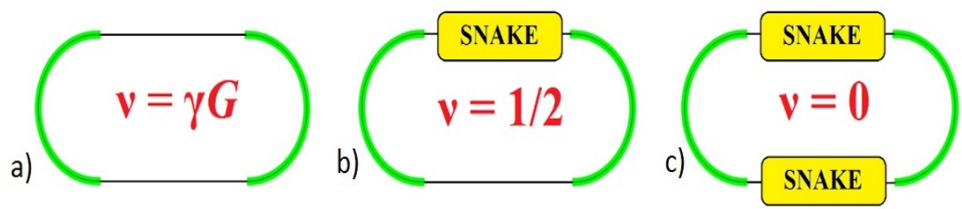


Figure 3.2: Possible operating modes with polarized beams at the NICA collider: a) without snakes, b) with one snake, c) with two snakes.

[370, 371].

The stable polarization direction in the NICA collider with snakes switched off is vertical at any point of the orbit in the NICA collider, whereas the spin tune is proportional to the particle energy: $v = \gamma G$, where G is the anomalous part of the gyromagnetic ratio and γ is the relativistic Lorentz factor. The collider operates in the DS-mode practically over the total energy range, because $\gamma \neq k/G$, where k is an integer. At integer spin resonances $\gamma G = k$ the collider operates in the ST-mode. After switching one of the two snakes on, the collider operates in the DS-mode with the spin tune equal to half, whereas if two snakes are switched on, it operates in the ST-mode with the spin tune equal to zero.

3.3 Specifications to the polarized beams in the collider

Different experiments are planned with polarized proton, deuteron, and helium-3 (in the future) beams to identify and study various observables for multiple physics tasks: Drell-Yan, J/ψ , high- p_T hadrons, exotic states, etc. The polarization control system should satisfy the following main conditions:

- obtain both longitudinal and transverse polarization in the MPD and SPD detectors with a polarization degree not less than 70% and a polarization lifetime of not less than the beam lifetime;
- provide collision luminosity of $\sim 10^{30} \div 10^{32} \text{ cm}^{-2}\text{s}^{-1}$ over the particle momentum range from 2 to 13.5 GeV/c ;
- provide the particle energy scan with a step of $1 \div 2 \text{ GeV}$ within the energy range of $7 \div 27 \text{ GeV}$ and 0.3 MeV at lower energies. The deuteron beam at $\sim 5.6 \text{ GeV/u}$ is a special case;
- provide a possibility of operation in the asymmetric particle momentum mode;
- make simultaneous spin-flips for all bunches in the case of Spin Flipping experiments (SF-system).

3.4 Polarization control in the NICA collider without snakes in the ST-mode

The ST-mode is enabled at the discrete energy points corresponding to the integer spin resonances: $\gamma = k/G$. For protons, the number of points corresponding to the ST-mode is 25 starting from the minimal energy $E_{kin}^{min} = 108 \text{ MeV}$ with a step of $\Delta E = 523 \text{ MeV}$. For deuterons, there is only one point $E_{kin} = 5.63 \text{ GeV/u}$ corresponding to the momentum 13 GeV/c . A possible scheme of the ion polarization control in

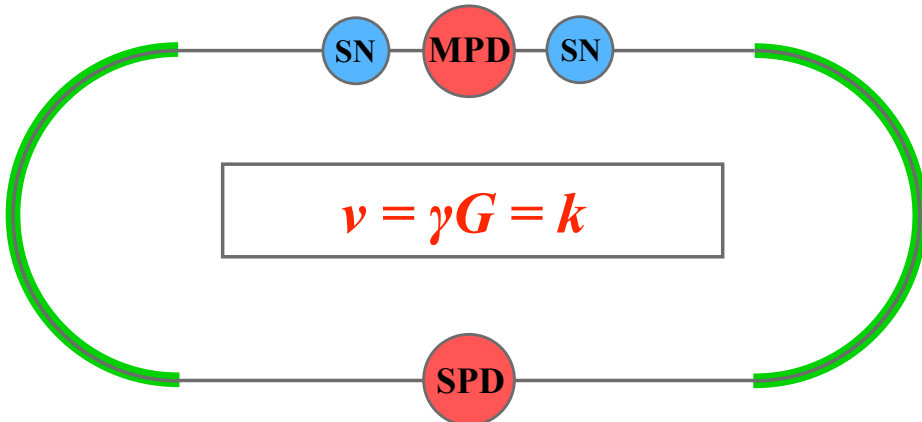


Figure 3.3: General scheme of the polarization control at integer spin resonance points.

the collider at the integer spin resonances is presented in Fig. 3.3. Two spin navigator insertions (SN) placed near MPD are used to stabilize the needed polarization direction at any point of the collider ring,

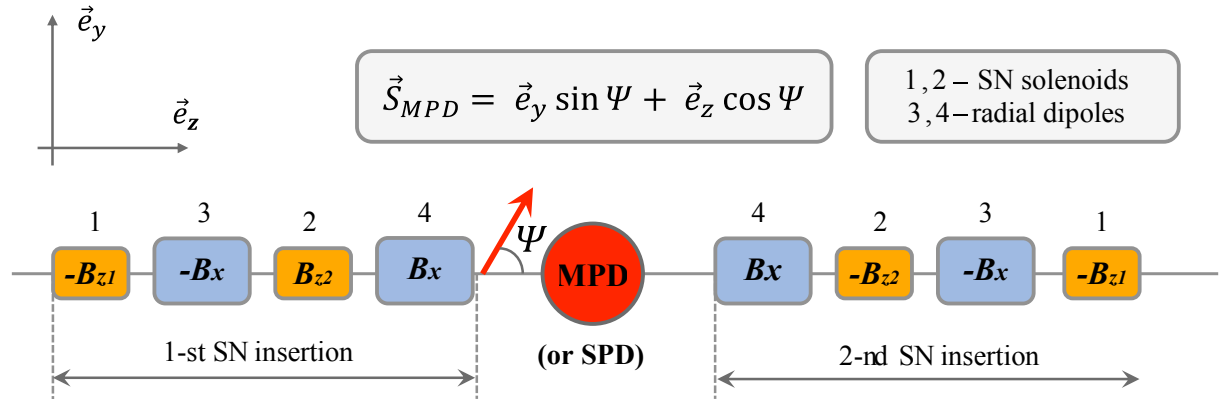


Figure 3.4: Detailed scheme of the spin navigator insertion in the collider in the ST-mode.

including the collision points, at injection, etc. A detailed scheme of the SN's is presented in Fig. 3.4. The SN solenoids (marked as 1 and 2) generating longitudinal magnetic fields B_{z1} and B_{z2} are placed among the collider structural magnets (marked as 3 and 4) that generate radial fields $\pm B_x$, deflecting the beams to the collision plane of MPD [366].

The scheme makes the ion polarization control possible in the vertical plane (yz) in MPD or SPD (Ψ is the angle between the polarization and the particle velocity vectors). A field integral of $0.6 T \times m$ of one of the navigator solenoids provides stable operation of the scheme in the entire energy range. The spin tune for protons is then $\nu = 0.01$. If we limit the field maximum to 1.5 T, the magnetic length of the SN solenoid unit will be 40 cm. The real relative scale of the SN solenoid (40 cm long), the radial dipoles, and the distances between them are shown in Fig. 3.5.

The scheme of the SN solenoids installation in the vertical plane together with the collider lattice elements is presented in Fig. 3.6. The beam convergence angle in vertical plane, which is defined by the dipoles with magnetic fields transverse to the beam axis is $\alpha_x = 0.04$ rad. The distance between the collider rings in the vertical plane is 32 cm. The distances between the closed particle orbits in the vertical plane are $\Delta y_{dip} = L_x a \approx 5.5$ cm and $\Delta y_{sol} = \Delta y_{dip} + 2L_1 a \approx 22$ cm at the output of the common radial dipole and at the exits of the control solenoids, respectively.

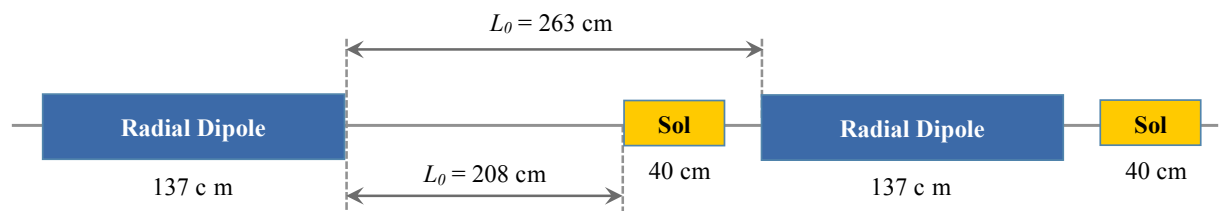


Figure 3.5: Placement of the SN solenoids in the horizontal plane.

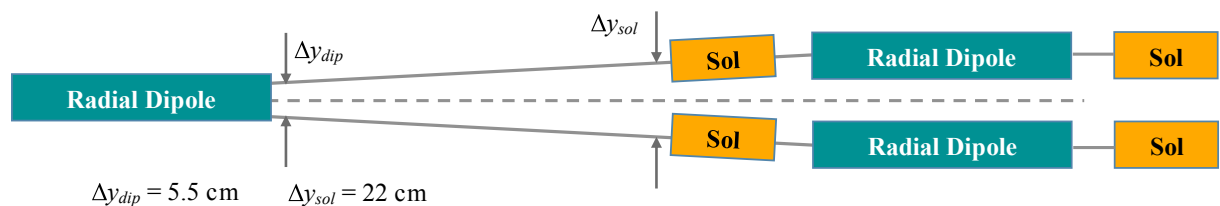


Figure 3.6: Placement of the SN solenoids in the vertical plane together with the radial dipoles.

3.5 Ion polarization control in the ST-mode by means of two snakes

Two solenoidal snakes installed symmetrically relative to both MPD and SPD setups will provide implementation of the ST-mode in the NICA collider (Fig. 3.7).

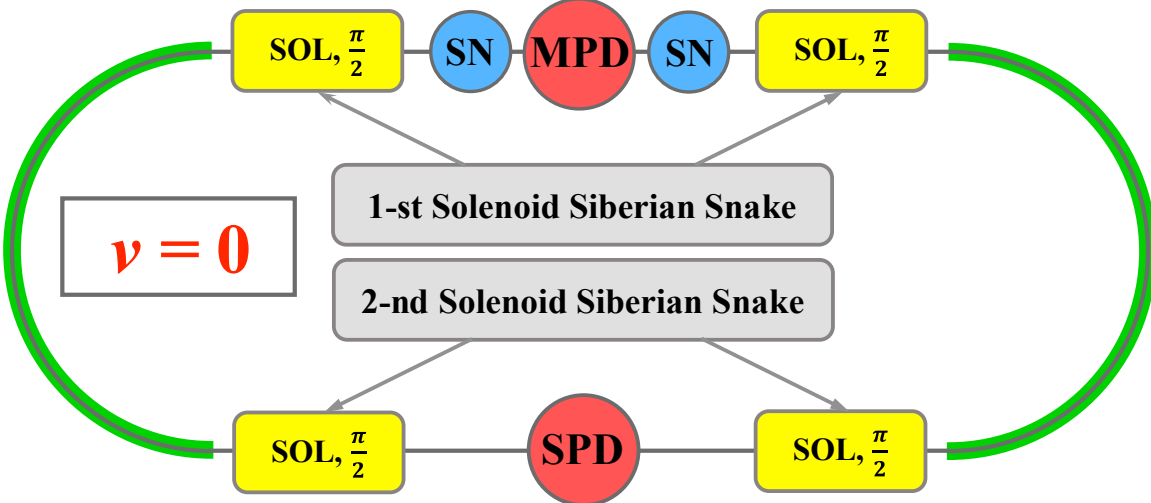


Figure 3.7: Implementation of the ST-mode in the NICA collider.

The configuration makes it possible to turn the spin in the vertical plane (yz) of MPD or SPD detector, whereas in the collider magnet arcs the polarization vector is moves in the median plane (xz) [372]. The ST scheme with two snakes provides a zero spin tune at any point of the particle energy. It is very important for optimization of the effective NICA operation at the highest possible luminosity of p - p collisions, due to a necessity of storing particles at an energy level that provides proper conditions for electron cooling of the stored beam. Only in this case it is possible to form particle bunches with a high number of particles and a high degree of polarization at low energy (about 1 GeV) with further acceleration up to the experiment energy. The total integral of the longitudinal solenoidal field should reach $4 \times 25 \text{ T} \times \text{m}$ per ring at a proton momentum of $13.5 \text{ GeV}/c$ and $4 \times 80 \text{ T} \times \text{m}$ for deuterons, respectively. A distributed system consisting of short solenoids is possible, i.e. in the case of 6 T solenoids the total length of 4.2 m is sufficient to form a half-length snake. It is possible to adopt the collider lattice structure optimized for a heavy ion beam for the case of the ST-mode at the protons mode over the total energy range. Weak control solenoids barely distort the orbital motion in the collider, whereas strong solenoids of the snakes lead to a strong betatron tunes coupling. As the longitudinal field of the snakes changes proportionally to the particle momentum, the collider magnetic optics stays adequate to the stable motion of a polarized particle during the beam acceleration phase. Matching the solenoids with the collider structure is provided by means of a proper choice of the work point by means of structural KF (focusing) and KD (defocusing) quadrupole lenses. A possible scheme of the distributed snake (one half) based on short 6 T superconducting (SC) solenoids is shown in Fig. 3.8. The elements are the following: SOL-SC solenoid,

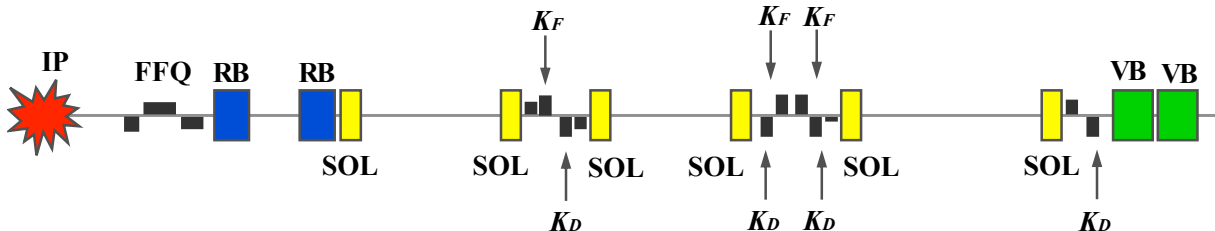


Figure 3.8: Distributed snake (one half) based on short 6 T SC solenoids.

FFQ – final focus triplet of the collider, VB – structural dipole magnets; RB – bending dipoles with a transverse field making for converging bunches in the interaction point [373].

3.6 Stability of spin motion

In the absence of a spin navigator, polarization is strongly influenced by the fields of lattice imperfections and fields associated with betatron and synchrotron oscillations, i.e. with orbital beam emittances. The magnitude of this effect on polarization is determined by the strength of the zero spin tune resonance. To stabilize the polarization during the acceleration process or when controlling the polarization direction in the ST-mode it will be necessary to maintain the spin tune caused by the spin navigator much higher than the strength of the zero spin tune resonance. The calculations have shown that the level of 10^{-2} for protons and 10^{-4} for deuterons would be sufficient [374]. These values impose limitations on the minimum field integral in each of the weak control solenoids – $0.6 \text{ T} \times \text{m}$.

3.7 Spin flipping system

The spin flipping (SF) system makes it possible to carry out spin physics experiments at a much higher level of accuracy [375]. Being equipped with such a system, the SPD setup will have following advantages:

- no need for reversing the polarization direction at the polarized ion source;
- no need for bunch-to-bunch luminosity measurements and a bunch monitoring system;
- the possibility of comparing collisions of bunches of any particle spin directions (vertical-longitudinal, vertical-radial, radial-longitudinal, etc.).

The SF-system based on quasi-stationary fields is naturally implemented in the ST collider mode. The pair of SN solenoids provides simultaneous influence on the polarization direction and the spin tune. Thus, the possibility of the spin tune stabilization during the spin flipping appears, preventing both zero spin tune and higher-order spin resonance crossing. The polarization degree will preserve an exponential accuracy, provided the field of the SN solenoids changes slowly. A typical flipping time is approximately estimated as 1 ms and 10 ms for the proton and deuteron, respectively. Enabling the SF-system in the DS-mode will require inserting an RF-module of a several MHz range and the field total integral of $1 \text{ T} \times \text{m}$, which is a rather challenging technical task.

3.8 Online control of the polarization in the collider

A unique possibility of online polarization control becomes available when the collider operates in the ST-mode [361]. Since the field ramp in the SN solenoids ($t_{change} \sim 0.2 \text{ s}$) is much larger than the spin precession period around the induced spin field ($t_{rev} \sim 10^{-4} \text{ s}$), any manipulations with the spin direction at the spin tune will occur adiabatically and the polarization degree during the experiment time will be maintained constant with an exponent accuracy. The direction of the polarization vector will be a function of the SN solenoids field and can be defined by means of the SN field measurements. Thus, the ST-mode makes it possible to carry out experiments at the NICA collider at a new level of accuracy.

3.9 Polarized beams dynamics in the Nuclotron

As it was already mentioned, the stable polarization direction in the Nuclotron is vertical, and the spin tune is proportional to the beam energy: $v = \gamma G$, which definitely leads to the crossing of spin resonances during particle acceleration and, as a consequence, to resonance depolarization of the beam. There is no problem with deuterons: the only one integer spin resonance at $E_{kin} = 5.6 \text{ GeV}$ exists in the NICA energy

range. The spin direction at this point can be controlled also by means of a weak solenoid inserted into the accelerator lattice. The number of different spin resonances in the proton mode is much larger. Logarithmic graphs of linear spin resonance strengths scaled to the specific strength corresponding to complete depolarization of the beam are presented in Fig. 3.9 [376–378]. The proton energy range E_p corresponds to the one available at the Nuclotron. Each graph is divided into three areas that correspond to the intermediate crossing (between the horizontal lines), fast crossing (below the green line) and adiabatic crossing (above the blue line). The lines of the fast and adiabatic crossing correspond to 1% loss of the polarization degree.

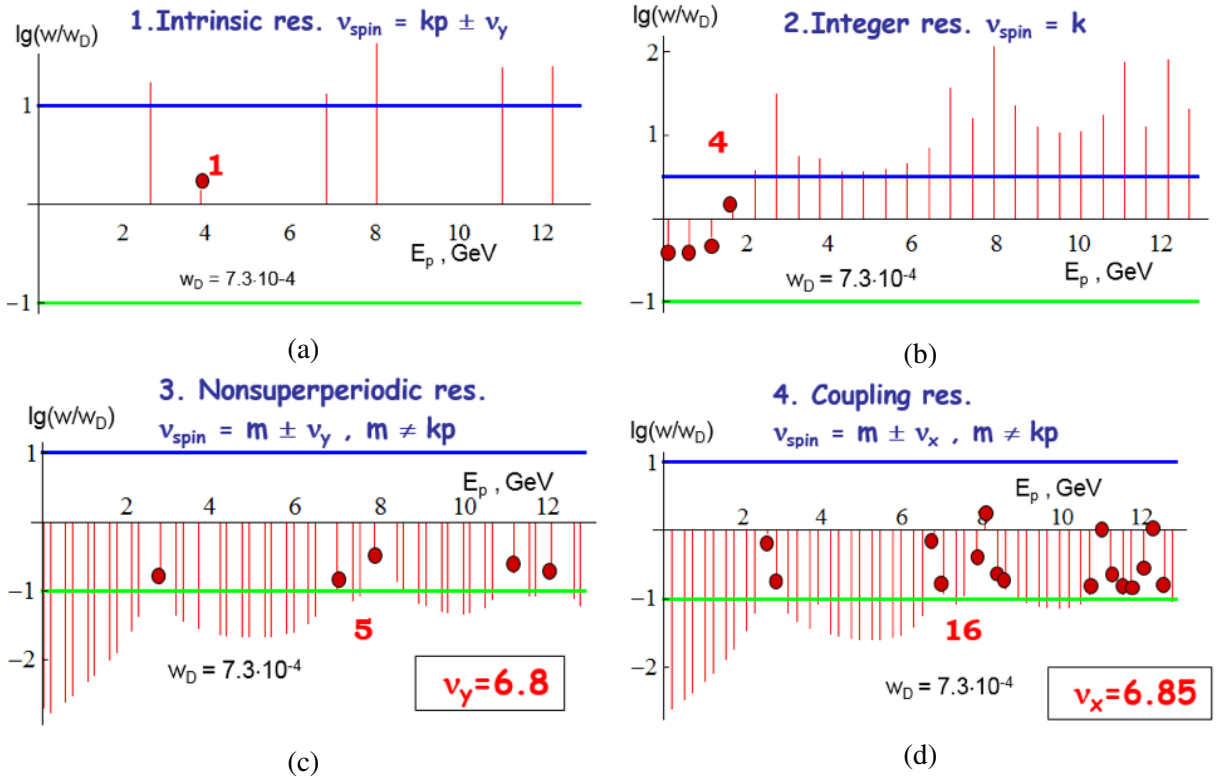


Figure 3.9: Linear spin resonances in the Nuclotron in the polarized proton mode.

The parameters taken for calculation of the spin resonance strengths were the following: magnetic field ramp – 1 T/s; beam emittance (horizontal and vertical) at the injection energy – 45π mm·mrad; quadrupole misalignment errors – 0.1 mm; errors of angular alignment of the structural dipole and quadrupole magnets – 0.01 rad; and the relative error of the quadrupole gradients – 0.001. The resonances marked with red circles are dangerous and lead to the beam depolarization after their crossing.

To keep the polarization of the proton beam at a proper level, a partial Siberian snake based on a solenoid will be used. Two options have been considered: i) using a weak 5% snake with a field integral of 0.65 T·m, which can save the proton beam polarization up to 3.4 GeV/c and ii) using a 25% snake (~ 12 T·m) [379–381]. The first one is efficient if the collider operates in the ST-mode with two snakes and injection of the beam is provided at a low energy (around 1 GeV), whereas the strong enough snake used in the second option could save the polarization over the total energy range in the Nuclotron and is suitable for the operation at integer resonances. The choice of energy points is limited to the points of integer resonances.

Table 3.2: Polarization in the SPD and MPD interaction points in the DS- and ST-modes.

Collider configuration	Spin tune	Spin mode	Polarization direction at SPD and MPD
Without snakes	$\gamma G \neq k$	DS	Vertical at SPD and MPD
Without snakes	$\gamma G = k$	ST	Any direction at SPD or MPD
With one snake (SPD)	1/2	DS	Longitudinal at MPD
With one snake (MPD)	1/2	DS	Longitudinal at SPD
With two snakes	0	ST	Any direction at SPD or MPD

Table 3.3: Features of the operation with polarized protons and deuterons in the NICA collider.

Collider configuration	Spin mode	SF-system	Online polarimetry	Energy energy
Without snakes	DS	No	No	No
Without snakes	ST	Yes	Yes	No
With one snake	DS	No	No	Yes
With two snakes	ST	Yes	Yes	Yes

3.10 Operation modes of the NICA collider with polarized beams

The NICA collider with two solenoidal snakes will make the following configurations possible (see Table 3.2) [366].

If the snakes installed in SPD and MPD sections are switched off, the DS-mode with vertical polarization at any point of the collider orbit is activated. Certain narrow energy gaps where the ST-mode at integer resonances exist, give possibility of having any direction of the polarization in both detectors. After switching one of the snakes on, the collider will operate in the DS-mode with the spin tune 1/2. The snake transforms the spin motion completely, providing a stable longitudinal direction of the polarization in the collider orbit section opposite the snake.

If two dynamic solenoid snakes are switched on, the ST-mode is activated. The spin tune does not depend on the particle energy and is equal to zero, which gives a possibility to obtain any direction of polarization at any point of the collider orbit. The features of the collider operation in the polarized modes are shown in Table 3.3.

It is very important to implement the possibility of polarized beam acceleration in the NICA collider without loosing the polarization degree. The problem of reaching the highest possible luminosity of polarized proton collisions is connected with the particle multi-bunch storage in the collider and electron cooling of the stored beam during the process. The optimal proton beam kinetic energy at the beam injection into the collider is about 1 GeV [362, 382].

3.11 Conclusion

The proposed scheme of the ion polarization control in the NICA collider is adapted easily to the collider magnetic optics at any modes of the polarization control. Significant advantages could be gained by using the spin transparency mode. A polarization degree of about 70% is provided at the collision points. The polarization lifetime is expected to last for several hours that is comparable with the beam lifetime. We have not mentioned particular measurement and monitoring systems that should be designed at the

stage of the technical project preparation, and namely: precise measurement of the luminosity, absolute polarimeter based on a gas jet, targeting stations, etc.

Chapter 4

Detector layout

1 General design

The physics tasks presented in Chapter 2 impose general requirements on the concept of the Spin Physics Detector. Unlike the case of high-energy collisions where the collision energy \sqrt{s} is a few orders of magnitude higher than a typical hard scale Q of the studied reactions, at the SPD energies for all the probes planned to be used to access the gluon content of the colliding particles $Q \sim M_{J/\psi} \sim 2M_D \sim p_T \gamma_{min}$ is just a few times less than $\sqrt{s}/2$. Therefore, one should expect quite a uniform distribution of all signal particles (muons from the J/ψ decay, prompt photons, products of D -mesons decay, etc.) over the kinematic range. In other words, there is no preferable range in rapidity, which could be specified for each probe for the optimal overall performance. Together with relatively small cross-sections of the discussed probes, this fact leads one to a requirement of $\sim 4\pi$ coverage of the SPD setup.

The Spin Physics Detector must have sufficient tracking capabilities and a magnetic system for spectrometric purposes for the majority of the addressed physics tasks. It has to be equipped with a muon system thick enough for effective separation of muons and hadrons to make it possible to deal with the decay $J/\psi \rightarrow \mu^+ \mu^-$. A precision vertex detector is needed for the recovering of the secondary vertices from the decays of $D^{\pm/0}$ mesons and other short-lived particles. An electromagnetic calorimeter ensures capability to detect signal and background photons. A low material budget and general transparency of the setup should also provide favorable conditions for the photon physics. Hadron identification capability is needed for any physics task with protons and/or kaons in the final state, in particular, to enforce a signal-to-background ratio for D -mesons selection, and also to improve tracking at low momenta. Since tiny effects are intended to be investigated, a triggerless DAQ system is planned in order to minimize possible systematic uncertainties of the measurements.

Strict limitations to the SPD detector layout arise from the external conditions, such as the maximal possible load to the floor of the SPD experimental hall (1500 tons together with the lodgement and the detector moving system). Together with the requirement to have the overall thickness of the muon system not less than 4 nuclear interaction lengths (Λ_I), this limits the outer size of the SPD detector and the size of the inner part of the detector. The location of the collider infrastructure, in particular, focusing elements, also defines the size of the SPD setup along the beam axis. More details could be found in Chapter 3.

The general layout of the SPD is shown schematically in Fig. 4.1. The detailed description of each subsystem could be found below. Table 4.1 brings together the elements of the SPD physics program and the requirements to the experimental setup. We would like to emphasize here that the most part of the SPD gluon program can not be performed at MPD [219], another detector at the NICA collider,

optimized for operation at a high multiplicity of charged tracks and relatively low luminosity.

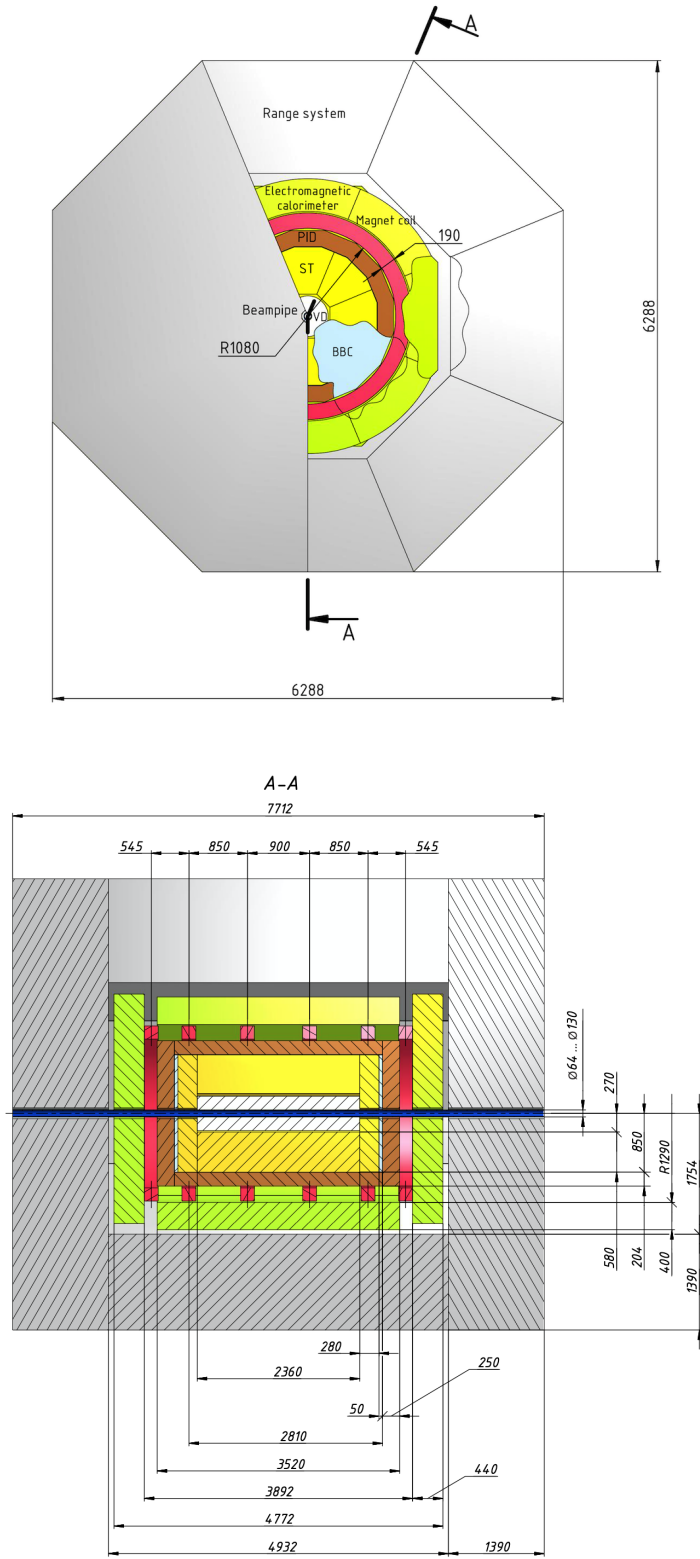


Figure 4.1: General layout of the Spin Physics Detector. All dimensions are in millimeters.

Table 4.1: Required setup configuration for each point of the SPD physics program. (+++) - absolutely needed, (++) - extremely useful, (+) - useful, (-) - not needed.

Program	Vertex detector	Straw tracker	PID system	Electromagnetic calorimeter	Beam-beam counter	Range system
Gluon content with:						
charmonia	+	++	+	++	+	+++
open charm	+++	++	++	+	+	++
prompt photons	+	+	-	+++	+	-
SSA for π and K	+	++	+++	++	+	-
Light vector meson production	+	++	-	+	+	-
Elastic scattering	+	++	-	-	+++	-
\bar{p} production	+	++	+++	++	+	-
Physics with light ions	++	+++	+	++	++	+

2 Magnetic system

The SPD Magnetic System (MS) should satisfy the following criteria:

- minimization of the material inside the detector inner part;
- a magnetic field integral of $(1 \div 2)$ T· m along the particle tracks, whereas the peak value of the field should be limited to 0.8 T over the straw tracker volume;
- minimization of the total weight, the cross-section of the current coil (coils), and the overall amount of the MS material, i.e. the MS should have perfect mechanics.

Several options of MS's were considered:

1. Solenoid – a uniform multi-turn coil placed between the ECal and the muon range (RS) systems;
2. Toroidal MS (inside ECal): $3 \times 8 = 24$ coils forming a toroidal distribution of the field in the detector volume only;
3. Hybrid system consisting of a combination of toroidal coils in the barrel and solenoidal ones in the front/rear parts. Both room and cryogenic temperatures were considered;
4. System of 4 separate coils inside the ECal: a) all coils are connected in series, and b) right and left hand pairs are connected opposite to each other;
5. Hybrid system consisting of a combination of 8 toroidal coils in the barrel and 2 pairs of separate solenoidal coils in the front/rear parts. Both room and cryogenic temperatures were considered;
6. System of 6 separate coils placed between the ECal and the RS system of the reduced diameter.

Thus, more than 10 different options of the 3D magnetic field configurations were analyzed. The calculated field maps were used for the Monte Carlo simulation of the SPD performance (see Chapter 9). Conceptual analysis of the considered MS systems was performed also. Certain data were reported at the European Conference on Applied Superconductivity EUCAS2019 [383]. The general conclusions are briefly summarized below.

1. The most well-known system is a classical solenoid. Experience in design and construction of superconducting solenoids has been collected by numerous groups worldwide, including the NICA MPD. The MPD solenoid manufacturing is completed and the assembling has been started in the experimental hall. The main disadvantage for SPD of a solenoid similar to the MPD MS would be a lot of material in front of the ECal as well as its high cost. Moreover, the fixed geometry of the field gives no universality of the SPD experimental program.
2. The toroidal MS was considered in its “warm” and “cold” options. The warm one was rejected due to the material budget: the necessary ampere-turns led to an unacceptable cross-section of the coils and hence the amount of copper. The problem is solved partially in the case of superconducting coils. Nevertheless, the complexity of design of the coil system is very high in any case. The most important negative effect can occur due to concentration of the coil material closer to the bunch crossing area.
3. The MS consisting of separated coils is absolutely transparent for the particles passing through the inner volume of the detector and contains “target” material for the secondary particles in the limiting volume at the ECal inner part. The amount of material depends directly on the necessary ampere-turns of the coil and the achievable current density. The last point gives evidence in favor of the superconducting approach. The magnetic field radial and axial distribution is not so uniform in comparison with a solenoid, especially in the area close to the coils. Nevertheless, the accuracy of modern 3D calculation codes for non-linear magnetic fields and precise magnetic measurements can guarantee the necessary accuracy of real field mapping. Optimization of the coil cross-section is also very important.
4. The hybrid MS consisting of a toroidal system in the barrel part of the SPD and two pairs of separate coil was considered as a compromise, and namely: minimization of the magnetic field near the polarized particles interaction zone and a solenoidal-type distribution in the front and rear parts of the detector.

More advanced analysis of the detector and the collider system has shown that partial compensation of the magnetic field at the axis will give not so many advantages. However, it would be more beneficial, somehow, if there was no the spin control system in the collider lattice. The NICA collider will be equipped with such a system. The elements aimed at the particle spin control at the NICA collider were proposed and are under technical design now. The general description of the spin control system is presented in section 3. Thus, the condition of a “zero” magnetic field along the beam axis is not a critical issue in our case. An updated choice of the SPD MS was made in favor of a separate 6-coil design. The geometrical model of the coil system is presented in Fig. 4.2, and the field calculation data in Figs. 4.3 and 4.4.

As it is clear from Fig. 4.3, the longitudinal variation of an axial magnetic field is varied from about 5% at the beam axis to about 12% at a radial distance of 2 cm from the coil inner turns. The number of 12% can be further improved by the coils system optimization. We consider the technology of superconducting coils manufacturing based on a hollow high-current cable similar to the one used for the Nuclotron magnet or the one used in the ITER systems. The manufacturing technology of a hollow cable made of NbTi/Cu composite wires cooled at 4.5 K with a forced helium flow is well developed at the Laboratory. The magnets of the NICA booster and collider are being manufactured at the Laboratory magnet facility (VBLHEP JINR). The coil containing 80 turns will provide $800 \text{ kA} \times \text{turns}$ and generate the necessary magnetic field in the detector volume. Some of the SPD 6-coil MS are presented in Table 4.2 in comparison with the other detectors.

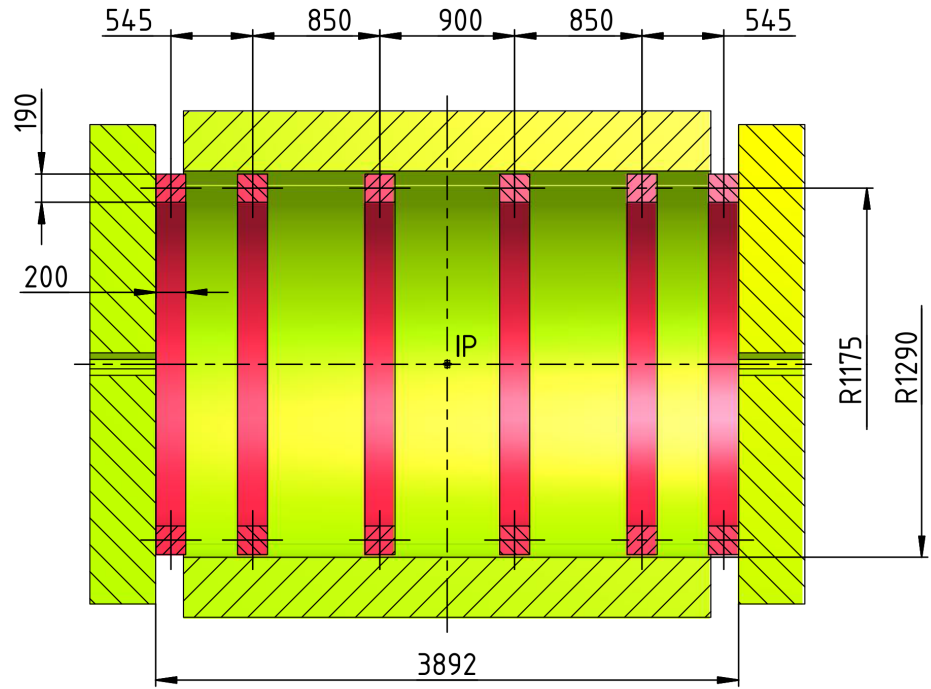


Figure 4.2: Geometrical model of the 6-coil magnetic system. All dimensions are in millimeters.

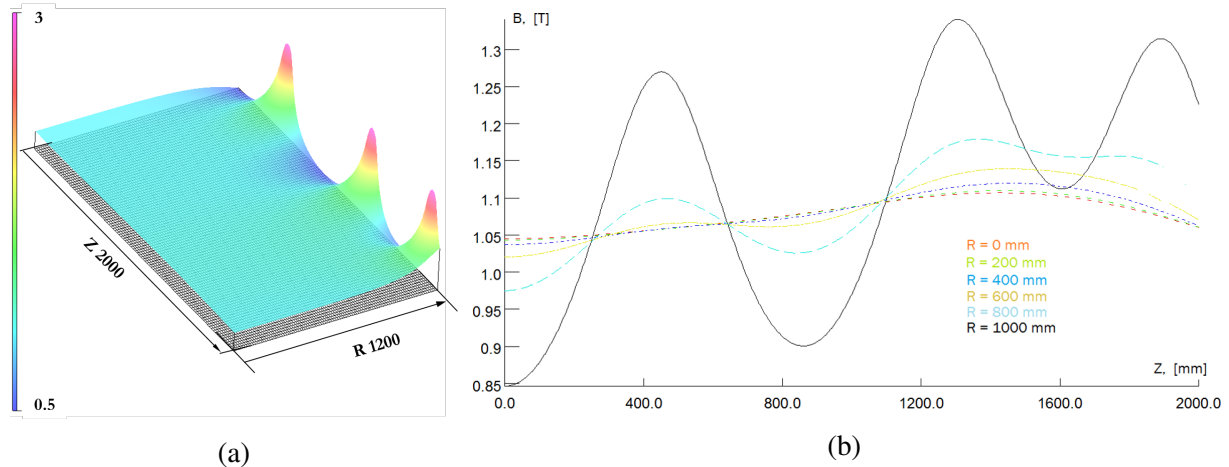


Figure 4.3: Field calculation results: (a) B_z as function of r, z ; (b). B_z as function of z at different r . All dimensions are in millimeters.

3 Beam pipe

A beam pipe separates the detector and high vacuum of the accelerator. It must be mechanically sturdy on the one hand and thin enough in terms of the number of radiation lengths to minimize multiple scattering and radiation effects, on the other hand. The diameter of the beam pipe is a compromise between the radial size of the beams and the requirement to put coordinate detectors as close to the interaction point as possible for better reconstruction of the primary and secondary vertices. A beryllium beam pipe with outer diameter of about 6 cm with 0.5mm wall thickness is proposed to be used.

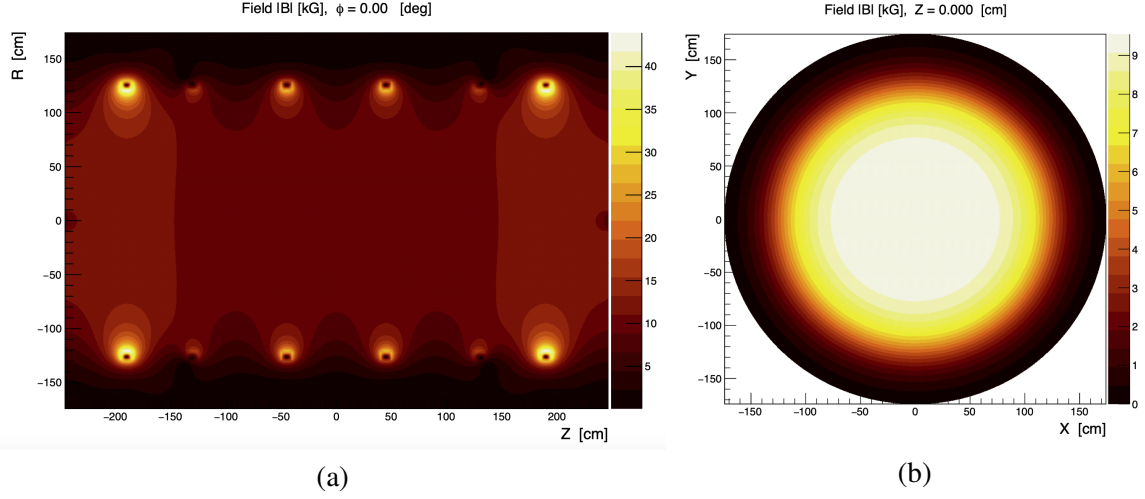


Figure 4.4: Magnetic field in the inner part of the SPD setup (a) z - r section; (b) x - y section at $z = 0$.

Table 4.2: Comparison of the SPD (NICA) and CMS (LHC) magnetic systems.

Parameter	SPD/NICA	CMS/LHC
Size (diam./length), m/m	2.9/6.0	6.5/12.7
Magnetic system	6 coils	solenoid
Peak magnetic field, T	1.0 (axis)	4.5
Coil average diam., m	~ 2.5	~ 6.5
Field volume, m^3	~ 45	~ 414
Stored energy, MJ	~ 40	~ 2800
Coil turns	80	2112
Operating current, kA	8.75	20
Total inductance, H	~ 0.2	12.6

The schematic view of the beam pipe and its positioning inside the SPD is shown in Fig. 4.5.

At the first stage of the SPD running a cheap stainless steel beam pipe could be used.

4 Vertex detector

4.1 General overview

The SPD Vertex Detector (VD) is a silicon-based part of the spectrometer responsible for precise determination of the primary interaction point and measurement of secondary vertices from the decays of short-lived particles (first of all, D -mesons). The Vertex Detector is divided into the barrel and two end-cap parts (Fig. 4.6). Two different versions of the VD design are discussed: i) five layers based on double side silicon detectors (DSSDs) and ii) three inner layers based on Monolithic Active Pixel Sensors (MAPS) and two outer layers based on DSSDs. The VD Barrel consists of five layers based on double side silicon detectors (approximately 4.2 m^2). The end-cap regions consist of five disks each (approximately 0.4 m^2). The VD Barrel covers a radius from 96 to 500 mm (Fig. 4.7). All five cylindrical layers are set with rectangular two-coordinate silicon strip detectors and give information on the coordinates of the tracks (r, ϕ, z) (which makes it possible to measure a point in each layer). The end-cap regions detect particles in the radial region between 96 mm and 500 mm. Each of the five disks is set with a DSSD with

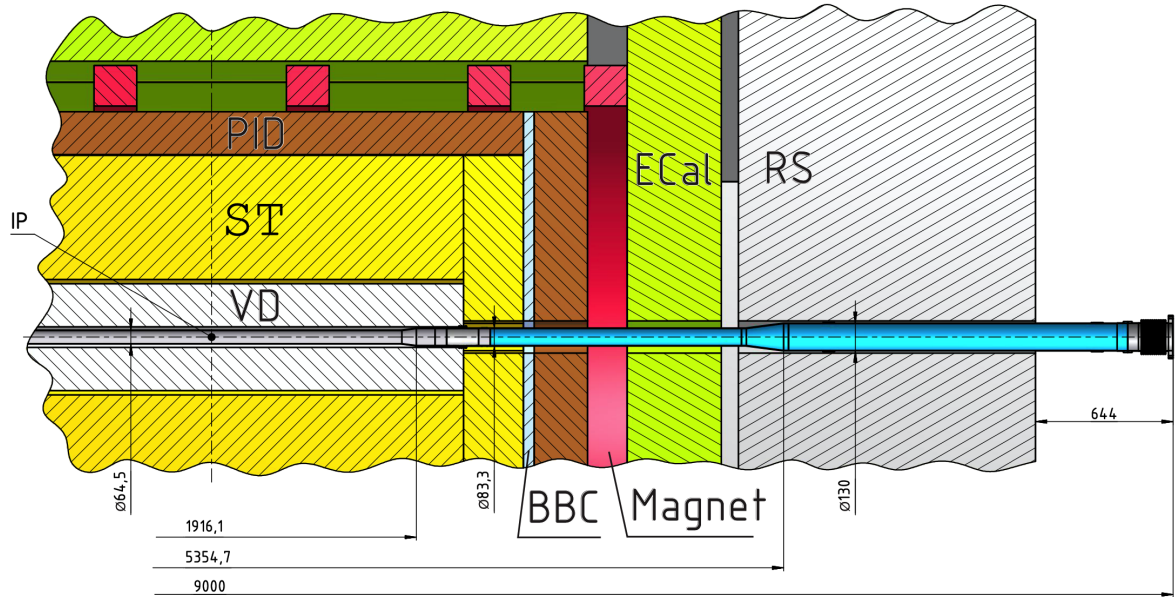


Figure 4.5: SPD beam pipe inside the setup. All dimensions are in millimeters.

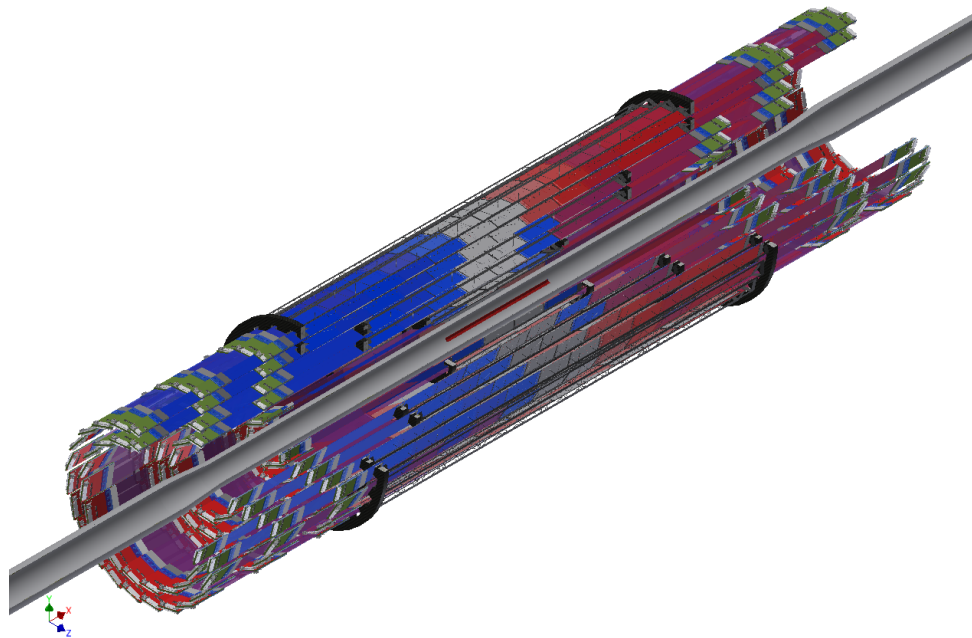


Figure 4.6: General layout of the SPD Vertex Detector.

concentric (r) strips and radial (ϕ) strips. The VD has a length of about 1.1 m and covers the region of pseudo-rapidity up to $|\eta| < 2.0$. Each DSSD has a 300- μm thickness and a strip pitch in the range from 95 μm to 281.5 μm . The DSSDs are assembled into detector modules by two detectors per module, forming 18-cm long strips. The detectors and the front-end electronics boards (FEE-PCB) are connected via low-mass polyimide microcables and assembled on the extra-light carbon fiber mechanical supports with a cooling system in the similar way as it was done for the ALICE outer barrel (see Fig. 4.10). The relevant numbers for the barrel part of the VD for the DSSD configuration are presented in Tab. 4.3.

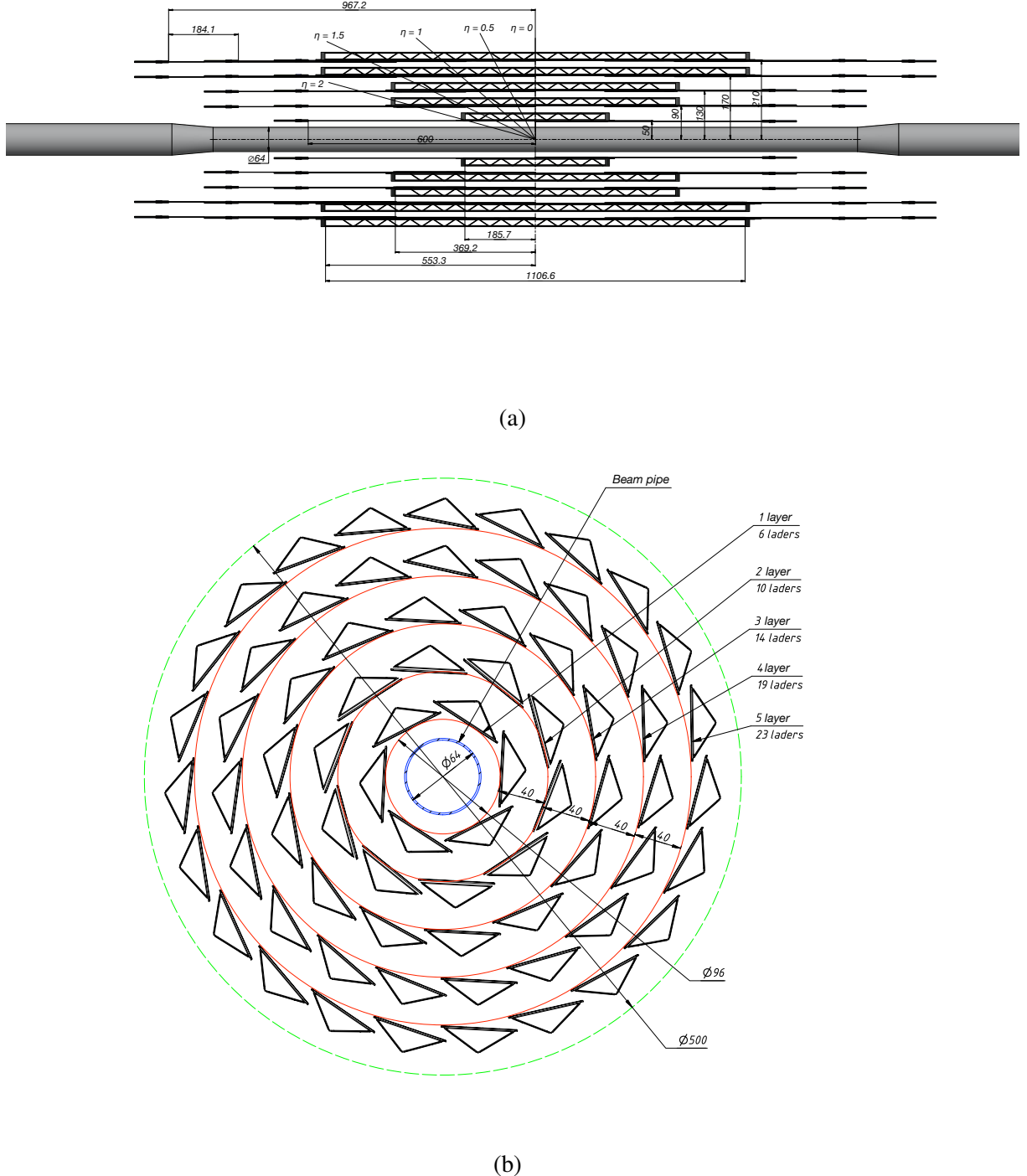


Figure 4.7: Longitudinal (a) and transversal (b) cross-sections of the barrel part of the Vertex Detector. All dimensions are in millimeters.

From the general conditions of the SPD setup the VD performance requirements are i) geometry close to 4π ; ii) track reconstruction efficiency for muons greater than 99% at $p \leq 13$ GeV/c (for $0 \leq |\eta| \leq 2.5$); iii) low material budget; iv) coordinates resolutions for vertexing: $\sigma_{r,\phi} < 50 \mu\text{m}$, $\sigma_z < 100 \mu\text{m}$. The lifetime of the Vertex Detector is required to be not less than 10 years of NICA running.

Table 4.3: Relevant numbers for the barrel VD (DSSD configuration).

Parameter	Layer 1	Layer 2	Layer 3	Layer 4	Layer 5	Total
N_{DSSD}/module	2	2	2	2	2	
$N_{\text{modules}}/\text{ladder}$	2	4	4	6	6	
$N_{\text{ladders}}/\text{layer}$	6	10	14	19	23	72
N_{DSSD}/layer	24	80	112	228	276	720
$N_{\text{chip}}/\text{module}$	10	10	10	10	10	
$N_{\text{chip}}/\text{layer}$	120	400	560	1140	1380	3600
$N_{\text{channel}}/\text{layer}$	15360	51200	71680	145920	176640	460800

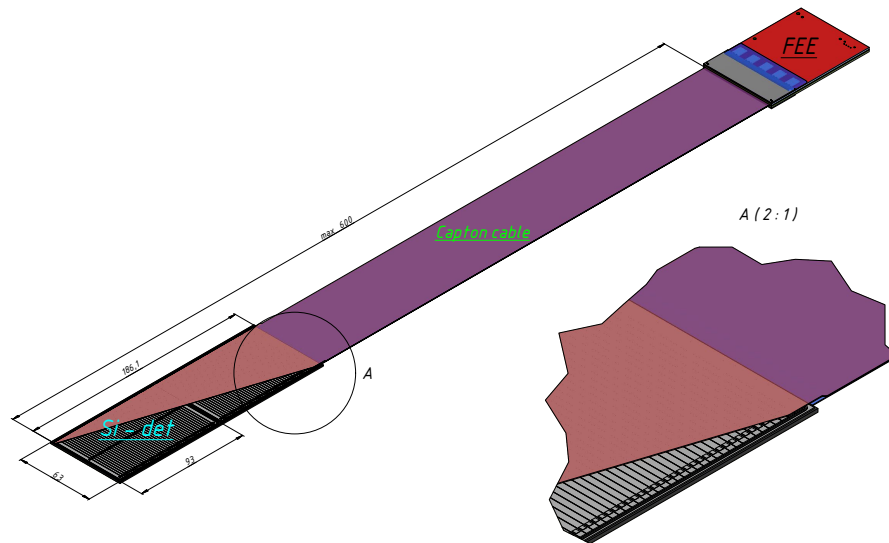


Figure 4.8: Concept of the barrel DSSD module. All dimensions are in millimeters.

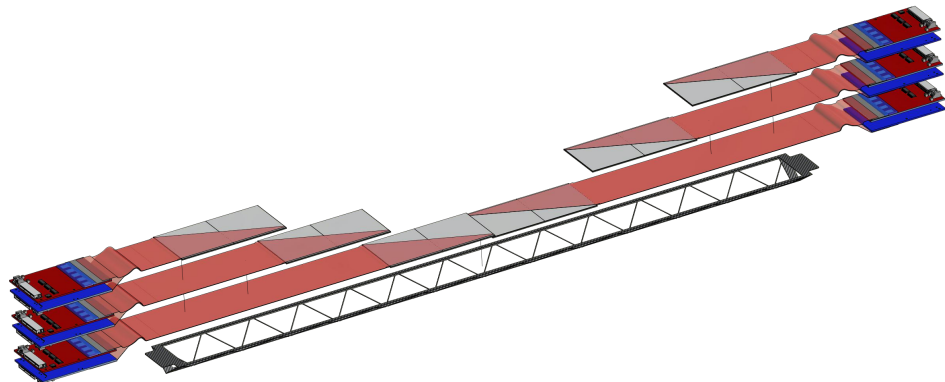


Figure 4.9: Conceptual layout of the barrel ladder.

Table 4.4: Possible ASIC readout solution for the Vertex Detector.

ASIC	APV25	VATAGP7.3	n-XYTER	TIGER
Number of channels	128	128	128	64 (128)
Dynamic range	-40fC – 40fC	-30fC – 30fC	Input current 10 nA, polarity + and –	1–50fC
Gain	25mV/fC	20 μ A/fC		10.35mV/fC
Noise	246 e ⁻ +36 e ⁻ /pF	70e ⁻ +12 e ⁻ /pF	900 e ⁻ at 30pF	2000 e ⁻ at 100pF
Peaking time	50ns	50ns/500ns	30ns/280ns	60ns/170ns
Power consumption	1.15mW/ch.	2.18mW/ch.	10mW/ch.	12mW/ch.
ADC	No	No	16fC, 5 bit	10-bit Wilkinson ADC
TDC	No	No		10-bit Wilkinson ADC

4.2 Double-sided silicon detectors

The concept of the barrel DSSD module is shown in Fig. 4.8. The module consists of two silicon detectors wire bonded strip to strip for the p^+ side (to reduce the number of readout channels), glued to the plastic frame and connected with two front-end electronic boards via a low-mass polyamide cable.

The Silicon Detector is made using a planar double-side technology based on the n-type conductivity 6-inch float-zone Silicon wafers (produced by ZNTC, Zelenograd, Russia). Its size is 63x93 mm² and its thickness is 300 μ m thickness. The pitch for the p^+ side is 95 μ m and for the n^+ side 281.5 μ m. The number of strips is 640 and 320 for the n^+ and p^+ side, respectively. The stereo angle between the strips is 90 degrees. The excepted spatial resolution for such a detector topology is $pitch_{p(n)+}/\sqrt{12} = 27.4$ (81.26) μ m for $r - \phi$ and $r - z$ projections, respectively. As mentioned before the barrel DSSD module contains two DSSDs (p^+ strips wire bonded strip to strip) and has 640 strips at each side.

To bring the front-end electronics out of the tracker volume, two thin polyimide cables with aluminum traces (for each side of the module) will be used. The cable consists of several layers: signal, perforated or solid dielectric (polyimide), and a shielding layer. Cable pins were designed for the tape-automated bonding with the detector and the pitch adapter sides. The maximum cable length is 60 cm, and the total thickness of all cable layers is less than 0.15% of X_0 .

Since the DSSDs have a DC topology, it is necessary to supply bias voltage to the detector and electrically decouple the DC current from the ASICs electronics inputs. For this purpose, an integrated RC circuit (sapphire plates with Si-epitaxial layer Silicon On Insulator (SOI)) Pitch Adapter (PA) will be used for each side of the module (produced by ZNTC, Zelenograd) designed with different topologies for each side. After the pitch adapter the detector signal goes to ASIC. Table 4.4 shows a possible ASIC readout solution. The optimal choice should be done after the ongoing R&D.

4.3 Mechanical layout

The concept of the barrel DSSD ladder is shown in Fig. 4.9. The silicon modules are laying on a carbon fiber support from center to edge. The detectors are connected with the FFE via thin low-mass cables. The front-end electronics is located at the edges of the ladder and is placed in the conical caves as shown in Fig. 4.10 to provide a connection to the voltage supply, DAQ, and the cooling ASIC chips subsystems.

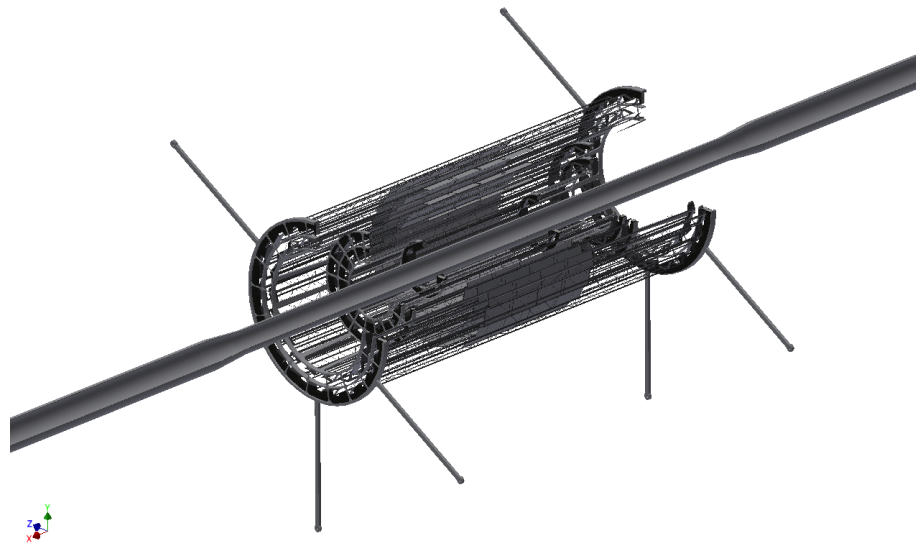


Figure 4.10: Schematic exploded view and cross section of the Outer Barrel module similar to ALICE outer barrel design.

4.4 MAPS option

To improve the spatial resolution of the vertex reconstruction the two inner layers could be replaced by the MAPS-ALPIDE detectors, designed and produced for the ALICE experiment basing on the TowerJazz technology [384]. Each chip has the pixel size of $29 \mu\text{m} \times 27 \mu\text{m}$. The scheme of a MAPS pixel is shown in Fig. 4.11. One of the options of the MAPS sensors layout could be based on the current ITS2 Inner Barrel design of ALICE [384], that has achieved the record minimal level of material budget and provides precise determination of D -meson decay vertices, (see Fig. 4.12). The impact of such replacement to the vertex reconstruction and, in turn, to the proposed physics with D -mesons is discussed in Chapter 9. The more advanced option like ALICE ITS3 [385] could be also considered for the inner layers of SPD.

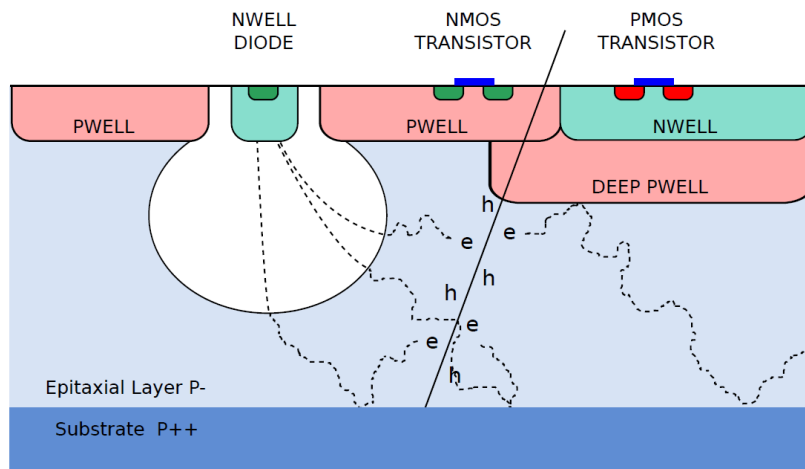


Figure 4.11: Scheme of a MAPS pixel [384].

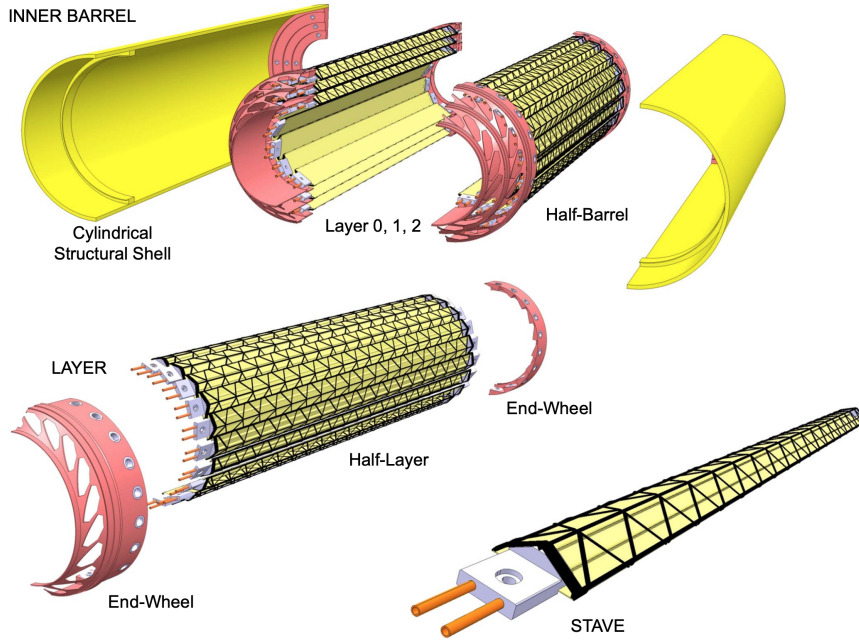


Figure 4.12: ALICE ITS2 Inner Barrel design [384].

4.5 Cost estimate

Preliminary cost estimation for the DSSD and DSSD+MAPS configurations of the Vertex Detector is presented in Tab. 4.5. The total cost of the detecting elements in both cases is about 9.5 M\$. As for the FFE, very rough estimation for both variants gives 6.5 and 7 M\$, respectively.

Table 4.5: Cost estimation for the VD configurations (DSSD / DSSD+MAPS).

Layer	Number of sensors	Number of ASICs	Barrel area, m ²	End-cup area, m ²	Cost barrel, M\$	Cost end-cup, M\$
1	36 / 440	180 / 0	0.22 / 0.20	0.38 / 0.38	0.40 / 0.36	0.69 / 0.69
2	80 / 840	400 / 0	0.47 / 0.38		0.86 / 0.69	
3	112 / 1736	560 / 0	0.66 / 0.78		1.20 / 1.42	
4	228 / 228	1140 / 1140	1.34 / 1.34		2.43 / 2.43	
5	368 / 368	1840 / 1840	2.16 / 2.16		3.92 / 3.92	
Total	824 / 3612	4120 / 2980	4.85 / 4.86	0.38 / 0.38	8.81 / 8.82	0.69 / 0.69

5 Straw tracker

The purpose of Straw Tracker (ST) is to reconstruct tracks of primary and secondary particles with high efficiency, to measure their momenta with high precision based on a track curvature in a magnetic field, and participate in particle identification via energy deposition (dE/dx) measurement. A spatial resolution of ST is expected to be about 150 μm and the drift time is about 120 ns for tubes of 1-cm diameter. The detector is planned to be built of low-mass straw tubes similar to the ones used in many modern experiments such as NA62 [386], COMET [387], SHiP [388], Mu2e [389], COMPASS [390, 391], and NA64 [392]. The technology is quite well established and a detailed R&D is not needed. The concept of the SPD ST is similar to the ATLAS TRT [393–395] and PANDA [396] straw trackers.

5.1 Straw technology

The straw manufacturing process in general follows the procedure developed for NA62 [397]. The tubes are manufactured of PET foil 36 μm thick, coated on one side with two thin metal layers (0.05 μm of Cu and 0.02 μm of Au) in order to provide electrical conductivity of the cathode and to improve the gas (Ar+CO₂ mixture) impermeability. NA62 has demonstrated that these straws can be operated in vacuum [386]. A leak rate of only about 7 mbar/min for the whole detector (7168 straws) was measured [397].

A few straws with a diameter of 10 mm were used for dedicated mechanical tests. They were cut in 20 segments of about 25 cm long and tested under overpressure until the breaking point. The other straws were cut to 5.3 m and the cut ends were preserved for further analysis. The breaking pressure was found to be 9 bar on average and no one sample broke under 8.5 bar. The quality control procedure was the same as for NA62 straws. During the ultrasonic welding process the seam quality was verified by a digital microscope (recorded to file for each straw). Furthermore, the seam quality was checked by an operator in real time. All 50 tubes produced so far have good seams.

Several measurements and tests are performed post-fabrication. The seam width and straw inner diameter are measured by an optical method. The cathode electrical DC resistance is measured. The elongation and breaking force are both measured on the test samples (cut straw ends). The straws undergo a long-term overpressure test with temporary end-plugs glued into both ends of each straw. An overpressure test to $\Delta P \approx 2$ bar is performed for a period of about 1 hour. Subsequently, the straw is subjected to a long term overpressure test at $\Delta P \approx 2$ bar for a period of at least 30 days. Gas leak estimation is obtained by measuring the loss of pressure over time. The local straw deformation is measured under an applied weight of 300 g, and the pressure is derived from the calibrated relation between loss of pressure and deformation. Design of an individual straw tube is shown in Fig. 4.13 (a).

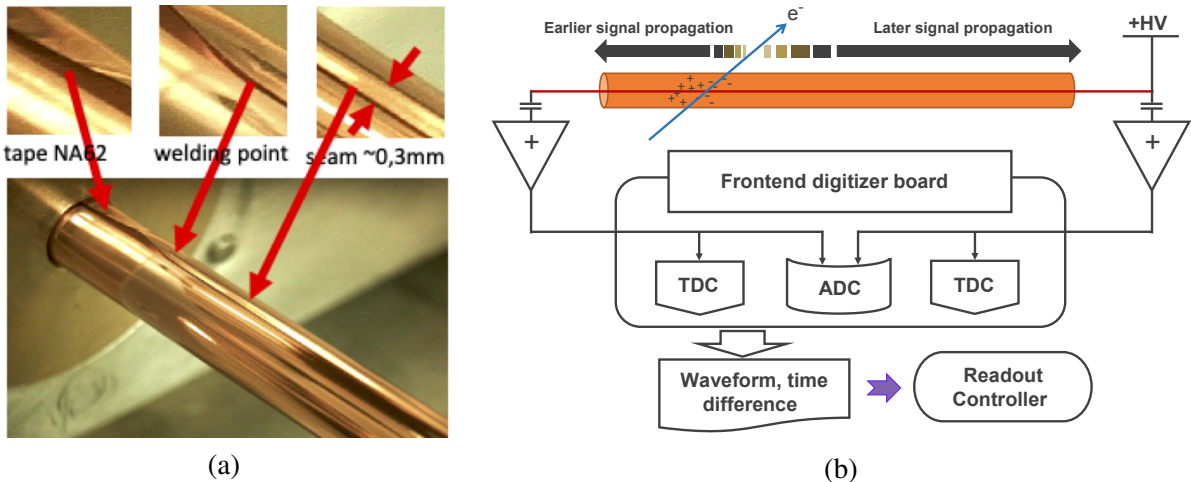


Figure 4.13: Individual straw tube of the SPD ST (a). Schematic representation of a 2-side straw readout (b).

5.2 General layout of the ST

The mechanical construction of the SPD Straw Tracker is based on engineering solutions which were already efficiently applied in ATLAS and PANDA experiments. The ST consists of three parts: a barrel part and two end-caps. The barrel has the external radius of 850 mm and the internal hole with radius of 270 mm. It is subdivided azimuthally into 8 modules, each with 30 double layers of straw tubes. Each tube has a diameter of 10 mm. Four modules are fixed together by a carbon fiber frame, thus forming a pair of independent semi-cylinders. This design provides a possibility to assemble and disassemble the ST in the presence of the beam pipe.

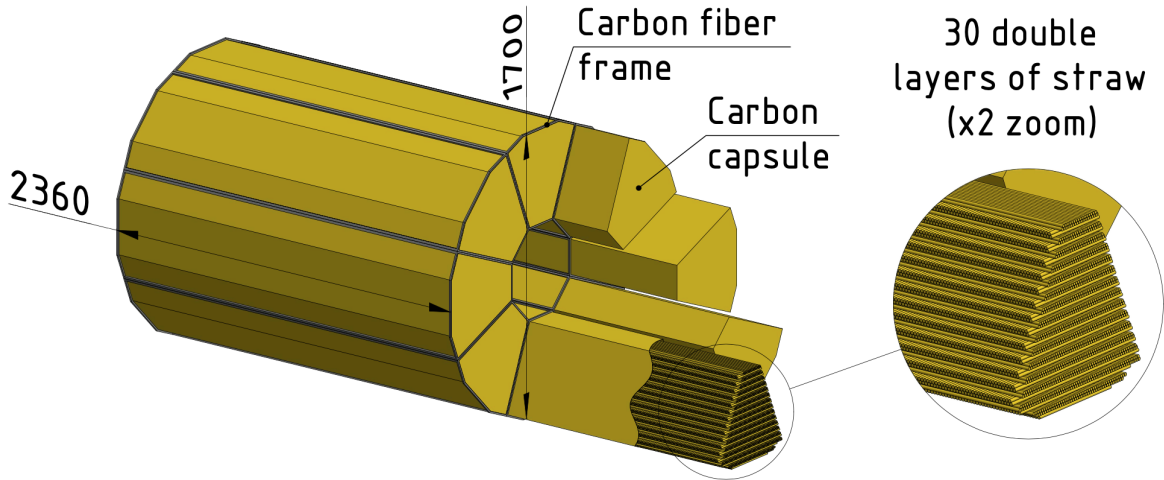


Figure 4.14: Layout of the barrel part of ST which shows 8 modules with 30 double-layers of straw in each capsule. Straws of adjacent double layers oriented perpendicular to each other. All dimensions are in millimeters.

Each module is enclosed in a 400- μm carbon fiber capsule. The capsule provides the positioning of individual straw tubes with 50 μm accuracy. One side and two ends of the capsule have 5 mm holes where straw end-plugs will be fixed. FE electronic boards which will be connected to these plugs will additionally serve as capsule covers, thereby isolating the inner volume from the external environment. Long straws oriented along the beam line will be read out from both ends in order to obtain an additional coordinate along the straw axis via mid-time calculation as shown in Fig. 4.13 (b). While short straws oriented perpendicular to the beam line will have electronics only on one side. Each capsule contains about 1500 tubes with parallel and 6000 tubes with perpendicular to the beam orientations. The total number of electronic channels per capsule is 9000. Thus, the total number of channels in the barrel part of ST is 72 000.

The rigidity of the structure is assured by the low overpressure of gas inside the tubes and their fixation inside the capsule volume. The anode wire positioning accuracy is achieved by the wire fixation in the carbon fiber covers. The capsule also serves for thermostabilization of the gas mixture inside detector volume and for protection of the straw surface from humidity. The layout of the barrel part of the Straw Tracker is shown in Figure 4.14.

Each end-cap part of ST comprises 3 modules along the beam axis. Each module consists of 4 identical hexadecimal cameras (for measurement of the 4 coordinates: X, Y, U and V). By construction, the cameras are divided into halves. Each module has a technological hole $\varnothing = 160$ mm for the beam pipe. The mechanical support is provided by carbon fiber frames. The total amount of electronic channels in both end-caps is 7200. The layout of one straw end-cap is shown in Fig. 4.15.

5.3 Front-end electronics

The Straw Tracker is designed for precision measurements which require excellent spatial, angular and timing resolutions to meet physics goals. Moreover, an amount of charge collected by anode will be used to identify particles. In view of this, requirements for the straw readout electronics are the following:

- to measure time and energy deposit (dE/dx);
- time resolution not worse than 1 ns for the drift measurements and 0.1 ns for the case of the 2 side readout to determine the coordinate along the wire;

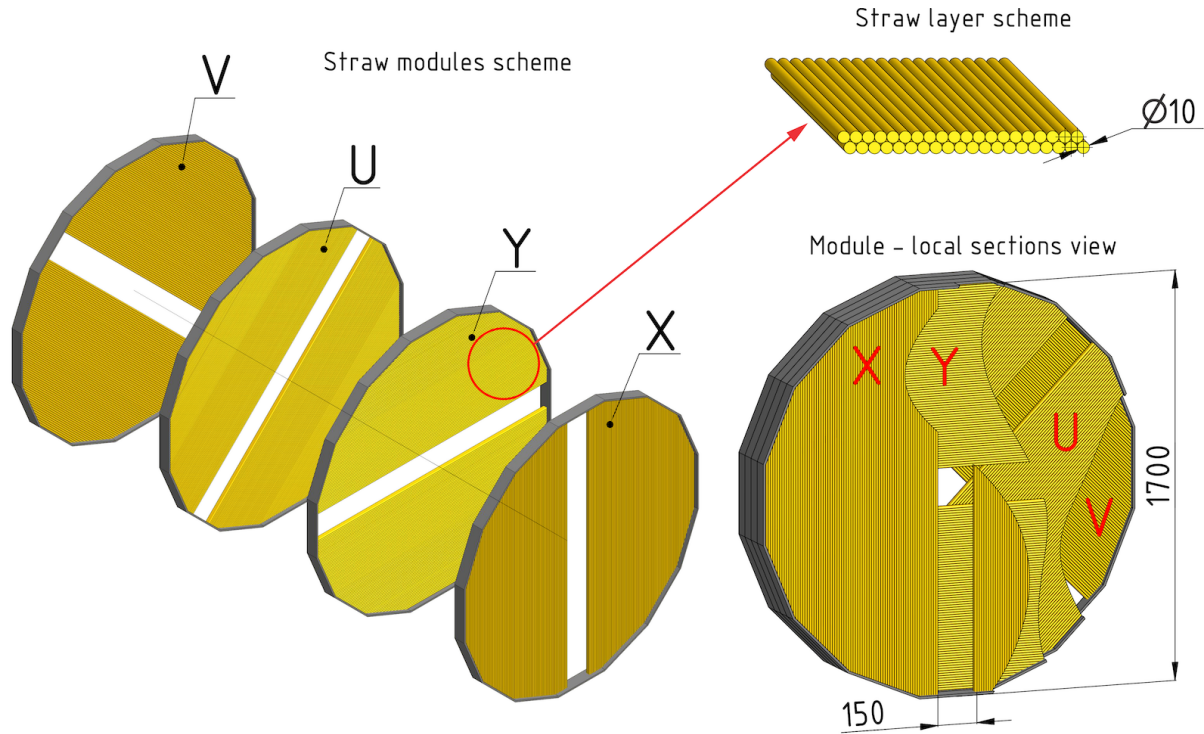


Figure 4.15: Layout of one end-cap part of the ST. It includes 3 modules along the beam axis where every module consists of 4 identical hexadecimally cameras (X, Y, U and V). All dimensions are in millimeters.

- low threshold to identify a charge from primary electron-ion clusters;
- dynamic range of about 1000;
- low power consumption to reduce heating.

Two options of electronics are under consideration now. The first one is the front-end electronics designed for the NA64 experiment [392]. It is a 32-channel amplifier-discriminator board based on AST-1-1 chip, developed by the Institute of Nuclear Problems of the Belarusian State University. The amplifier sensitivity is $K=100 \text{ mV}/\mu\text{A}$ ($20 \text{ mV}/\text{fC}$). The discriminator threshold is adjustable in the range ($2 \div 20$) fC. The delay of LVDS output signal is 6 ns. The amplifier has an ion tail compensation (BLR). The LVDS output signals are sent to the 64-channel time-to-digital converters (TDC).

The second option is to take the front-end electronics designed for DUNE experiment [398], which is based on 64 channel VMM3 a custom Application Specific Integrated Circuit (ASIC), developed by BNL for the LHC experiments at CERN. A low power consumption and a low per-channel cost (about 0.9 \$/ch) of the chip are valuable futures for a compact multichannel detector readout. Each channel has ADC and TDC circuits. Fast serial outputs are used for readout. Each of the 64 ASIC channels is highly configurable and combines a preamplifier shaping circuit with an ADC to allow independent digitization of triggered input signals. These digitized signals can be output with four different data readout options, which provides flexibility to accommodate different detector requirements and data rates. Each input channel has an individual preamplifier and dedicated digitizing logic. Each channel can be configured to accommodate a variety of input signal sizes, polarity and capacitance. The preamplifier shaping circuit can be configured to use one of four different peaking times (25, 50, 100, and 200 ns) and eight gain settings (0.5, 1, 3, 4.5, 6, 9, 12, 16 mV/fC). A channel-specific discriminator triggers on input signals above a configurable threshold to initiate digitization of the amplified pulse with a 10-bit Analogue to Digital Converter (ADC). Discriminator thresholds are adjusted by a global 10-bit Digital to Analogue

Converter (DAC) with additional channel-specific 5-bit trimming DACs. These features allow the VMM3 to satisfy the SPD TR requirement of measuring the collected charge and signal time in each channel. An equivalent noise charge of better than $1000e^-$ can be achieved with input capacitance less than 100 pF. On the basis of this performance, it is reasonable to expect that VMM3 can meet the SPD TR requirement of low charge threshold for the straw tube gain greater than $G = 10^4$ and the input capacitance less than 100 pF.

It was shown that the time resolution better than 1 ns was obtained for 6 pF input capacitance and input charge greater than 1 fC. A much better time resolution can be achieved for higher input signal amplitudes. This suggests that VMM3 can satisfy the SPD TR requirements for the time resolution with sufficiently high gain and appropriate input capacitance. The channel thresholds are individually adjusted by a global 10-bit DAC and an individual channel 5-bit trimming DAC. This suggests that the required low charge threshold can be achieved.

5.4 Cost estimate

Presently, we estimate the cost of the SPD ST development and construction at 2.4 M\$.

6 Electromagnetic calorimeter

The calorimeter should meet the criteria imposed by the physical goals of the SPD experiment of different nature and importance. The most important criteria arise from the physical requirements to the accuracies of measurement of energies, trajectories, and timings of photons and electrons. Technological possibilities of modern experimental physics should be taken into account when choosing the calorimeter setup. Price factors should also be considered to ensure the feasibility of the project. High multiplicity of secondary particles leads to a requirement of high segmentation and dense absorber medium with a small Molière radius. It is needed in order to have sufficient spacial resolution and a possibility to separate overlapping showers. The transverse size of the calorimeter cell should be of the order of the Molière radius. A reliable reconstruction of photons and neutral pions is possible only for small shower overlaps. Occupancy should not exceed 5%, so that it is possible to determine photon reconstruction efficiency with high precision.

The SPD experiment imposes the following requirements on the calorimeter characteristics:

1. reconstruction of photons and electrons in the energy range from 50 MeV to 10 GeV;
2. energy resolution for the above-mentioned particles: $\sim 5\%/\sqrt{E}[\text{GeV}]$;
3. good separation of two-particle showers;
4. operation in the magnetic field;
5. long-term stability: 2÷3% in a six month period of data taking.

The energy range requirement follows from the kinematic range of secondary particles, which are produced in a collision of protons with energy up to 27 GeV and emitted into 4π solid angle. Good energy resolution is required for identification and quantitative measurement of single photon and neutral pion energies. Good two-particle separation is needed to separate photon showers from the π^0 decay in order to suppress background events in measurements with prompt photons. Long-term stability is necessary for polarization measurements featuring π^0 reconstruction in the calorimeter, especially in the end-caps. Calorimeter instability may result in false asymmetry values. While it is essential to meet the physics requirements imposed on the calorimeter design, one should also take into account the cost estimate and

the technical feasibility when choosing its granularity, as the larger number of cells leads to larger costs of the manufacturing technology and readout electronics.

6.1 Overview of the SPD calorimeter

The SPD electromagnetic calorimeter is placed between the Range System and the magnet coils, as shown in Figs.1.2 and 4.1. It consists of a barrel and two end-caps, covering a 4π solid angle. The outer dimensions of the calorimeter are determined by the inner size of the muon system. The thickness of the calorimeter is determined by the required thickness of the active part and the size of the readout block consisting of photodiode and amplifier boards, as well as by the size of the flexible part of the fibers.

For efficient absorption of electrons and photons with energies up to 10 GeV, the calorimeter thickness, which is defined by the number of sampling layers, should be at least $18 \div 20 X_0$ in terms of radiation lengths X_0 . For the sampling structure of a 1.5-mm scintillator and 0.5-mm lead, 200 layers are required for a thickness of $18.6 X_0$, which sets the length of the active part to 400 mm. The period of the structure is set to 2 mm in order to avoid optical contact between the lead and the scintillator, and because of the connection technique involving special "Lego" spikes. The flexible parts of the fibers take up 8 cm. The transverse size of the calorimeter cell should be of the order of the effective Molière radius of the calorimeter medium, which is, in its turn, defined by the scintillator-to-lead sampling ratio. The selected structure has a Molière radius of 2.4 cm. The separation efficiency of two photons with energies from 200 MeV to 500 MeV depends on the cell size and reaches a plateau at a cell size of 40 mm, as was determined in the MC simulation. Therefore, we have selected 40 mm cell granularity for both barrel and end-caps. Cells in the barrel part of the calorimeter have trapezoidal shape in the azimuthal direction to minimize the gaps between the modules. The vertex angle of the trapezoid equals 1.58° .

A schematic drawing of the calorimeter, which is limited in size by the muon system, is shown in Fig.4.16(a). The limits of the calorimeter zone are shown as a thick line. Holes of the size 160×160 mm² in the centers of the end-caps for the beam pipe are shown.

The inner size of the barrel part is limited by radius of the magnetic coils, whereas the outer size is limited by the dimensions of the muon range system. The thickness of the active part is 400 mm, which corresponds to $18.6 X_0$. This corresponds to 200 layers of the scintillator and lead of 1.5 mm and 0.5 mm width.

The barrel part of the calorimeter has 19712 cells of trapezoidal shape in the azimuthal direction with a vertex angle of 1.58° , and a front face size of 34 mm, and rectangular shape in the direction along the beam axis with a size of 40 mm (Fig.4.16(b)). The total weight of the barrel part is 40 tons.

Each end-cap (one is shown in Fig.4.17) consists of 4 sectors of 1308 cells per sector. The cell cross-section is 40×40 mm². There is a hole for the beam pipe in the center of each end-cap. The hole has a size of 160×160 mm², which is equivalent to 16 cells. Each end-cap has 5232 cells. The thickness of the active part of an end-cap cell is 440 mm (Fig.4.16), which corresponds to $20.4 X_0$. The weight of one end-cap is 14 tons. The total weight of two end-caps is, therefore, 28 tons. In total, there are 10464 cells in both end-caps, each with dimensions of $40 \times 40 \times 440$ mm³.

The total weight of the calorimeter is $68 = 40 + 28$ tons composed of the barrel and two end-caps. The total number of cells of size about 40×40 mm² is $30176 = 19712 + 10464$ for the barrel and the end-caps, respectively.

A possibility to use another type of modules in the central part of the end-cups in order to improve energy and spatial resolution of the calorimeter for energetic photons is also under discussion.

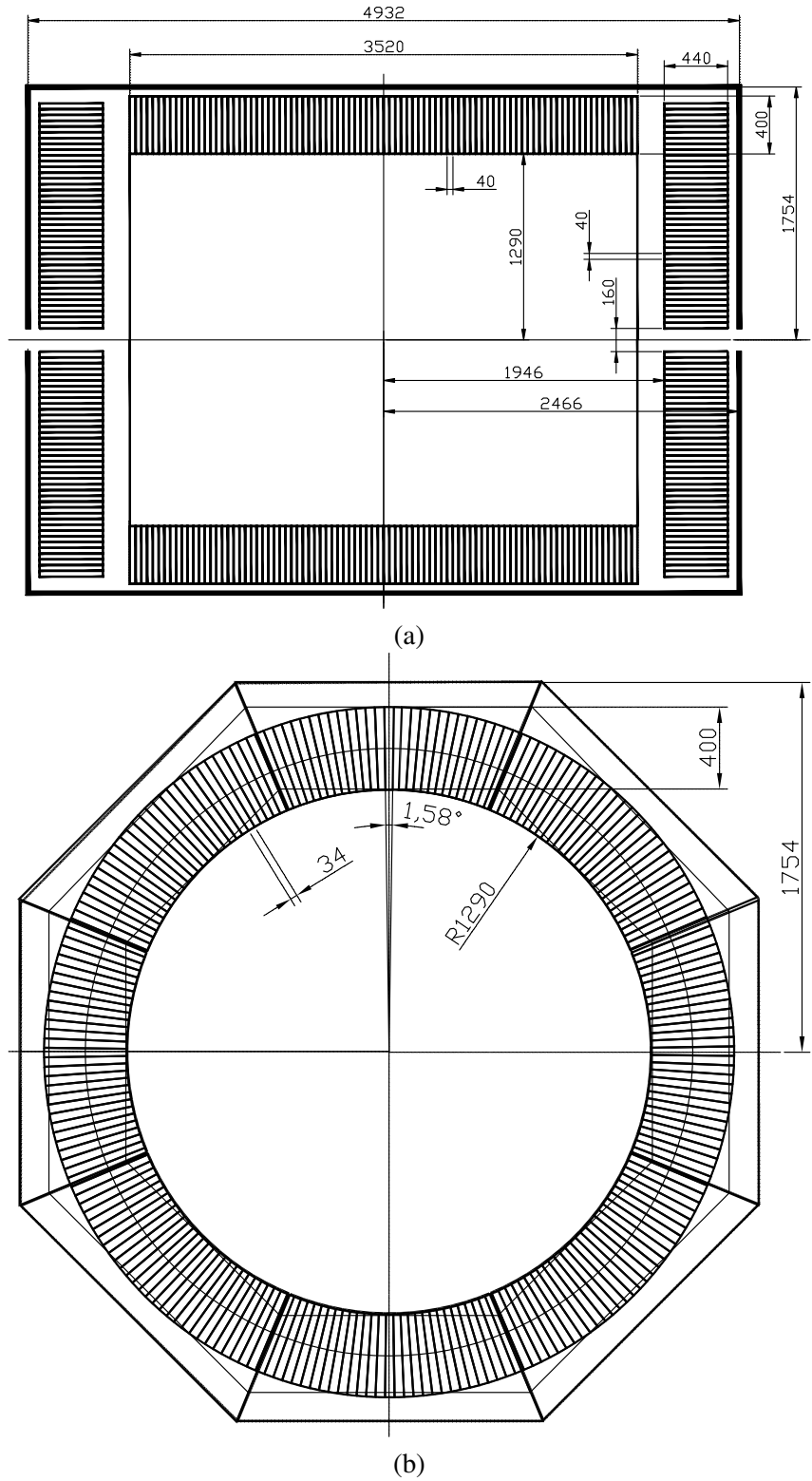


Figure 4.16: (a) Barrel and end-cap parts of the calorimeter. The holes of size 160×160 mm 2 for the beam pipe can be seen in the centers of the end-caps. (b) Schematic drawing of a cross-section of the barrel part of the calorimeter. It is sectioned into 224 azimuthal sectors (8 sections, 28 cells per section) with vertex a angle of 1.58° . All dimensions are in millimeters.

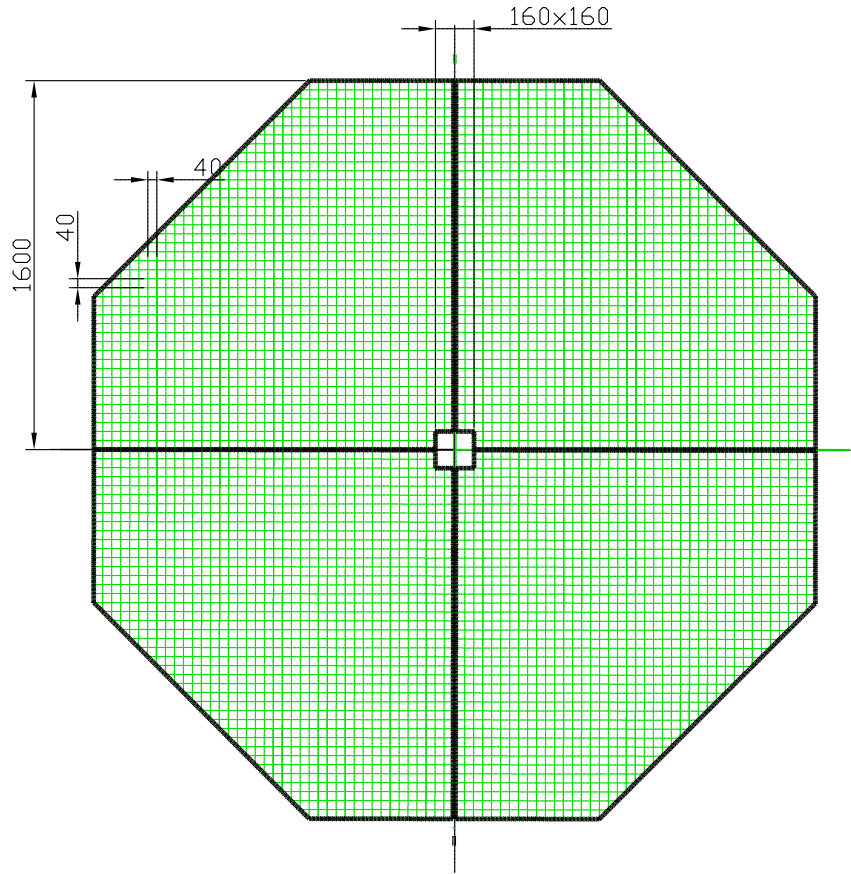


Figure 4.17: The end-cap part of the calorimeter consists of 4 sectors, 1308 cells each. In total, there are 5232 cells in one end-cap, and 10464 cells in both end-caps. All dimensions are in millimeters.

6.2 Design of the calorimeter module prototype

The initial version of the module, which was made for testing purposes, consisted of alternating layers of polystyrene scintillator and lead with a thickness of 1.5 mm and 0.3 mm, respectively. The selected number of layers is 220, setting the number of radiation lengths to $12.6X_0$. The lead plates are intended to absorb the particle energy and develop an electromagnetic shower, whereas the scintillator plates produce an amount of light proportional to the energy of particles. The properties of the absorber and the scintillator define the Molière radius, which is equal to 3.5 cm for the selected structure. The energy resolution for 1 GeV photons is assumed to depend on the calorimeter sampling fraction and is expected to be 4.15%. The test results of the present work are given for this particular design of the module.

The scintillator plates are made of polystyrene beads with an added luminophore admixture of 1.5% p-Terphenyl and 0.05% POPOP ($C_{24}H_{16}N_2O_2$) [399]. It has scintillation time of about 2.5 ns and light output of 60% of anthracene, which are good results. The radiation hardness of the scintillator is sufficient for radiation doses up to about 10 Mrad, which is important for operating the calorimeter in the radiation field of secondary particles in the vicinity of the interaction point.

The luminophore admixtures re-emit the energy of excitations in polystyrene in the form of visible light. The first admixture (p-Terphenyl) emits light with a wavelength of maximum emission at 340 nm. This light is absorbed by the second admixture (POPOP) and is re-emitted into a spectrum with a wavelength of maximum emission of 420 nm, which is seen as a light blue glow.

The light from the scintillator plates is gathered using wavelength shifting fibers (WLS) [400]. Fibers of type Y-11(200) manufactured by KURARAY are used. The fibers absorb the light from the POPOP and



Figure 4.18: Photo of a single module consisting of 4 cells with 220 layers of the scintillator and the absorber with a thickness of 1.5 mm and 0.3 mm, respectively. Four bundles of fibers for guiding the light to the multi-pixel photon counters (MPPC) can be seen.

re-emit it into a spectrum with a wavelength of maximum emission of 490 nm. Thirty-six WLS fibers go along each cell, gather in one bundle and transmit light to one multi-pixel $6 \times 6 \text{ mm}^2$ photodiode (multi-pixel photon counter, or MPPC). In this prototype, counters of types S13160-6025, S13160-6050, S14160-6050, and FC-6035 [401] are used.

The size of the cell for cosmic ray testing with the purpose of estimating signals from the MIP was chosen to be $55 \times 55 \text{ mm}^2$. It consists of 220 layers of the scintillator and lead with widths of 1.5 mm and 0.3 mm respectively.

The module consists of 4 cells with a cross-section of $55 \times 55 \text{ mm}^2$ combined into one tower with a cross-section of $110 \times 110 \text{ mm}^2$ and a length of 440 mm. Nine modules of the calorimeter, each consisting of 4 cells, were manufactured for testing at the experimental test benches in VBLHEP and outside. Four of them were tested on cosmic rays. The test results are shown in Section 6.6.

In the photo (Fig.4.18), a module of trapezoidal shape is shown, which is obtained after milling a rectangular parallelepiped at a 2 degrees angle. The cell size of $40 \times 40 \text{ mm}^2$ at the front face and $55 \times 55 \text{ mm}^2$ at the back face allows one to implement projective geometry (if necessary) in the SPD electromagnetic calorimeter.

6.3 Multi-pixel photodiodes

All of the MPPC's, that are used in this prototype have the same size of $6 \times 6 \text{ mm}^2$, but have different dynamic and time characteristics. The S13160-6025 series has the best response speed, low capacitance and a large number of pixels, but the largest temperature coefficient of $K_T \sim 0.054 \text{ V}^\circ\text{C}$. The temperature coefficient shows a linear dependence of the breakdown voltage on the temperature and leads to a change in signal amplification. To achieve calorimeter stability of about 2%, one needs to ensure the stability of the surrounding environment, or use the breakdown voltage compensation scheme $U_{OP} = U_{BR} + \Delta U - K_T \times \Delta T$, where U_{OP} and U_{BR} are the operation and the breakdown voltages, respectively, ΔU is a voltage bias and ΔT is a deviation of the current temperature from the nominal one, e.g. 20°C .

The S14160-6050 series has high photo detector efficiency, but fewer pixels, which is worse in terms of the dynamic range. This series has a small temperature coefficient. An optimal solution would be to

manufacture a similar photodiode series, but with a smaller pixel size of $15 \div 20 \mu\text{m}$, which would make them more suitable for a calorimeter.

6.4 MPPC readout and the high-voltage control

Four MPPC's are surface mounted on a circuit board, as shown in Fig.4.19. A thermistor is also installed to measure the photodiode temperature. The circuit board is connected to a module in such a way that the photodiodes are placed at the positions of fiber bundles. There is no optical contact between the photodiode and the WLS, instead there is an air gap of about 0.1 mm. Optical grease is not used in order to avoid instability in the conditions of light guiding. A light insulating basket made of black plastic is installed on top of the circuit board.

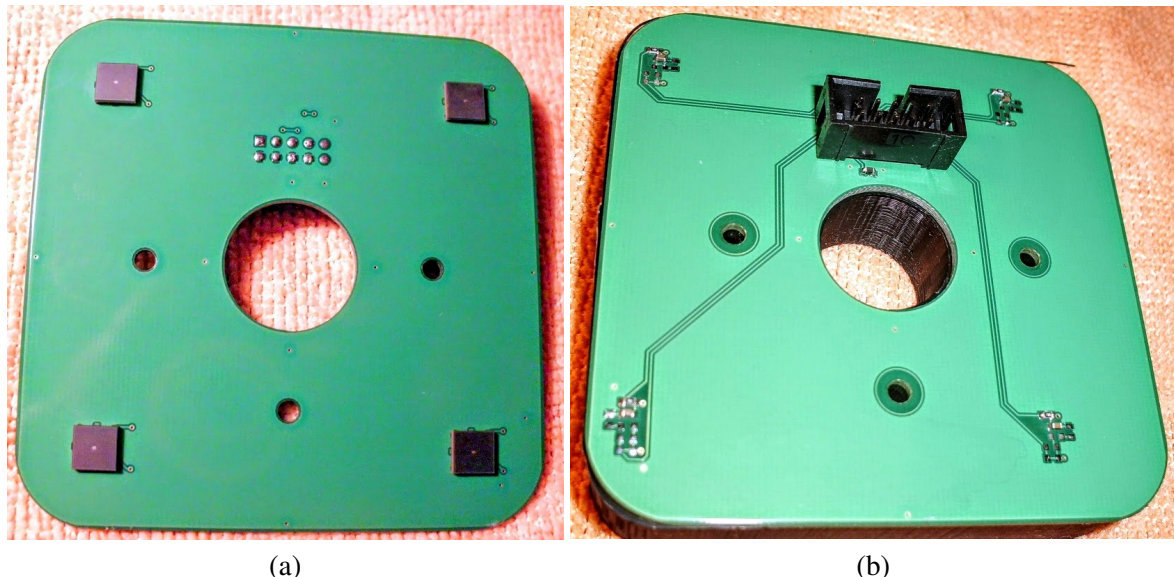


Figure 4.19: Printed circuit board with 4 MPPC diodes: front (a) and back (b) sides.

The MPPC are connected to the amplifier board (Fig.4.20) using a 1-meter 17-pair flat twisted-pair cable. Five pairs of wires transmit signals to the amplifiers [402]. Two wires are used to send base voltage of $\sim 40 \text{ V}$ and connect the thermistor. Channel voltages are transmitted via signal wires as a small bias from 0 to 5 V. This way, the bias voltage can be precisely set in a small range, but with 10-bit precision (i.e. about 5 mV).

The voltage control is implemented at a software level, taking into account the temperature from the thermistor installed on the circuit board. This allows for operation without special equipment for temperature stabilization. Signal stability of the order of $0.1 \div 0.2\%$ is achieved during measurement over an extended period of time.

6.5 Readout electronics

The readout electronics consists of an analog-to-digital converter ADC-64 [403] (Fig.4.20(a)). The ADC receives continuous-time samples of the input signal with a fixed frequency and provides full digital representation of signals in time. Samples are received at a 64-MHz frequency, which corresponds to the time period of 15.625 ns. Each sample is measured with a 12-bit precision. At present, there is an ADC-64-ECal modification, which improves the precision up to 14-bit and significantly extends the range of the measured amplitudes. The new ADC modification also allows for operation in strong magnetic fields, which is necessary for experiments at the NICA accelerator complex.

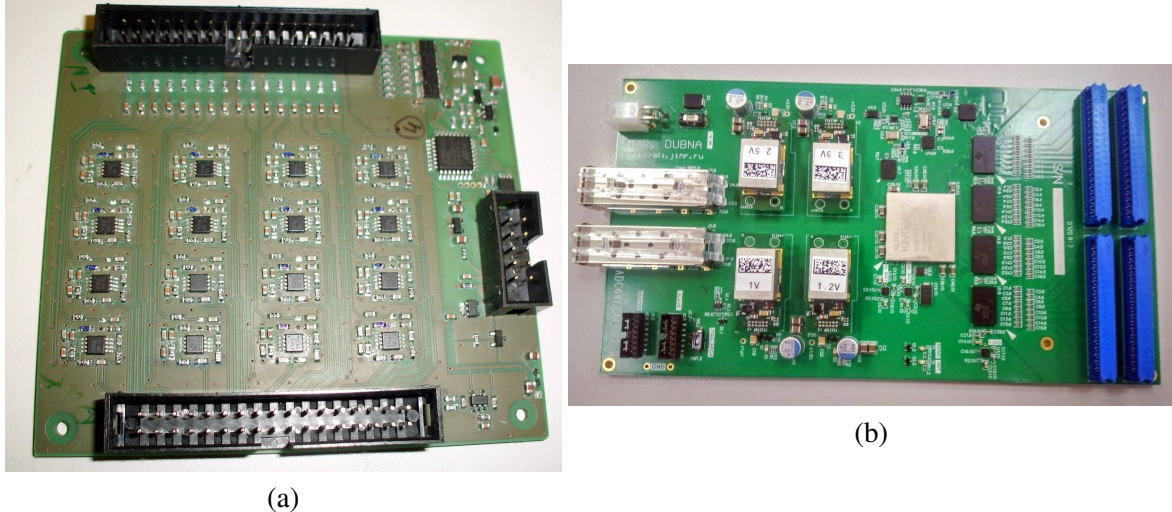


Figure 4.20: (a) 16-channel amplifier board is used to control the MPPC High Voltage and transmit signals to the ADC-64. The power consumption is about 16 mW per 16 channels. (b) 64-channel ADC-64- specifically designed for calorimeter operation in the magnetic field. The power consumption is about 120 W per one board (64 channels).

An Ethernet connector for data transfer can be seen in Fig.4.20 (b), together with a coaxial input for readout synchronization, which serves as a trigger. The ADC can also operate in streamer mode due to dedicated firmware. Using the White Rabbit technology provides sub-nanosecond synchronization accuracy.

6.6 Cosmic ray test results

For testing on cosmic rays, a small setup of 4 (Fig.4.21) modules (each $11 \times 11 \text{ cm}^2$), of the total cross-section of $22 \times 22 \text{ cm}^2$, was used. The cells, each $55 \times 55 \text{ mm}^2$, are assembled in a 4×4 setup. The modules are placed vertically, while the direction of the registered cosmic rays is determined by trigger counters. The counters are multi-pixel photodiodes of type FC6035 and size $6 \times 6 \text{ mm}^2$. All the photodiodes are included in a coincidence trigger for the ADC. The trigger includes the signal from the generator, which starts the LEDs for control, calibration of calorimeter cells using the estimates of the light yield, and long-term stability control. Data acquisition is conducted at the ADC using the software provided by the developer. During a data taking period of 5-6 days, statistics of the order of million triggers was obtained.

The setup allows one to measure energy depositions and trajectories of cosmic ray particles. Relativistic muons with energy above 250 MeV pierce through the calorimeter and form a peak in the deposited energy distribution. In order to select straight tracks of particles, which pass vertically through one module, only those events are selected, where the number of hits is equal to 1.

Signals obtained on cosmic muons are used for amplitudes alignment and calorimeter energy calibration. Only events with exactly one cell hit are selected. The bordering cells have more events with smaller amplitudes due to angled tracks. We perform calorimeter calibration using only vertical tracks. Each maximum value in terms of ADC units is mapped to the corresponding energy deposition. The energy scale is determined from the Monte-Carlo simulation as the scale factor between the energy deposition of an electron with a 1-GeV energy, and a relativistic muon with an energy above 1 GeV, in scintillator plates for the given structure. From this proportion we estimate the MIP signal in this calorimeter to be 240 MeV. This value divided by the position of the muon peak maximum is used as a calibration coefficient for each cell. This calibration procedure involving the MIP energy deposition is not absolute



Figure 4.21: Photo of the calorimeter test setup consisting of 4 modules of the size $11 \times 11 \text{ cm}^2$, with the total cross-section of $22 \times 22 \text{ cm}^2$.

or conclusive. Primarily, it aligns the amplification coefficients in each cell to ensure equal response of each cell. The measured electron or photon energy can be further revised by reconstructing neutral pions or calibrating the calorimeter using electron or photon beams of the given energy.

The electromagnetic calorimeter measures electron or photon energy by summing up signals from all 16 cells. Each cell can only contain a fraction of energy deposited by the particle in the calorimeter (if the particle is not a relativistic muon, or a MIP). If the calorimeter is calibrated with a precision of several percent, the total energy weakly depends on the particle angle and the resolution increases only by 1.4%.

The energy resolution of the calorimeter for vertical cosmic ray particles is 9.6% (Fig.4.22 (a)). This number corresponds to energy deposition of 240 MeV. Assuming the resolution depends on the energy as $E^{-1/2}$, the energy resolution at 1 GeV is estimated to be 5%.

Time resolution for calorimeters of such types is about 175 ps for the MIP (Fig.4.22 (b)) and can be improved for high-energy electrons. This can be applied to identify particles in the energy range of 50 \div 1550 MeV.

6.7 Dependence of the calorimeter response on the number of photoelectrons

Cosmic ray testing allows one to obtain dependences of energy and time resolution on the number of photoelectrons (NPE) produced during the MIP passing through a cell. For each channel, time is calculated as zero intersection of the waveform. This method, Constant Fraction Discriminator, is used for determining a time value on a constant fraction of the pulse leading edge. The energy and time resolution

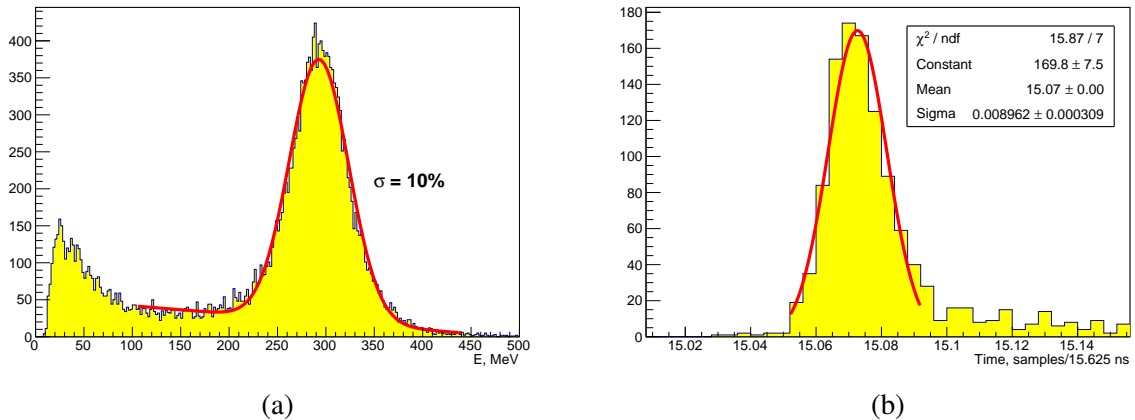


Figure 4.22: (a) Total energy deposition in the calorimeter for the MIP obtained by summing up signals from 16 cells while selecting 1-hit events. (b) Time resolution for calorimeter cell #11 is equal to 175 ps.

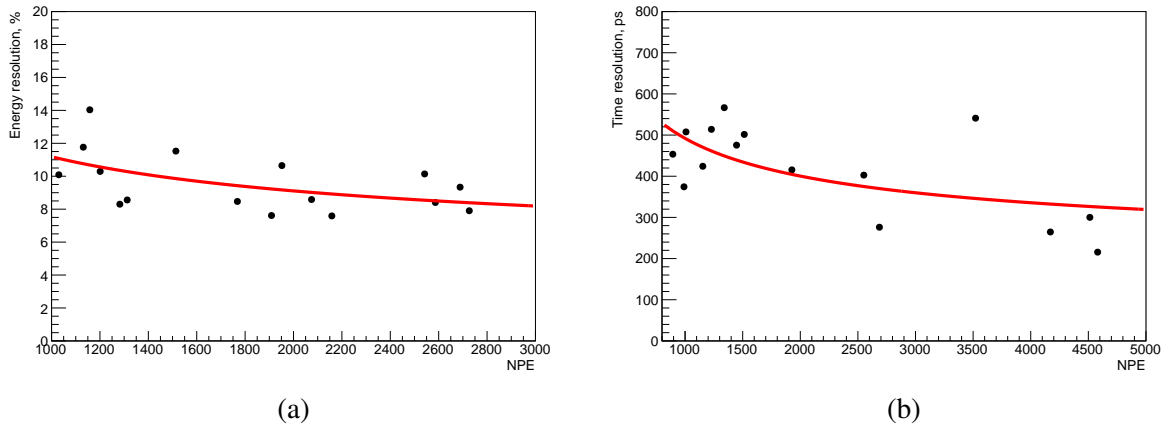


Figure 4.23: Dependence of energy (a) and time (b) resolution for different calorimeter cells on the number of photoelectrons (NPE).

of the calorimeter depend on the NPE as $1/\sqrt{NPE}$.

Different conditions of light guiding were used in this 4-module calorimeter. These conditions included forming reflective surfaces on the edges of the WLS, or using the fibers as U-shaped loops. Differences in light guiding conditions lead to large variations in the NPE in the range between 1000 and 3000 photoelectrons per MIP for different cells. In terms of the amount of deposited energy, this corresponds to $4000 \div 12000 \text{ NPE/GeV}$.

Information on the number of photoelectrons for each cell allows one to obtain dependence of energy and time resolution on the NPE . The presented dependences of energy and time resolution are displayed in Fig.4.23 and show that the limit for large values of the NPE is 6.2% and 197 ps for energy and time resolutions, respectively.

6.8 Long-term stability

Temperature dependence of calorimeter stability was investigated using daily temperature variations in the range of 18–22 °C. During the measurement of signals from cosmic ray particles over 5 days, signals from LEDs of a 1-Hz frequency were also measured. Photodiode temperature is constantly monitored using a high-voltage system. The voltage bias on photodiodes is corrected during a temperature mea-

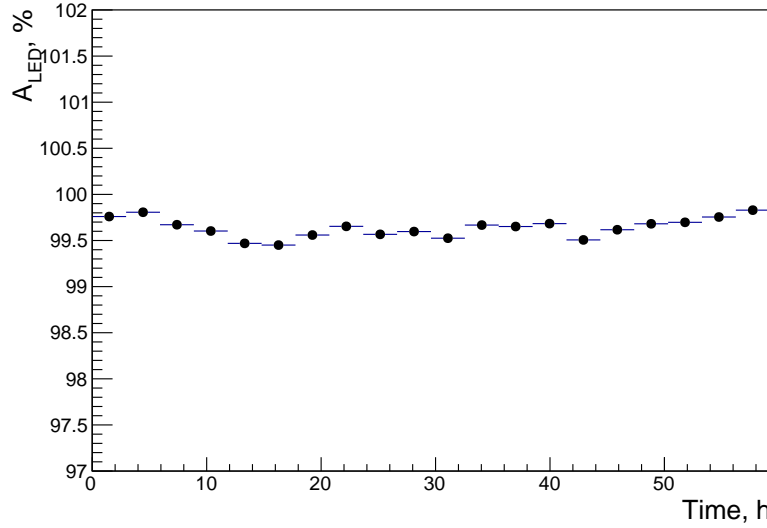


Figure 4.24: Dependence of the sum (average value) of signals from the calorimeter (in % with respect to the first 5 minutes of the measurement period) on the time of measurement (in hours) with temperature-dependent voltage compensation.

Table 4.6: Contributions of separate elements to the cost of the ECal.

	Ecal cell	WLS	ADC	HV	MPPC	Total
Cost per 1 cell, \$	300	270	80	20	30	700
Cost for 30.176 cells, M\$]	9.1	8.1	2.4	0.6	0.9	21.1

surement using a linear dependence: $U_{out} = U_{bias} - k \times (20 - T)$.

Daily temperature variations during the measurement were about 5°C. The temperature coefficient $k = 0.034$ V/°C is used for temperature compensation of the operating voltage. After compensation, variations in the signal amplitude are constrained within $\pm 0.4\%$. The plots are normalized to the start of the measurement. The first 300 signals (5 min) are used to normalize the full measurement period. The calorimeter can operate with a stability of $\sim 0.8\%$ if the temperature compensation of the operating voltage is maintained, as it can be seen from these results and is shown in Fig. 4.24.

6.9 Cost estimate

The cost of the calorimeter is proportional to the number of channels. Mechanical assembly of a calorimeter cell from the scintillator and the lead plates costs 300\$ per channel. Another expensive element is the wavelength shifting fibers. For a 40×40 mm² cell, 9 fibers of the total length of 54 m are used. Assuming an average price of 5\$/m, the price per channel amounts to 270\$. The cost of photodiodes depends on the quantity. For purchases of tens of thousands of units, their price is about 30\$ per unit. The electronics also contributes significantly to the total cost, especially the ADC with a price of 80\$ per channel. The cost of the supply and voltage control systems is 20\$ per channel. The total cost of a calorimeter cell is about 700\$. Thus, the total cost of a 30176-cell calorimeter is 21.1 M\$.

7 Range (muon) system

7.1 General description

The Range System of the SPD detector serves for the following purposes: (i) identification of muons in presence of a remarkable hadronic background and (ii) estimation of hadronic energy (coarse hadron calorimetry). It is important to stress that the system is the only device in the SPD setup, which can identify neutrons (by combining its signals with the electromagnetic calorimeter and the inner trackers). Muon identification (PID) is performed via muonic pattern recognition and further matching of the track segments to the tracks inside the magnets. The precise muon momentum definition is performed by the inner trackers in the magnetic field. The Mini Drift Tubes [404, 405] are used in the Range System as tracking detectors providing two-coordinate readout (wires and strips running perpendicularly). Such readout is mostly needed for the events with high track multiplicity and also for the reconstruction of the neutron space angle.

As for the design and construction of the present system, we assume to capitalize on the experience gained by the JINR group in the development of the PANDA (FAIR, Darmstadt) Muon System [406]. These two systems (PANDA and SPD), dealing with muons of comparable momentum ranges and solving the same PID tasks, should look very similar in their design and instrumentation.

7.2 System layout

The Range System serves as an absorber for hadrons and a ‘filter’ for muons. It also forms the magnet yoke. It consists of a barrel and two end-caps. Each end-cap, in its turn, consists of an end-cap disk and a plug. The schematic 3D view of the system and its main sizes are shown in Fig.4.25 (a). The absorber structure is shown in Fig.4.25 (b). The outer 60-mm Fe layers are used for bolting the modules together. The interlayer gaps of 35 mm are taken for reliable mounting of the detecting layers comprising the MDTs proper, the strip boards and the front-end electronic boards on them. The 30-mm thickness of the main absorber plates is selected as comparable with muon straggling in steel, thus giving the best possible muon-to-pion separation, and also providing rather good sampling for hadron calorimetry.

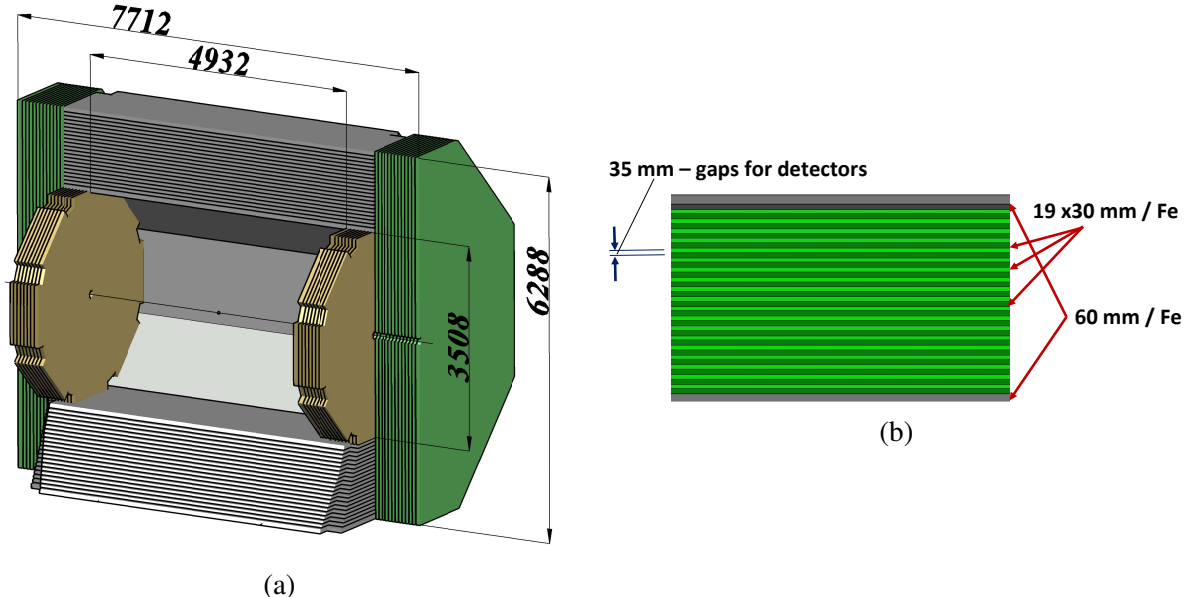


Figure 4.25: 3D view (half cut) of the Range (muon) system: (a) Barrel is shown in grey, End Cap Disks – in green, and End Cap Plugs – in yellow; (b) absorber structure.

The Barrel consists of eight modules, and each end-cap disk consists of two halves divided vertically.

Such subdivision of the system (14 pieces in total) is chosen to optimize its further assembly and to satisfy the constructional requirements of the SPD experimental hall (cranes capability and floor load). The total weight of the system is about 810 tons, including 30 tons of detectors. The total number of MDT detectors is about 8000 units. The MDTs are deployed in the following way: along the beam direction in the Barrel, and perpendicular to the beam (horizontally) in the end-caps.

The absorption thicknesses of the barrel and end-caps are selected to be equal to 4 nuclear interaction lengths (λ_l) each. It provides uniform muon filtering in all directions. Together with the thickness of the electromagnetic calorimeter ($\sim 0.5 \lambda_l$) the total thickness of the SPD setup is about $4.5 \lambda_l$.

7.3 Mini drift tubes detector

The Mini Drift Tubes (MDT) detector was initially developed and produced at JINR for the Muon System of the D0 experiment at FNAL [407]. Later on, an MDT-based muon system was also produced for the COMPASS experiment at CERN [408]. Developed two-coordinate readout modification of the MDT with open cathode geometry and external pickup electrodes was proposed to and accepted by the PANDA collaboration at FAIR for the muon system of their experimental setup. This new version of the MDT is proposed for the SPD project, as it has all the necessary features – radiation hardness, coordinate resolution and accuracy, time resolution, robustness, as well as advanced level of already conducted R&D within the PANDA project.

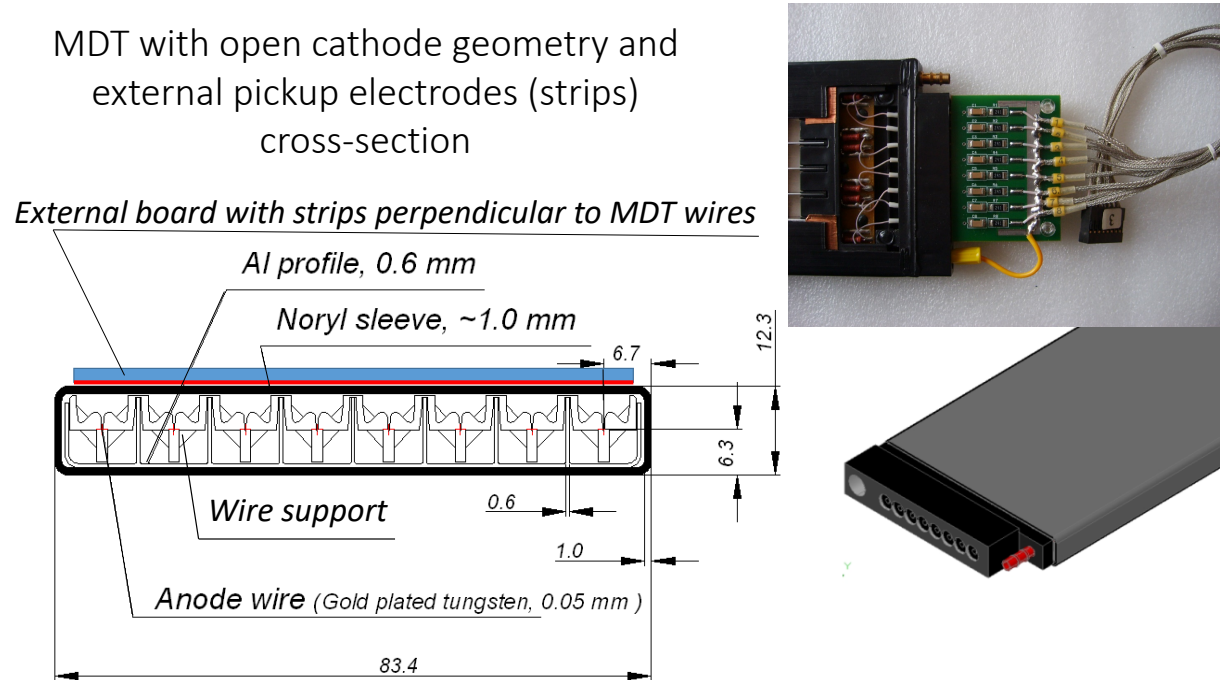


Figure 4.26: Mini Drift Tube with open cathode geometry cross-section (left) and layout (right).

The cross-section and layout of the MDT with open cathode geometry are shown in Fig.4.26. The detector consists of a metallic cathode (aluminum extruded comb-like 8-cell profile), anode wires with plastic supports, and a Noryl envelope for gas tightness. The comb-like profile of the cathode provides each wire with an opening left uncovered to induce wire signals on the external electrodes (strips) perpendicular to the wires. The strips are applied to obtain the second coordinate readout. The shape of the induced signal repeats the initial one, having the opposite polarity, but the amplitude is about 15% of the wire signal (see Fig.4.27). Thus, the strip signal readout requires higher signal amplification and proper electromagnetic shielding.

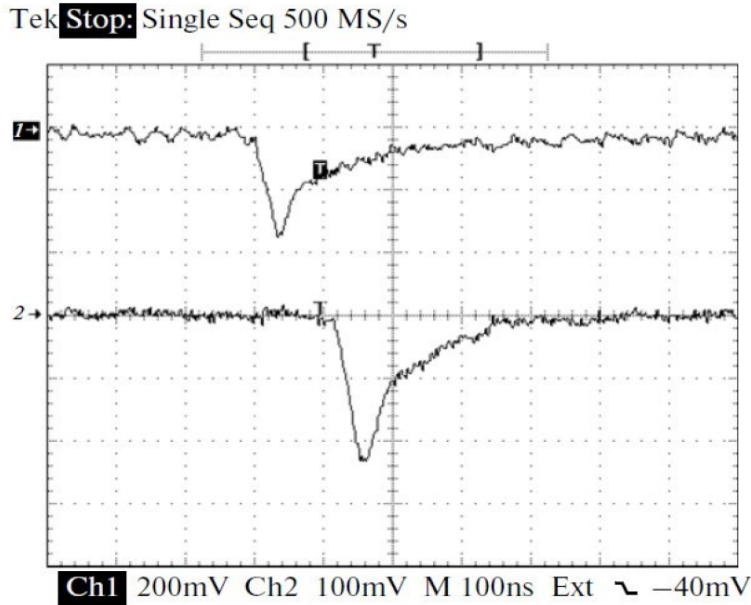


Figure 4.27: Oscilloscopes of single signals: from the anode wire (1) and the strip (2, inverted); the conversion factors are 60 and 480 mV/ μ A, respectively.

Application of an open cathode leads to the loss of the electric field symmetry in each of the 8 detector cells, resulting in lower gas gain for the applied voltage comparing to the standard MDT (cathode openings closed with stainless steel lid). The conducted R&D proved that the MDT with open cathode geometry easily achieves the parameters of the one with a closed cathode at higher voltages. The comparative plots of the counting rate, efficiency, and gas gain for both detector types (see Fig.4.28) show that the MDT with open cathode geometry repeats the standard MDT performance at a high voltage shift of +100 V. The drift time and the amplitude spectra of both detector variants also match, if we set this voltage shift between their operating points.

According to the results of the MDT (open cathode geometry) ageing tests, accumulation of a 1 C/cm total charge does not produce any significant effect on the detector performance. To monitor the ageing effects, measurements of the counting rate curves (Co-60 source) together with oscilloscopic observations of the MDT average signals (256 events) for Co-60 and X-rays were made twice a week over the whole period of intense irradiation (see Fig.4.29). Later on, this measurement (with X-rays) was conducted up to 3.5 C/cm of irradiation without any visible degradation of the MDT performance. It should ensure stable MDTs performance for the lifetime of the SPD project.

All R&D studies were made with a gas mixture of 70% Ar + 30% CO₂ at atmospheric pressure, the one to be used in the proposed SPD Muon System. It is inflammable, radiation hard and fast enough (150-200 ns drift time). The wire pitch in the present design equals 1 cm, and a 3-cm strip width is selected for the second coordinate. These spatial parameters provide the Range System with coordinate accuracy well enough for identification of muons and give the system the features of a digital hadron calorimeter.

7.4 Front-end electronics

We plan to use the analog front-end electronics (with probable minor modifications) developed for the D0/FNAL and COMPASS/CERN experiments and also accepted by PANDA/FAIR. It is based on two ASIC chips: 8-channel amplifier Ampl-8.3 [409] and 8-channel comparator/discriminator Disc-8.3 [410].

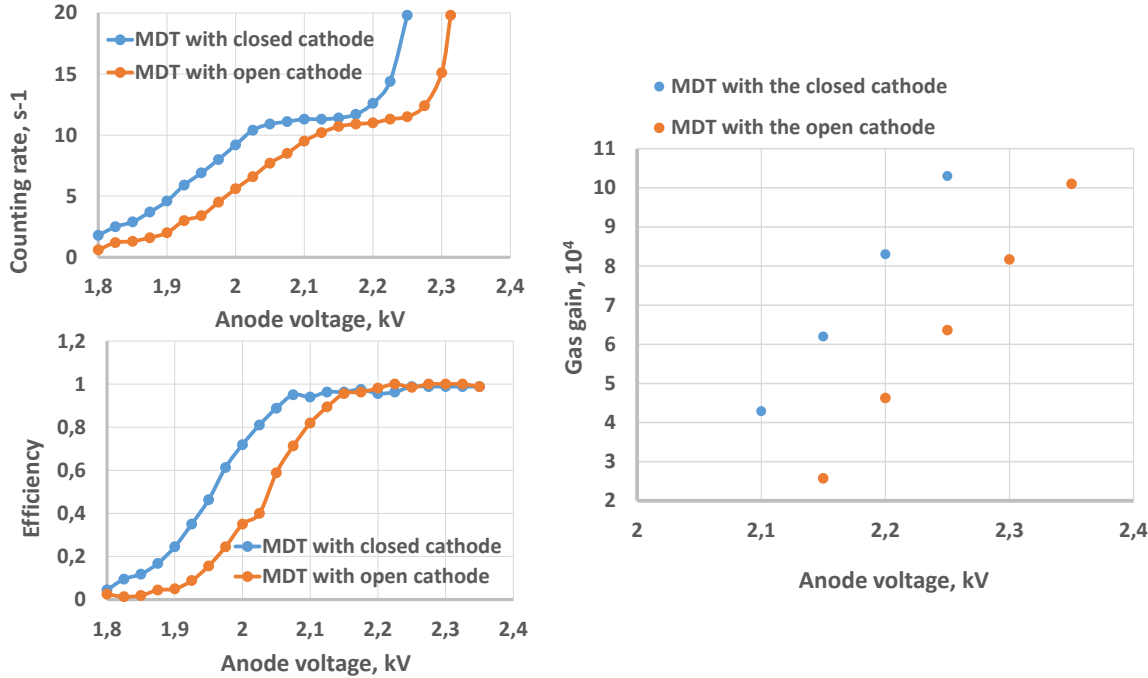


Figure 4.28: Comparative plots of the counting rate, efficiency, and gas gain versus the supply voltage for the MDT with closed and open cathode geometry.

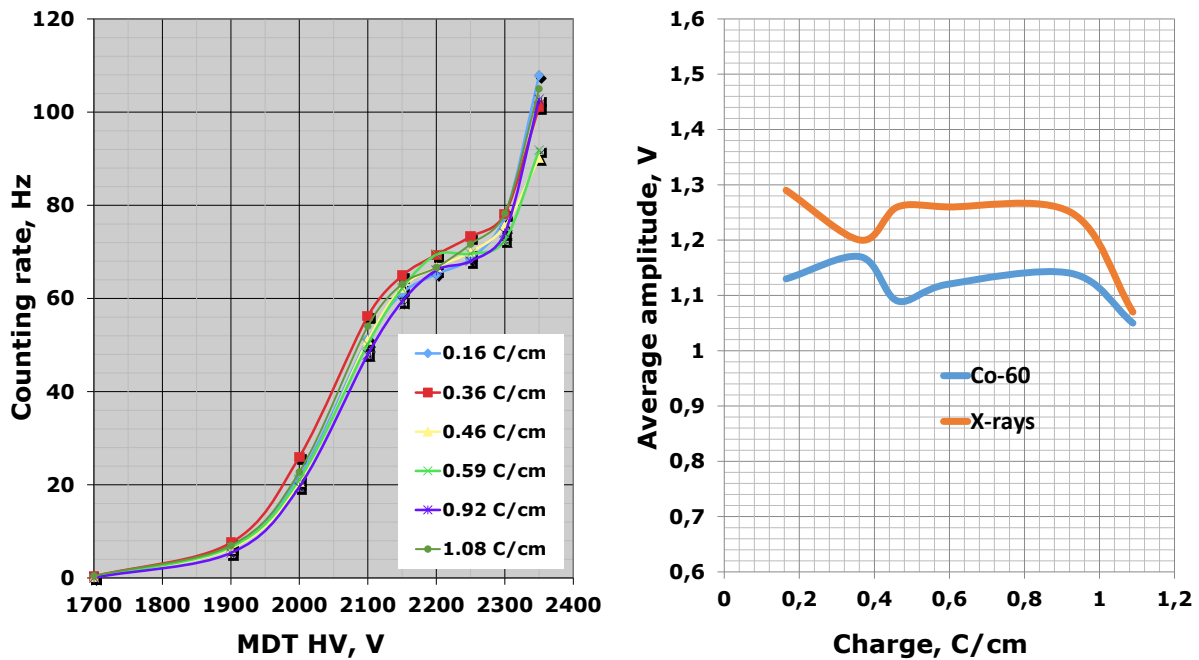


Figure 4.29: Counting rate curves for different accumulated charges ($0.16 \div 1.08 \text{ C/cm}$) (left); average wire signal amplitudes vs accumulated charge for Co-60 and X-ray sources (right).

The HVS/A-8 card serves for two purposes – as MDT high voltage distributor and a signal amplifier designed to be the first stage of the Barrel and the End Cap Plugs wire signal readout. It is followed by Disc-8.3 based discriminating electronics (design in process) to fulfill the readout.

The ADB-32 card (initially designed for D0/FNAL) [411] is used for the End Cap Disks wire readout.

It amplifies and discriminates the MDT signal, shaping it to the LVDS standard for further treatment by the digital front-end electronics.

An A-32 preamplifier card is used to start the strip signal readout in the whole system. It should be terminated (similarly to wire readout) by Disc-8.3-based discriminating electronics. In case of the End Cap Disks an ADB-32 card will be used for this purpose. The view of the basic FEE cards is shown in Fig.4.30.

Totally, the Range System has 106000 readout channels (65000 of which are wires and 41000 strips).

After having been shaped to the LVDS standard, the signals from the analog electronics go to the digital front-end electronics for further treatment.

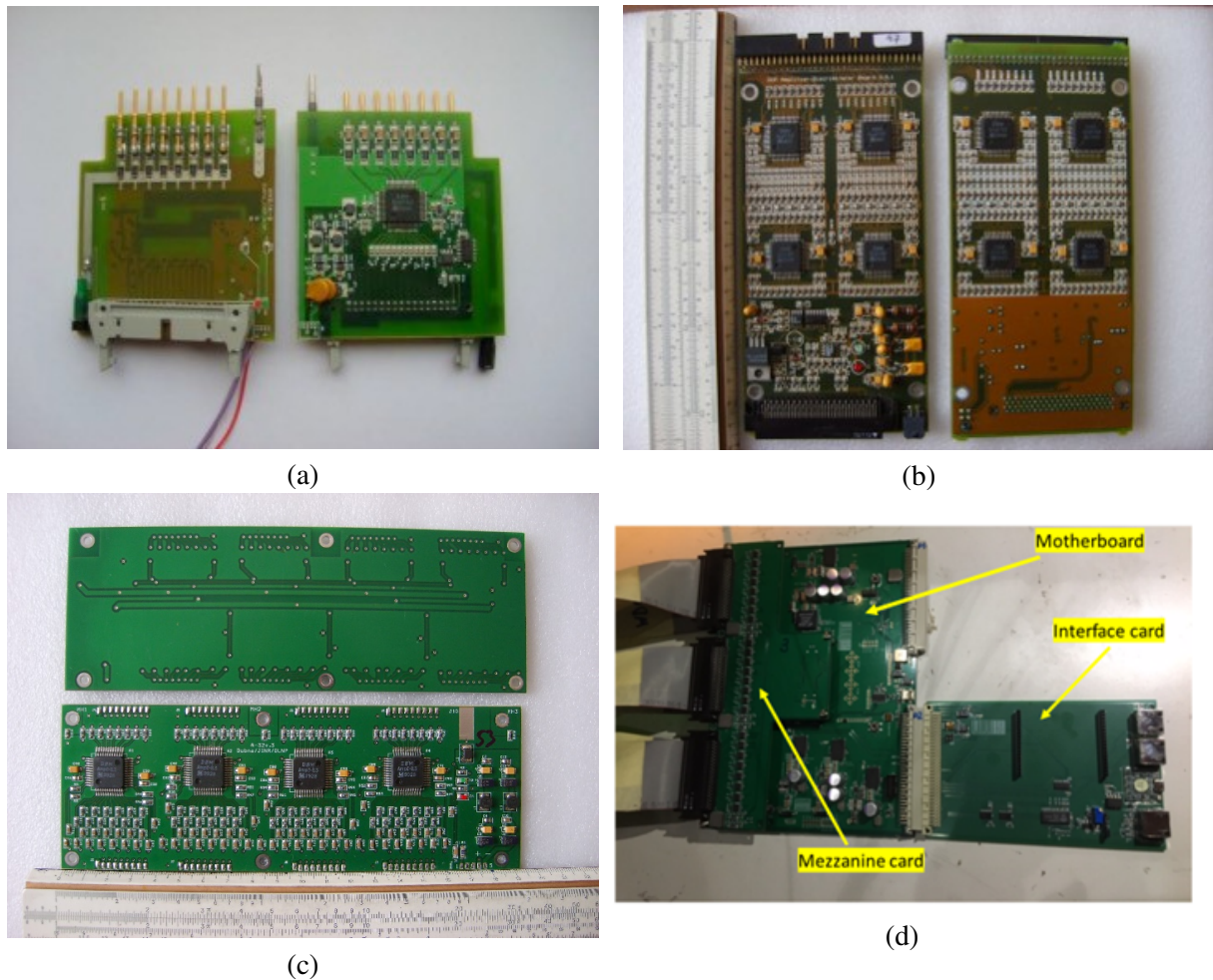


Figure 4.30: Front-end analog electronics cards: HVS/A-8 (a), ADB-32 (b) and A-32 (c). (d) Digital 192-channel MFDM module.

The digital electronics being created for the Muon System is based on the use of FPGA chips. The prototype of the digital 192-channel MFDM module (see Fig. 4.30 (d)) (Muon FPGA Digital Module) that we have developed includes a XC7A200T chip of the Xilinx Artix 7 family. This unit is functionally, mechanically, in data format and DAQ interface, compatible with the previously developed MWDB (Muon Wall Digital Board) unit [412] made on the basis of TDC F1 (ASIC) and successfully used for data readout from the Muon System of the COMPASS experiment (CERN). This approach allows both types of units to be used in the same readout system, thus making it possible for the new MFDBs cards to be tested under actual operating conditions.

The unit includes three electronic boards (Fig.4.31): motherboard, mezzanine card, and interface card. The motherboard accepts 96 LVDS signals from the analog electronics through 3 high-density connectors, converts them to LVTTL levels and writes to the FPGA, and also communicates with two other boards. The mezzanine card also accepts 96 LVDS signals through 3 connectors, converts them to LVTTL levels and transmits through the 120-pin board-to-board connector to the motherboard. The interface card is designed to connect the MFDM module with the DAQ via the HotLink interface (RJ45 connector), to download the firmware to the FPGA from a local computer, as well as to download the firmware via the RS-485 interface (RJ45 connector) from a remote computer.

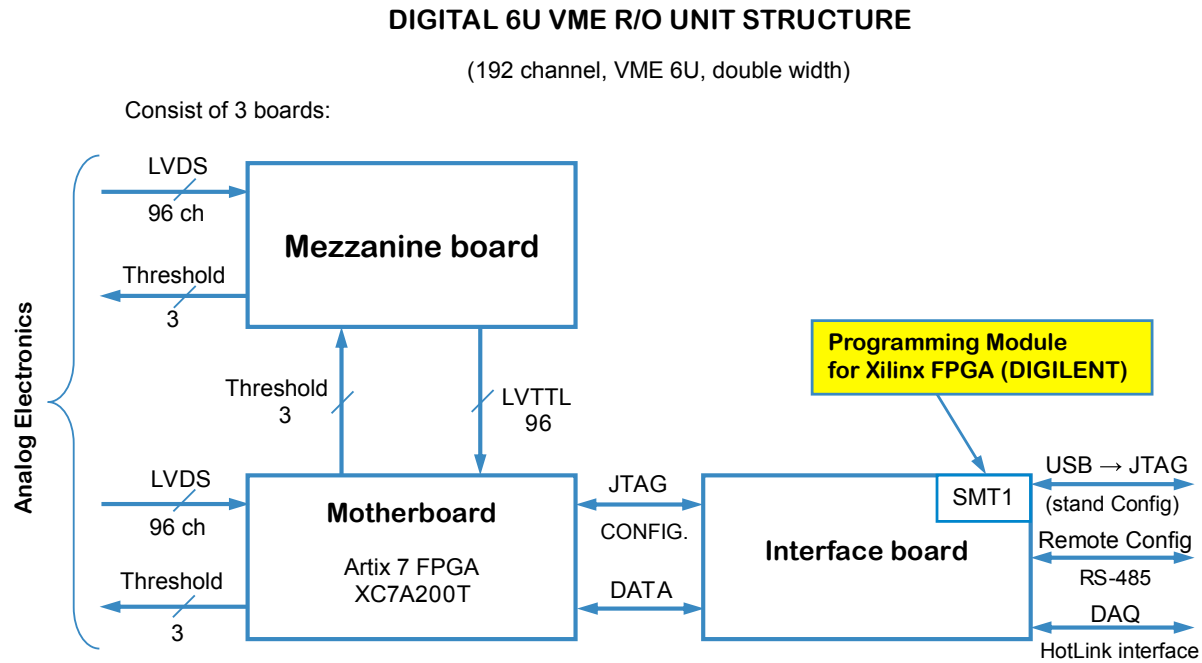


Figure 4.31: Block-diagram of the MFDM module.

Tests performed at CERN with the Muon System prototype on cosmic muons gave encouraging results. The further tests will be conducted with a prototype of the SPD range system (~ 1200 channels of wire and strip readout) at the Nuclotron test beam area.

In the future, after the final tuning of the unit, we are planning to replace the HotLink interface in the MFDM module with the S-Link interface for direct connection of the Muon System digital electronics to the FPGA-based SPD DAQ. A general view of the data flow structure for the Muon System is shown in Fig.4.32.

7.5 Performance figures

The evaluation of the main parameters of the proposed Range System is being performed with big prototype installed at CERN within the PANDA program. The prototype (see Fig.4.33) has a total weight of about 10 tons (steel absorber and detectors with electronics) and comprises 250 MDT detectors with 4000 readout channels (2000 for the wires and 2000 for the strips, 1 cm wide). It has both samplings (3 cm and 6 cm) present in the system (Barrel and End Caps), thus providing an opportunity for direct calibration of the response to muons, pions, protons, and neutrons.

Fig.4.34 gives the examples of the prototype response to different particles. The patterns demonstrate excellent PID abilities of the Range System. The data were taken during the May and August runs of 2018 at the T9/PS/CERN test beam. The beam particles hit the prototype from the top of the picture. The beam momentum for all the particles is 5.0 GeV/c. Neutrons were generated by a proton beam on a

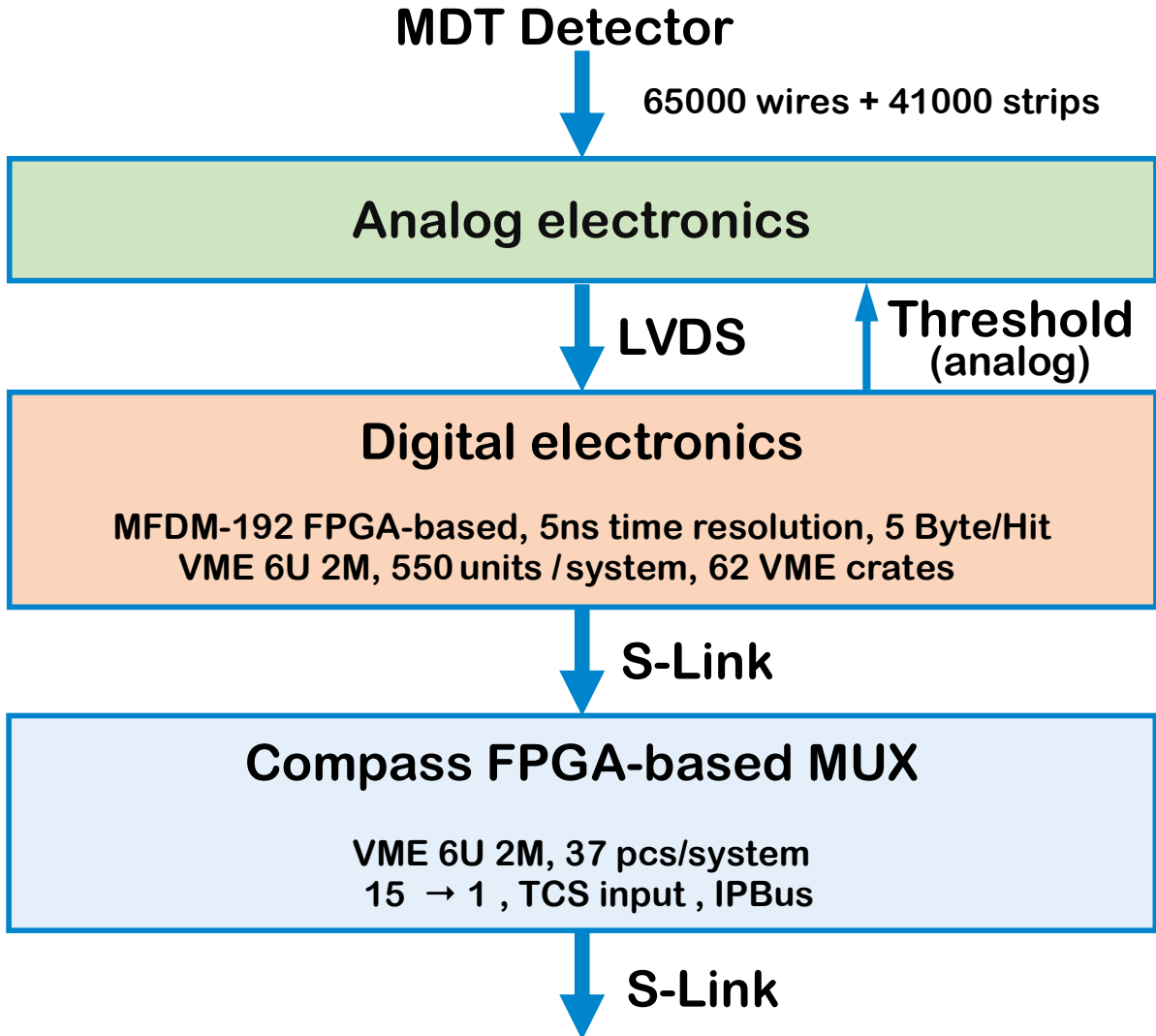


Figure 4.32: Data flow diagram – from the RS to the DAQ.

carbon target placed in the very vicinity of the first detecting layer. The points on the pictures represent hit wires, thus giving the impression of a typical device response with an accuracy ~ 1 cm.

7.6 Cost estimate

The preliminary cost estimate for the Range System is presented in Tab. 4.7.

8 Particle identification system

This Section describes detectors providing identification of particle types such as π , K , p . The particle identification system of SPD will include a time-of-flight detector (TOF) and a Cherenkov threshold detector with aerogel used as a radiator. Their data will be used in conjunction with the energy loss data registered by the straw tubes. The latter will serve to identify mainly soft particles which cannot travel more than a meter in the radial direction because of either decays or interactions. Whereas particles with longer trajectories will be able to reach and therefore can be identified using the TOF and aerogel counters.

The barrel part of the PID system will be located inside the magnet coils which will limit the radial

PANDA Muon System Prototype @ PS/T9/CERN Beam Line

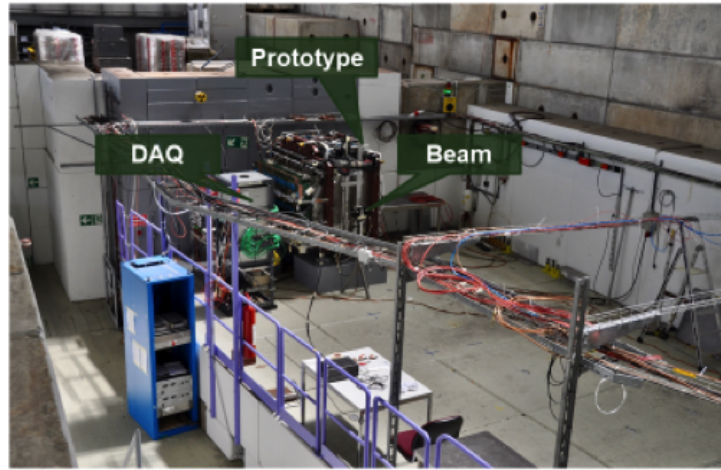


Figure 4.33: Range System prototype (10 ton, 4000 readout channels) at CERN.

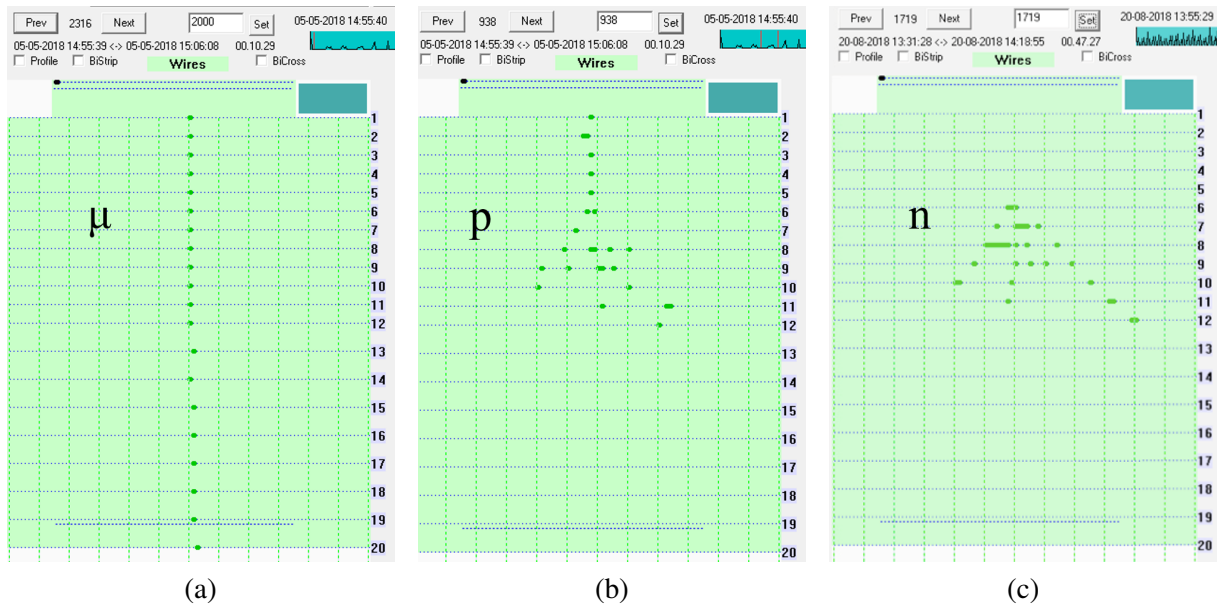


Figure 4.34: Demonstration of PID abilities: patterns for - (a) muon, (b) proton and (c) neutron.

flight distance for particles to 108 cm. The detectors will occupy a maximum radial thickness of 20 cm between the coils and the Straw Tracker (see Fig. 4.1). Spatial constraint for the end-caps is weaker. In this section, two technologies for the TOF and one for the Cherenkov aerogel counter are described. The choice for the baseline option will be made after comparing the respective performances, costs and availability of group which will be able to build the detector.

8.1 Time-of-flight system

The purpose of the time-of-flight (TOF) system is to discriminate between charged particles of different masses in the momentum range up to a few GeV/c . A short distance of 108 cm between the collision point and the TOF dictates the requirement for the time resolution of the TOF to be better than 70 ps. In

Table 4.7: Cost estimate for the RS.

	Cost, M\$
MDT detectors with strip boards	2.35
Analog front-end electronics (including cabling)	2.78
Digital front-end electronics (including VME crates and racks)	3.05
Yoke/absorber (without supporting structure and movement system)	6.00
Total	14.18

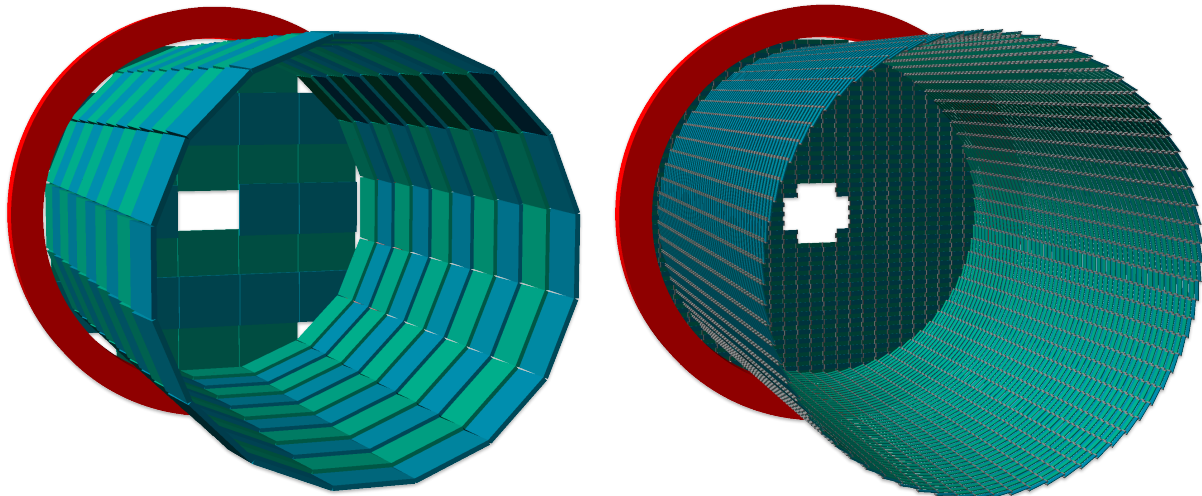


Figure 4.35: Two technologies are being considered for the time-of-flight system of SPD: the multigap Timing Resistive Plate Chamber, mRPC (left) and the plastic scintillator option (right). Barrel and one of two end-cap parts are shown for both options. One of six magnet coils limiting the volume of TOF is shown in red.

view of the uncertainty related to the length of the interaction region (about 60 cm), the time t_0 which can be assigned to the collision vertex will only be on the order of 1 ns, so it is useless for identification purposes. Therefore the particle identification (together with the t_0 determination) can only be done for multi-track events, where several particles emerged from a same primary vertex hit active elements of the TOF. A certain mass hypothesis will have to be applied in this procedure. For details of this analysis see Section 1.4 of Chapter 9. In addition to the particle identification, the detector will also provide a start time to the straw drift tubes.

The TOF system will consist of a barrel and two end-cap parts with an overall active area of 27.1 m². The charge particle rate that detector will have to withstand is 0.1 kHz/cm² for the barrel. The rate increases rapidly when moving closer to the beam axis. Thus, for the TOF elements located in the end-caps 20 cm off the beam axis, the rate of about 1 kHz/cm² is expected (see Fig. 9.3 for details). Two alternative technologies are being considered for the detector: a multigap Timing Resistive Plate Chamber (mRPC) and a plastic scintillator with Silicon Photomultiplier (SiPM) reading. Both are shown in Fig. 4.35. These two technologies, in general, can provide about the same efficiency and time resolution, require similar readout electronics and have about the same cost per channel. Main features as well as pros and cons of both options are listed below:

- *The multigap Timing Resistive Plate Chamber.* It is a stack of resistive glass plates with high voltage applied to external surfaces. Pickup electrodes are located inside the chamber separating

	MPRC	Plastic scintillator
Active area: barrel + 2×end-cap	$19.8 \text{ m}^2 + 2 \times 3.7 \text{ m}^2 = 27.1 \text{ m}^2$	
Area of readout element: pitch × length	strip $1.25 \text{ cm} \times 40 \text{ cm} = 50 \text{ cm}^2$	tile $2.9 \text{ cm} \times 9 \text{ cm} = 26.1 \text{ cm}^2$
Size of chamber or tile: W × L × H	chamber (24 strips) $33 \text{ cm} \times 40 \text{ cm} \times 2.5 \text{ cm}$	tile $3 \text{ cm} \times 9 \text{ cm} \times 0.5 \text{ cm}$
Number of chambers or tiles: barrel + 2×end-cap	chambers $160 + 2 \times 30 = 220$	tiles $7.3\text{k} + 2 \times 1.4\text{k} = 10.1\text{k}$
Number of DAQ channels	10.6k	20.2k

Table 4.8: Dimensions and numbers of the TOF elements for two technologies: mRPC and plastic scintillator.

two stacks, 6 gas each. A fast signal induced on the pickup electrodes by an electron avalanche is further transported to FEE located nearby. The schematic cross-section of the mRPC is shown in Fig. 4.36. All aspects of this technology are well tested and deployed in a number of projects like MPD [413] and BM@N which is described later. Overall dimensions of one mRPC is $400 \times 330 \times 25 \text{ mm}^3$ which corresponds to a PCB with 24 readout strips, each 10 mm wide and 400 mm long. The detector is composed of 220 chambers: 160 and 30 chambers for the barrel and each end-cap, respectively. Adjacent mRPCs will be positioned in such a way as to create an overlap of 1 strip at the edge of the active area. This will ensure the inter-calibration of the mRPCs using tracks crossing both chambers. A rectangular shape of each chamber, which is quite large and can not be modified, creates a certain inconvenience for covering the end-cap parts of detector. Contributions of all parts of the TOF to the radiation length is about $0.14X_0$ in average [413].

– *The plastic scintillator option.* The basic element of the detector is a plastic scintillator tile with dimensions of $90 \text{ mm} \times 30 \text{ mm} \times 5 \text{ mm}$. Scintillation photons produced by an ionizing particle are read out on two ends of tile by an array of 4 SiPMs soldered to custom pre-amplifier PCBs. A schematic view to the plastic scintillator tile of the TOF/PANDA is presented in Fig. 4.37. The TOF/SPD detector will be composed of 10.1k staggered tiles: 7.3k and 1.4k tiles for the barrel and each end-cap, respectively. Having much smaller size of a single element of detector, it can easier adopt the cylindrical shape of magnetic coils and the beam hole. Furthermore, the system is much lighter in weight than the one of the mRPC and the number of radiation lengths for particle crossing the detector is smaller by the factor of 5. The system manufactured with this technology is easier to maintain than the one of the mRPC since it does not require gas circulation, neither high voltage is needed (no trips due to sparks). This kind of setup, however, was not used at JINR experiments before and will require a detailed R&D. The resistance of scintillator to the radiation level has also to be studied.

Dimensions and numbers of the TOF elements for the two options are given in Tab. 4.8. The choice of the technology for the baseline option will be made after more detailed studies of the actual particle rates, comparing the respective performances, the calibration strategy and the costs.

8.1.1 ToF-system based on the mRPC

The required time resolution for SPD is better than 70 ps while the efficiency of particle registration at high rate (few kHz/cm²) should be above 98%. Based the experience of building similar systems in such experiments as ALICE [414], HARP [415], STAR [416], PHENIX [417] and BM@N [418], a glass

multigap Resistive Plate Chamber could be used as base time detector. For example, the ToF-700 wall in the BM@N experiment, placed at a distance of 8 m from the target, provides one the π/K separation up to 3 GeV/c and p/K separation up to 5 GeV/c under the assumption that the time resolution of the start timing detector is <40 ps.

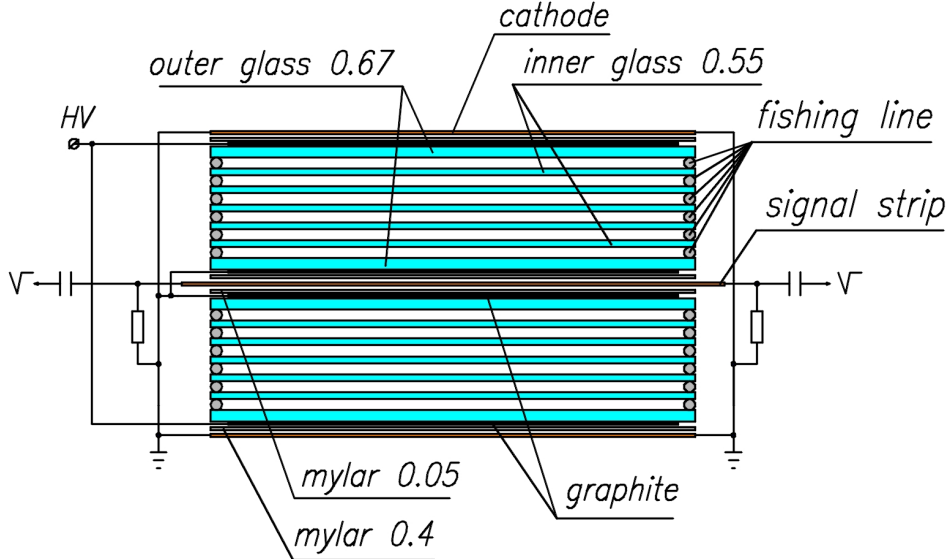


Figure 4.36: Schematic view of the twelve-gap mRPC [419].

The design of the BM@N ToF-700 wall is based on experimental results obtained during multiple tests of various modifications of the glass mRPC exposed in charge particles beam. The count rate for a standard glass mRPC is limited to several hundreds Hz/cm^2 due to the use of conventional float glass plates with a bulk resistivity in the range $10^{12} - 10^{13} \Omega \cdot \text{cm}$. Therefore, the extension of the counting rate capabilities of the mRPC has become an important issue.

One of the ways to increase the mRPCs performance at high rates is to use the low resistivity glass (less than $10^{10} - 10^{11} \Omega \cdot \text{cm}$) [420–422] or ceramics [423] as the electrode materials. For instance, time resolutions below 90 ps and efficiencies larger than 90% were obtained for particle fluxes up to 25 kHz/cm^2 for the 10-gap mRPC [424]. An alternative method is to reduce the glass stack resistance by minimizing the used electrode thickness and increasing a temperature of the glass [425, 426]. It was shown that such method can provide high time resolution at continuous rate up to $20 \text{ kHz}/\text{cm}^2$ [427].

Schematic cross-section of the mRPC used at BM@N is shown in Fig. 4.36. It consists of two identical 6-gap stacks with anode strip readout plate in between. The size of mRPC is $473 \times 279 \times 17 \text{ mm}^3$ with the working area of $351 \times 160 \text{ mm}^2$. Each mRPC has $3210 \times 160 \text{ mm}^2$ readout strips with 1 mm gaps between them.

Each stack is formed by seven glass plates with the $2 \times 10^{12} \Omega \cdot \text{cm}$ bulk resistivity. The 0.22-mm gap between the glasses is fixed by spacers – usual fishing-lines, which ran directly through the RPC working area. The graphite conductive coating with surface resistivity of $\sim 1 \text{ M}\Omega$ is painted to the outer surfaces of the external glass plates of each stack to distribute both the high voltage and its separate ground to form a uniform electrical field in the stack sensitive area. The anode readout strips plate is a one-sided printed PCB with the thickness of 100 mm. The thickness of the copper layer is 35 μm . Signals are taken from the both ends of the anode strips. The entire mRPC assembly is put into a gas-tight box. The bottom of box is made of a double-sided PCB (motherboard) with a thickness of 2.5 mm, the side frame of the box is made of aluminum profile, the top of box is closed by the 1.5-mm aluminum cover. The paper [428] presents the performance of the 12-gap mRPC in the range of the counting rate from

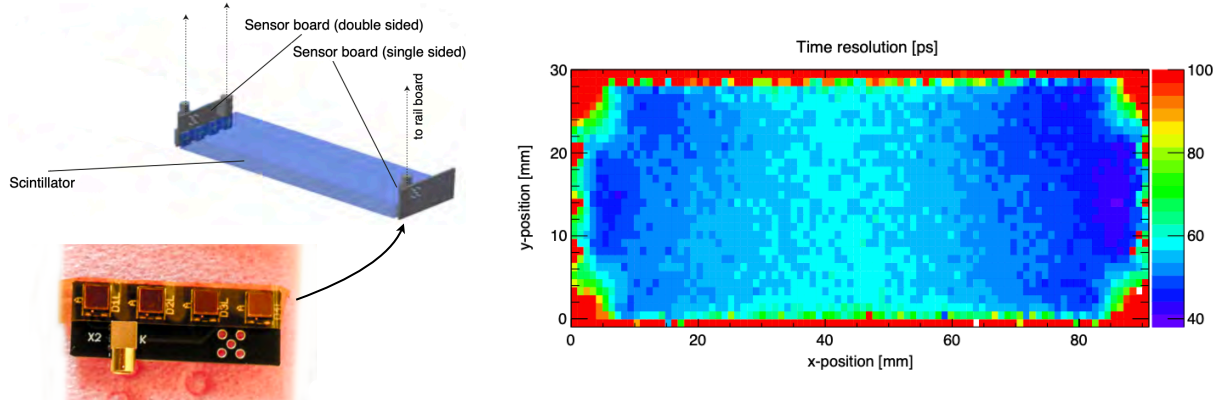


Figure 4.37: Left: schematic view to the plastic scintillator tile and a photo of the 4 SiPM board of PANDA [429]. Right: time resolution obtained from a position scan of a $90 \times 30 \times 5 \text{ mm}^3$ EJ-232 scintillator tile read out by Hamamatsu SiPMs attached to opposite sides, 4 SiPMs in series per side [429].

0.45 kHz/cm² up to 10 kHz/cm² obtained using the secondary muon beam from the U70 accelerator at Protvino. The measurements at different rates were performed in the temperature range 25-45 °C with the step of 5 °C. The time resolution is reached up to 50-60 ps with good and stable efficiency under the temperature of 40-45 °C.

Since the particle flux in the SPD experiment is expected to be up to 1 kHz/cm², a similar approach could be used to build the mRPC-based high-speed TOF with time resolution of about 50 ps.

8.1.2 TOF system based on plastic scintillator

This option was inspired by the TOF system of the MEGII [430] and PANDA [429] experiments. The surface of the TOF is segmented into many small scintillator tiles made of a fast scintillating organic material. The optical readout is performed by Silicon Photomultipliers (SiPM) attached to the ends of every tile. A typical number of optical photons produced by a minimum-ionising particle crossing a 1 cm plastic scintillator is $\sim 10^4$. A resulting number of detected photons depends on a signal propagation and photosensor efficiencies. Nowadays, large-area SiPMs have appeared on the market at relatively moderate cost and offer several advantages over PMTs: magnetic field tolerance, a much smaller volume and footprint allowing a compact design for bars without light-guides, low operation voltage and high photon detection efficiency (PDE). Thus, they ideally meet the requirements dictated by a thousand tile system of the TOF/SPD.

The choice of the scintillator material is primarily driven by the requirement for a short emission time. Organic scintillators based on a plastic matrix of polyvinyl-toluene, such as EJ-228 (BC-420) or EJ-232 (BC-422), have an attenuation length of about 10 cm, rise time of 0.5 ns and wavelength of maximum emission in UV region of 391 nm. They are commonly used for applications as the one discussed in this Section. Note that, contrarily to the mRPC, the time resolution of a plastic scintillator detector degrades exponentially with increase of distance between the interaction point and photosensor. It is especially crucial for UV photons. Therefore the choice of scintillator is all the time a compromise between the attenuation length (visible light) and fast emission (UV region).

In the case of the TOF/PANDA, a scintillator tile with dimensions of $90 \times 30 \times 5 \text{ mm}^3$ was read out by 4 Hamamatsu SiPMs coupled to opposite sides as shown in Fig. 4.37 (left). Each SiPM has its sensitive area of $3 \times 3 \text{ mm}^2$, thus the array of four can detect about a quarter of photons reaching the edge of tile. This configuration was chosen as a baseline for estimates for the TOF system of SPD. The time resolution obtained from a position scan is shown in Fig. 4.37 (right). One can see that the resolution varies from

50 ps in the near-to-SiPM region to 60 ps in the center of tile. The resolution of 100 ps around the end of tile is, presumably, due to tracks only partially crossing the volume of scintillator.

Summarizing the advantages of the plastic scintillator option versus the mRPC, one can say that the assembling is faster, easier and does not require clean environment; it is easier to maintain the detector (no gas flow, only LV); the detector can be squeezed within 5 cm radially, thus leaving space for the aerogel option which is described in the next section; the circular cross-section of the barrel can be approximated exactly matching the magnet coils from the outside; the radiation length is only 2% of X_0 . The weak points of the plastic option are: an exponentially drop of the resolution vs distance, which will require larger number of SiPMs for the case of longer tile; a smaller surface of a single tile, 26 cm^2 vs 50 cm^2 of a mRPC's strip, doubles the number of read channels; the organic material is sensitive to radiation. Although this option is promising it will require a detailed study before being accepted.

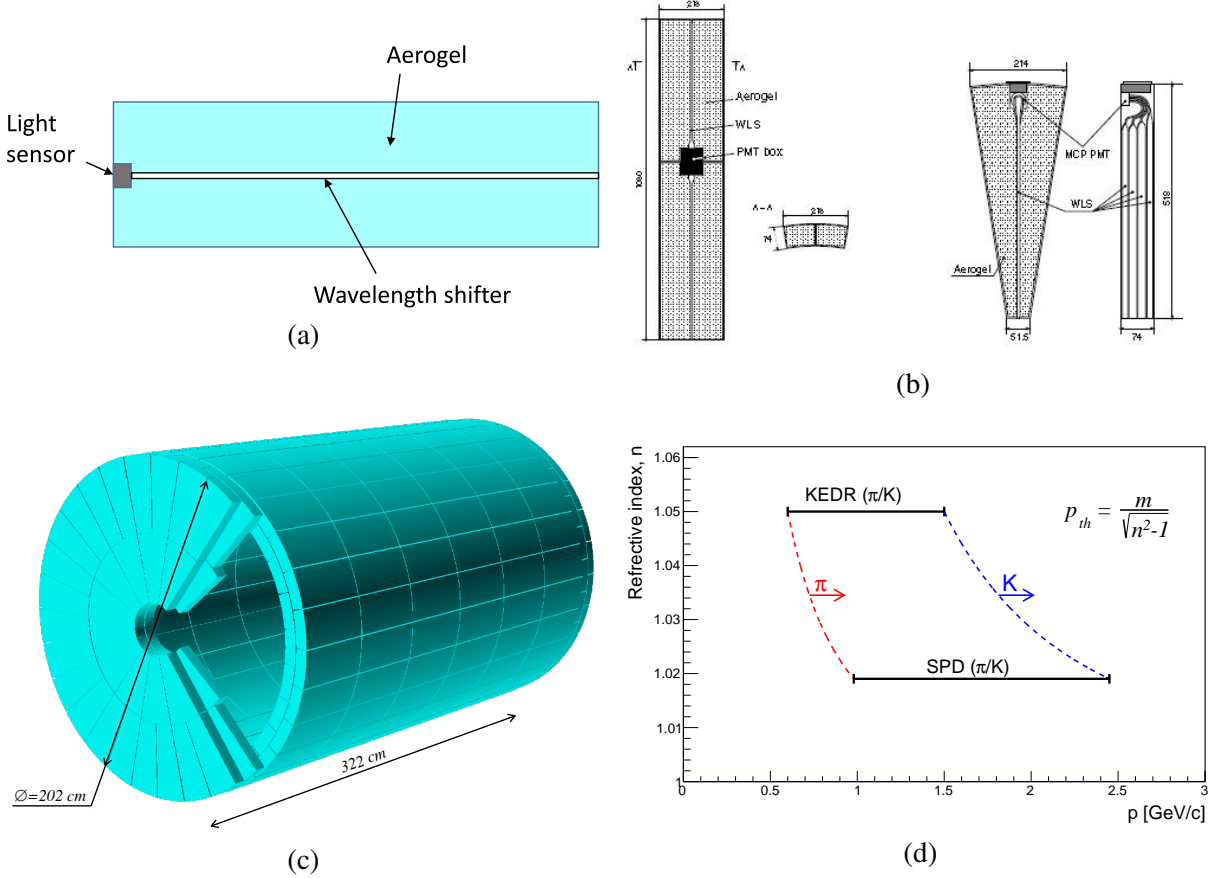


Figure 4.38: (a) Principle of ASHIPH operation. (b) KEDR aerogel counters: two barrel counters in a single housing (left), end-cap counter (right) [431]. (c) Possible arrangement of barrel and end-cap counters in SPD. (d) Momentum intervals of KEDR and SPD where the π/K separation is possible.

8.2 Aerogel counters

Another option for the system of particle identification is aerogel Cherenkov counters. Aerogel is a synthetic porous ultralight material which has found an application, in particular, as a radiator in Cherenkov counters. Aerogel may have a refractive index in the range between 1.0006 and 1.2, the exact value of the refractive index being specified at the production stage. In fact, aerogel fills the gap in the refractive index values between gases and liquids. This feature of aerogel allows one to use it in Cherenkov counters for particle identification in conditions when other Cherenkov radiators are not applicable, for

instance, for π /K separation at the momenta from few hundred MeV/c to about $3 \text{ GeV}/c$. The selection of the refractive index value defines the region of momenta where the separation is effective.

There exists a good experience of using threshold aerogel Cherenkov counters, in particular, in experiments KEDR (BINP, Novosibirsk) [431], [432], BELLE (KEKB, Tsukuba) [433]. In the BELLE experiment a threshold aerogel Cherenkov counter with refractive index from 1.010 to 1.030 provided π /K separation in the momentum region up to $3.5 \text{ GeV}/c$. In the KEDR detector the aerogel counters with refractive index 1.05 provided π /K separation in the range from 0.6 to $1.5 \text{ GeV}/c$.

Aerogel has a short scattering length of light, 12-40 mm depending on wavelength. Therefore, directivity of Cherenkov light cannot be used because directivity disappears soon after emission. For this reason diffusive reflectors are used at the walls. No scintillation has been observed in aerogel. Aerogel samples suffered from hygroscopicity for a long time, but in the 1990s the technology of hydrofobic aerogel has been developed.

In KEDR, the aerogel counters received the name ASHIPH (Aerogel, SHIfter, PHotomultiplier). In Fig. 4.38 (a) a principle scheme of the counter is shown. Cherenkov light from aerogel is captured by a wavelength shifter (WLS). PMMA light guide doped with BBQ dye is used as wavelength shifter, cross-section of WLS is $3 \times 17 \text{ mm}^2$. WLS absorbs Cherenkov photons at short wavelengths where Cherenkov radiation is more intensive and re-emit photons at large wavelength bringing them to a light sensor. In Fig. 4.38 (b) the counters of KEDR are shown. The microchannel plate photomultipliers served as light sensors in KEDR, but for later developments the APD were used (BELLE-II), also SiPM are proposed for aerogel detectors in PANDA (GSI) and FARICH (for Super Charm-Tau Factory in Novosibirsk).

If a particle crosses WLS, it produces a much higher signal than the particle traversing aerogel. To avoid misidentification, two-layer structure in KEDR is used with shifted layers with respect to WLS position, so that a particle cannot cross WLS in both layers. The thickness of one layer is 74 mm, a total amount of material in both layers is $0.24X_0$.

For relativistic cosmic muons that cross both counter layers of KEDR the average number of photoelectrons was 9.3 ± 0.4 , and the detection efficiency $99.3 \pm 0.1\%$ at the threshold that equals to 2 photoelectrons. For under-Cherenkov-threshold muons ($200 < p_\mu < 300 \text{ MeV}/c$) the efficiency was $3 \pm 1\%$.

In SPD aerogel counters *a la* ASHIPH can be inserted between the Straw tracker and ECAL. Possible arrangement of barrel and end-cap counters in SPD is shown in Fig. 4.38 (c). The barrel of SPD is a factor of 2 longer and 50% wider as compared to the one of KEDR. Thus the amount of aerogel will have to be three times larger in volume: 1 m^3 and 3.2 m^3 for KEDR and SPD, respectively. The number of counters will also increase by about the same value.

The value of refractive index can be selected for the momentum region where π /K separation is the most important. As will be shown in Fig. 9.10, this separation up to $1 \text{ GeV}/c$ can be provided by the TOF. Aerogel will be employed for momenta above this value which corresponds to the refractive index equal to 1.02 as shown in Fig. 4.38 (d). One can see from the figure that kaons begin generating a signal in the counters having momenta above $2.5 \text{ GeV}/c$, which defines the region of detector applicability.

The detector is thin (in terms of X_0), fast and rather simple in operation. We estimate its cost to be of about 5 M\$.

9 Beam-beam counters

Two Beam-Beam Counters (BBCs) are planned to be located just in front of the PID system in the end-cups of the SPD setup. The detector should consist of two parts: the inner and the outer one, which are based on different technologies. The inner part of the BBC will use fast segmented MicroChannel Plate

(MCP) detectors and should operate inside the beam pipe, while the BBC outer part will be produced from fast plastic scintillator tiles. The inner part covers the acceptance $30 \div 60$ mrad and should be separated into 4 layers consisting of 32 azimuthal sectors. The outer part covering the polar angles between 60 and 500 mrad will be divided into 5 or 6 concentric layers with 16 azimuthal sectors in the each of them. The final granularity is the matter of further optimization for the entire energy range of collisions at SPD. The concept of the BBC is shown in Fig.4.39. The magenta part represents the MCP detector while the internal layer of the outer part is shown in red.

The main goals of the Beam-Beam Counters are: i) the local polarimetry at SPD basing on the measurements of the azimuthal asymmetries in the inclusive production of charged particles in the collisions of transversely polarized proton beams, ii) the monitoring of beam collisions and iii) participation in the precise determination of the collision time t_0 for events in which other detectors can not be used for that (for instance in case of elastic scattering).

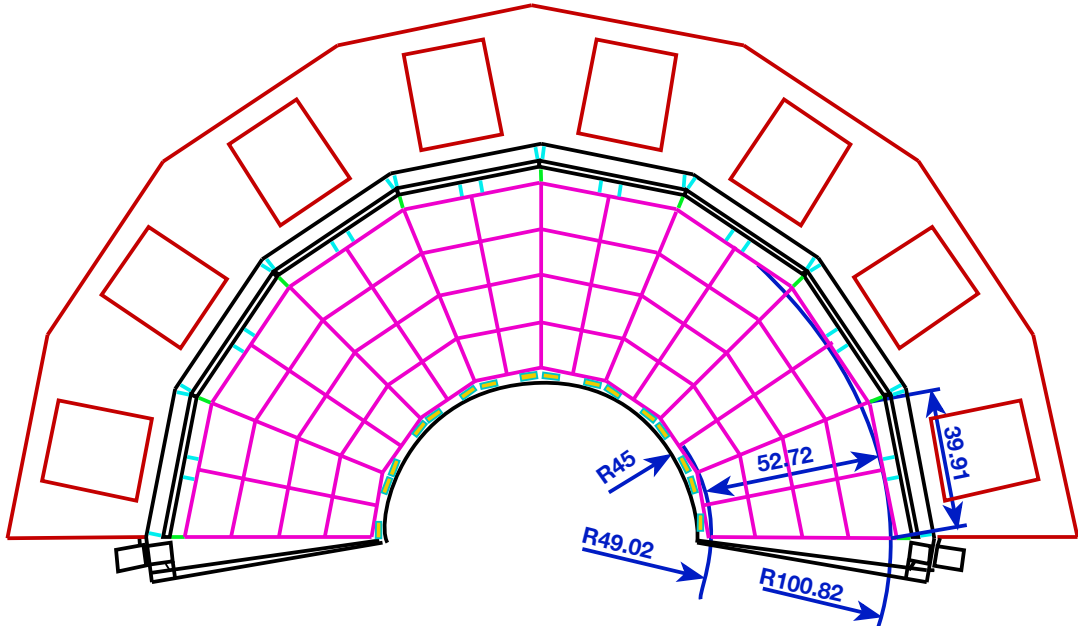


Figure 4.39: Beam-Beam Counter: azimuthal and polar angle segmentation [434]. All dimensions are in millimeters.

Another important goal of the BBCs is fast preselection of different types of events for monitoring purposes. The Monte Carlo simulation shows that in the p - p collisions at $\sqrt{s}=27$ GeV at least one BBC should have a signal in 79% of events (51% of events has a signal in the both BBCs). However, for the hard processes, in 97% of events the only one BBC will be hit, while hits for both counters could be expected in 68% of cases. Therefore, the requirement of the BBC signals allows one to preselect hard processes.

9.1 Inner part of the BBC: MCP

The concept of the MCP-based Fast Beam-Beam Collision (FBBC) monitor is described in details in [435]. Two ring beam-beam collision detectors (FBBC-left and FBBC-right) could be located inside the vacuum beam line together with two 2D position-sensitive beam imaging detectors (BPMs) (see Fig. 4.40). The FBBC uses the concept of the isochronous multi-pad fast readout and the precise timing determination of short (~ 1 ns) MCP signals. Individual fast readout of pads is being also considered. New MCPs with the improved characteristics, such as small diameter ($8\mu\text{m}$) channels, low resistivity ($100 \div 500$ M Ω), high gain ($\sim 10^7$), short fast rise-time (~ 0.8 ns) signals, could be used.

Fig.4.41 shows a typical MCP signal from the detector prototype. The colliding beams pass through the central opening of the MCP, and the outer edges of the MCP capture secondary particles flying a definite distance from the interaction point. The signals are recorded at the sectorized cathode and their arrival times are digitized along with the multiplicity information. The main feature of the new MCP is a high secondary emission coefficient and fast fronts of the output signal. The new MCPs have a fast leading edge and high gain.

The feasibility of the event-by-event monitoring of the beam-beam interactions at NICA is confirmed both by the previous developments of the UHF-UHV technology and by the beam tests (at JINR and CERN) [434–436] of the prototype detectors and electronics, as well as by the in-lab tests of new 8-channel MCPs with the improved characteristics.

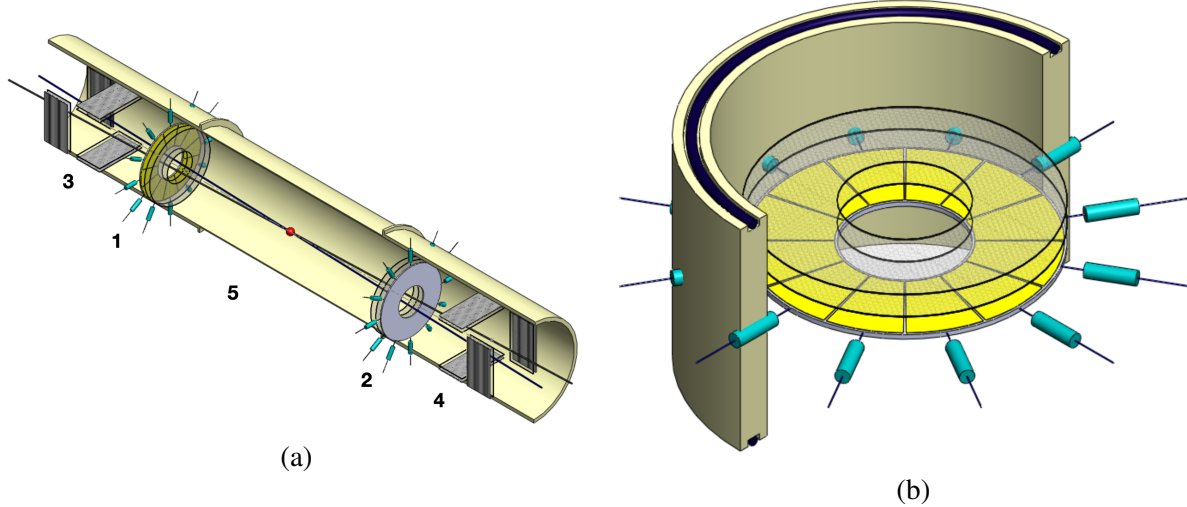


Figure 4.40: (a) Possible layout: the Fast Beam-Beam Collision (FBBC [435]) monitor composed of MCP discs (1 and 2) in combination with the Beam Position devices (BPM) (3 and 4) are situated symmetrically to the Interaction Point (5) inside the vacuum beam pipe of the NICA collider. (b) Compact module of the Fast Beam-Beam Collision Monitor (FBBC) based on circular MCPs. Sector cathode readout pads and two MCP setups are embedded into a separate flange with a hermetic 50- Ω signal and HV feedthroughs (the latter are not shown).

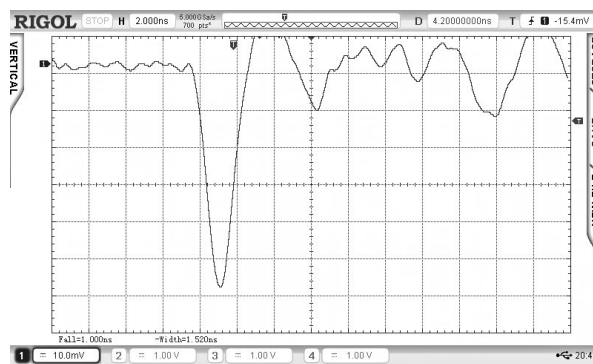


Figure 4.41: A typical MCP signal from the detector prototype.

9.2 Outer part of the BBC: scintillation tiles

The scintillation part of the BBC will consist of tiles viewed by the SiPMs. The measurement of the signal amplitude is required for time-walk correction to improve the time resolution.

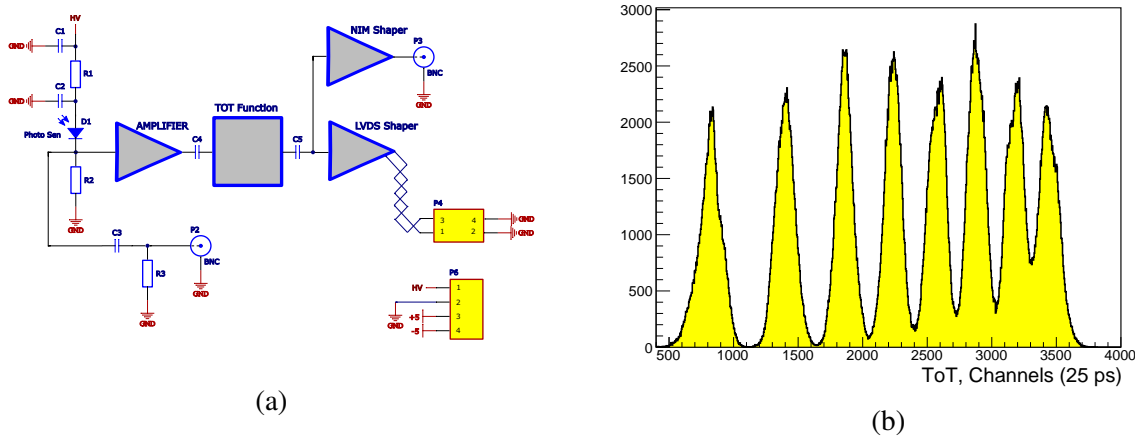


Figure 4.42: (a) Schematic view of the front-end electronics with a ToT function, (b) Distribution of the ToT for LED signal.

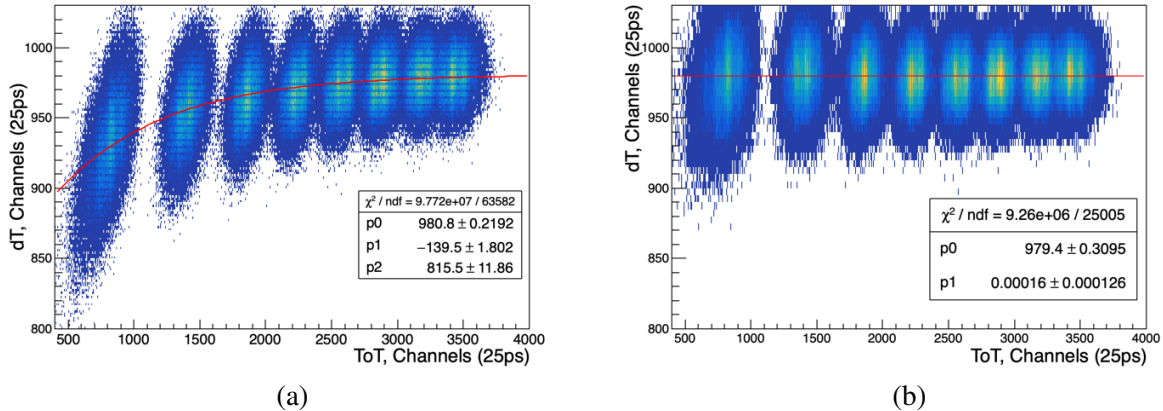


Figure 4.43: (a) dT ($T_{SiPM1} - T_{SiPM2}$) correlation on the ToT. (b) Result after the time-walk correction for the dT ($T_{SiPM1} - T_{SiPM2}$) correlation on the ToT.

With a single-channel prototype of the detector we will be able to measure the amplitude using the developed FEE based on the Time-over-Threshold (ToT) technique. This technique is a well-known method that allows us to measure the energy deposited in the material by reconstructing the given property of the output current pulse – the total charge collected, the pulse amplitude, etc. The ToT method converts the signal pulse height into a digital value in the early stage of the FEE, which greatly simplifies the system in comparison to analog detectors with serial readout through ADCs. The measurement of the ToT is composed of two measurements of time for the signal going above (leading) and returning below (trailing) the given threshold. The first version of the prototype includes a power supply and electronics (Fig.4.42(a)) made on a separate PCB. This PCB is used for each cell of the SiPM. The power supply for the SiPM provides a voltage of up to 65 V with an individual channel adjustment within 0-10 V, manual tuning, and a built-in voltmeter for the voltage monitoring. It is possible to connect eight cells simultaneously. The amplifiers used for that do not change the leading edge of the signal. This allows us to get a time stamp of the event. Afterwards, the signal is integrated and transmitted to the comparator.

The response of the Hamamatsu S12572-010P SiPM [437] with the FEE to the LED has been studied. The electrical signal from a LEMO output of the LED was used as a trigger. The illumination was performed by uniform light in a light-isolated box. In addition to the ToT information (Fig.4.42(b)),

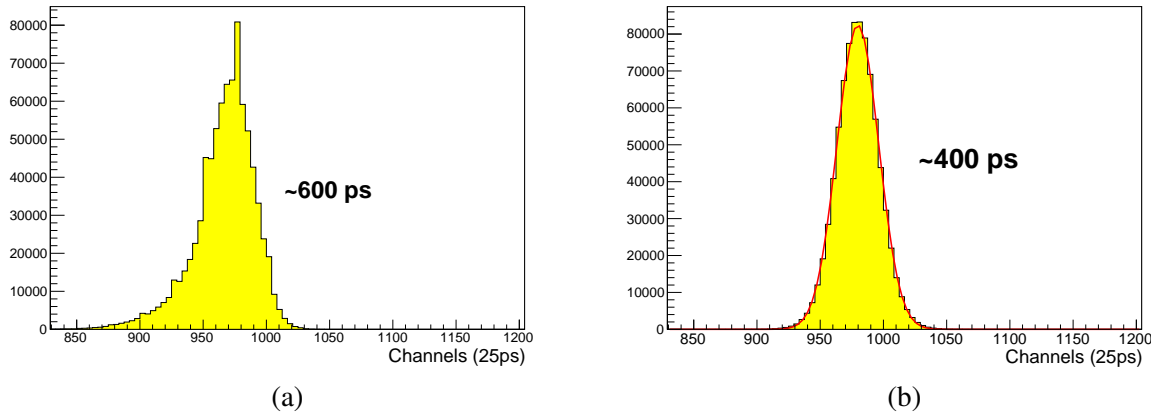


Figure 4.44: (a) $dT (T_{SiPM1} - T_{SiPM2})$. (b) Result after the time-walk correction for the $dT (T_{SiPM1} - T_{SiPM2})$.

the time stamp of the event for each SiPM cell was investigated. The distribution (Fig.4.43(a)) shows the correlation of these values and that the signal in the region of small amplitudes comes later in time. This is due to signal latency (the so-called time-walking effect). This delay occurs due to the difference between the time when a photon or a charged particle passes through the detecting element and the time when the electronics registers this signal. This leads to deterioration in the time resolution. After performing the correction (see Fig.4.43(b)), the time-walking effect has been removed [438].

The time resolution was defined as the RMS and was approximately 600 ps. Taking into account the non-Gaussian waveform (Fig.4.44(a)) and the fact that the time resolution is not the maximum allowed for this type of the detector, the time-walk correction has been applied. The most important result of the correction was a time resolution of approximately 400 ps (Fig.4.44(b)), which is 1.5 times better than the resolution before the correction.

The first version of the prototype using developed front-end electronics based on the Time-over-Threshold method was tested. After the time-walk correction, the time resolution improved up to 400 ps. Taking into account the SiPM suboptimal for precise time measurements, the result is promising. Further development of the FEE with a ToT function allows using standard TDCs for timing measurements.

10 Zero degree calorimeter

A zero degree calorimeter (ZDC) will be installed in the beam separation areas on both sides of the SPD interaction point as it is shown in Fig. 4.45, where all charged particles originating from the interaction region are swept out by the strong magnetic field. Main goals of the ZDC are:

- luminosity measurement;
- local polarimetry with forward neutrons (see Chapter 5);
- spectator neutron tagging;
- time tagging of the events for event selection.

The ZDC is a standard system used for the purposes mentioned above in many collider experiments. The strong magnetic field before a ZDC efficiently removes all charged particles allowing clean measurement of neutrals, so the device can work till very high luminosities. Scattering at zero angle is insensitive

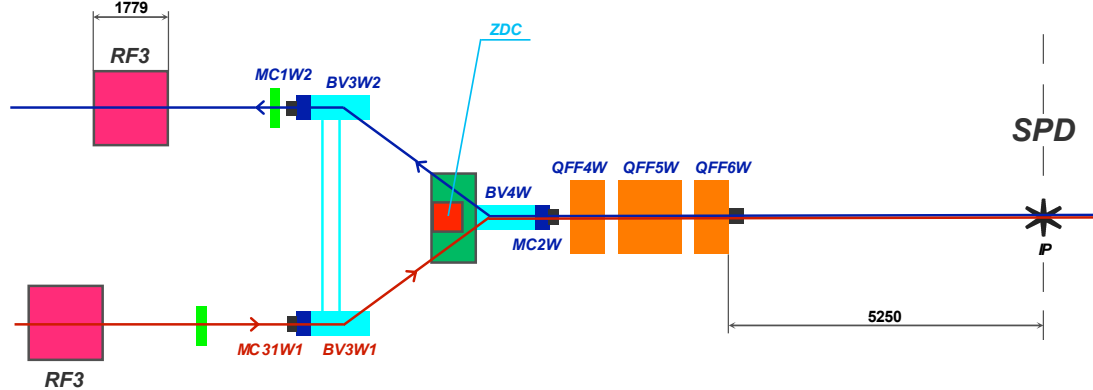


Figure 4.45: ZDC placement at the collider. All dimensions are in millimeters.

to transverse polarization and provides offset-free luminosity measurement, very useful for luminosity crosschecks. The device could provide an additional time stamp for an event. Standard usage of ZDC includes local polarimetry with forward neutrons [439]. The main purpose is the verification of longitudinal polarization settings. One can expect $1 \div 2\%$ asymmetry for very fast neutrons at the position of the detector. Precise tagging of very forward spectator neutrons provides a range of opportunities in study of diffractive processes. To accomplish these tasks, the following performance parameters should be met:

- time resolution $150 \div 200$ ps;
- energy resolution for neutrons $50 \div 60\%/\sqrt{E} \oplus 8 \div 10\%$;
- neutron entry point spatial resolution 10 mm.

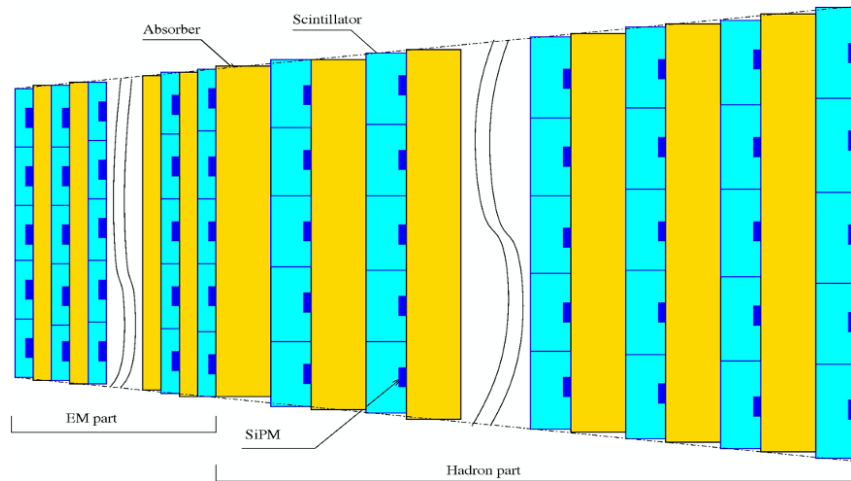


Figure 4.46: Schematic view of the ZDC.

The design of the Zero Degree Calorimeter was optimized on the basis of the Monte Carlo simulation to obtain the necessary energy, spatial and time resolutions. We propose to use a fine segmented calorimeter based on plastic scintillator active tiles with direct SiPM readout and tungsten absorber plates similar to the calorimeter proposed for the CALICE [440]. A schematic view of the calorimeter is shown in Fig. 4.46. In order to achieve good energy resolution for photons the first 10 layers will have smaller thickness compared to the rest of the calorimeter (see Tab. 4.9). This allows to get reasonable energy resolution for photons, while keeping reasonable number of readout channels. Each scintillator layer has 25 tiles

arranged in 5×5 grid with tile size growing from $17 \times 17 \text{ mm}^2$ for the first layer to $28 \times 28 \text{ mm}^2$ at the last layer. Each tile is covered by a chemically produced thin white reflective layer with a small transparent window for optical readout, done by HAMAMATSU SiPMs S13360-3050PE directly coupled to the tiles. Output signals are digitized by 500 MHz flash ADC 16 channel boards. A fast output for SPD trigger system is also produced. The ZDC will be placed inside the beam separation magnet and its size is limited to $88 \times 88 \text{ mm}^2$ at front side and $140 \times 140 \text{ mm}^2$ at rear side. The length is limited to 650 mm.

Table 4.9: The parameters of the ZDC layers.

Parameter	Electromagnetic part	Hadron part
Number of layers	10	26
Scintillator thickness, mm	5	10
Absorber thickness, mm	5	10
Total absorber thickness, mm	45	260
Part thickness, X_0	13	75
Part thickness, λ_I	0.5	2.9
Number of channels	250	650

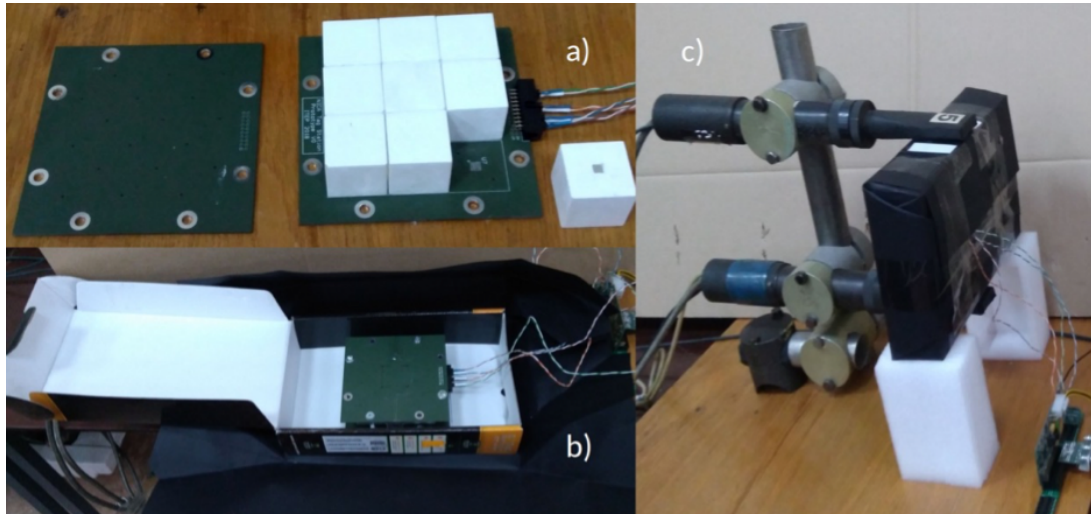


Figure 4.47: One layer prototype: a) 9 cubes of $30 \times 30 \times 30 \text{ mm}^3$ plastic, SiPM board and support board; b) the prototype assembly in a box before wrapping in black paper; c) the box in place for cosmic muon tests.

The expected energy resolution for neutrons is about $50\%/\sqrt{E} \oplus 30\%$ while the energy resolution for photons is about $20\%/\sqrt{E} \oplus 9\%$. Spatial resolution for photons is estimated to be below 3 mm for 1 GeV and about 1.8 mm for 12 GeV which corresponds to 0.3 and 0.18 mrad for the $L \sim 10 \text{ m}$ distance from the interaction point. For neutrons, the space resolution is 10÷13 mm within energy range 1÷12 GeV. Longitudinal energy distributions for photons and neutrons are very different and can be used for neutron/photon separation.

For experimental estimates of the time resolution an assemblage of 9 plastic cubes laid on a printed circuit board with mounted SiPMs and fixed with a support board (see Fig. 4.47) was tested with cosmic muons. Each cube was of $30 \times 30 \times 30 \text{ mm}^3$ in size and is chemically covered with a thin light reflecting layer. A numerical simulation has shown the mean number of cells hit in an event is more than 20 for

both photons and neutrons. It means the total thickness of scintillator plates of the order of 15 cm (5 times more than for tested prototype). The test results obtained for the prototype were extrapolated to the full ZDC. Thus the expected time resolution has to be about 150 ps.

The proposed design of the ZDC calorimeter satisfies most of its physics goals in the limited space inside the magnet. The exception is the energy resolution for neutrons, which is reached by larger calorimeter only. Nevertheless even this goal could be achieved by more elaborated analysis taking advantage from the calorimeter fine granularity.

Chapter 5

Local polarimetry

The main goal of the local polarimetry at SPD is the permanent monitoring of the beam polarization during data taking to reduce the systematic uncertainty coming from the beam polarization variation. Another task is beam polarization monitoring independent on the major polarimeters (CNI and the absolute one), as well as possible usage of this tool to tune the beam polarization axis. Since the SPD energy range is relatively new for spin physics, there is a lack of precise polarization data allowing one to find the explicit solution for the local polarimetry.

1 Asymmetry in inclusive production of charged particles

One of the tools to control the proton beam polarization is the measurement of the azimuthal asymmetry in inclusive production of charged particles in collisions of transverse polarized proton beams. Such a method is well adopted at the STAR detector. Two Beam-Beam Counters (BBCs) are used for this purpose. Each BBC consists of two zones corresponding to different rapidity range. The inner and outer zones cover $3.3 < |\eta| < 5.0$ and $2.1 < |\eta| < 3.3$, respectively. The BBCs detect all the charged particles produced in the forward direction within their acceptance.

The correlation of the beam asymmetries measured by the RHIC pC CNI polarimeter [441, 442] and the STAR BBCs is demonstrated in Fig.5.1. One can see that the measurements by BBCs are sensitive to the transverse polarization of the colliding beams. The value of the effective analyzing power A_N for inclusive production of charged particles at $\sqrt{s} = 200$ GeV is about $(6 \div 7) \times 10^{-3}$. At NICA energies it will have, in principle, the same magnitude, or even a larger one due to a larger analyzing power for the p - p elastic scattering. Therefore, the BBCs can be used for the local polarimetry at SPD. The design of the SPD BBCs is described in the previous section.

2 Inclusive π^0 production

One of the reactions to measure and to monitor the vertical component of the polarized proton beam is the inclusive $pp \rightarrow \pi^{\pm,0}X$ reaction. Fig.5.2(a) demonstrates the single transverse spin asymmetries A_N obtained in the p - p collision for π^+ , π^0 and π^- inclusive production at 200 GeV ($\sqrt{s} \sim 20$ GeV)[176, 177]. The data demonstrate large values of the single transverse spin asymmetries with their signs following the polarization of the valence quarks in the pions. This regime occurs already at 22 GeV [443] corresponding to $\sqrt{s_{NN}} \sim 7$ GeV for the collider option. Therefore, the inclusive neutral pion production can be used for the polarimetry over the full energy range of the SPD experiment.

The value of the single transverse spin asymmetry in the $pp \rightarrow \pi^0X$ reaction is almost twice smaller than

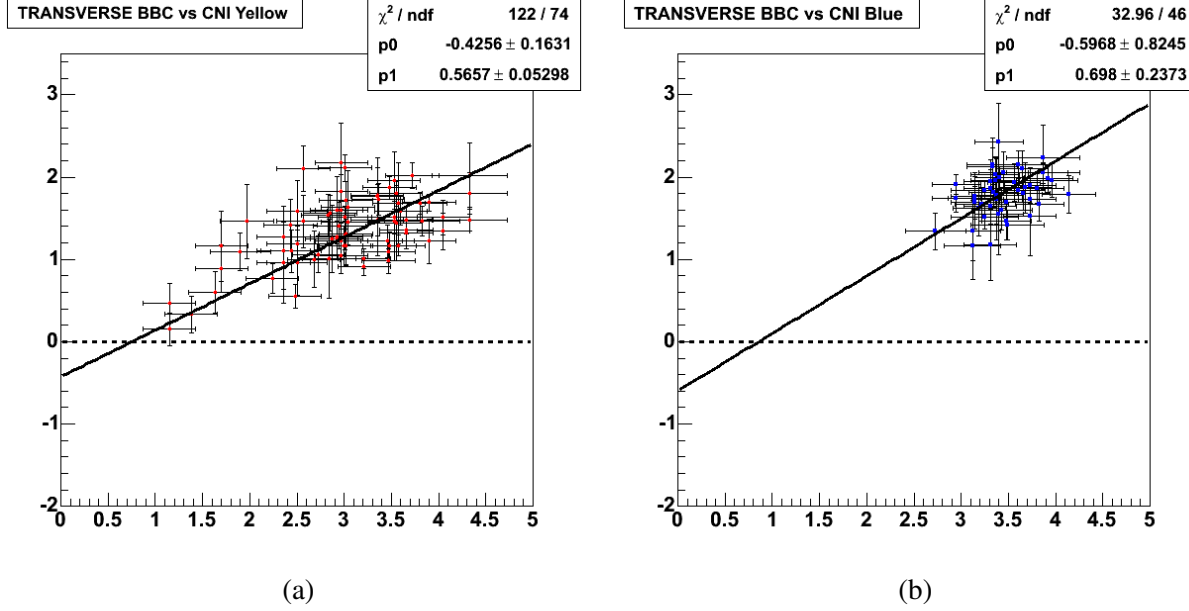


Figure 5.1: Correlation of the beam asymmetries measured by the RHIC pC CNI polarimeter [441, 442] and left (a) and right (b) STAR BBCs (in arbitrary units).

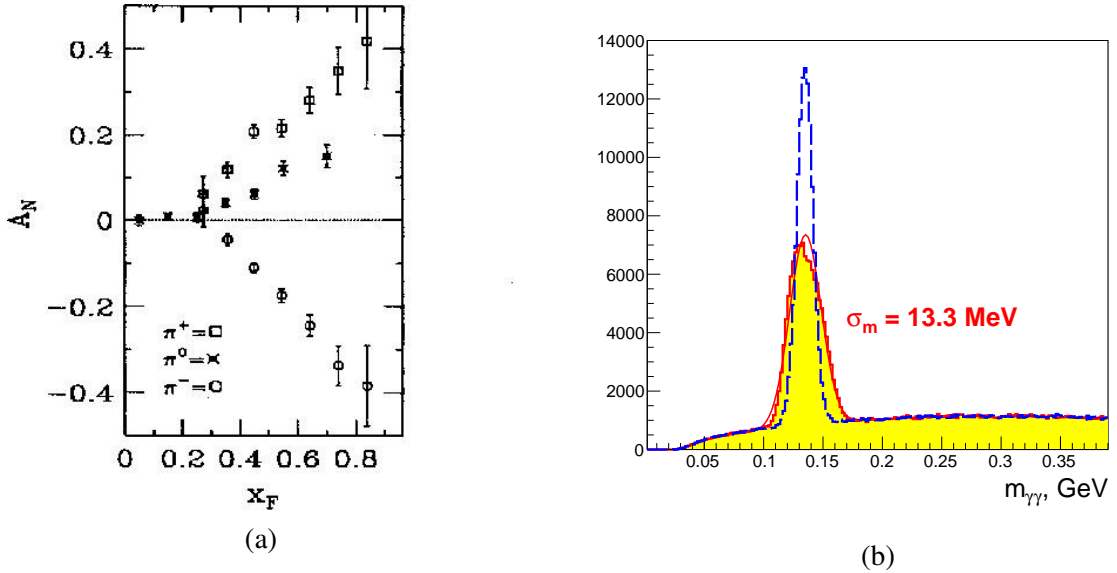


Figure 5.2: (a) Single transverse spin asymmetry A_N for inclusive pion production in $p-p$ collisions at 200 GeV [176, 177].. (b) The π^0 reconstruction in the SPD ECal end-cup with (blue) and without (red) vertex position information.

for the charged pions production. However, the π^0 selection can be done more easily, since it does not require track reconstruction.

For online local polarimetry one can use the parts of the ECal end-cups placed around the beam pipe. Fast π^0 reconstruction algorithms will not include the information on the vertex position along the beam axis, therefore, the width of the π^0 peak will increase. The Monte-Carlo results obtained for $\sqrt{s_{NN}} \sim 27$ GeV and presented in Fig.5.2(b) demonstrate such enlargement. However, one can see that the selection of π^0 is good enough for the local polarimetry purposes. The effective analyzing power $\langle A_N \rangle$ for the kinematic range of produced π^0 $p_T > 0.5$ GeV/c and $x_F > 0.5$ is about 0.1. The rate of π^0 decays reconstructed

in the end-caps of the calorimeter provides statistical accuracy of the beam polarization estimation at a few-percent level after 10 minutes of data taking at $10 \text{ GeV} < \sqrt{s} \leq 27 \text{ GeV}$. The corresponding accuracy of the spin direction reconstruction is about a few degrees.

3 Single transverse spin asymmetry for very forward neutron production

The energy dependence of the single transverse spin asymmetry, A_N , for neutron production at very forward angles was measured in the PHENIX experiment at RHIC for the polarized p - p collisions at $\sqrt{s}=200 \text{ GeV}$ [439]. The neutrons were observed in the forward detectors covering an angular range of up to 2.2 mrad. The observed forward neutron asymmetries are large, reaching $A_N = -0.08 \pm 0.02$ for $x_F=0.8$; the measured backward asymmetries, for negative x_F , are consistent with zero. The results of the x_F dependence of A_N for neutron production in the (upper) ZDC trigger sample and for the (lower) ZDC \otimes BBC trigger sample are shown in Fig.5.3(a). The error bars show statistical uncertainties, and the brackets show the p_T -correlated systematic uncertainties. The data were obtained for 2 types of triggers: the first one is the ZDC trigger for neutron inclusive measurements, requiring an energy deposit in the ZDC to be greater than 5 GeV. The other one was a ZDC \otimes BBC trigger, a coincidence trigger of the ZDC trigger with the BBC hits defined as one or more charged particles in both of the BBC detectors.

The observed large asymmetry for forward neutron production was discussed within the pion exchange framework, with interference between the spin-flip amplitude due to the pion exchange and the non-flip amplitudes from all Reggeon exchanges. The numerical results of the parameter-free calculation of A_N are in excellent agreement with the PHENIX data (see Fig.5.3(b)). One can see that A_N is increasing almost linearly as a function of the neutron transverse momentum q_T . One can expect the A_N value of ~ -0.02 at $\sqrt{s}=27 \text{ GeV}$. Therefore, the p $p \rightarrow nX$ reaction with neutron emission at very forward angles can be used at SPD at least at high energy.

Very forward neutrons are detected by two zero-degree calorimeters (ZDCs) [445] placed in the gaps between the ion tubes of the colliding beams on the left and right from the center of the detector. Two ZDCs will be also placed at SPD. These ZDCs can be considered as an additional tool for the local polarimetry for pp-collisions at the highest NICA energy.

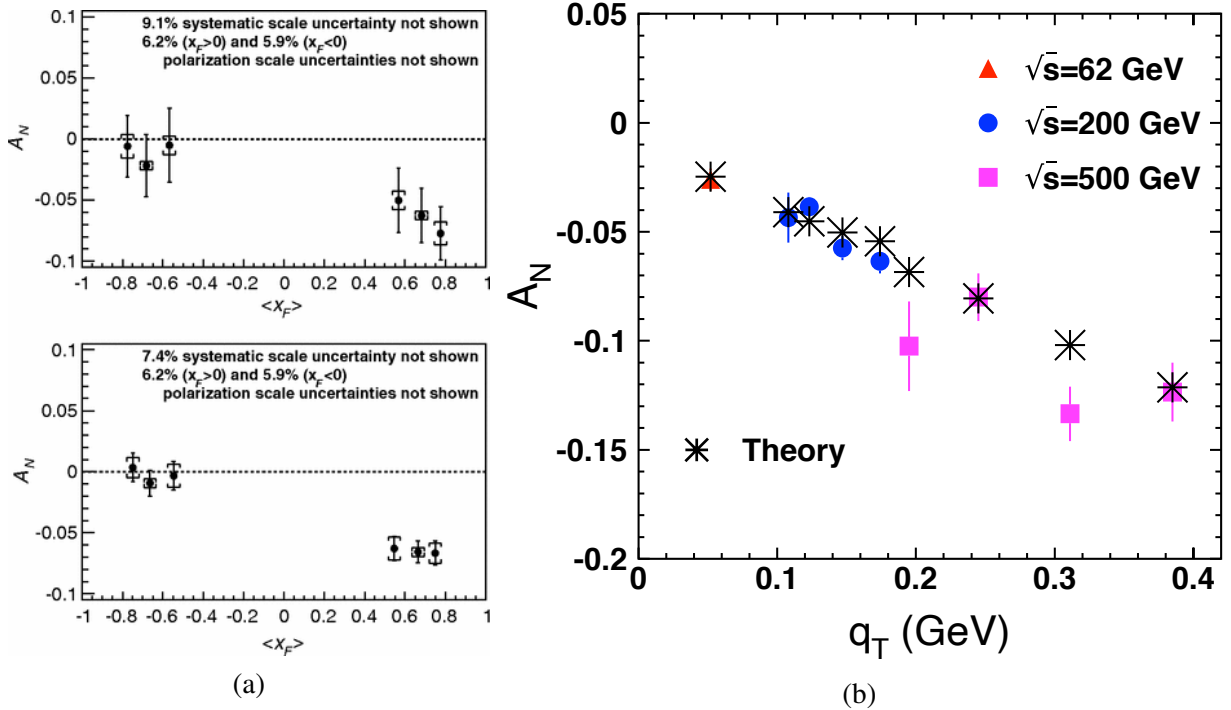


Figure 5.3: (a) x_F dependence of A_N for neutron production in the (upper) ZDC trigger sample and for the (lower) ZDC \otimes BBC trigger sample. (b) Single transverse spin asymmetry A_N in the reaction $pp \rightarrow nX$ measured at $\sqrt{s} = 62, 200, 500$ GeV at PHENIX as a function of the transferred momentum q_T . The asterisks show the result of the theoretical calculations [444].

Chapter 6

Detector control system

The SPD detector control system (DCS) is designed to control the basic operating modes of the detector parts and the detector as a whole, and to continuously monitor slowly changing parameters of the detector, engineering means which provide the detector operation, and the environment. The DCS is synchronized with the basic operating modes of the NICA accelerator complex by means of a synchronization subsystem shared between the DCS and the SPD DAQ. The DCS provides parameterization of the managed object (i.e. the SPD detector), implements algorithms for normalization, parameters measurement and control based on these parameters, and generates the necessary sets of abstractions and options for presenting these abstractions to the operator in an intuitive manner. Critical values of the parameters going beyond the predefined limits in predetermined situations cause emergency events and initiate procedures for handling such events, including the procedure for an automatical detector shutdown in order to prevent its damage. Parameter values are archived in a database for long-term monitoring of the detector operation and identify possible failures in the operation of the equipment and emergency situations. The configurations of the detector parameters saved in the database make it possible to start the detector promptly and use it with various preset parameters and in various operating modes in accordance with the requirements of a particular physics experiment. The DCS allows autonomous operation of each detector subsystem at the stage of the initial start-up as well as its periodic maintenance, calibration sessions, and planned upgrades. The number of parameters in the system is expected to be significant, therefore, it is assumed that the system should be extendable and flexibly configurable. Architectural and software solutions based on the event-driven model [446] and client-server and producer-consumer [447] interaction models should be preferred for communication, when building the general DCS and the control systems of each part of the detector. Centralized systems operating in the master-slave polling mode should be avoided.

1 DCS concept

Most of high-energy physics detectors include parts consisting of similar systems built from devices, sensors, and actuators with similar or identical functionality. This determines parameterization of the entire detector as a managed object. Such systems include:

1. high voltage (HV) power supply system for powering gas detectors and light (photon) sensors (PMT and SiPM);
2. low voltage (LV) power supplies for powering magnets, digital and analog electronics;
3. cryogenic systems;

4. gas supply and mixing systems;
5. vacuum systems;
6. front-end electronic LV powering control and temperature monitoring;
7. different cooling and temperature control systems;
8. DAQ system;
9. accelerator interface and synchronization;
10. general external electricity and water cooling stations, etc.

The SPD detector is no exception and includes almost all of these systems spread among different parts of the detector, as shown in the layout diagram, Fig. 6.1. Each part of the detector refers to one or more subsystems. The composition of the systems will be refined, as the individual parts of the detector are developed.

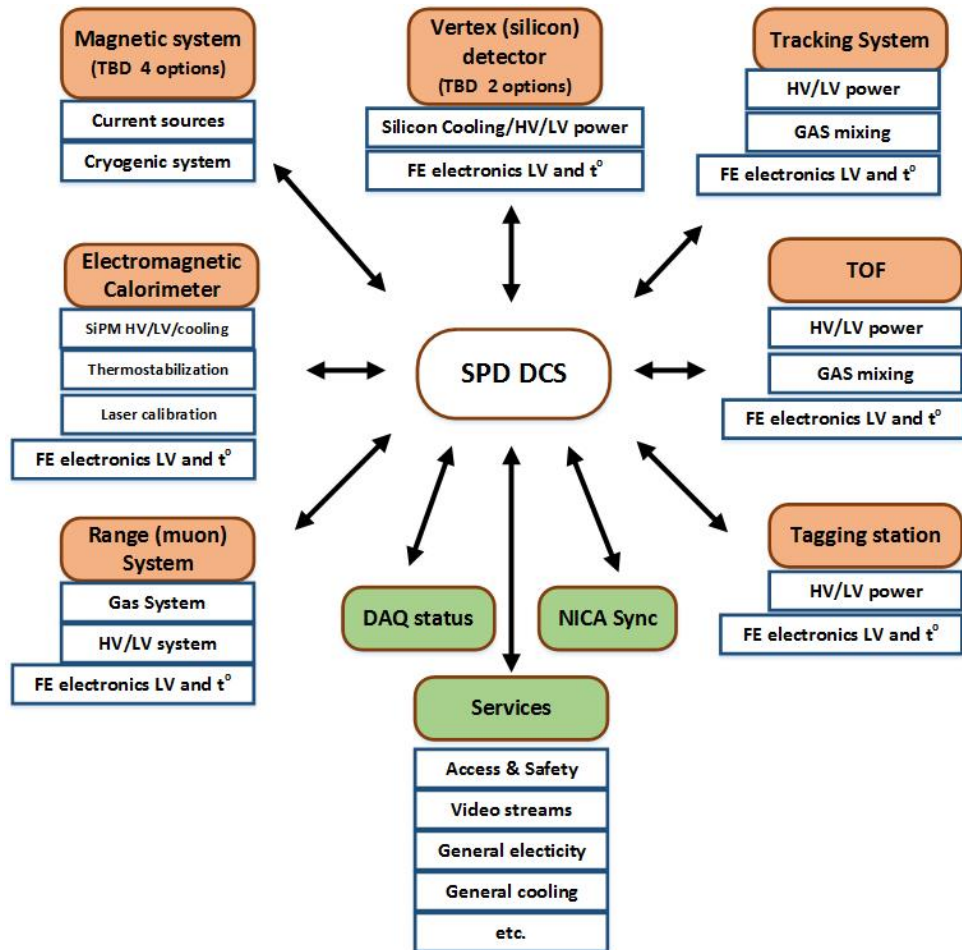


Figure 6.1: SPD detector control system layout.

All the systems can be similarly parameterized and shown to the operator in an intuitive presentation in order to simplify the operator's decision-making algorithm. However, the physical implementation at the hardware level of these elements may vary significantly in different parts of the SPD, because:

- the parts inherit the experience of their developers gained in previous experiments;
- hardware and software components are selected based on their cost and availability;
- parts of the detector are manufactured at different times.

Nevertheless, in order to optimize financial and human resources costs for the creation of the entire detector and the DCS, in particular, it is necessary to recommend the developers of the detector parts to strive for standardization of the used hardware and embedded software. This will significantly reduce the efforts put into developing, deploying, and operating the detector and will result in significant cost savings. To achieve these goals, at the stage of prototyping the detector systems it is advisable to work out not only the detector itself, the front-end electronics and the DAQ, but also the slow control systems. This work can be carried out in the beam test zone (BTZ), for which the BTZ slow control system must be made as similar to the final DCS version as possible.

2 DCS architecture

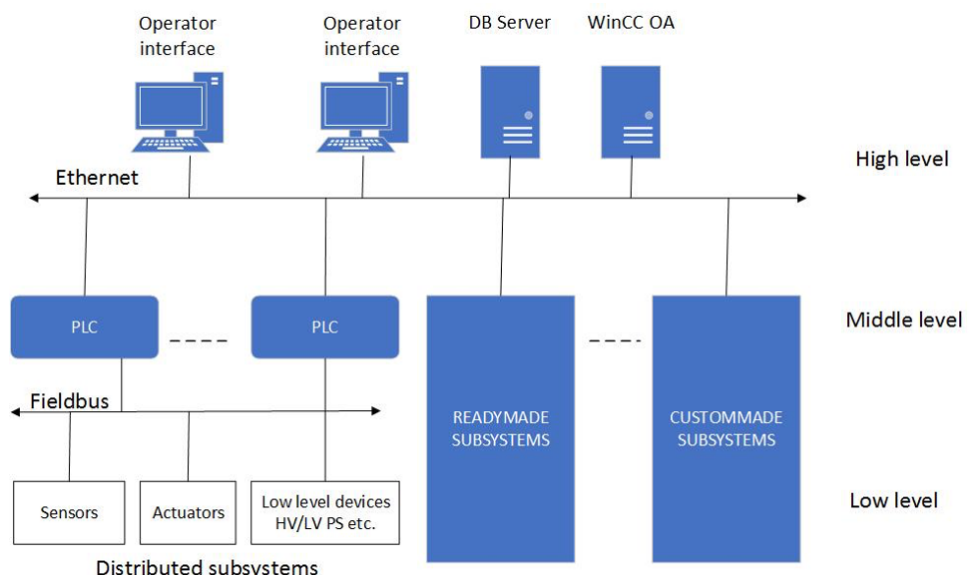


Figure 6.2: SPD detector control system architecture.

The detector control system is divided into three logical levels (Fig. 6.2). The lower level includes measurement channels built into the Front End Electronics (FEE) and Data Acquisition (DAQ) of the detector parts, various stand-alone sensors, I/O devices, and low and high voltage power supplies. The middle level is represented by programmable logic controllers and integrated ready-made and custom-made subsystems (vacuum posts, gas consoles, multichannel ready-made power subsystems, etc.). The interfaces to the FEE and DAQ that provide data for the detector control system are also on this level. The upper level is designed to provide a human-machine interface for operators, implement a database of detector parameters and configurations, communicate with the external world (accelerator, engineering support systems, access system, etc.), and implement macro-control algorithms common for the entire detector. All these levels are connected in a hierarchical network using fieldbuses between the first and the second level, for example, a CAN-bus with a CANopen protocol. An Ethernet LAN is used between the middle and the upper levels. At the top level, special software, such as SCADA (Supervisory Control And Data Acquisition), is used, which provides control, collection and storage of data in real time. It is

proposed to use the WinCC OA system common at CERN, as a SCADA system. We understand that for smooth and reliable communication with the control system of the Nuclotron, a gateway to the Tango Controls [448, 449] system should be developed and deployed.

3 SCADA for the DCS

WinCC OA (ex PVSS-II) [450, 451] is a commercial SCADA system. It is a software component constructor that allows one to use both preinstalled prototypes and templates, and software modules and system components developed in C. This system is actively used in many experiments at CERN and has support and safety certificates in the Russian Federation. The following properties make WinCC OA an attractive solution to be used in the DCS SPD:

- object-oriented approach built into the system ensures an efficient development process and the ability to flexibly expand the system;
- capability to create distributed systems - up to 2048 WinCC OA servers;
- scalability from a simple single-user system to a distributed redundant network system with > 10 million tags (physical and synthetic parameters);
- platform independent system is available for Windows and Linux;
- event-driven system;
- hot standby and 2x2 redundancy (DRSystem), the required level of availability and reliability;
- wide range of drivers and options for communication OPC, OPC UA, S7, Modbus, IEC 60870-5-101/104, DNP3, XML, JSON, SOAP, ...;
- support by major manufacturers of electronic devices for building automation systems in high energy physics.

Each functional unit of the system that is software implemented as a separate process is called manager. A set of managers forms a system. Data exchange and communications between managers are done via TCP. The data is exchanged by means of passing events. The system allows parallelizing processes (managers) by running them on different computers with different OS. The system is scalable and balances the load on the control computers. The required managers start only if necessary and multiple instances may run simultaneously. Managers can be distributed across multiple computers/servers. The WinCC OA block diagram is shown in Figure 6.3. The main process is the Event Manager, it contains and manages the process image (current values of all process variables), receives and qualifies data (central message manager), distributes data across other managers, acts as a data server for others, manages users authorization, manages the generation and status of alarm messages. The Database Manager receives data from the Event Manager and handles it according to its own algorithm. The historical database can use either a proprietary database (HDB) or an Oracle DBMS (the Oracle Real Application Clusters configuration is also supported). Parallel archiving in Oracle and HDB databases is possible. It is also possible to record user-defined data and log system events and messages in an external relational database (MS SQL, MySQL, Oracle, etc).

The WinCC OA Report Manager supports different ways of generating reports:

- in Microsoft Excel format;

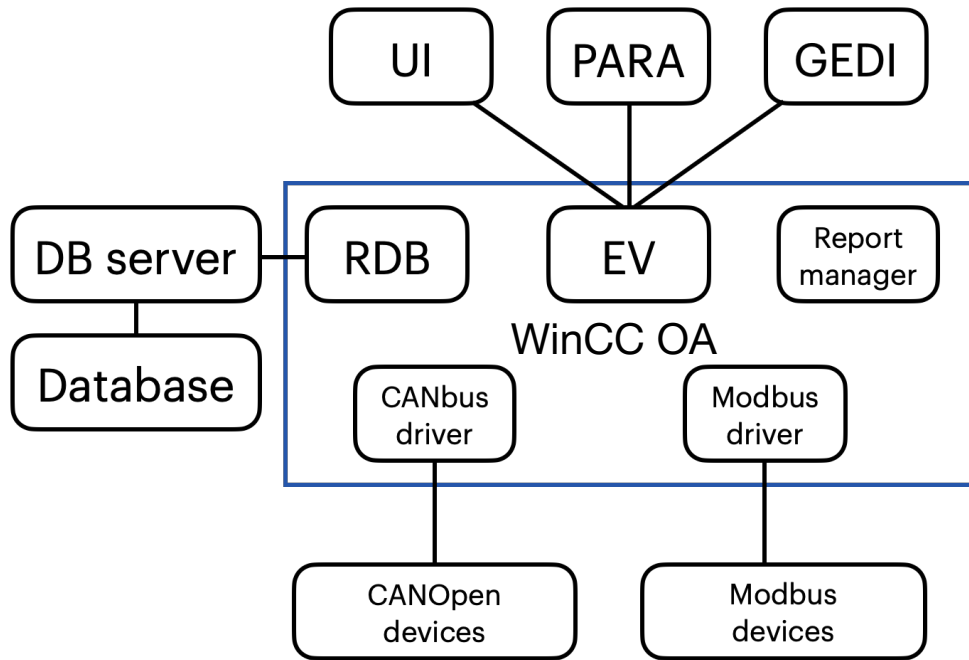


Figure 6.3: SCADA structural scheme of the WinCC OA software.

- in the *xml* format with the ability to display in any external tool for working with reports (Eclipse BIRT, Crystal Reports, SYMATIC Information Server etc.), SOAP (Simple Object Access Protocol) protocol is also supported.

Project development for the WinCC OA system is based on an object-oriented approach. In the WinCC OA data model, objects are represented as data points that characterize the image of a specific physical device or process. For each data point (called tag) element, properties and actions, such as signal processing (smoothing, setting limits, etc.), communication with external systems, archiving, generation of alarm messages (alarms), etc. can be defined in accordance to it. Typing and inheritance are supported, therefore arbitrary hierarchical data structures can be created. Similarly, the principles of inheritance and reusability are implemented for graphical objects. The WinCC OA IDE includes the PARA configuration editor and the GEDI graphical editor of the User Interface Manager (UI) (includes a data model editor, mass configuration tools, administration tools, an interface to version control systems, a debugger, etc.). Changes to data structures and graphics are applied without restarting the project. Writing custom scripts can be done using CONTROL++ (a programming language, the syntax of which is similar to C/C++). Such scripts can be both event handlers associated with the elements of the graphical interface, and data processing procedures. The system includes a standard graphical objects library; it can be extended by developing user objects or using the Qt Toolkit widgets. It is also possible to use the JavaScript libraries available on the market or included JavaScript scripts. Thanks to the open API (C++ / C# API), it is possible to create managers, drivers, widgets, and CONTROL++ extensions. A new set of tools is available for the concept of High Speed Programming implementation, which supports documentation build-up from the source code, unit testing and autocompletion of program structures.

It is also planned to provide data exchange between the WinCC OA and Tango Controls, which is used as the upper level of the Nuclotron control system. This can be implemented using standard OPC technologies with a client-server architecture, or it can be implemented using SQL tools as a common database for both SCADA systems used for the accelerator and the detector. The final choice of a suitable solution will be made at the stage of system implementation.

Chapter 7

Data acquisition system

1 Introduction

The data acquisition system of the SPD should provide continuous data taking, including data readout from the front-end electronics, data consistency check, event building and writing events to a storage. The system should have no dead time or minimal dead time. *These features will be implemented with the DAQ operating in a free-running (triggerless) mode.*

Other important tasks of the DAQ are:

- initialization of hardware;
- control and monitoring of the data taking process: control of the status of all hardware devices including front-end electronics, status of software, quality of collected data;
- monitoring of the parameters characterizing the detector performance (accumulation of time, amplitude and hit distribution histograms, detector rates, etc.);
- logging of information and errors;
- distribution of data over computing nodes for further online analysis;
- etc.

The data acquisition system of SPD should withstand the data flux from p - p , p - d or d - d interactions at the extreme conditions of high luminosity. At the highest NICA energy and luminosity, $\sqrt{s} = 27$ GeV and $L = 10^{32} \text{ cm}^{-2}\text{s}^{-1}$, the interaction rate within the SPD aperture will be 3 MHz, and the average multiplicity of about 15. This drastically differs from the conditions of another NICA experiment, MPD, where the collision rate of heavy ions is orders of magnitude less, but the multiplicity is much higher.

The structure of DAQ will be similar to recently modernized DAQ of the COMPASS experiment at CERN [452–458]. The COMPASS DAQ extensively uses logical programmable integrated circuits FPGA at different levels of the system. This allows one to handle large data streams with minimal latency and provides very good flexibility. Unlike the COMPASS experiment, which uses the beam of the CERN SPS with a spill time structure, the SPD DAQ will deal with a continuous beam.

The DAQ of SPD will operate in a free-running mode, when the readout is not controlled by a trigger system, but occurs with a fixed frequency. It requires all front-end electronics running in a self-triggered mode, and the readout happens synchronously with a common clock distributed by the precise timing

Table 7.1: Summary of detectors outputs to DAQ. Information type: T means time, A – amplitude (or charge).

Sub-detector	Information type	Number of channels	Channels per FE card	Number of outputs
Vertex detector 5 DSSD	T + A	460800	640	720
Vertex detector 3 MAPS+ 2 DSSD	T + (T + A)	(3024 + 596)*		864 + 596
Straw tracker	T + A	79200	64	1238
Calorimeter	T + A	30176	64	472
PID-ToF	T	20200	32	632
PID-Aerogel	T + A	320	32	10
BBC (inner+outer)	T + (T + A)	256 + 192	32	8 + 6
Range system	T	106000	192	553
ZDC	T + A	250 + 650	16	57
Total (max)		698044**		4436

* – number of sensors, see Section 4 of Chapter 4

** – for DSSD version

system. All the data received between the acts of readout are accumulated in the memories implemented in the front-end electronics modules and are stored there until the next readout. The readout frequency value will be chosen depending on the detector rates and memory depths available in the front-end cards. The width of the time slice between the successive readouts should be much larger than the response time of the sub-detectors in order to minimize the probability of separating an event into two slices.

Digitization of data and zero suppression occur in the front-end electronics. It is expected that the so-called "feature extraction algorithm" will be implemented in the front-end electronics of the vertex detector and the calorimeter. This algorithm, which is under development in several collaborations (in particular, PANDA [459], COMPASS [460–462]), allows transferring only the extracted time and amplitude, instead of many samples of the digitizer, thus greatly decreasing the amount of data to be transferred.

For now the expected data flux in the hardest conditions of the experiment (maximum energy and luminosity) has been estimated without detailed simulations, but using the current knowledge of the sub-detector structure, particle multiplicity per event, hit multiplicity in different detectors, expectations about the front-end electronics parameters and, where relevant, results of the beam tests at other experiments (MPD, PANDA). The total number of channels to be read out is about 700 thousand, with the major part coming from the vertex detector (~ 460 thousand for the VD strip option). The full numbers are given in Table 7.1. Preliminary estimation for the data flow is about 20 GB/s including some margin of safety.

2 DAQ structure

The scheme of the DAQ is presented in Fig. 7.1. The data from the front-end electronics cards come to the detector interface cards (FE concentrators). Now the existing electronics card with 12 input is considering as FE concentrators [454]. The Data-Handler multiplexers (UDHmx) are configured on the base of FPGA. The multiplexer has 48 high speed input and up to 8 output interfaces. They verify the

consistency of data and store them until receiving the readout signal.

The two Data-Handler Switches (UDHSw) function as a 10×10 switch and perform event building with a maximum throughput rate of 10 GBytes/second. The UDHSw's perform the final level of event building and distribute the assembled events to 20 readout computers. The Data-Handler Switches and Data-Handler multiplexers are implemented on the same electronics cards by means of different firmware. Each readout computer is equipped with a dedicated PCIe buffer card for data collection. These cards are built on a FPGA chip and are commercially available. The current version of the card used in COMPASS has a bandwidth close to 1 GB/s [457]. Finally, the continuous sequence of slices is formed below the Network Switch in each of on-line computers to be used for on-line filtering and event monitoring.

The slow control software accesses the front-end electronics via the FE concentrators using the UDP-based IPBus protocol [463]. The interface cards retransmit control and clock signals provided by the time distribution system to the corresponding front-end electronics, and convert the detector information from the detector specific interfaces to a common high-speed serial interface running over optical fiber. It is foreseen to use UCF [464] as a standard high speed link protocol within the DAQ.

The White Rabbit system [465, 466] is planned to be used at NICA for time synchronization. It provides synchronization for large distributed systems with a time-stamping of 125 MHz, sub-nanosecond accuracy and ~ 10 ps precision. Signals from the White Rabbit system will be used as an input for the Time Control System (TCS) [467] which will distribute clock signals through the whole electronic system.

3 Data format

The time structure of the expected data flow during a run is shown in Fig. 7.2. All processes are synchronized with a 125-MHz clock coming from the White Rabbit system. A Run is started after the reset procedure which includes all initialization processes. Afterwards, the continuous date flow is divided into a sequence of time slices. The proposed time slice duration can be selected in the range from 1 μ s to 8.3 ms and will be chosen according to the data flux and capacity of the whole chain of data collection. Longer slices are preferable, because the longer the slice, the less the probability an event falling into two adjacent slices. The slices have a continuous numbering within a frame, a wider time interval, which can extend from 65 ms to 549.7 s. The slice numbering is reset in every frame by the Start of the frame signal.

The proposed formats of the collected data are shown in Figs. 7.3–7.7. The data are formatted at all stages of transfer from the Front-End Concentrators to the Data-Handler Switches. The required headers and checksums are added at all stages.

In Fig. 7.3, the structure of a Run is shown. The Run consists of a sequence of Frames (Fig. 7.4) numbered from 0 to N, where N, the maximum number of frames in the Run, is assigned by the TCS controller. The Frame consists of a sequence of slices numbered from 0 to K, the maximum number of slices in the Frame, which is also assigned by the TCS controller.

Fig.7.5 shows the structure of the Slice. The Slice contains a sequence of Data Blocks from the Data Concentrators (Fig. 7.6). Finally, the lowest unit in the Data Format chain is the Data Block of FE Concentrators (Fig. 7.7) which contains Physical Data from several ports the amount of which depends on the FE card type.

The proposed format provides a unique connection of the physical information to the detectors geometry and the event time.

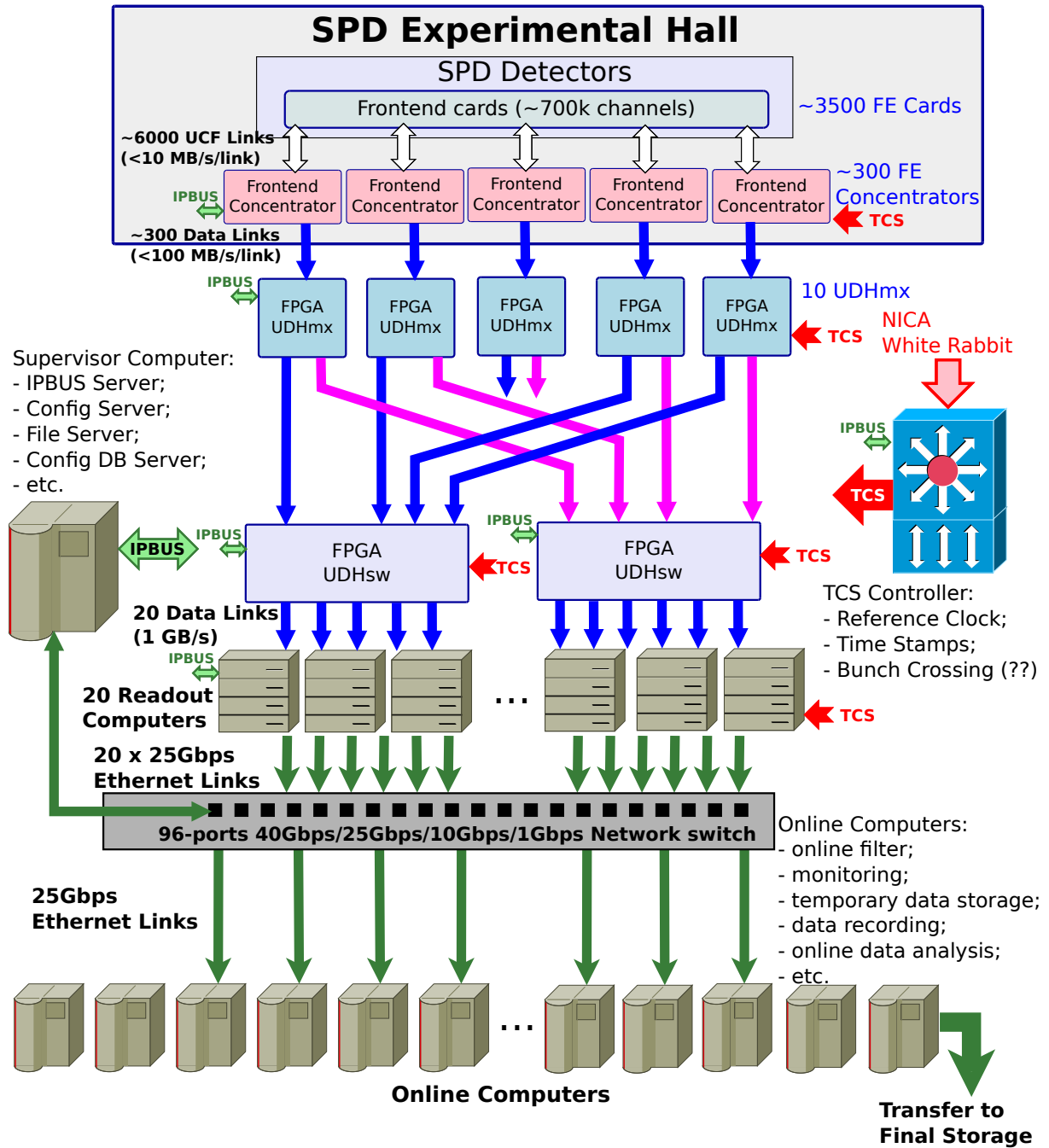


Figure 7.1: General structure of DAQ-SPD.

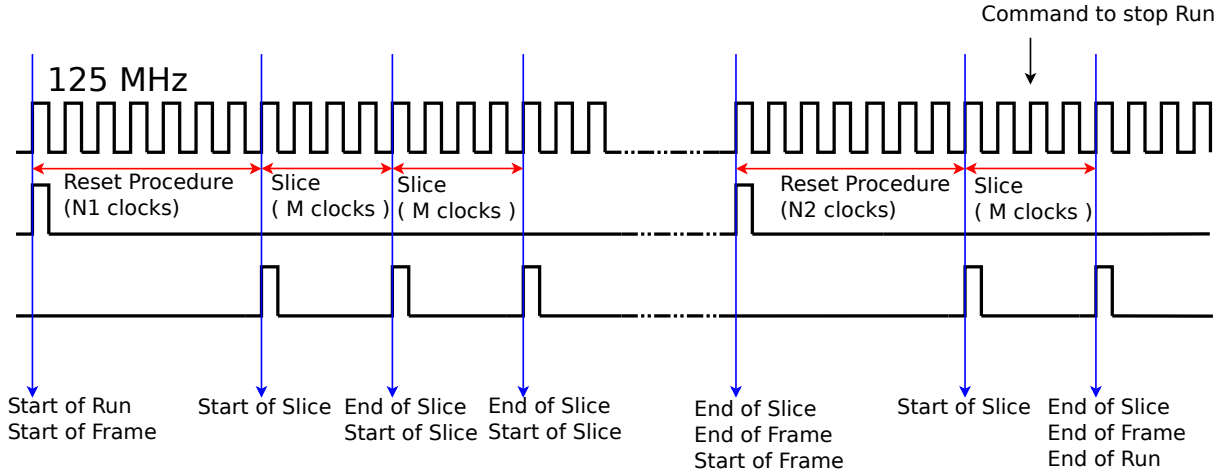


Figure 7.2: Time diagram of a sequence of clocks, Slices and Frames within the Run.

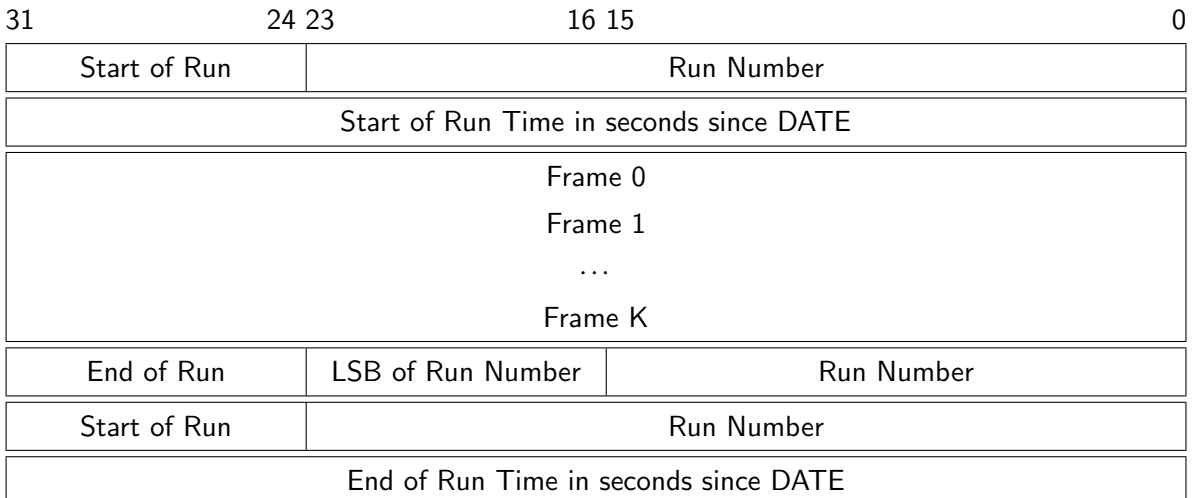


Figure 7.3: Data Format: Run structure.

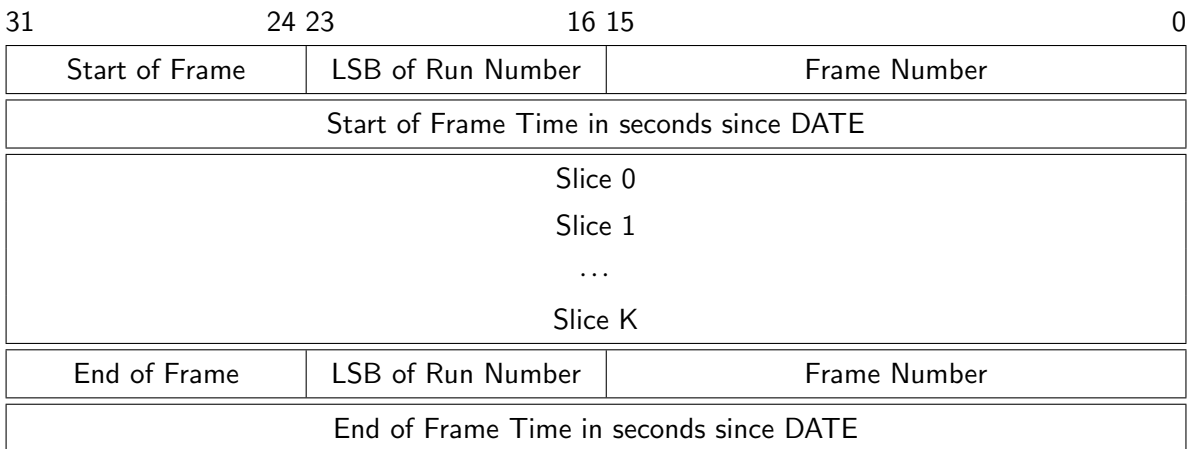


Figure 7.4: Data Format: Frame structure.

31	24 23	16 15	0			
Start of Slice	Slice Number					
LSB of Run Number	Frame Number					
Total size of all data blocks in 32-bit words or Number of Blocks						
Block 0						
Block 1						
...						
Block X						
End of Slice	Slice Number					

Figure 7.5: Data Format: Slice structure.

31	28 27	24 23	16 15	0				
Block Size in 32-bits words								
Version	Reserved	Block Type	Concentrator ID					
Frame Number	Slice Number							
Data blocks from low level Data Concentrators with the same data strurture or physical data FE electronics for lowest Data Concentrators								
CheckSum								

Figure 7.6: Data Format: structure of Data Blocks of High Level.

31	28 27	24 23	16 15	0				
Block Size in 32-bits words								
Version	Reserved	Block Type	Concentrator ID					
Frame Number	Slice Number							
Physical Data from port 0								
Physical Data from port 1								
...								
Physical Data from port Z								
CheckSum								

Figure 7.7: Data Format: structure of Low Level Data from FE Concentrators.

Table 7.2: Cost estimation of the DAQ

	Number	Cost (k\$)	Total (k\$)
FE concentrators	380	3.5	1330
UDHmx modules	12	17.5	210
UDHsw modules	3	17.5	52
Case for UDHmx modules	6	2.3	14
Time Distribution	1	35	35
Online Computers	20	12	240
VME crates	45	6	270
Consumables			100
Contingencies			≈350 (15%)
Total			2600

4 Cost estimate

The numbers of modules and their preliminary cost estimation are summarized in Table 7.2.

Chapter 8

Computing and offline software

1 SPD computing model

Expected event rate of the SPD experiment is about 3 MHz (pp collisions at $\sqrt{s} = 27$ GeV and 10^{32} $\text{cm}^{-2}\text{s}^{-1}$ design luminosity). This is equivalent to the raw data rate of 20 GB/s or 200 PB/year, assuming the detector duty cycle is 0.3, while the signal-to-background ratio is expected to be in order of 10^{-5} . Taking into account the bunch crossing rate of 12.5 MHz, one may conclude that pile-up probability will be sufficiently high.

The key challenge of the SPD Computing Model is the fact, that no simple selection of physics events is possible at the hardware level, because the trigger decision would depend on measurement of momentum and vertex position, which requires tracking. Moreover, the free-running DAQ provides a continuous data stream, which requires a sophisticated unscrambling prior building individual events. That is the reason why any reliable hardware-based trigger system turns out to be over-complicated and the computing system will have to cope with the full amount of data supplied by the DAQ system. This makes a medium-scale setup of SPD a large scale data factory 8.1.

The continuous data reduction is a key point in the SPD computing. While simple operations like noise removal can be done yet by DAQ, it is an online filter that is aimed at fast partial reconstruction of events and data selection, thus being a kind of a software trigger. The goal of the online filter is to decrease the data rate at least by a factor of 50 so that the annual upgrowth of data including the simulated samples stays within 10 PB. Then, data are transferred to the Tier-1 facility, where full reconstruction takes place and the data is stored permanently. Two reconstruction cycles are foreseen. The first cycle includes reconstruction of some fraction of each run necessary to study the detector performance and derive calibration constants, followed by the second cycle of reconstruction of full data sample for physics analysis. The data analysis and Monte-Carlo simulation will likely run at the remote computing centers (Tier-2s). Given the large data volume, a thorough optimization of the event model and performance of reconstruction and simulation algorithms are necessary.

Taking into account recent advances in the computing hardware and software, the investment in the research and development necessary to deploy software to acquire, manage, process, and analyze the data recorded is required along with the physics program elaboration and the detector design. While the core elements of the SPD computing system and offline software now exist as prototypes, the system as a whole with capabilities such as described above is in the conceptual design stage and information will be added to SPD planning documents as it is developed.

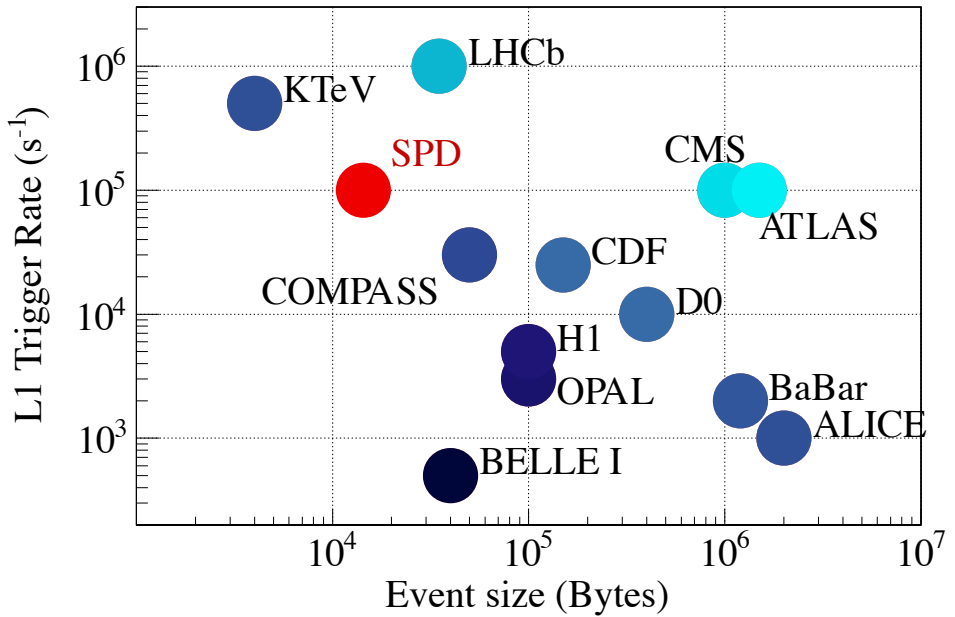


Figure 8.1: Expected event size and event rate of the SPD setup after the online filter compared with other experiments [468].

2 Online filter

The SPD online filter facility will be a high-throughput system which will include heterogeneous computing platforms similar to many high performance computing clusters. The computing nodes will be equipped with hardware acceleration. The software framework will provide the necessary abstraction so that common code can deliver the selected functionality on different platforms.

The main goal of the online filter is a fast reconstruction of the SPD events and suppression of the background ones at least by a factor of 50. This requires fast tracking and fast clustering in the electromagnetic calorimeter, followed by reconstruction of event from a sequence of time slices and an event selection (software trigger). Several consecutive time slices shall be considered, tracker data unpacked and given for a fast tracking. The result of the fast track reconstruction is the number of tracks, an estimate of their momentum and an estimate of primary vertex (to distinguish between tracks belonging to different collisions). Using this outcome, the online filter should combine information from the time slices into events and add a trigger mark. The events shall be separated in several data streams using the trigger mark and an individual prescale factor for each stream is applied.

One of the most important aspects of this chain is the recognition of particle tracks. Traditional tracking algorithms, such as the combinatorial Kalman filter, are inherently sequential, which makes them rather slow and hard to parallelized on modern high-performance architectures (graphics processors). As a result, they do not scale well with the expected increase in the detector occupancy during the SPD data taking. This is especially important for the online event filter, which should be able to cope with the extremely high data rates and to fulfill the significant data reduction based on partial event reconstruction ‘on the fly’. The parallel resources like multicore CPU and GPU farms will likely be used as a computing platform, which requires the algorithms, capable of the effective parallelization, to be developed, as well as the overall cluster simulation and optimization.

Machine learning algorithms are well suited for multi-track recognition problems because of their abil-

ity to reveal effective representations of multidimensional data through learning and to model complex dynamics through computationally regular transformations, that scale linearly with the size of input data and are easily distributed across computing nodes. Moreover, these algorithms are based on the linear algebra operations and can be parallelized well using standard ML packages. This approach was already applied successfully to recognize tracks in the BM@N experiment at JINR and in the BESIII experiment in IHEP CAS in China [469, 470]. In the course of the project an algorithm, based on recurrent neural networks of deep learning, will be developed to search for and reconstruct tracks of elementary particles in SPD data from the silicon vertex detector and the straw tube-based main tracker. The same approach will be applied to the clustering in the SPD electromagnetic calorimeter, and fast π^0 reconstruction. The caution is necessary, though, to avoid possible bias due to an inadequacy of the training data to the real ones, including possible machine background and the detector noise. A dedicated workflow that includes continuous learning and re-learning of neuron network, deployment of new versions of network and the continuous monitoring of the performance of the neural networks used in the online filter is necessary and needs to be elaborated.

Besides the high-level event filtering and corresponding data reduction, the online filter will provide input for the run monitoring by the shift team and the data quality assessment, as well as local polarimetry.

3 Computing system

The projected rate and amount of data produced by SPD prescribe to use high throughput computing solutions for the processing of collected data. It is the experience of a decade of the LHC computing that already developed a set of technologies mature enough for the building of distributed high-throughput computing systems for HEP.

3.1 Computing model

The 'online' part of computing systems for the SPD experiment, namely the online filter described above, is an integral part of experimental facilities, connected with the 'offline' part using a high throughput backbone network. The entry point to 'offline' facilities is a high capacity storage system, connected with 'online facility' through a multilink high-speed network. Data from high capacity storage at the Laboratory of Information Technologies will be copied to the tape-based mass storage system for long term storage. At the same time, data from high capacity storage will be processed on different computing facilities as in JINR as in other collaborative institutions.

The hierarchy of offline processing facilities can be introduced:

- Tier 1 level facilities should provide high capacity long term storage which will have enough capacity to store a full copy of primary data and a significant amount of important derived data;
- Tier 2 level facility should provide (transient) storage with capacity that will be enough for storing of data associated with a period of data taking;
- optional Tier 3 level are opportunistic resources, that can be used to cope with a pile-up of processing during some period of time or for special analysis.

Offline data processing resources are heterogeneous as on hardware architecture level so by technologies and at JINR site it includes batch processing computing farms, high performance (supercomputer) facilities, and cloud resources. A set of middleware services will be required to have unified access to different resources.

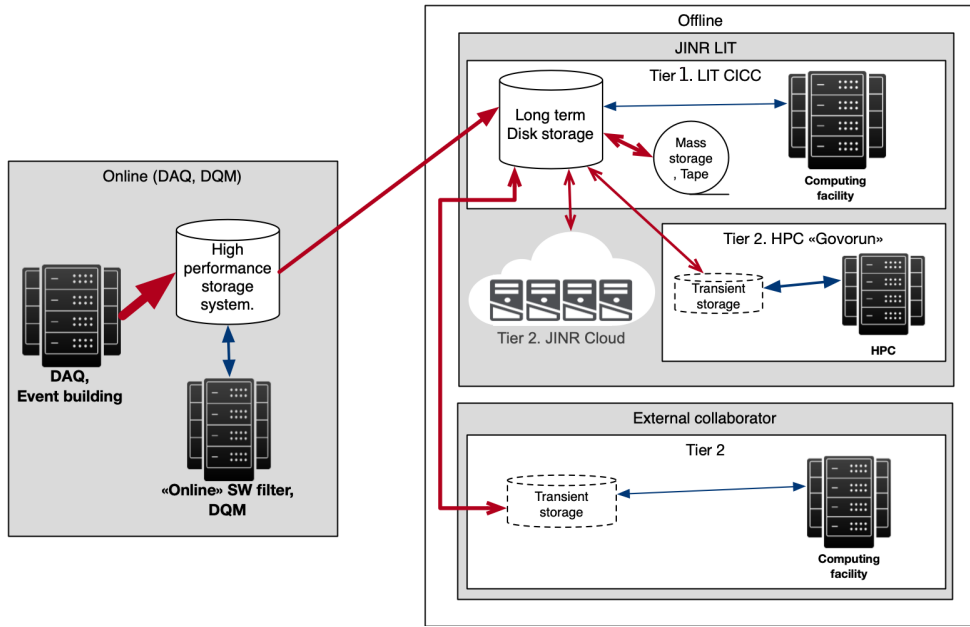


Figure 8.2: Scheme of the SPD computing system

3.2 Computing services

Computing systems for NICA at JINR are naturally distributed. Experimental facilities and main data processing facilities placed across two JINR sites and, *inter alia*, managed by different teams. That causes some heterogeneity not only on hardware systems but also on the level of basic software: different OSs, different batch systems etc.

Taking into account the distributed nature and heterogeneity of the existing infrastructure, and expected data volumes, the experimental data processing system must be based on a set of low-level services that have proven their reliability and performance.

It is necessary to develop a high-level orchestrating system that will manage the low-level services. The main task of that system will be to provide efficient, highly automated multi-step data processing following the experimental data processing chain.

The Unified Resource Management System is a IT ecosystem composed from the set of subsystem and services which should:

- unify of access to the data and compute resources in a heterogeneous distributed environment;
- automate most of the operations related to massive data processing;
- avoid duplication of basic functionality, through sharing of systems across different users (if it possible);
- as a result - reduce operational cost, increase the efficiency of usage of resources;
- transparent accounting of usage of resources.

Many distributed computing tools have already been developed for the LHC experiments and can be re-used in SPD. For the task management one can use PANDA [471] or DIRAC [472] frameworks. For the

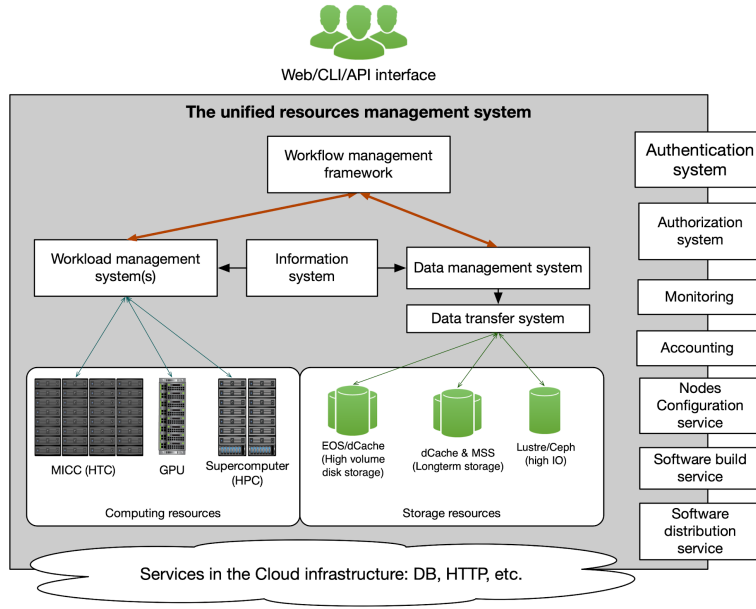


Figure 8.3: Distributed SPD computing services

distributed data management RUCIO [473] package has been developed. For the massive data transfer FTS [474] can be used. Evaluation of these tools for the SPD experiment and their implementation within the SPD Unified Resource Management System is planned in scope of the TDR preparation.

4 Offline software

Offline software is a toolkit for event reconstruction, Monte-Carlo simulation and data analysis. Linux is chosen as a base operating system.

Currently, the offline software of the SPD experiment – SpdRoot – is derived from the FairRoot software [475] and it is capable of Monte Carlo simulation, event reconstruction, and data analysis and visualization. The SPD detector description is flexible and based on the ROOT geometry package. Proton-proton collisions are simulated using a multipurpose generator Pythia8 [476]. Deuteron-deuteron collisions are simulated using a modern implementation of the FRITIOF model [477, 478], while UrQMD [479, 480] generator is used to simulate nucleus-nucleus interactions. Transportation of secondary particles through the material of the SPD setup and the simulation of detector response is provided by Geant4 toolkit [481–483]. Track reconstruction uses GenFit toolkit [484] and KFparticle package [485] is used to reconstruct primary and secondary vertices. The central database is going to be established to keep and distribute run information, slow control data and calibration constants.

Recent developments in computing hardware resulted in the rapid increase of potential processing capacity from increases in the core count of CPUs and wide CPU registers. Alternative processing architectures have become more commonplace. These range from the many-core architecture based on x86_64 compatible cores to numerous alternatives such as other CPU architectures (ARM, PowerPC) and special co-processors/accelerators: (GPUs, FPGA, etc). For GPUs, for instance, the processing model is very different, allowing a much greater fraction of the die to be dedicated to arithmetic calculations, but at a price in programming difficulty and memory handling for the developer that tends to be specific to each processor generation. Further developments may even see the use of FPGAs for more general-purpose tasks.

Table 8.1: Required SPD computing resources

	CPU [cores]	Disk [PB]	Tape [PB]
Online filter	6000	2	none
Offline computing	30000	5	9 per year
Cost estimate [kUSD]	4000	8000	4500 per year

The effective use of these computing resources may provide a significant improvement in offline data processing. However, the offline software should be capable to do it by taking advantage of concurrent programming techniques, such as vectorization and thread-based programming. Currently, the SPD software framework, SpdRoot, cannot use these techniques effectively. The studies of the concurrent-capable software frameworks (e.g. ALFA [486], Key4Hep [487]) are needed to provide input for the proper choice of the offline software for Day-1 of the SPD detector operation, as well as a dedicated R&D effort to find proper solutions for the development of efficient cross-platform code.

A git-based infrastructure for the SPD software development is already established at JINR [488].

5 Resource estimate

For the online filter we assume the CPU consumption of 1000 SPD events/core/second. This requires 3000 cores simultaneously for the fast tracking. Taking into account additional expenditures to the event unscrambling and data packing and including a real efficiency of CPU which will be lower than 100%, one derives the CPU resources for the online filter as 6000 CPU cores. This number sets the upper limit and the required computing power may decrease substantially if an efficient way to use GPU cores is implemented for the event filtration. As for the data storage, a high performance disk buffer of 2 PB capable to keep data of about one day of data taking is needed.

For the offline computing, the data storage is determined by the data rate after the online filter, or 4 PB/year of raw data. Besides that, we may expect the comparable amount of simulated data and estimate the long term storage as 10 PB/year, assuming two cycles of data processing and possible optimization of the data format and data objects to be stored permanently. We assume that a half of the annual data sample (~ 5 PB) is kept on disk storage, and the rest is stored on tape. The CPU power necessary to process the amount of data like this and to run Monte-Carlo simulation is estimated as many as 30000 CPU cores. The summary of computing resources is given in Table. 8.1. The cost estimate is conservative and will be defined more exactly in the TDR, when detailed hardware solutions and their actual price in the market will be considered.

The burden of the SPD computing system operation is a subject of sharing between the computing centers of the participating institutes.

Chapter 9

Physics performance

1 General performance of the SPD setup

1.1 Minimum bias events

The total cross-section of the p - p collisions in the full energy range of SPD operation is a constant and equals about 40 mb. The main contributions to that cross-section, i. e. the elastic scattering, the diffractive and non-diffractive processes, are shown in Fig. 9.1. The cross-section of "hard" processes, the QCD processes with partonic transverse momentum $\hat{p}_T > 1 \text{ GeV}/c$, is also shown as a part of the non-diffractive cross-section. The beam particle collisions in the interaction point are the source of numerous secondary charged and neutral particles in the SPD setup that fully defines our experimental conditions (the load of the detector, radiation environment, etc.). The fluxes of different kinds of the charged and neutral particles produced in the interaction point as a function of the polar angle are shown in Fig. 9.2(a) and (b) for $\sqrt{s} = 27$ and 13.5 GeV, respectively. Table 9.1 shows the total cross-section of the p - p

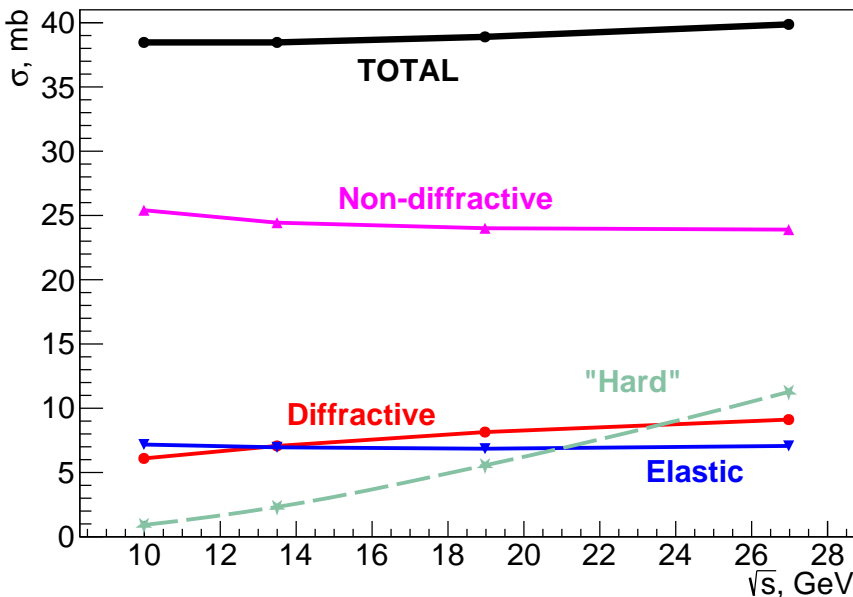


Figure 9.1: Main contributions to the total cross-section of p - p interaction as a function of \sqrt{s} . The "hard" cross-section is a part of the non-diffractive one.

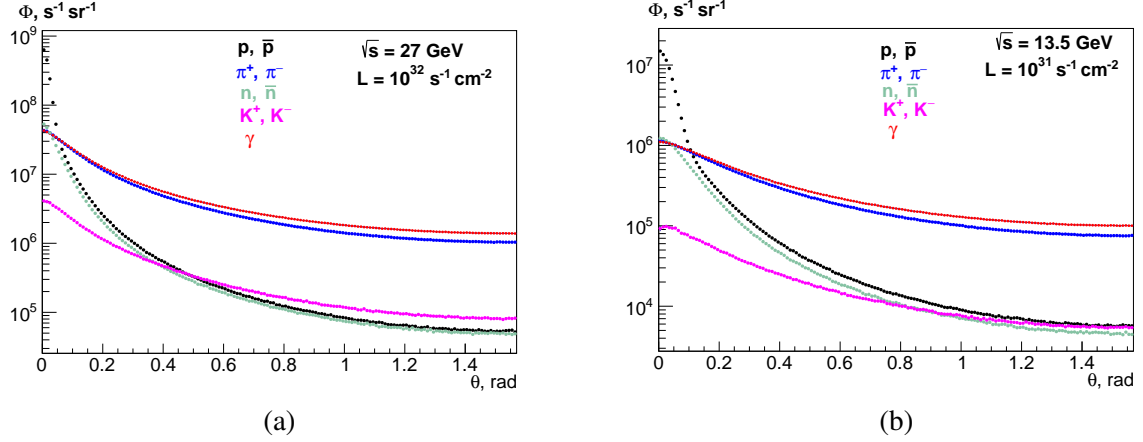


Figure 9.2: Fluxes of $p + \bar{p}$, π^\pm, K^\pm , $n + \bar{n}$ and γ as a function of the polar angle θ for (a) $\sqrt{s} = 27 \text{ GeV}$ and (b) 13.5 GeV .

collisions and the multiplicity of charged and neutral particles for different collision energies \sqrt{s} .

The secondary interactions in the material of the setup, the multiple scattering, the decays of unstable particles, and the influence of the magnetic field modify the radiation environment inside the SPD setup significantly. All these factors are taken into account in Figure 9.3 that illustrates the fluxes of the charged particles, photons, and neutrons at different points of the SPD setup for $\sqrt{s} = 27 \text{ GeV}$ and $L = 10^{32} \text{ cm}^{-2}$

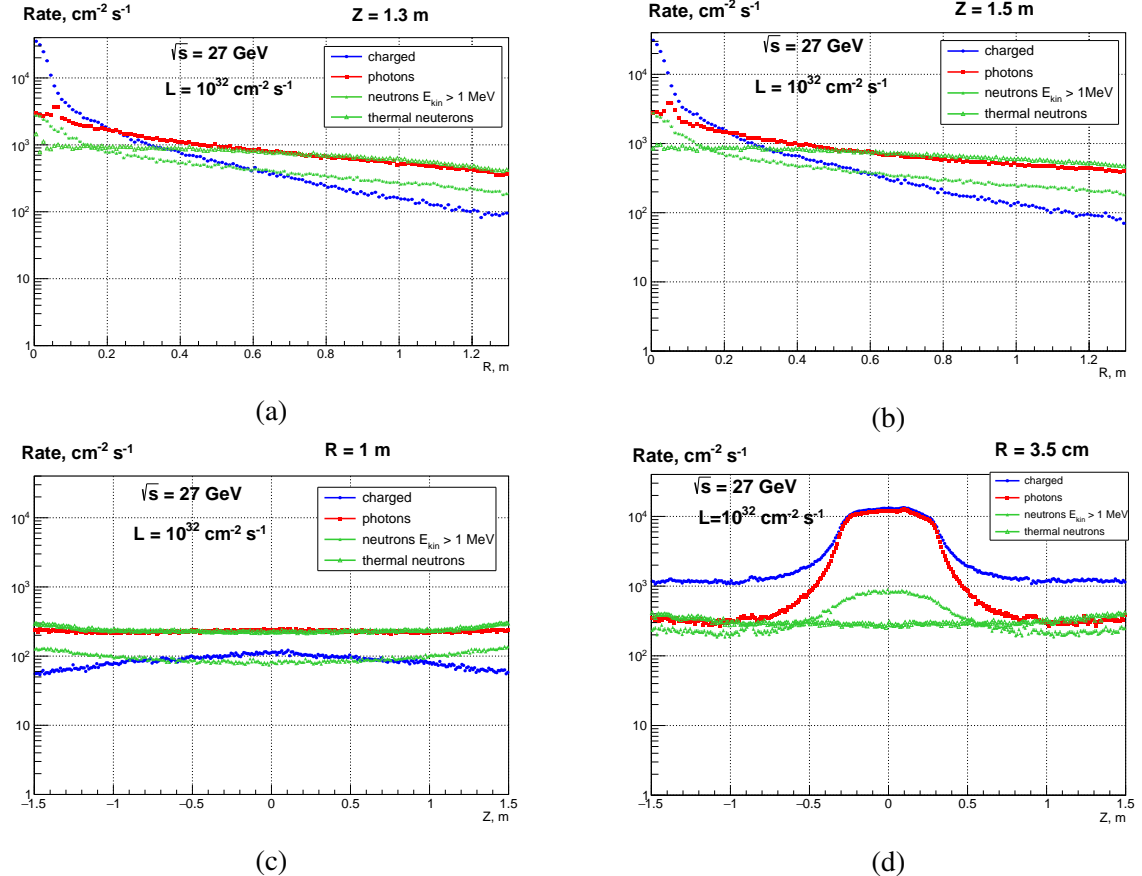


Figure 9.3: Flux of charged particles, photons, and neutrons in the radial direction at (a) $Z=1.3 \text{ m}$, (b) $Z=1.5 \text{ m}$, (c) $R=1 \text{ m}$, and (d) $R=3.5 \text{ cm}$.

s^{-1} : Z=1.3 m (a), Z=1.5 m (b), R=1 m (c), and R=3.5 cm (d).

Table 9.1: Total cross-section and the average multiplicity of the charged and neutral particles produced in the p - p collisions as a function of \sqrt{s} .

\sqrt{s} , GeV	σ_{tot} , mb	Charged multiplicity	Neutral (γ) multiplicity
13	38.4	5.9	4.6 (3.8)
20	38.9	7.2	6.0 (5.0)
26	39.7	7.8	6.5 (5.5)

1.2 Tracking

Traditionally, the track reconstruction procedure is divided into two separate tasks: track finding (or pattern recognition) and track fitting. Since the track multiplicity in the p - p collisions is low enough (see Tab. 9.1) the occupancy of the coordinate detectors is not really a problem. Thus, we hope to have the efficiency of the track finding to be not less than 90% in the most of our acceptance and we are not paying too much attention to the pattern recognition algorithms now. However, high multiplicity will limit the SPD performance in the case of NICA operation with heavy-ion beams.

The SPD magnetic system provides the conditions for measurement of the charged particle momenta. The track length in the SPD tracking system for charged particles of different momenta emitted from the interaction point at different polar angles as well as the trajectories for muons with momentum of 0.25 GeV/ c emitted at different polar and azimuthal angles $\theta = \phi$ are presented in Fig. 9.4 (a) and (b), respectively.

The track fitting procedure uses measured hits in the tracking detectors (or simulated points for Monte Carlo events) as an input, and calculates the most probable track parameters at any given point along the track, together with the corresponding covariance matrix. The fitting procedure also takes into consideration such effects related to the particle interaction in the material as multiple scattering, energy losses, and magnitude and configuration of the magnetic field. For the track fitting at SPD the well-known Kalman filter [489] implemented within the GenFit2 package [484] is used. The GenFit2 extrapolates

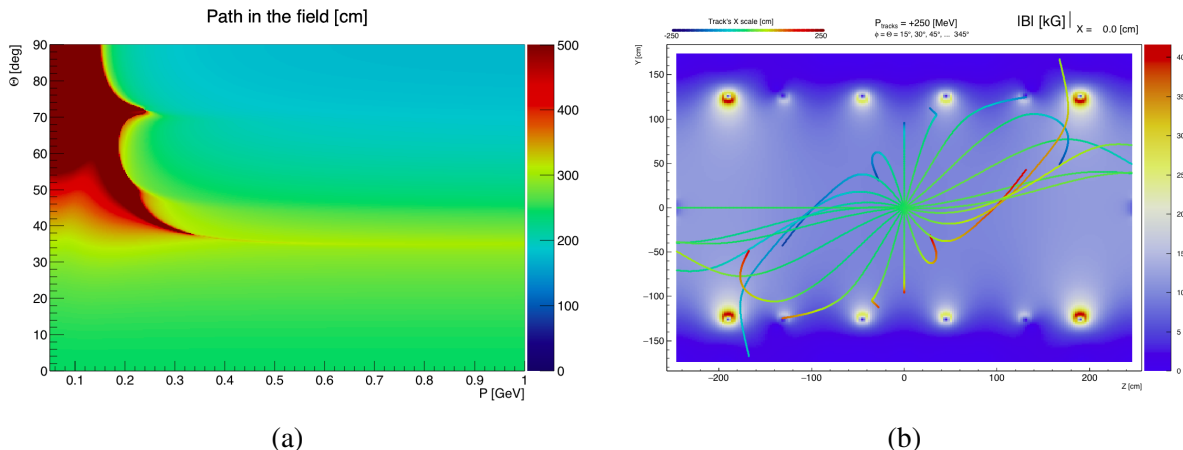


Figure 9.4: (a) Track length in the SPD tracking system for charged particles of different momenta emitted from the IP at different polar angles. (b) Trajectories for muons with momentum of 0.25 GeV/ c emitted from the IP at different polar and azimuthal angles $\theta = \phi$.

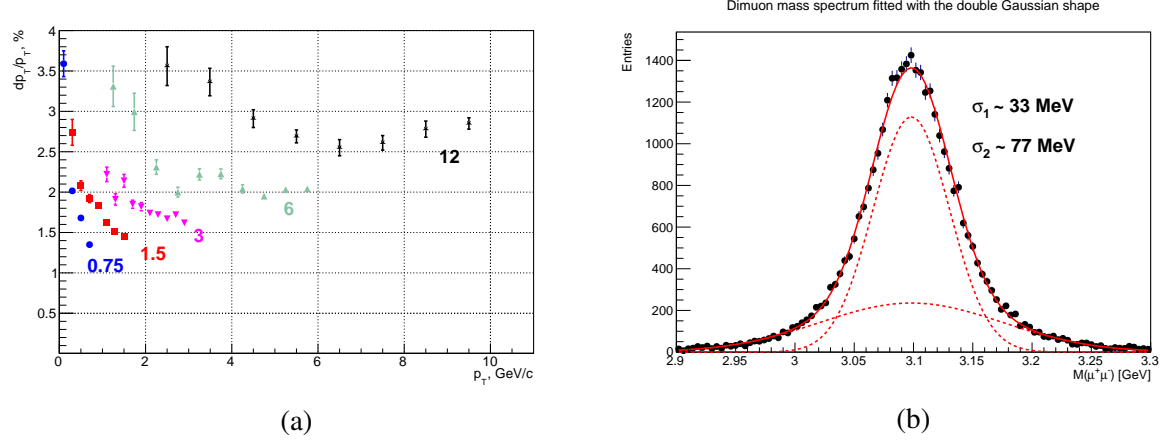


Figure 9.5: (a) Expected resolution for the transverse momentum σ_{p_T}/p_T of muons with momentum 0.75, 1.5, 3, 6, and 12 GeV/c . (b) J/ψ peak from the dimuon decay.

tracks using the standard Runge-Kutta-Nyström method [490] modified by Bugge and Myrheim to carry along the Jacobian matrix [491, 492].

The expected transverse momentum resolution σ_{p_T}/p_T for muons with different momenta for the maximal magnetic field 1.0 T at the beam axis is shown in Fig. 9.5(a). The corresponding resolution for muons emitted at the polar angle $\theta = 90^\circ$ could be expressed as

$$\sigma_p/p|_{\theta=90^\circ} = 1.3\% + 0.1\% \times p + 0.003\% \times p^2. \quad (9.1)$$

The width of the J/ψ peak shown in Fig. 9.5(b) is a good indicator of the tracking performance. The SPD tracking system demonstrates the width at the level of 40 MeV. It is 1.5 times better than at the fixed-target COMPASS experiment with the open setup (~ 60 MeV [493]) and much better than in the fixed-target beam dump experiments like NA3 (80–120 MeV [494]), COMPASS (~ 200 MeV [187]), SeaQuest (~ 150 MeV [495]), which worked successfully on the study of the partonic structure of the nucleon at the discussed energy range.

1.3 Vertex reconstruction

The only subsystem that defines reconstruction of primary vertices is the silicon vertex detector. Its impact on the accuracy of the vertex reconstruction depends on the baseline (the radial distance between layers), the amount of passed material producing the multiple scattering effects, and the spatial resolution of the detector. The latter is a rather complex function of the number of fired strips (or pixels). We estimate the effective spatial resolution of the DSSD layer as $\sigma_\phi = 11 \mu\text{m}$, $\sigma_z = 23 \mu\text{m}$, while the resolution of the MAPS layer is $\sigma_{\phi,z} = 4 \mu\text{m}$. σ_ϕ here denotes the resolution in the direction perpendicular to the beam line. The effective values are about two times smaller than the corresponding pitch divided by $\sqrt{12}$. The amount of the material corresponds to $300 \mu\text{m}$ and $50 \mu\text{m}$ of silicon per one layer of the DSSD and MAPS, respectively. Figure 9.6(a) shows the accuracy of the primary vertex position reconstruction as a function of the number of outgoing tracks for two configurations of the vertex detector: (i) 5 layers of the DSSD, (ii) 3 layers of the MAPS and 2 layers of the DSSD. In both cases the accuracy becomes better with an increasing number of outgoing tracks, as expected. The DSSD+MAPS configuration demonstrates a 1.5 times better precision.

The silicon vertex detector is also fully responsible for reconstruction of the decay vertices of short-lived ($c\tau < 1 \text{ cm}$) particles. We use the $D^0 \rightarrow K^+\pi^-$ decay as an example (see the sketch in Fig. 9.6 (b)), but all the conclusions are also valid qualitatively for the decays like $D^+ \rightarrow K^-\pi^+\pi^-$, $\Lambda_c^+ \rightarrow p\pi^+K^-$

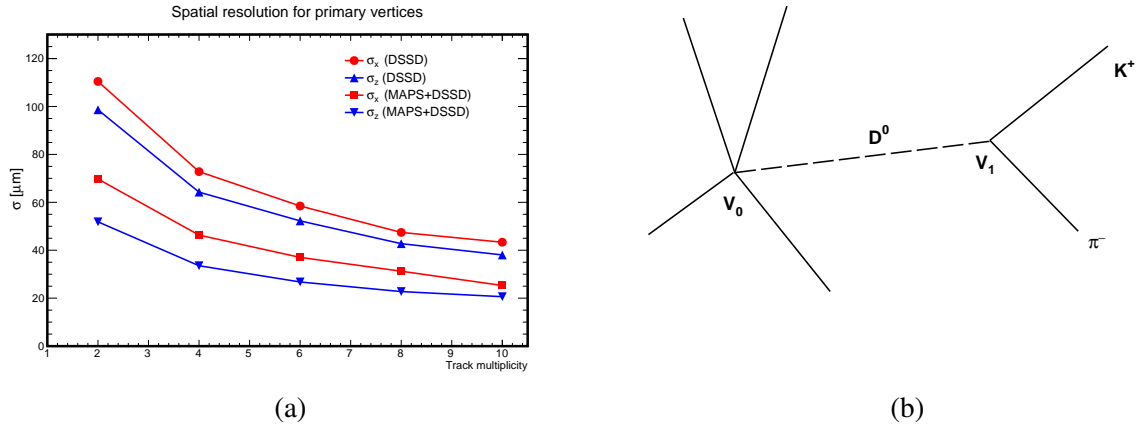


Figure 9.6: (a) Accuracy of the primary vertex position reconstruction as a function of the number of outgoing tracks for two configurations of the vertex detector. (b) Sketch of D^0 -meson production and decay.

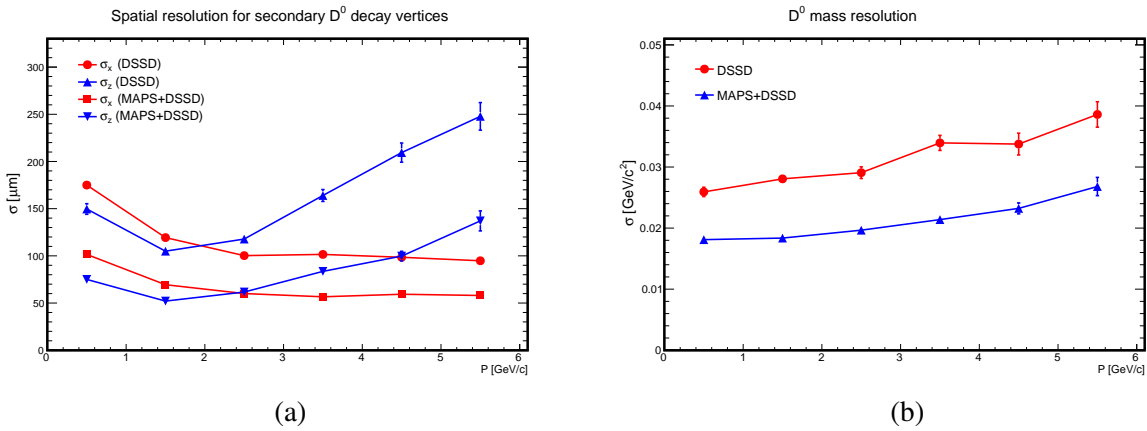


Figure 9.7: (a) Accuracy of the D^0 -decay vertex reconstruction as a function of the D^0 momentum. (b) D^0 peak width as a function of the D^0 momentum.

etc. The accuracy of the D^0 -decay vertex reconstruction as a function of the D^0 momentum is shown in the Fig. 9.7 (a). The Gaussian width of the D^0 -meson peak in the $K^+\pi^-$ mass spectrum determined by the tracking accuracy (mainly by the momentum resolution) is 27.2 and 25.0 MeV for the DSSD and DSSD+MAPS configurations, respectively. The constrained fit of the D^0 -decay, where the angle between the reconstructed D^0 momentum and the line connecting the primary and secondary vertices is forced to be zero and the found vertex is included in the track fitting, reduces the width to 21.4 and 18.0 MeV. That improves, respectively, the signal-to-background ratio by the factor of 1.3 and 2.4. The D^0 -peak width obtained from the constrained fit as a function of D^0 momentum is shown in Fig. 9.7 (b). The impact of the secondary vertex reconstruction procedure on our expectations for the asymmetries measurement is discussed in Sec. 2.

The decays of relatively long-lived unstable particles like Λ^0 , K^0 , Σ^- etc. occur mainly within the straw tracker. The $\Lambda^0 \rightarrow p^+\pi^-$ peak is presented in Fig. 9.8(a) as an example.

1.4 Particle identification

The effective $\pi/K/p$ separation is required first of all for such physics tasks as the open charm production (identification of kaons from $D^{\pm,0}$ decays, see Fig. 9.8 (b)); measurement of the SSA for charged kaons,

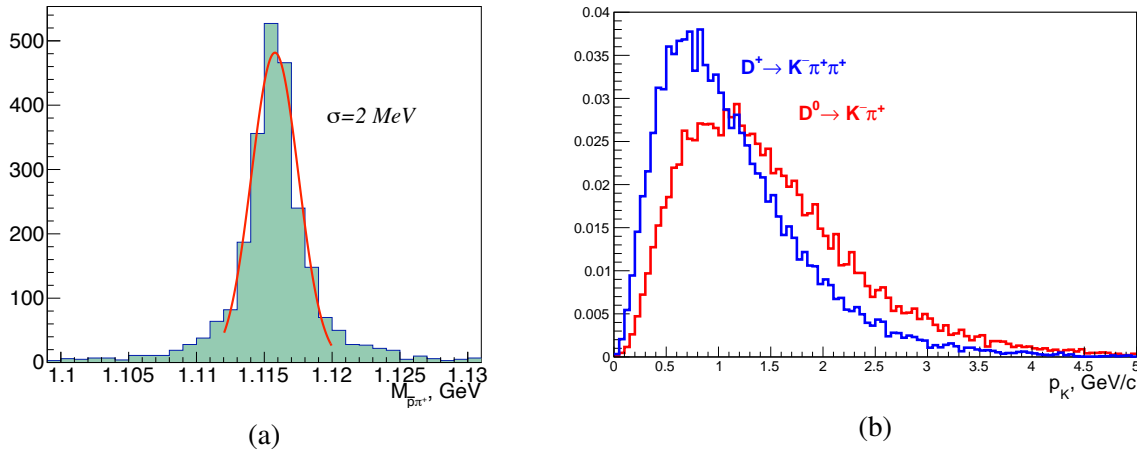


Figure 9.8: (a) Λ peak in the $p\pi$ mass spectrum. (b) Kaon spectra from the decays $D^0 \rightarrow K^- \pi^+$ (red) and $D^+ \rightarrow K^- \pi^+ \pi^+$ (blue) produced at $\sqrt{s} = 27 \text{ GeV}/c$.

and the study of the antiprotons yield. The proposed SPD setup has three instruments for identification of charged hadrons. The energy deposit dE/dx in the straw tubes of the ST can be used for particle identification at lowest momenta. The TOF system could extend the separation range up to $1.5 \text{ GeV}/c$ and $\sim 3 \text{ GeV}/c$ for π/K and K/p , respectively. The separation for the higher range of hadron momenta could be provided only by the aerogel detector.

1.4.1 Identification using dE/dx

The energy deposit dE/dx in the straw tubes is plotted in Fig 9.9 (a) for the particles emitted at $\theta = 90^\circ$ in respect to the beam axis as a function of their momenta. The truncated mean approach, where 20% of the measurement results from the individual straw tubes is discarded, was applied. The straw tracker is able to provide π/K and K/p separation up to $0.7 \text{ GeV}/c$ and $1.0 \text{ GeV}/c$, respectively. With respect to the TOF method (see below), the efficiency of the dE/dx method does not degrade at the low polar angles, since the end-cup part of the ST has enough layers for the precision measurement of the energy deposit.

1.4.2 TOF performance

Particle identification with a TOF detector is based on comparison between the time of flight of the particle from the primary vertex to the TOF detector and the expected time under a given mass hypothesis. For particle identification, the presence of only one plane of the TOF detector requires precise knowledge of the event collision time t_0 . It can be estimated by the TOF detector on an event-by-event basis, using the χ^2 minimization procedure for the events with two and more reconstructed tracks. Having N tracks in the event, which are matched to the corresponding hits on the TOF plane, it is possible to define certain combinations of masses \vec{m}_i , assuming the p , K , or p mass for each track independently. The index i indicates one of the possible combinations $(m_1, m_2, \dots, m_{N \text{ tracks}})$ among the $3N$ -track ones [496].

To each track the following weight is attributed

$$W_i = \frac{1}{\sigma_{TOF}^2 + \sigma_{t_{exp. i}}^2}. \quad (9.2)$$

Here σ_{TOF} and $\sigma_{t_{exp. i}}$ are the time resolution of the TOF detector and the uncertainty of the expected time of flight under a given mass hypothesis $t_{exp. i}$, respectively. The latter is defined by the uncertainty of the momentum and track length measurements.

The following χ^2 function has to be minimized

$$\chi^2(\vec{m}_i) = \sum_N W_i ((t_{TOF} - t_0(\vec{m}_i)) - t_{exp. i})^2. \quad (9.3)$$

Here

$$t_0(\vec{m}_i) = \frac{\sum_N (t_{TOF} - t_{exp. i})}{\sum_N W_i}. \quad (9.4)$$

The mass vector \vec{m}_i that minimizes χ^2 in Eq. 9.3 can be used in Eq. 9.4 for determination of the event collision time t_0 . For unbiased particle mass determination, each track has to be subsequently excluded from the t_0 calculation procedure.

Figure 9.9 (b) illustrates the accuracy of t_0 reconstruction as a function of the number of tracks for $\sigma_{TOF} = 70$ ps. One can see that σ_{t_0} is proportional to $1/\sqrt{N}$ and for the track multiplicity 10 (typical for hard interaction events) is about 30 ps. Pion, kaon, and proton separation with the TOF detector is shown in Fig. 9.10. The π/K and K/p separation power as a function of the particle momenta and the emission angle θ in the primary vertex is presented in Fig. 9.11 (a) and (b), respectively, for the time of flight ($t_{TOF} - t_0$) resolution equal to 80 ps. It is mostly defined by the time measurements, while the accuracy of the momentum reconstruction becomes sizable only for $\theta < 10^\circ$.

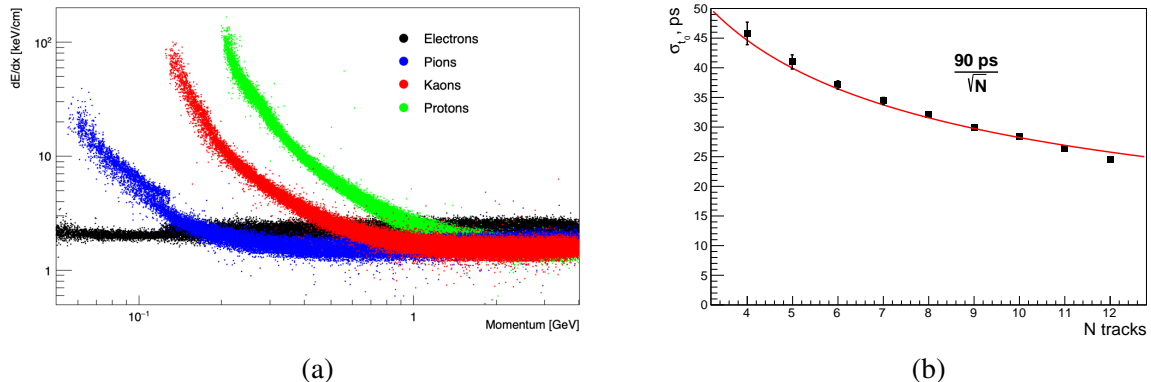


Figure 9.9: (a) Energy deposit dE/dx at the ST for particles emitted at $\theta = 90^\circ$ in respect to the beam axis. (b) Accuracy of the t_0 reconstruction as a function of the number of tracks in the primary vertex.

1.5 Calorimetry

The electromagnetic calorimeter is one of the main detectors for the SPD gluon program. Its functions are: (i) to measure the energy and the position of the hard prompt photons, and the photons from the radiative decays of π^0 - and η -mesons; (ii) to reconstruct the soft photons (~ 0.5 GeV) from the decays $\chi_{c1,2} \rightarrow J/\psi\gamma$; (iii) to provide identification of the electrons and positrons by comparing the energy deposit in the ECal and their momentum measured in the tracking system. The end-cup part of the ECal participates also in the online polarimetry with the inclusive π^0 production at high x_F (see Sec. 2).

The transparency of the SPD setup allows us to detect photons produced in the interaction point in a wide kinematic range. The efficiency of photon detection as a function of the production angle θ with respect to the beam direction and as a function of the transverse momentum p_T is shown in Fig. 9.12(a) and (b), respectively. The expected energy resolution of the ECal obtained from the Geant4-based Monte Carlo simulation for the normal incidence of photons and for the angle of 30° with respect to the normal line is shown in Fig. 9.13(a). Such effects as the individual cell energy threshold at the level of 50 MeV, the

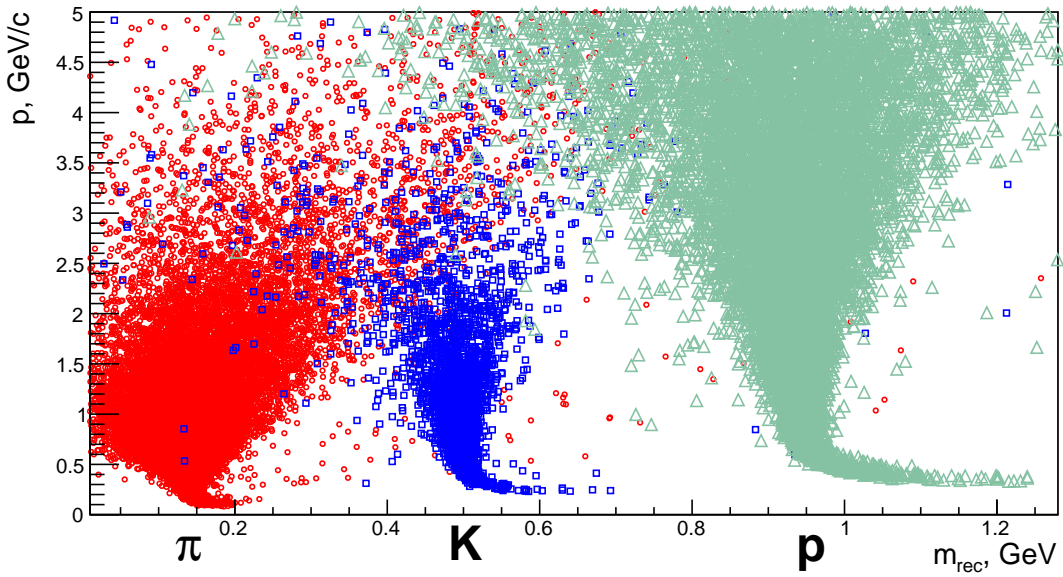


Figure 9.10: Reconstructed mass vs. the particle momentum for pions, kaons, and protons.

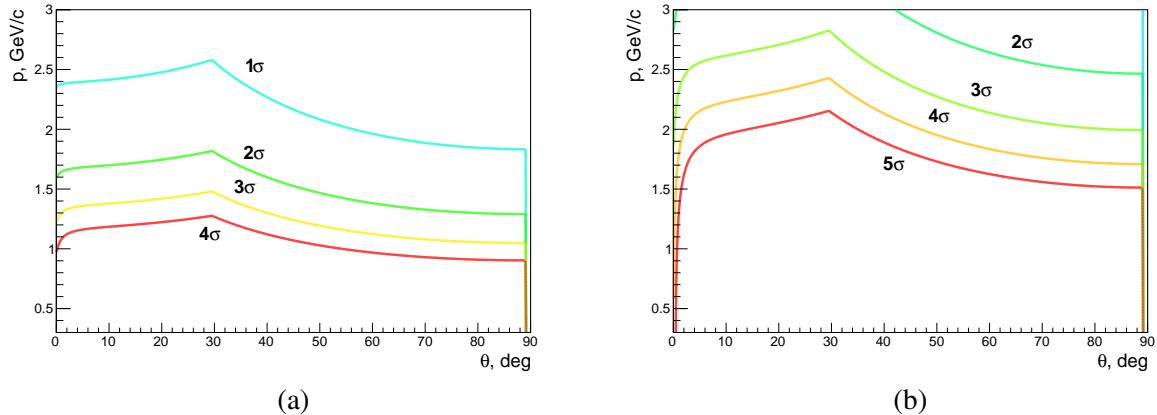


Figure 9.11: π/K (a) and K/p (b) separation power of the TOF system as a function of the particle momenta and the emission angle.

light absorption in the optic fibers, and the fluctuation of the number of photons are taken into account. The fitted curve has the shape:

$$\sigma_E/E = A \oplus \frac{B}{\sqrt{E/GeV}} \oplus \frac{C}{E/GeV}, \quad (9.5)$$

where the parameters A , B , and C are 0.9%, 5.9%, 1.7% and 0.0%, 6.0%, 2.2%, respectively, for 0° and 30° of the incidence angle. The superconducting coils of the magnetic system (about $1.2 X_0$ of the material) placed in front of the calorimeter practically do not reduce its acceptance for the hard photons and do not produce any sizable impact on the energy resolution. For instance, the average resolution for the 1 GeV photons passing through the coil changes from 6.1% to 6.3%.

As long as the internal longitudinal and transverse size of the ECal is small, there is a probability for photons from the high-energy pions decay ($E_{\pi^0} \gtrsim 6$ GeV) to produce a single cluster and be misidentified as a single high-energy photon. That is especially important for the prompt-photon part of the physics

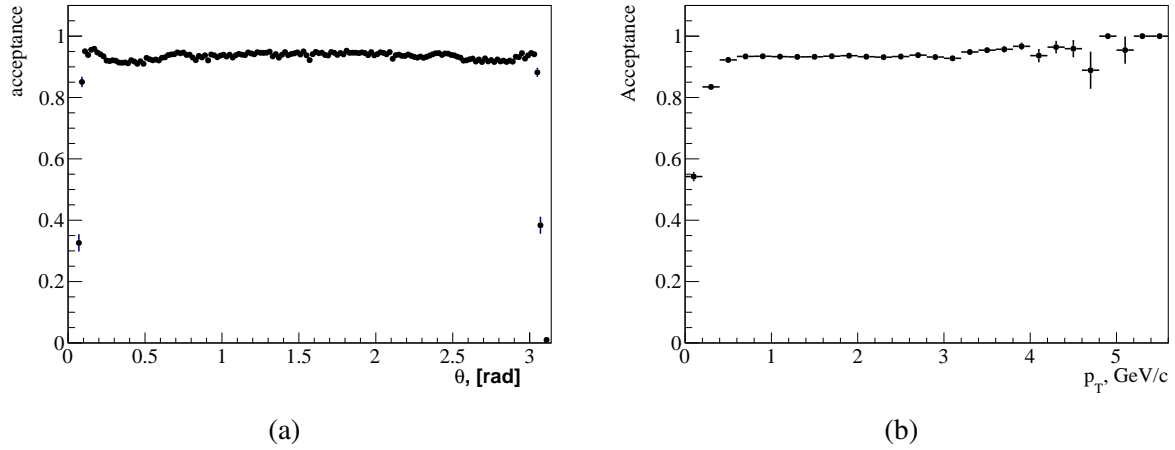


Figure 9.12: Efficiency of photon detection as a function of (a) polar angle θ and (b) transverse momentum p_T .

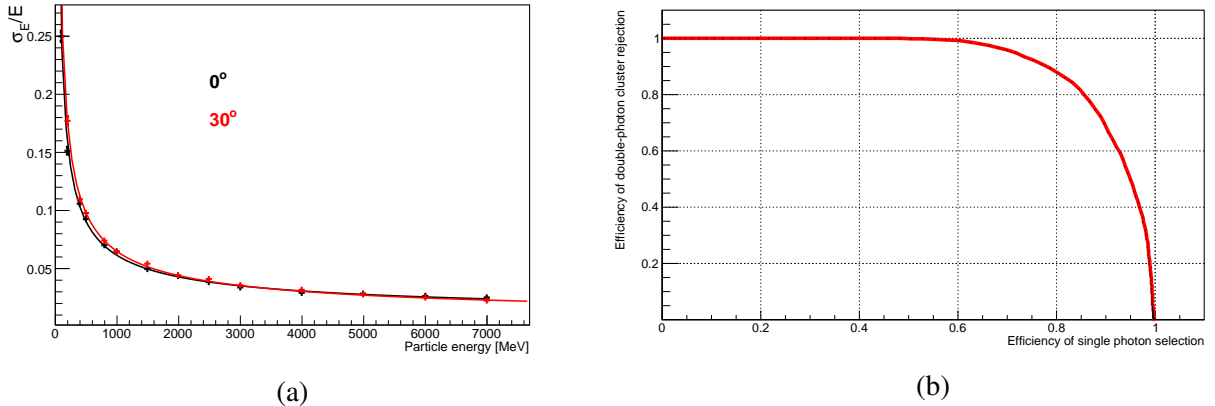


Figure 9.13: (a) Energy resolution of the ECal for the normal incidence of photons and for the angle of 30° . (b) Purity of the double-photon clusters rejection vs. the efficiency of the single-photon reconstruction for 6 GeV photons and two 3 GeV photons separated by a distance of 4 cm, based on the cluster shape analysis.

program. However, it is possible to identify such clusters with a certain precision performing the cluster shape analysis. The cluster shape can be characterized using such variables as dispersion or the second-order moment (in one or two dimensions), the fourth-order moment, the ratio of the major and the minor semiaxes of the cluster ellipse, etc. Machine learning classification techniques are planned to be applied (the multilayer perceptron, the k-nearest neighbors, etc.), using these variables as an input to distinguish between single- and double-photon clusters. Figure 9.13(b) illustrates the purity of the double-photon rejection vs. the efficiency of the single-photon reconstruction for 6 GeV photons and two 3 GeV photons separated by a distance of 4 cm (exactly the ECal cell size), based on the cluster shape analysis.

The impact of the ECal energy resolution on the reconstruction of such states as π^0 , η is shown in Fig. 9.14(a). The relative width of the π^0 and η peaks is 7.3% and 6.9%, respectively, for $E_\gamma > 0.5$ GeV. The reconstruction of the charmonium states $\chi_{c,1,2}$ via their radiative decays is presented in Fig. 9.14(b). The χ_{c1} and χ_{c2} peaks cannot be fully resolved ($\Delta M/\sigma_M \approx 1.5$), but, nevertheless, the relative contribution of these states could be estimated based on the detailed peak shape analysis.

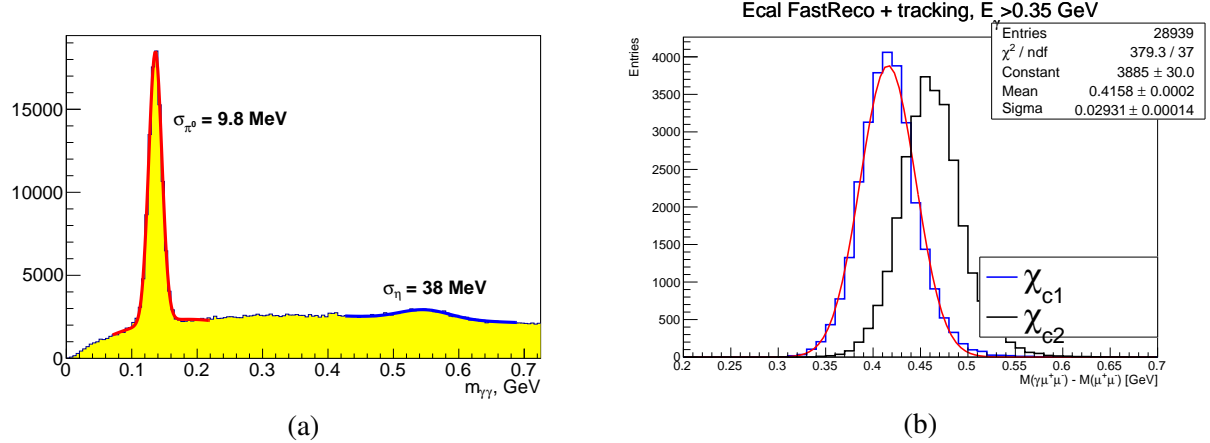


Figure 9.14: (a) π^0 -peak in the $\gamma\gamma$ mass spectrum. (b) Mass resolution for $\chi_{c1,2}$ reconstructed via their decay into $J/\psi\gamma$ final state.

2 Accuracies of the asymmetries measurement

The results presented in this section illustrate general possibilities of the SPD setup to deal with spin asymmetries and should be treated as preliminary. The most of them require further optimization of the selection criteria and could be significantly improved.

The single transverse (A_N) and the double longitudinal and transverse (A_{LL} and A_{TT}) spin asymmetries are the main observables to be accessed at SPD. The asymmetry A_N is denoted as

$$A_N = \frac{\sigma^\uparrow - \sigma^\downarrow}{\sigma^\uparrow + \sigma^\downarrow}, \quad (9.6)$$

where σ^\uparrow and σ^\downarrow denote the inclusive production cross-sections with the opposite transverse polarization of one of the colliding particles. In practice, taking into account the 2π coverage of the SPD setup in azimuthal angle ϕ , the A_N can be extracted from the azimuthal modulation amplitude of the differential cross-section $d\sigma/d\phi$

$$d\sigma/d\phi \propto 1 + PA_N \cos(\phi - \phi_0), \quad (9.7)$$

where P and ϕ_0 are the beam polarization and its direction. All estimations for the accuracy of the SSA measurement are performed under assumption that only one of the two beams is transversely polarized. In the case of two polarized beams the statistical uncertainty could be reduced by the factor of $\sqrt{2}$.

The double longitudinal spin asymmetry can be expressed via the number of events for the same (N^{++}) and the opposite (N^{+-}) spin orientations of colliding protons:

$$A_{LL} = \frac{\sigma^{++} - \sigma^{+-}}{\sigma^{++} + \sigma^{+-}} = \frac{1}{P_1 P_2} \times \frac{N^{++} - RN^{+-}}{N^{++} + RN^{+-}}. \quad (9.8)$$

σ^{++} and σ^{+-} denote the cross-sections with the same and the opposite proton helicity combinations, respectively. P_1 and P_2 are the absolute values of proton beams polarizations and $R = L_{++}/L_{+-}$ is the ratio of the integrated luminosities for the samples with the same and the opposite spin orientations. Assuming the same amount of data collected with both spin orientations Eq. 9.8 can be rewritten as:

$$A_{LL} = \frac{1}{P_1 P_2} \times \frac{N^{++} - N^{+-}}{N^{++} + N^{+-}}. \quad (9.9)$$

The aforesaid is also valid for the A_{TT} asymmetry.

2.1 Charmonia production

According to the modern theoretical approaches, the charmonia production at the SPD energies ($10 \text{ GeV} \leq \sqrt{s} \leq 27 \text{ GeV}$) is dominated by the gluon-gluon fusion process. The inclusive J/ψ production has a large cross-section (200 \div 250 nb at the maximum energy) and clear experimental signature in the dimuon decay mode, and thus is a powerful probe of the internal structure of proton and deuteron. At the same time, the distinct J/ψ signal allows us to reconstruct excited charmonia states in the decays $\chi_{c1,2} \rightarrow \gamma J/\psi$ and $\psi(2S) \rightarrow \pi^+ \pi^- J/\psi$. There is also a possibility to reconstruct J/ψ from the $e^+ e^-$ final state, but it looks less promising due a much larger background, a larger observed J/ψ width, and a more complicated shape of the peak, which will significantly affect both statistical and systematic uncertainties. The study of the η_c production properties in the $p\bar{p}$ and $\Lambda\bar{\Lambda}$ decay modes may also be feasible.

Muons are identified in the RS. The system is expected to separate showers from strongly interacting pions and muon tracks (using standard or machine learning techniques). The main background is muons from pion decays and pions that passed a large distance in the RS. The pion decays result in a small kink of the charged track (about 2°), and the decay muon retains from 60% to almost 100% of the initial pion energy. There is a possibility that a fraction of decay muons can be suppressed by the search for a kink in the tracker or by considering the correlation between the particle momentum and the amount of material it crossed. However, the results in this section are based on a simplified model (gives a lower performance boundary). A particle is identified as a muon based on the amount of material it passes in the active part of the RS, this amount is given as a number of proton nuclear lengths (n_λ). Two possibilities are considered: a particle from the initial interaction and a muon from a pion decay (the pion must be from the initial interaction). In the latter case, if the pion decays in the RS, the amount of material is added for the pion and muon.

It is clear that higher running energies are preferable for the physics with charmonia due to larger production cross-section, a stronger boost for pions and more energetic muons. All estimates in this section assume a $p\bar{p}$ collision energy of 27 GeV, 10^7 s time of data taking (one year) with the maximum luminosity and a polarization P of 0.7. At these conditions one expects about 12 million $J/\psi \rightarrow \mu^+ \mu^-$ decays in the SPD detector.

The J/ψ events are simulated using Pythia8 and their number is normalized to a production cross-section of 200 nb. For the background minimum bias events generated with Pythia6 and Pythia8 are considered (giving almost the same predictions around the J/ψ peak). Approximately half of the background events are produced in the hard interaction, but a sizable fraction also comes from the diffraction processes. It appears that significant amount of background events can be suppressed by the requirement on the polar angle of a muon candidate. The $\mu^+ \mu^-$ invariant mass spectrum for the muon candidates with $n_\lambda > 3$ and satisfying $|\cos \theta| < 0.9$ after one year of data taking is shown in Fig. 9.15 (a). Approximately half of the background events under the J/ψ peak are two decay muons, the other half mostly consists of one decay muon and one pion that passed a large distance in the RS, and the rest are two pions misidentified as μ^+ and μ^- . The selection efficiency can be estimated to be around 35 \div 45%, depending on the cut on θ , resulting in 4 \div 5 million selected events. The barrel part of the RS is essential for reconstruction of approximately 90% of J/ψ events: for more than 50% of J/ψ events one lepton is reconstructed in the barrel and the other one in the end-caps, more than 35% of events are reconstructed solely in the barrel part of the detector. The statistical errors for observables can be estimated using a linear LSM fit [31]. As an example, the estimated statistical precision for the J/ψ polarization λ as a function of the transverse momentum p_T is shown in Fig. 9.15 (b). The estimation was done under the assumption $\lambda \ll 1$ based on the angular modulation of the differential cross-section

$$d\sigma/d\cos \theta_\mu \propto 1 + \lambda_\theta \cos^2 \theta_\mu, \quad (9.10)$$

where θ_μ is the angle between the muon momentum and the J/ψ momentum in the helicity frame.

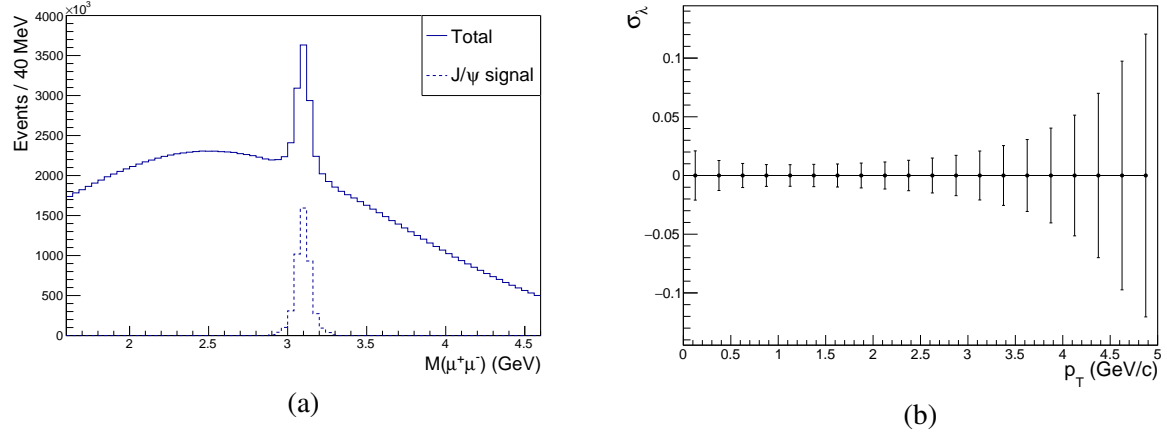


Figure 9.15: (a) Dimuon candidate spectrum and the J/ψ peak after one year of data taking. (b) Expected statistical precision for polarization λ_θ as a function of the J/ψ transverse momentum.

The transverse single-spin asymmetry A_N in J/ψ production probes the Sivers function. At $\sqrt{s} = 200$ GeV it was measured by the PHENIX Collaboration and found consistent with zero [18, 19]. To estimate our statistical precision, 8 bins in ϕ are considered (see Eq. 9.7). The same linear fit is used to, firstly, estimate the error in the bins based on the expected J/ψ number and, secondly, to extract A_N . The projected statistical uncertainties for A_N as a function of x_F are compared to the GPM model predictions from Ref. [497] in Fig. 9.16 (preliminary CGI-GPM calculations indicate lower asymmetries). Compared to the PHENIX measurement, we expect a much better precision and a much wider kinematic range in x_F . Our rapidity range is approximately $|y| < 2$.

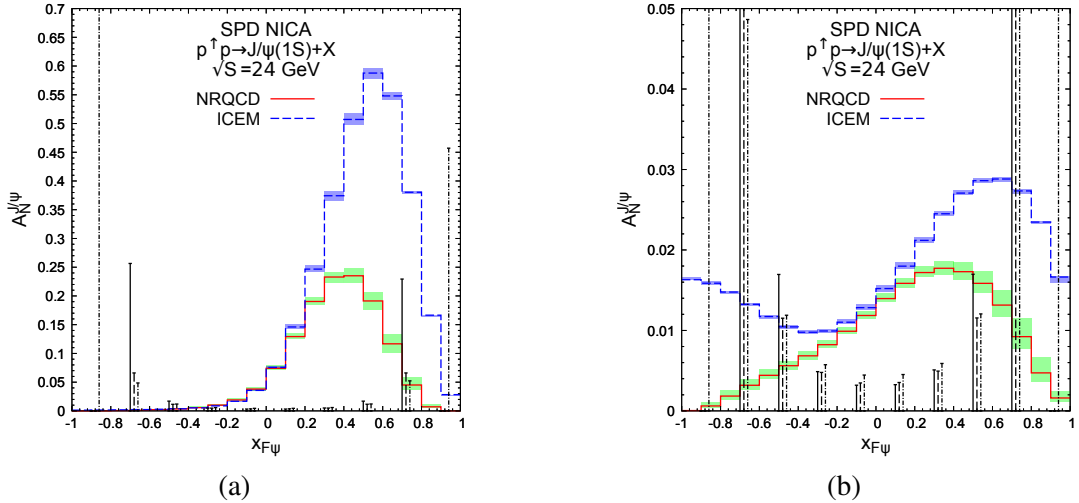


Figure 9.16: Projection of the estimated statistical uncertainties for A_N compared to the GPM predictions from Ref. [497] for SIDIS1 (a) and D'Alesio PDF parameterizations (b).

The statistical error of the longitudinal double spin asymmetry A_{LL} sensitive to the polarized gluon distribution was estimated basing on Eq. 9.8 and 9.9. In these formulas, we neglect the uncertainties of the measurement of the relative integrated luminosities and the beam polarizations. The projection of the statistical uncertainties as functions of p_T and $|y|$ are shown in Fig 9.17. Compared to the previous results obtained by the PHENIX Collaboration at $\sqrt{s} = 510$ GeV [120], we have a much better precision and probe a wider kinematic range.

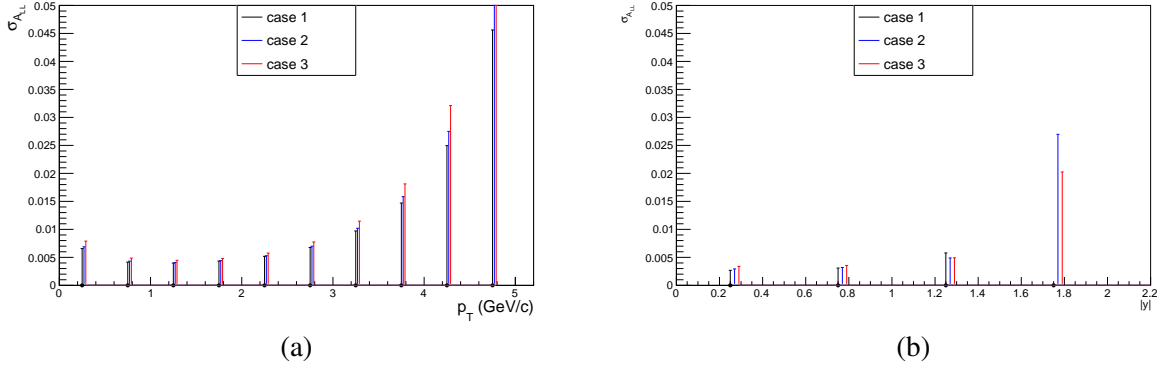


Figure 9.17: Estimated statistical precision of A_{LL} as a function of p_T (a) and rapidity (b). Three different cuts on the polar angle of muon candidates are considered.

The study of the associated J/ψ production will be strongly restricted by the insufficient expected statistics. The double J/ψ production cross-section was measured by the NA3 Collaboration [498] and was found to be 27 ± 10 pb in the proton-nucleus interaction at $\sqrt{s} \approx 27$ GeV. Optimistically, such a cross-section would result in $50 \div 100$ reconstructed events, if both e^+e^- and $\mu^+\mu^-$ modes are used to reconstruct J/ψ . It may be enough to determine low- p_T cross-section dependence, but the study of any angular modulation will not be possible. The study of $\gamma J/\psi$ production will be challenging experimentally due to a lack of statistics and a high expected background. Reasonable statistics might be expected for $J/\psi D$ production.

The $\psi(2S) \rightarrow \mu^+\mu^-$ decay is suppressed, as compared to $J/\psi \rightarrow \mu^+\mu^-$ by approximately a factor of 50 and its reliable extraction may not be feasible. At the same time, the decay $\psi(2S) \rightarrow \pi^+\pi^- J/\psi$ can be reliably identified as a narrow (about $10 \text{ MeV}/c^2$ wide) peak in the $M_{\pi^+\pi^-\mu^+\mu^-} - M_{\mu^+\mu^-}$ distribution. This distribution is shown in Fig. 9.18 (a). The expected statistics is about 1×10^5 selected events.

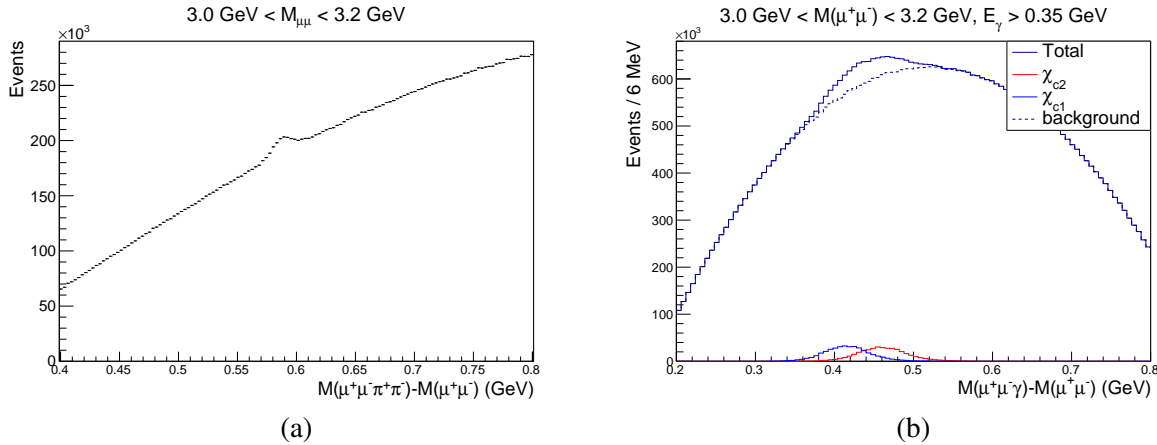


Figure 9.18: (a) $\psi(2S)$ signal in the $M_{\pi^+\pi^-\mu^+\mu^-} - M_{\mu^+\mu^-}$ distribution. (b) Preliminary estimation of the background for the χ_{c1} and χ_{c2} reconstruction. For this plot a feed-down fraction of 15% is assumed for both states.

The χ_{c1} and χ_{c2} states have a large partial width of decay to $J/\psi\gamma$ and can be reconstructed using it. The production properties of these states at low energies are poorly known (e.g. see the review of the experimental results in Ref. [32]). The identification of these decays at SPD relies on the ECal performance. The result of the MC simulation for $M_{\gamma\mu^+\mu^-} - M_{\mu^+\mu^-}$ is shown in Fig. 9.14(b). It will not be possible to separate χ_{c1} from χ_{c2} , but their relative fractions should be well-measurable. For the

expected statistics of approximately 0.5 million reconstructed decays per year (for both states together) it should be possible to measure the cross-section kinematic dependencies of these states. The major difficulty in the studying of these states is the high expected background. Its very rough estimation is shown in Fig. 9.18 (b).

The η_c production cross-section is highly uncertain. At $\sqrt{s} = 24$ GeV it is estimated that $\sigma_{\eta_c} \cdot B(\eta_c \rightarrow p\bar{p}) = 0.6^{+0.8}_{-0.4}$ nb [499] or 6×10^5 events per year. The typical momenta of p and \bar{p} is $1.5 - 2$ GeV/c, where these particles should be well-identified by the TOF system (see Fig. 9.10). The feasibility of the differential cross-section measurements requires detailed MC-simulations due to the high expected background. A very limited statistics, but a clearer signal may be also expected in the $\Lambda\bar{\Lambda}$ decay mode.

2.2 Prompt photon production

As it was already mentioned in Chapter 2, two hard leading-order processes determine the production of prompt photons in the p - p collisions in the leading order: gluon Compton scattering $gq(\bar{q}) \rightarrow \gamma q(\bar{q})$ and quark-antiquark annihilation: $q\bar{q} \rightarrow g\gamma$. The contribution of the latter process to the total cross-section does not exceed 20% in the discussed energy range. That is what makes the prompt photons a convenient probe for gluons inside the nucleon. The energy and angular distributions for prompt photons with $p_T > 3$ GeV/c are shown in Fig. 9.19. There we do not take into consideration fragmentation photons, photons produced by fragmentation of final-state parton, whose contribution is significant in the discussed range of p_T , and which should also be treated as a part of the signal. Figure 9.20 (a) gives one an idea concerning the relative fraction of the fragmentation photons contribution with respect to the leading-order one. In the ultrarelativistic approximation the minimal value of the longitudinal momen-

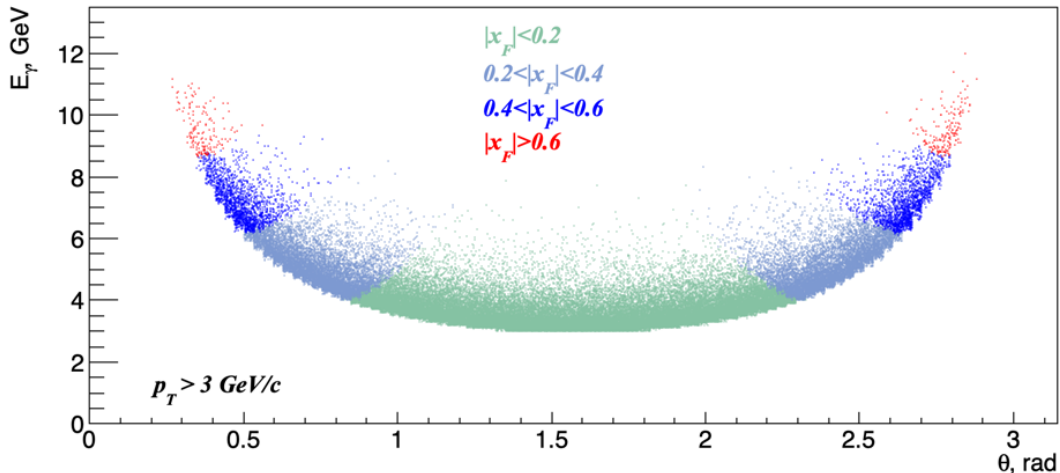


Figure 9.19: Expected uncertainty of the unpolarized cross-section $Ed^3\sigma/dp^3$ measurement as a function of polar angle θ .

tum fraction of a struck parton x_{min} accessible by detection of the prompt photon with the normalized transverse momentum $x_T = 2p_T/\sqrt{s}$ and the rapidity y can be expressed as [500]

$$x_{min} = \frac{x_T e^{-y}}{2 - x_T e^y}. \quad (9.11)$$

For fixed x_T , the minimal $x_{min} = x_T^2$ is reached at $y_0 = -\ln(x_T)$. The value x_{min} as a function of rapidity y and p_T of photon for $\sqrt{s} = 27$ GeV is shown in color in Fig. 9.20(b). Here a low- x parton goes against the z -axis. One can see that the possibility of accessing the low- x region is limited by our capability to

detect the prompt-photon signal at a low p_T and the angular acceptance of the experimental apparatus. The latter is especially important for collider experiments like SPD, where large absolute values of y correspond to the blind area near the beam pipe.

The huge rate of decay photons makes the determination of the prompt photon production cross-section rather difficult. The main source of the decay photons is the two-body decay $\pi^0 \rightarrow \gamma\gamma$. The second most important source is the decay $\eta \rightarrow \gamma\gamma$. In the kinematic range $p_T > 3 \text{ GeV}/c$ at $\sqrt{s} = 27 \text{ GeV}$ there are about 0.18 photons from the η -decay per one photon from the π^0 decay. The relative contribution of all other decay photons (ω, ρ, ϕ decays) does not exceed 0.03.

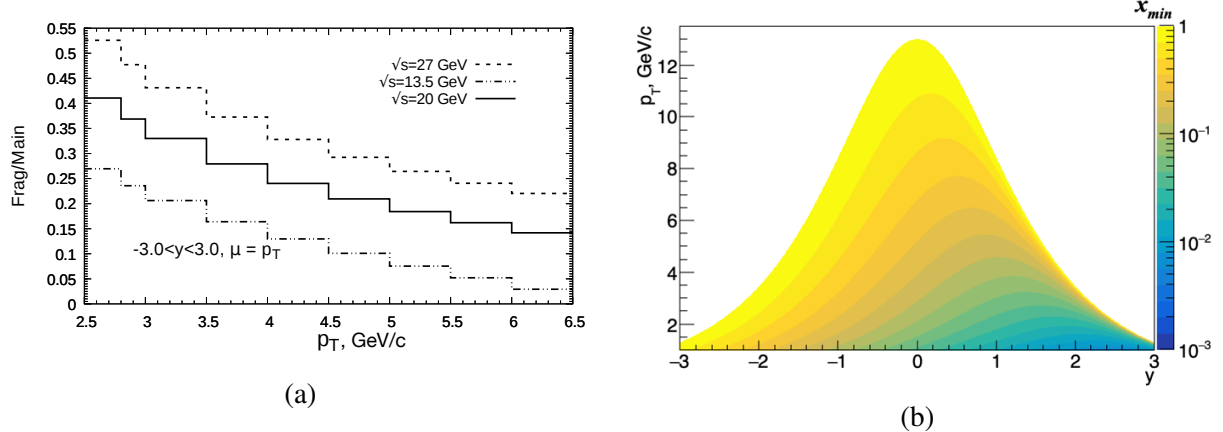


Figure 9.20: (a) Relative contribution of the fragmentation photons for the p - p collision energies $\sqrt{s} = 13.5, 20$, and 27 GeV . (b) Minimal value of gluon x accessible via registration of prompt photon with rapidity y and transverse momentum p_T at $\sqrt{s} = 27 \text{ GeV}$.

The p_T spectra for the prompt and decay photons expected at SPD after one year of running at $\sqrt{s} = 27 \text{ GeV}$ are presented in Fig. 9.21 (a). The result was obtained using the Pythia8 generator with the parameters tuned to reproduce the high- p_T spectra of the π^0 and prompt photons measured at similar energies by the WA70 ($\sqrt{s} = 22.96 \text{ GeV}$) [501, 502] and the UA6 ($\sqrt{s} = 24.3 \text{ GeV}$) [503] experiments, respectively. One can see that the p_T spectrum of the decay photons goes down with the growth of the p_T faster than for the prompt photons and their rates become comparable at $p_T \approx 7 \text{ GeV}/c$. The fitted functions presented on the plot have the shape

$$N(p_T) = A(1 - x_T)^n(p/p_0)^{-m}. \quad (9.12)$$

Each cluster of the energy deposition in the ECal with the energy above the threshold $E_0 = 100 \text{ MeV}$ that is not associated with any reconstructed tracks is treated as the prompt photon candidate. The momentum of such a photon is reconstructed under the assumption of its production in the primary vertex. In order to reject photons from the $\pi^0 \rightarrow \gamma\gamma$ decay the invariant mass of each two photons is calculated. If the difference between the reconstructed mass and the nominal mass of π^0 is smaller than 10 MeV, both photons are removed from the list of candidates. Nevertheless, this procedure removes just about 40% of false candidates. The photons from the $\pi^0 \rightarrow \gamma\gamma$ decay, whose partner was not reconstructed due to conversion in the material, too low energy or the acceptance issue, remain on the list of candidates. The photons from the radiative decays of other particles are also in the list. The list of candidates also includes photons associated with two or more overlapping clusters, first of all, the clusters from the decay of energetic π^0 's. A significant part of such false candidates could be rejected by a sophisticated analysis of the cluster shape. The clusters produced by the charged particles whose tracks are lost, the clusters deposited by the photons originated from the elements of the setup and the clusters induced by the neutral

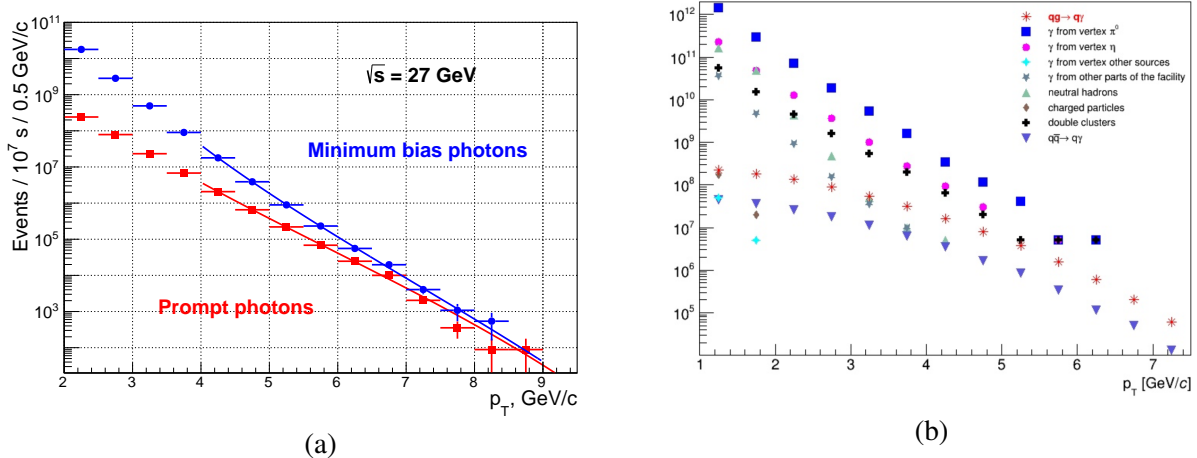


Figure 9.21: (a) p_T spectra of the produced prompt (red) and the decay or minimum bias (blue) photons in p - p collisions at $\sqrt{s} = 27$ GeV. Distributions are scaled to one year of data taking (10^7 s). (b) Contributions of different background components for the prompt photon production in p - p collisions at $\sqrt{s} = 27$ GeV (events per effective year of data taking) [504].

hadrons are also taken into account as the background. The typical contributions of each source of the background mentioned above are presented as a function of p_T in Fig. 9.21(b).

As one can see, the photons from the unreconstructed decays of neutral pions are the main source of the background. The fraction of such unreconstructed decays can be estimated from the Monte Carlo simulation and is about 50%. Based on the number N_{π^0} of the reconstructed $\pi^0 \rightarrow \gamma\gamma$ decays, the corresponding number of the remaining background photons $k \times N_{\pi^0}$ should be subtracted from the number of prompt-photon candidates N_γ in order to get an estimation of a true number of prompt photons:

$$N_{prompt} = N_\gamma - k \times N_{\pi^0}. \quad (9.13)$$

Here $k \approx 0.3$ is a coefficient calculated from the MC simulation that takes into account not only the inefficiency of the $\pi^0 \rightarrow \gamma\gamma$ decay reconstruction, but also the overall contribution of all other background photons including the photons from the radiative decays of η , ω , ρ , ϕ , etc. The described subtraction procedure has to be performed for each bin of p_T and x_F ranges. One should keep in mind that the background of the decay photons is also spin-dependent, since there is an indication of non-zero asymmetries A_{LL} and A_N in the inclusive π^0 and η production [111–113, 176, 177, 505].

The expected accuracy of the unpolarized cross-section $Ed^3\sigma/dp^3$ measurement after one effective year (10^7 s) of data taking is shown in Fig. 9.21(b). At a low p_T range the main contribution to the total uncertainty comes from the systematics of the π^0 background subtraction procedure while at high p_T the statistical uncertainty dominates. To estimate the systematics $dk/k = 1\%$ is assumed as a realistic value.

To estimate the A_N asymmetry the function

$$f(\phi) = C + P \times A_N \cos \phi \quad (9.14)$$

is fitted to the expected acceptance-corrected azimuthal distribution of the prompt-photon events. Here ϕ is the azimuthal angle of the photons produced in the laboratory frame in respect to the direction of the proton beam polarization. The expected accuracy of the A_{LL} and A_N measurement as a function of x_F is shown in Fig. 9.22 (b). The statistical part is shown in red, while the total error that also includes the systematics related to the background subtraction ($dk/k = 1\%$) is shown in blue. The error does not include the uncertainties related to luminosity and beam polarization measurement.

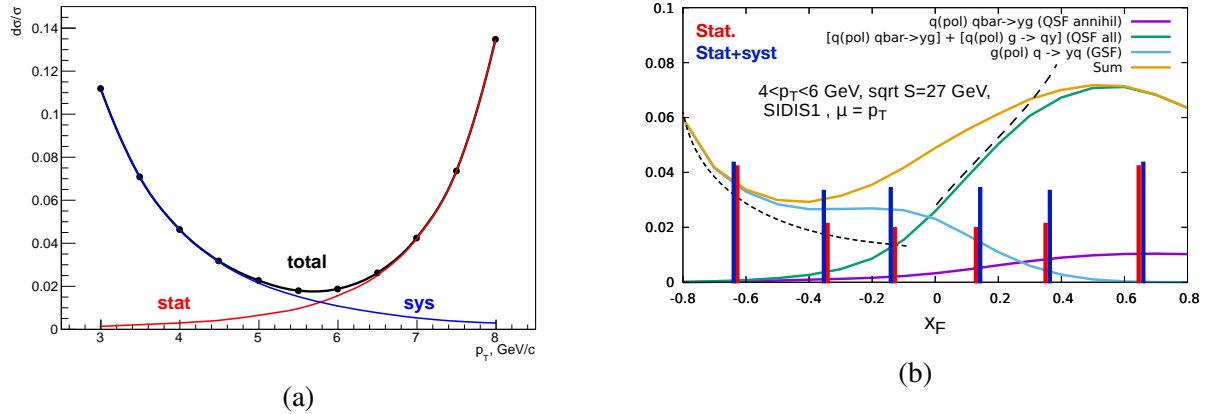


Figure 9.22: (a) Expected uncertainty of the unpolarized cross-section $Ed^3\sigma/dp^3$ measurement as a function of p_T . (b) Expected accuracy of the A_N measurement for the prompt photons with $p_T > 4$ GeV/c at $\sqrt{s} = 27$ GeV as a function of x_F . The theoretical predictions are also shown.

The systematic uncertainty related to the background subtraction could be partially reduced by the simultaneous study of the asymmetries in the production of prompt photons, π^0 , and η -mesons like it was demonstrated in the recently published analysis [153].

2.3 Open charm production

In spite of the relatively large cross-section of the open charm production, most of the D -meson decays cannot be reconstructed easily. The "golden" decay channels are: $D^0 \rightarrow K^-\pi^+$ and $D^+ \rightarrow K^-\pi^+\pi^+$ (BF=3.95% and 9.38%, respectively). The momentum distributions for D^\pm and D^0/\bar{D}^0 produced in p - p collisions at $\sqrt{s} = 27$ GeV are shown in Fig. 9.23(a). The difference between the red and blue curves reflects the fact that the probability for the c -quark to hadronize into the neutral D -meson is 2 times higher than into the charged one. Since the decay length $c\tau$ is 311.8 and 122.9 μm , respectively, which is larger than the spatial resolution of the vertex reconstruction, the VD allowing one to reconstruct the secondary vertex of the D -meson decay is the key detector for the open charm physics at SPD. The distribution for the spatial distance between the primary (production) and secondary (decay) vertices for $D^{\pm/0}$ mesons is presented in Fig. 9.23(b).

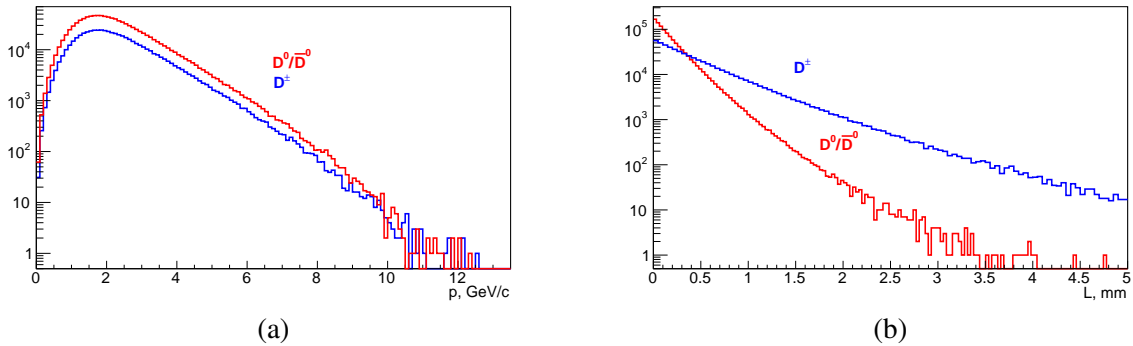


Figure 9.23: (a) Momentum distributions for D^\pm and D^0/\bar{D}^0 produced in p - p collisions at $\sqrt{s} = 27$ GeV. (b) Spatial distance between the production and the decay vertices for D -mesons.

We demonstrate the ability of the SPD setup to deal with the open-charm physics using the D^0/\bar{D}^0 signal. The following quantities can be used as selection criteria in order to suppress the combinatorial πK background together with the kaon identification by the PID system:

- the quality of the secondary vertex reconstruction (χ^2);
- the distance between the primary and secondary vertices (spatial or in projections) normalized to the corresponding uncertainty;
- the angle between the reconstructed momentum of the πK pair and the line segment connecting the primary and secondary vertices;

The kinematics of the πK pair (the angular and momentum distributions) could also be used for discrimination.

Figure 9.24 (a) presents the $K^- \pi^+$ invariant mass spectrum obtained as the result of such a selection for the D^0 -signal in the kinematic range $|x_F| > 0.2$ as an example for both variants of the VD after one year of data taking. About 96% of the $D^0 \rightarrow K^- \pi^+$ events were lost, while the combinatorial background under the D -meson peak was suppressed by 3 orders of magnitude. The signal-to-background ratio for D^0 is about 1.3% for the DSSD configuration and about 3.9% for the DSSD+MAPS one. Improving the signal-to-background ratio is the subject of further optimization of the selection criteria, as well as the reconstruction algorithms. The corresponding statistical accuracy of the SSA A_N measurement is illustrated by Fig. 9.24 (b), where both signals, D^0 and \bar{D}^0 , are merged. Similar or even better results (due to a larger $c\tau$ value) could be expected for the charged channel $D^\pm \rightarrow K^\mp \pi^\pm \pi^\pm$.

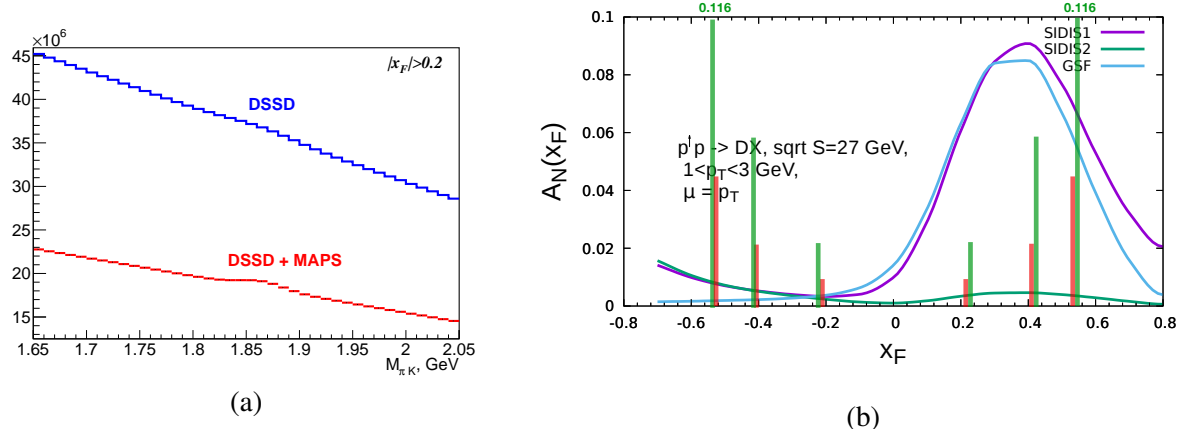


Figure 9.24: (a) $K^- \pi^+$ invariant mass spectrum after 1 year of data taking ($\sqrt{s} = 27$ GeV, $|x_F| > 0.2$). (b) Corresponding statistical accuracy of the A_N measurement for the $D^0 + \bar{D}^0$ mesons. The expected Sivers contribution to the SSA is also shown.

Another way to improve the signal-to-background ratio is tagging the D -mesons by their origin from the decay of a higher state $D^* \rightarrow D\pi$. The complexity of this approach lies in the need for detection of the soft pion ($p_\pi \sim 0.1$ GeV/c).

One more possibility to reduce the background is the tagging a leptonic decay of the second D -meson in the event via reconstruction of the corresponding muon in the RS. The corresponding branching fractions ($\mu + \text{anything}$) are $6.8 \pm 0.6\%$ and $17.6 \pm 3.2\%$ for D^0 and D^\pm , respectively.

Chapter 10

Integration and services

According NICA TDR [506] the SPD area is allocated in the southern point of beam collisions. The NICA complex with the SPD location is shown in Figure 10.1.



Figure 10.1: Schematic layout of the NICA facility with SPD.

The design of the SPD experimental hall is very similar to that of the MPD [507].

1 Experimental building of SPD

The top and side views of the SPD building are shown in Figures 10.2, 10.3, respectively. The building is divided into production and experimental sites with total area of about 2000 m^2 . Since the production site has a gate, it will be used to unload materials. The main gate for trucks is $4\text{m} \times 4\text{m}$, while the dismantling part of wall for wider equipment is $8\text{m} \times 8\text{m}$. The production site will also be used for preparation, test and maintenance of the detector subsystems. The floor of production site coincides with the ground level.

The experimental site is shown in the right side of the Figures 10.2, 10.3, below the level of the production site by 3.2 m. It is constructed in such a way in order to match the levels of the beam-line and the symmetry

axis of the detector. Two main rails are installed along the site to provide transportation of the SPD detector from the assembly to the operating (or beam) position. There are additional rails in the detector assembly area, transverse to the main one. They have a maximum load capacity of 130 ton and will be used to insert inner subdetectors using rail-guided support. All rails are electrically connected to the metal reinforcement of the building which, in turn, is connected to numerous rod-electrodes deepened down to the earth's surface by 3 m below the building for grounding.

The concrete solid floor of the hall has sufficient load-bearing capacity to allow the assembly and operation of the SPD detector, including auxiliary structures. It will be quite enough:

1. to withstand the weight of the fully assembled detector with all necessary services;
2. to preserve the integrity of the detector during its transportation on the rail-guided lodgement between the assembly and beam positions;
3. to provide a stable position of the detector with high accuracy during operating cycles.

An overhead traveling crane with a maximum lifting capacity of 80 tons will be installed in the hall of the building. The crane will be equipped with linear and H-shaped traverses with lifting capacity from few to 75 tons. The crane service area covers both the production and experimental sites.

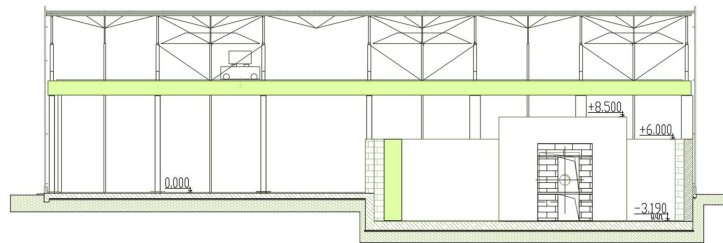


Figure 10.2: Side view to the SPD building.

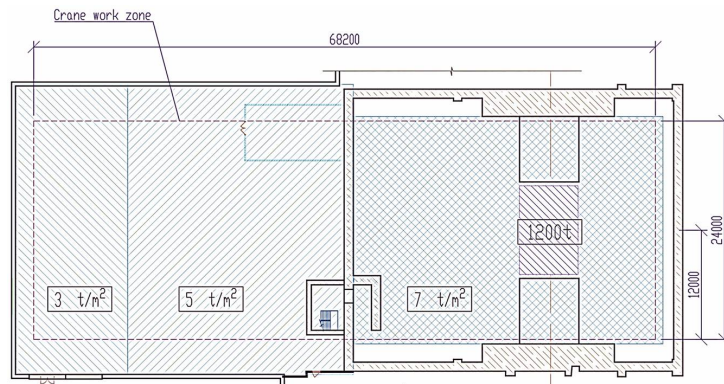


Figure 10.3: The view from the top of the SPD building.

2 Auxiliary equipment and services

Helium refrigerators have to be close to the detector to provide cryogenic fluids and gases for the magnet operation (see chapter 3.2). Presumably, they will be installed on a platform that will be located on top of the detector, as shown in Figure 10.4. Crates with electronics for the data acquisition systems and

power supplies of the detector subsystems should also be placed in the vicinity of the detector. They will be located on a special platform next to the detector. The platform will be attached to the detector, thus moving along the same rails as the detector itself. Bottles with Ar and CO₂ for supplying the RS and ST detectors, the corresponding gas recirculation compressors and monitoring systems, will be located on a similar platform from the opposite side of the detector (not shown in Figure 10.4). A dedicated radiation shielding can be installed between the detector and the platforms in order to provide access to the racks with the detector electronics and the gas system during data taking.

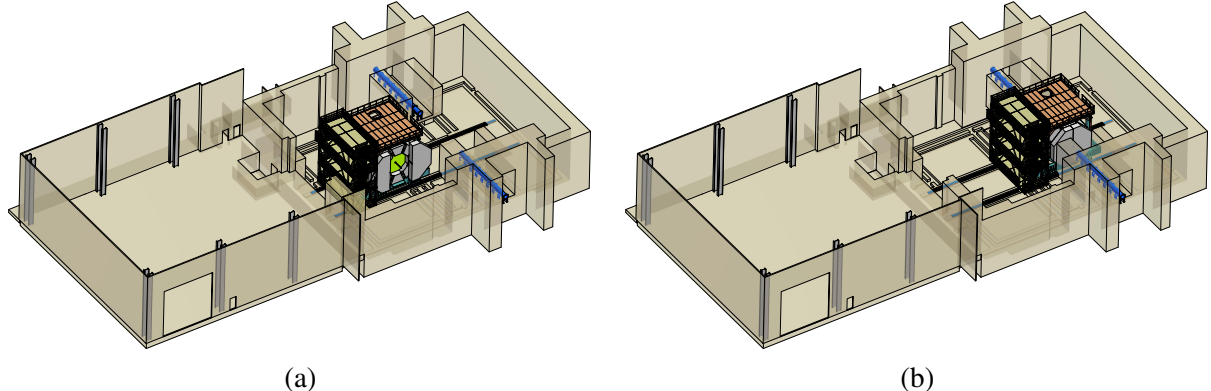


Figure 10.4: The 3D view of the SPD building. The detector assembly position (a) and the beam position of the detector (b) are shown. The beam line is highlighted in blue.

The total weight of the SPD detector is close to the maximum permissible limit of 1200 ton. The weight of each detector subsystem is presented in Table 10.1. The power consumption of subdetectors is currently under study. It is assumed that the maximum power supply capacity of the SPD hall should not exceed 1.2 MW.

Table 10.1: Technical requirements of the SPD detector subsystems (to be completed).

Subsystem	Weight, t	Power, kW	Special requirements
VD	< 0.1	1÷1.5	water cooling
ST	0.1	2÷4	Ar+CO ₂
ECAL	58	63	
RS	800	31	Ar+CO ₂
TOF (sci)	0.4	4	
BBC	0.1	12	
Magnet	50	< 100	cryogenics
Supporting structure	200	÷	
DAQ		46	
Total	~1110	~ 200	

Chapter 11

Beam test facilities

Two dedicated beam test facilities are planned to be operated for the benefit of the SPD project. The first one using secondary beams from the Nuclotron is foreseen to be constructed in building 205 (LHEP). It will be used for testing and certification of detector elements, electronics, data acquisition and slow-control systems under conditions close to those anticipated at NICA. Some elements can be studied using the SPD straight section of NICA before the Spin Physics Detector construction at the early phase of the collider running. The beam test facilities will be also used for training young specialists for the SPD project.

1 Test zone with extracted Nuclotron beams

Two specialized channels for secondary particles (electrons, muons, pions, kaons, protons, neutrons, light nuclei) will be organized: the Low Momentum Channel (LMC) and the High Momentum Channel (HMC) in the region of focus F4 of extracted Nuclotron beams. The LMC is designated for secondary beams with a momentum range from $100 \text{ MeV}/c$ to $2 \text{ GeV}/c$, while the momentum range of secondary particles at the HMC is from $1 \text{ GeV}/c$ to $10 \text{ GeV}/c$. After upgrading, the existing channel of the MARUSYA installation [508–511] will be used in the LMC construction. It is advantageous that there exists positive experience in working with extracted polarized beams at MARUSYA [512]. This would ensure physical measurements at the extracted beams using the existing experimental installation and infrastructure. The installation MARUSYA is well-suitable for the applied studies with secondary beams at the maximum possible intensity of the primary beam extracted to building 205 up to 10^{11} protons per acceleration cycle. The development of the HMC requires two new magnetic elements; therefore, it is considered as an independent installation to be put in operation at the second stage of upgrade in accordance with the existing regulations for the commissioning of experimental facilities. The layout of the main elements of the SPD test zone is shown in Fig. 11.1.

It is planned to use the SP12 magnet of the VP1 extraction channel situated directly in front of the F4 focus in order to turn the primary extracted beam toward the HMC. The calculations show that the primary beam can be turned to the required angle in a proton momentum range of $1\text{--}7 \text{ GeV}/c$. For higher-energy particles, it is necessary to use a target in the F4 focus. In this operation mode, secondary beams are formed at the LMC and HMC simultaneously. Note that this operation mode is possible with parallel operation of the other installations at the VP1 extraction channel, in particular, the BM&N setup. For the primary $5 \text{ GeV}/\text{nucleon}$ deuteron beam extracted to carbon targets with a thickness from 0.005 to $5 \text{ g}/\text{cm}^2$, the typical intensities for different species available at the LMC and HMC are shown in Tab. 11.1. There is also a possibility of forming a secondary quasi-monochromatic neutron beam via interaction of a deuteron beam in a target and deflecting out the charged component.

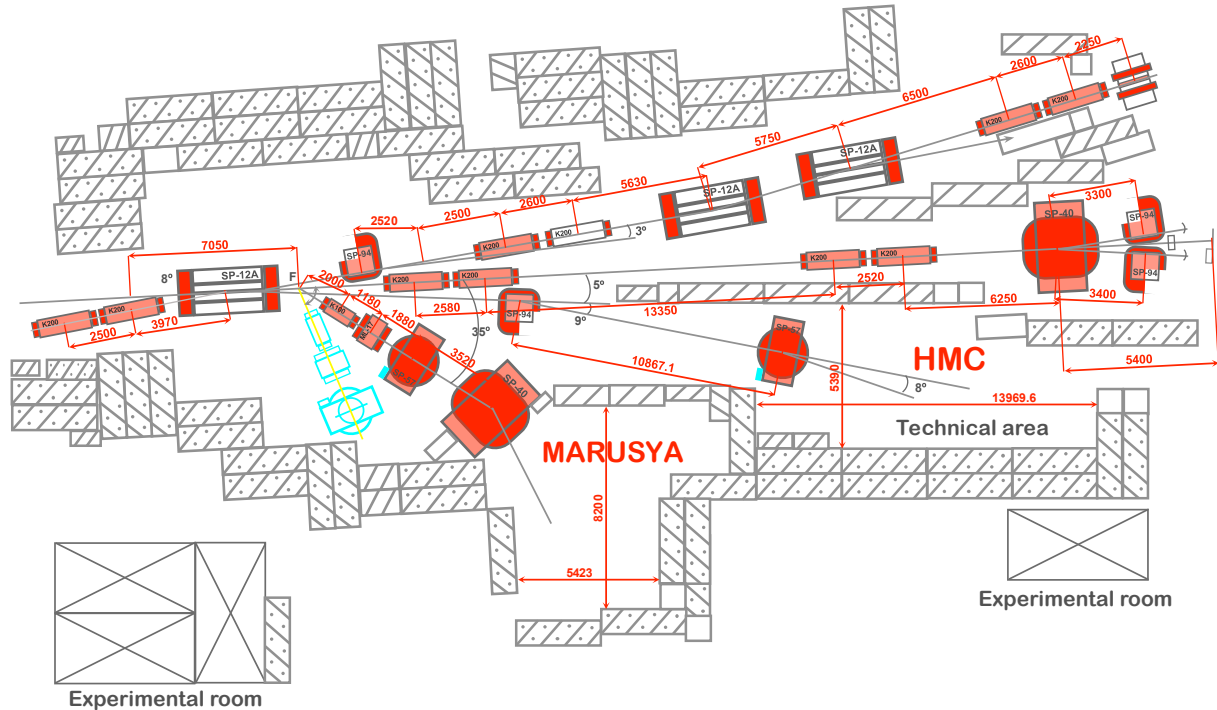


Figure 11.1: Layout of the main elements of the SPD test zone. All dimensions are in millimeters.

Table 11.1: Beam intensities feasible at the channel of the LMC and the HMC.

Channel	p, MeV/c	d	p,n	π^\pm	K^+	K^-	μ^\pm	e^\pm
LMC	400	10^3	10^5	10^5	10^3	10^2	10^3	10^3
LMC	800	10^3	10^4	10^4	10^3	10^2	10^3	10^3
LMC	1500	10^2	10^4	10^4	10^3	10^2	10^2	10^2
HMC	2000	10^4	10^5	10^4	10^3	10^2	10^2	10^2
HMC	7000	10^4	10^6	10^3	10^3	10^2	10^2	10^2

Each channel-spectrometer provides spatial registration, identification, and tagging of each particle hitting the detector, provided the electronic registration system of the installation matches the tested detector or the data acquisition system element. A prototype time-of-flight system based on scintillation hodoscopes demonstrated reliable identification of protons, pions, kaons in a momentum range of $600 \div 1200$ MeV/c for the LMC. TOF scintillation hodoscopes providing a momentum resolution of 0.5% and a time resolution at a level of 100 ps are capable of online detection and identification of secondary pions, kaons, and protons at the HMC. In order to extend the testing capabilities of the SPD test zone, it will be equipped with new coordinate detectors, a Cherenkov counter, and a BGO-based electromagnetic calorimeter.

2 Tests at the SPD straight section of the collider

We also suppose, that the beam test experiments and preparation for getting a luminosity of 10^{32} cm $^{-2}$ s $^{-1}$ at $\sqrt{s} = 27$ GeV, including the proton polarization control will be demonstrated by the SPD commissioning. For that reason we propose to install of the diagnostic and control equipment at the SPD straight section (see Fig. 11.2).

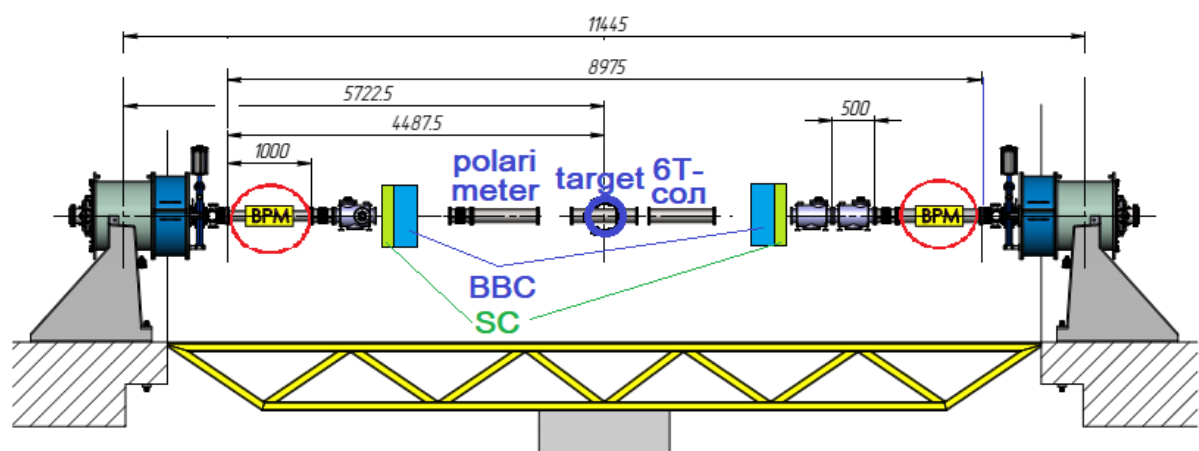


Figure 11.2: The SPD straight section equipped with the diagnostic and control units. All dimensions are in millimeters.

Chapter 12

Running strategy

1 Accelerator

We consider the strategy of the SPD operation as chain of successive experimental works with polarized proton and deuteron beams aimed at the obtaining of the ultimate polarized proton beam parameters at the collider and the use of the unique existing polarized deuteron beam for physics experiments from the early beginning of the collider commissioning. Polarized deuterons were first accelerated at the old LHEP proton accelerator Synchrophasotron in 1986 and much later at the new superconducting synchrotron – Nuclotron in 2002 (see Fig. 12.1).

Polarized protons were first obtained in 2017. The first test was performed after the analysis of proton spin resonances in 2018. The first dangerous proton spin resonance in Nuclotron corresponds to the beam momentum of about 3.5 GeV/c, whereas in the deuteron case the spin resonance will occur at the particle kinetic energy of 5.6 GeV/nucleon. This limit is practically equal to the maximum achievable energy corresponding to the magnetic rigidity of the Nuclotron dipoles.



Figure 12.1: View of the Nuclotron ring.

The existing polarized proton and deuteron ion source SPI provides up to a 3-mA pulse current over $t \approx 100 \mu\text{s}$. Thus, up to 1.5×10^{11} particles can be injected in the Nuclotron during the injection time (8 μs). The spin modes (pz, pzz): (0,0), (0,−2), (2/3,0), and (−1/3,+1) were adjusted. The polarization

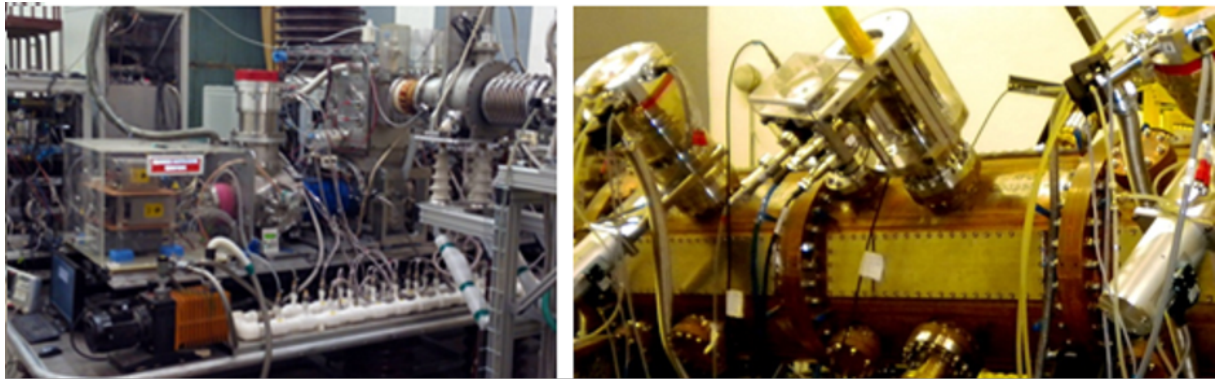


Figure 12.2: View of the SPI (left) and the existing RFQ (right).

degree of 80 % was achieved.

The existing pre-accelerator of RFQ-type gives the limit on the achievable proton energy in the next element of the injector chain - linac LU-20. We can obtain only 5 MeV at its output instead of 20 MeV that we have had in the past years. The new proton and light ion linac “LILAc” is now being manufactured [513]. The LILAc output energy will be 12 MeV. Its commissioning is scheduled for 2025–2026. The photos of the SPI and the existing RFQ are presented in Fig. 12.2.

The following tasks for the period of 2021–2025 are reasonable and necessary to start the SPD operation at the ultimate beam parameters:

- continuation of operation and further improvement of the polarized ion source SPI, waiting beam time at the Nuclotron – 2021–2022;
- upgrade of the polarimeters: linak output; coasting beam; extracted beam; new polarimeter for a proton energy of above 6 GeV – 2020–2023;
- manufacturing of the 6T SC-solenoid model for the SPD test bench – 2021–2022;
- design and manufacturing of the equipment for the SPD test bench at the collider – 2020–2023;
- LILAc manufacturing and tests – 2020–2025;
- analysis of the ${}^3\text{He}$ (2+) polarized ion source based on the SPI upgrade.

2 Spin Physics Detector

The physics program proposed in Chapter 2 covers at least 5 years of the SPD running. A tentative running plan is shown in Tab. 12.1.

Table 12.1: Tentative running plan for the Spin Physics Detector.

Physics goal	Required time	Experimental conditions
First stage		
Spin effects in p - p scattering dibaryon resonances	0.3 year	$p_{L,T}$ - $p_{L,T}$, $\sqrt{s} < 7.5$ GeV
Spin effects in p - d scattering, non-nucleonic structure of deuteron, \bar{p} yield	0.3 year	d_{tensor} - p , $\sqrt{s} < 7.5$ GeV
Spin effects in d - d scattering hypernuclei	0.3 year	d_{tensor} - d_{tensor} , $\sqrt{s} < 7.5$ GeV
Hyperon polarization, SRC, ... multiquarks	together with MPD	ions up to Ca
Second stage		
Gluon TMDs, SSA for light hadrons	1 year	p_T - p_T , $\sqrt{s} = 27$ GeV
TMD-factorization test, SSA, charm production near threshold, onset of deconfinement, \bar{p} yield	1 year	p_T - p_T , $7 \text{ GeV} < \sqrt{s} < 27 \text{ GeV}$ (scan)
Gluon helicity, ...	1 year	p_L - p_L , $\sqrt{s} = 27$ GeV
Gluon transversity, non-nucleonic structure of deuteron, "Tensor polarized" PDFs	1 year	d_{tensor} - d_{tensor} , $\sqrt{s_{NN}} = 13.5$ GeV or/and d_{tensor} - p_T , $\sqrt{s_{NN}} = 19$ GeV

Chapter 13

Cost estimate

The estimated cost of the Spin Physics Detector at current prices is 94.9 M\$. Taking into account the general uncertainty of the project timescale and that at the moment the SPD project is in the early stages of implementation, this value should be treated as a very preliminary estimation. This value does not include the construction of the SPD Test zone and possible R&D expanses. Any expanses related with development and construction of an infrastructure for polarized beams at NICA are also out of this estimation. The detailed contribution to the total cost is presented in Tab. 13.1.

Table 13.1: Preliminary cost estimate of the SPD setup.

	Subsystem	Option	Cost, M\$
SPD setup	Vertex detector: – DSSD – DSSD+MAPS	VD1 VD2	9.5+6.5 (FE) 9.5+7.0 (FE)
	Straw tracker		2.4
	PID system: – RPC-based TOF – Scintillator-based TOF – Aerogel PID system	PID1 PID2 PID3	5 4 5
	Electromagnetic calorimeter		21.1
	Range system		14.2
	ZDC		2
	BBC		0.4
	Magnetic system		10
	Beam pipe		2
General infrastructure			5
Slow control system			0.8
Data acquisition system			2.6
Computing			10
TOTAL COST	VD2+PID2+PID3		96.0

Chapter 14

Participating institutions and author list

National Science Laboratory, Armenia
Akopov N., Movsisyan A.

Institute of Applied Physics of the National Academy of Sciences of Belarus, Minsk, Belarus
Shulyakovskiy R.

Research Institute for Nuclear Problems of Belarusian State University, Minsk, Belarus
Korjik M.V., Lobko A.S., Makarenko V.V., Solin A.A., Solin A.V.

Universidad Andrés Bello, Santiago, Chile
Kuleshov S., Zamora J.

China Institute of Atomic Energy, Beijing, China
Chen Lei, Jia Shi-Hai, Li Pei-Yu, Li Xiao-Mei, Song Jin-Xin, Sun Hao, Sun Peng-Fei, Zhang Yun-Yu,
Zhang Jun-Wei, Zhao Ming-Rui, Zhi Yu

**Higher Institute of Technologies and Applied Sciences (InSTEC), Havana University,
Havana, Cuba**
Guzman F., Garsía Trapaga C.E.

Charles University, Prague, Czech Republic
Finger M., Finger M. (jr.), Prochazka I., Slunecka M., Sluneckova V.

Czech Technical University in Prague, Czech Republic
Havranek M., Jary V., Lednický D., Marcisovsky M., Neue G., Popule J., Tomasek L., Virius M.,
Vrba V.

University of Turin and INFN Section, Turin, Italy
Alexeev M., Amoroso A., Chiosso M., Denisov O.Yu., Kotzinian A., Maggiora A., Panzieri D.,
Parsamyan B., Tosello F.

Warsaw University of Technology, Warsaw, Poland

Buchowicz A., Dygnarowicz K., Galiński G., Klekotko A., Kurjata R., Marzec J., Pastuszak G., Rychter A., Zaremba K., Ziembicki M.

**Joint Institute for Nuclear Research, JINR, Dubna, Russia
Laboratory of High-Energy Physics**

Akhunzyanov R.R., Alexakhin V.Yu., Anosov V.A., Azorskiy N.I., Baldin A.A., Baldina E.G., Barabanov M.Yu., Beloborodov A.N., Belyaev A. V., Bleko V.V., Bogoslovsky D.N., Boguslavsky I.N., Burtsev V.E., Dunin V.B., Enik T.L., Filatov Yu.N.¹, Gavriishchuk O.P., Galoyan A.S., Glonti L., Golubykh S.M., Grafov N.O., Gribovsky A.S., Gromov S.A., Gromov V.A., Gurchin Yu.V., Gusakov Yu.V., Ivanov A.V., Ivanov N.Ya., Isupov A.Yu., Kasianova E.A., Kekelidze G.D., Khabarov S.V., Kharusov P.R., Khrenov A.N., Kokoulina E.S., Kopylov Yu.A., Korovkin P.S., Korzenev A. Yu., Kostukov E.V., Kovalenko A.D., Kozhin M.A., Kramarenko V.A., Kruglov V.N., Ladygin E.A., Ladygin V.P., Lednický R., Livanov A.N., Lysan V.M., Makankin A.M., Martovitsky E.V., Meshcheriakov G.V., Moshkovsky I.V., Nagorniy S.N., Nikiforov D.N. Nikitin V.A., Parzhitsky S.S., Pavlov V.V., Perepelkin E.E., Peshekhonov D.V., Popov V.V., Reznikov S.G., Rogachevsky O.V., Safonov A.B., Salamatin K.M., Savenkov A.A., Sheremeteva A.I., Shimanskii S.S., Starikova S.Yu., Streletskaia E.A., Tarasov O.G., Terekhin A.A., Teryaev O.V., Tishevsky A.V., Topilin N.D., Topko B.L., Troyan. Yu.A., Usenko E.A., Vasilieva E.V., Volkov I.S., Volkov P.V., Yudin I.P., Zamyatin N.I., Zemlyanichkina E.V., Zhukov I.A., Zinin A.V., Zubarev E.V.

Laboratory of Nuclear Problems

Abazov V.M., Afanasyev L.G., Alexeev G.D., Balandina V.V., Belova A.P., Bobkov A.V., Boltushkin E.V., Brazhnikov E.V., Datta A., Denisenko I.I., Duginov V.N., Frolov V.N., Golovanov G.A., Gridin A.O., Gritsay K. I., Guskov A.V., Kirichkov N.V., Komarov V.I., Kulikov A.V., Kurbatov V.S., Kutuzov S.A., Maltsev A., Mitrofanov E.O., Nefedov Yu.A., Pavlova A.A., Piskun A.A., Prokhorov I.K., Rezvaya E.P., Romanov V.M., Rudenko A.I., Rumyantsev M.A., Rybakov N.A., Rymbekova A., Samartsev A.G., Shaikovsky V.N., Shtejer K., Sinitsa A.A., Skachkov N.B., Skachkova A.N., Tereschenko V.V., Tkachenko A.V., Tokmenin V.V., Trunov N.O., Uzikov Yu.N., Verkheev A.Yu., Vertogradov L.S., Vertogradova Yu.L., Vesenkov V.A., Zhemchugov A.S., Zhuravlev N.I.

Laboratory of Theoretical Physics

Anikin I.V., Arbuzov A.B., Efremov A.V., Goloskokov S.V., Klopot Ya., Strusik-Kotlozh D., Volchansky N.I.

Laboratory of Information Technologies

Goncharov P.V., Oleynik D.A., Ososkov G.A., Petrosyan A.Sh., Podgainy D.V., Pelevanyuk I.S., Polyakova R.V., Uzhinsky V.V., Zuev M.I.

St. Petersburg Nuclear Physics Institute, Gatchina, Russia

Barsov S.G., Fedin O.L., Kim V.T., Kuznetsova E.V., Maleev V.P., Shavrin A.A., Zelenov A.V.

Lebedev Physical Institute of the Russian Academy of Sciences, Moscow, Russia

Andreev V.F., Baskov V.A., Dalkarov O.D., Demikhov E.I., Gerasimov S.G., L'vov A.I., Negodaev M.A., Nechaeva P.Yu., Polyansky V.V., Suchkov S.I., Terkulov A.R., Topchiev N.P.

Skobeltsin Institute of Nuclear Physics of the Moscow State University, Moscow, Russia

Aleshko A.M., Belov I.N., Berezhnoy A.V., Boos E.E., Bunichev V.E., Chepurnov A.S., Gribkov D.Y., Merkin M.M., Nikolaev A.S.

¹also Moscow Institute of Physics and Technology, Dolgoprudny, Russia

Institute for Theoretical and Experimental Physics, Moscow, Russia

Akindinov A.V., Alekseev I.G., Golubev A.A., Kirin D.Yu., Luschevskaya E., Malkevich D.B., Morozov B., Plotnikov V.V., Polozov P., Rusinov V., Stavinskiy A.V., Sultanov R.I., Svirida D.N., Tarkovskyi E.I., Zhigareva N.M.

Institute for High-Energy Physics, Protvino, Russia

Vorobiev A.

Samara National Research University, Samara, Russia

Karpishkov A.V., Nefedov M.A., Saleev V.A., Shipilova A.V.

St. Petersburg Polytechnic University, St. Petersburg, Russia

Berdnikov A.Ya., Berdnikov Ya.A., Borisov V.S., Larionova D.M., Mitrankov Yu.M., Mitrankova M.M.

St. Petersburg State University, St. Petersburg, Russia

Feofilov G.A., Kovalenko V.N., Valiev F.F., Vechernin V.V., Zhrebchevsky V.Yo.

Tomsk State University, Tomsk, Russia

Chumakov A., Lyubovitskij V., Trifonov A., Zhevlakov A.

Belgorod State University, Belgorod, Russia

Kaplui A., Kishchin I., Kluev A., Kubankin A., Kubankin Yu.

University of Belgrade, Institute of Physics Belgrade, Belgrade, Serbia

Jokovic D., Maletic D., Savic M.

V.N. Karazin Kharkiv National University, Kharkiv, Ukraine

Kovtun V.E., Lyashchenko V.N., Malykhina T.V., Reva S.N., Sotnikov V.V.

Institute for Scintillation Materials National Academy of Sciences of Ukraine (Kharkiv, Ukraine)

Boyarintsev A.Yu., Eliseev D.A., Grinyov B.V., Zhmurin P.N.

Individual contributors:

Abramov V. (IHEP, Russia), El-Kholy R. (Cairo University), Haidenbauer J. (IAS and IKP, Forschungszentrum Jülich), Kondratenko A.M. (STL "Zaryad", Novosibirsk, Russia and Moscow Institute of Physics and Technology, Dolgoprudny, Russia), Kondratenko M.A. (STL "Zaryad", Novosibirsk, Russia and Moscow Institute of Physics and Technology, Dolgoprudny, Russia), Konorov I. (Technical University of Munich), Richard J.-M. (Université de Lyon), Semak A.A. (Institute of High Energy Physics, Protvino, Russia) Strikman M. (Penn State University), Temerbayev A. (L.N. Gumilyov Eurasian National University, Nur-Sultan), Tomasi-Gustafsson E. (DPhN, IRFU, CEA, Université Paris-Saclay), Tsenov R. (University of Sofia), Wang Q. (South China Normal University, Guangzhou), Zhao Q. (Institute of High Energy Physics, CAS, Beijing)

We are also grateful to Kukhtin V. V., Nagaytsev A.P., Savin I.A., Shevchenko O. Yu., and Sisakyan A.N. for their invaluable contribution to the SPD project at earlier stages of its implementation.

Acknowledgements.

This work is supported by the RFBR research projects No. 18-02-40097 and 18-02-40061.

Chapter 15

Conclusion

The proposed physics program and the concept of the SPD facility presented in the document, are open for exciting and challenging ideas from theorists and experimentalists worldwide. The Conceptual Design Report of the Spin Physics Detector was presented and discussed at the 54th meeting of the JINR Program Advisory Committee for Particle Physics on January 18, 2021. The following recommendations were obtained: *The PAC thanks the SPD (proto-)collaboration for the preparation of the comprehensive CDR and recommends the NICA management to appoint an appropriate Detector Advisory Committee for a thorough review of the CDR and its subsequent evolution into an SPD TDR (Technical Design Report). The PAC encourages the team to pursue every effort to form an international collaboration, find adequate resources and attract students and young scientists.*

The international Detector Advisory Committee (SPD DAC) was formed in April 2021. The Committee is chaired by A. Bressan (University of Trieste, Italy) and includes P. Di Nezza (National Institute for Nuclear Physics, Frascati, Italy) and a member of the PAC P. Hristov (CERN, Switzerland). The report was presented by A. Bressan on behalf of the SPD DAC at the 56th meeting of the JINR Program Advisory Committee for Particle Physics on January 24, 2022. As an outcome of the report, the PAC issued the following recommendations:

The PAC notes with interest the evaluation report presented by A. Bressan on behalf of the SPD DAC. The Committee held several meetings with the SPD team and asked several questions concerning the SPD detector concept. In addition to that, issues related to the NICA complex infrastructure for polarized beams and possible interactions between the SPD and MPD experiments were discussed in depth. The answers to the DAC's questions were satisfactory and the presentations during the joint meetings were well received by the committee. The DAC particularly appreciated the improvements in the SPD conceptual design with respect to the original CDR, namely changing the magnet location to be outside the ECAL, the possible use of a full MAPS inner tracker, and the clarifications on the straw detectors and the ZDC. On the basis of all that, and following the recommendation of the DAC, the PAC approves the SPD CDR and asks the SPD team to move forward to the TDR preparation. The PAC appreciates the important role of the DAC in the SPD project evaluation and requests periodic DAC reports.

Chapter 16

List of abbreviations

ADC – Analogue-to Digital Converter
ASIC – Application-Specific Integrated Circuit
BBC – Beam-Beam Counter
BF – Branching Fraction
BPM – Beam Position Monitor
CCR – Constituent Counting Rules
CEM – Color Evaporation Model
CM – Center-of-Mass
CPM – Collinear Parton Model
CPQ – Chromomagnetic Quark Polarization
CR – Cosmic Rays
CT – Color Transparency
DAC – Digital-to-Analogue Converter
DAQ – Data AcQuisition
DIS – Deep Inelastic Scattering
DS(-mode) – Distinct Spin mode
DSSD – Double-Sided Silicon Detector
DY (process) – Drell-Yan process
ECal – Electromagnetic Calorimeter
ExEP – Extended Equivalence Principle
FBBC (monitor) – Fast Beam-Beam Collisions (monitor)
FEE – Front-End Electronics
FF – Fragmentation Function
GF – Gluon Fusion
GPD – Generalized Parton Distributions
GPM – Generalized Parton Model
GSF – Gluon Sivers Function
GTMD (PDF) – Generalized Transverse Momentum Dependent (PDF)
HMC – High Momentum Channel
ICEM – Improved Color Evaporation Model
IP – Interaction Point
ISM – InterStellar Medium
LDME – Long-Distance Matrix Element
LMC – Low Momentum Channel

MAPS – Monolithic Active Pixel Sensor
MCP – MicroCannel Plate
MDT – Mini Drift Tubes
ML – Machine Learning
MIP – Minimum Ionizing Particle
MPD – MultiPurpose Detector
MPPC - MultiPixel Photon Counter
MRPC - Multigap Resistive Plate Chamber
MS – Magnetic System
NICA – Nuclotron-based Ion Collider fAcility
NPE – Number of PhotoElectrons
NPQCD – Non-Perturbative QCD
NRQCD – Non-Relativistic QCD
PDF – Parton Distribution Function
PGF – Photon-Gluon Fusion
PID – Particle IDentification
pQCD – perturbative QCD
PRA – Parton Reggeization Approach
QGP – Quark Gluon Plasma
QSF – Quark Sivers Function
RMS – Root Mean Square
RS – Range System
SF – Spin Flipping
SIDIS – Semi-Inclusive Deep-Inelastic Scattering
SiPM – Silicon PhotoMultiplier
SN – Spin Navigator (solenoid)
SPD – Spin Physics Detector
SRC – Short Range Correlations
ST(-mode) – Spin Transparency (mode)
SSA – Single Spin Asymmetry
ST – Straw Tracker
STSA – Single Transverse Spin Asymmetries
TMD (PDF) – Transverse Momentum Dependent (PDF)
TMDShF – TMD Shape Function
TOF (system) – Time-Of-Flight (system)
VD – Vertex Detector
WLS - WaveLength Shifter
ZDC – Zero Degree Calorimeter

Bibliography

- [1] SPD web site <http://spd.jinr.ru>.
- [2] Aram Kotzinian. New quark distributions and semiinclusive electroproduction on the polarized nucleons. *Nucl. Phys. B*, 441:234–248, 1995, hep-ph/9412283.
- [3] P. J. Mulders and R. D. Tangerman. The Complete tree level result up to order $1/Q$ for polarized deep inelastic lepton production. *Nucl. Phys.*, B461:197–237, 1996, hep-ph/9510301. [Erratum: *Nucl. Phys.*B484,538(1997)].
- [4] Daniel Boer and P.J. Mulders. Time reversal odd distribution functions in lepton production. *Phys. Rev. D*, 57:5780–5786, 1998, hep-ph/9711485.
- [5] K. Goeke, A. Metz, and M. Schlegel. Parameterization of the quark-quark correlator of a spin-1/2 hadron. *Phys. Lett. B*, 618:90–96, 2005, hep-ph/0504130.
- [6] Alessandro Bacchetta, Markus Diehl, Klaus Goeke, Andreas Metz, Piet J. Mulders, and Marc Schlegel. Semi-inclusive deep inelastic scattering at small transverse momentum. *JHEP*, 02:093, 2007, hep-ph/0611265.
- [7] R. Angeles-Martinez et al. Transverse Momentum Dependent (TMD) parton distribution functions: status and prospects. *Acta Phys. Polon. B*, 46(12):2501–2534, 2015, 1507.05267.
- [8] S. Bastami et al. Semi-Inclusive Deep Inelastic Scattering in Wandzura-Wilczek-type approximation. *JHEP*, 06:007, 2019, 1807.10606.
- [9] S. Arnold, A. Metz, and M. Schlegel. Dilepton production from polarized hadron hadron collisions. *Phys. Rev.*, D79:034005, 2009, 0809.2262.
- [10] S. Bastami, L. Gamberg, B. Parsamyan, B. Pasquini, A. Prokudin, and P. Schweitzer. The Drell-Yan process with pions and polarized nucleons. 5 2020, 2005.14322.
- [11] Andreas Metz and Anselm Vossen. Parton Fragmentation Functions. *Prog. Part. Nucl. Phys.*, 91:136–202, 2016, 1607.02521.
- [12] Mauro Anselmino, Asmita Mukherjee, and Anselm Vossen. Transverse spin effects in hard semi-inclusive collisions. 1 2020, 2001.05415.
- [13] Harut Avakian, Bakur Parsamyan, and Alexey Prokudin. Spin orbit correlations and the structure of the nucleon. *Riv. Nuovo Cim.*, 42(1):1–48, 2019, 1909.13664.
- [14] Matthias Grosse Perdekamp and Feng Yuan. Transverse Spin Structure of the Nucleon. *Ann. Rev. Nucl. Part. Sci.*, 65:429–456, 2015, 1510.06783.

- [15] Mariaelena Boglione and Alexei Prokudin. Phenomenology of transverse spin: past, present and future. *Eur. Phys. J. A*, 52(6):154, 2016, 1511.06924.
- [16] Christine A. Aidala, Steven D. Bass, Delia Hasch, and Gerhard K. Mallot. The Spin Structure of the Nucleon. *Rev. Mod. Phys.*, 85:655–691, 2013, 1209.2803.
- [17] A. Adare et al. Measurement of transverse-single-spin asymmetries for midrapidity and forward-rapidity production of hadrons in polarized p+p collisions at $\sqrt{s} = 200$ and 62.4 GeV. *Phys. Rev. D*, 90(1):012006, 2014, 1312.1995.
- [18] A. Adare et al. Measurement of Transverse Single-Spin Asymmetries for J/ψ Production in Polarized $p + p$ Collisions at $\sqrt{s} = 200$ GeV. *Phys. Rev. D*, 82:112008, 2010, 1009.4864. [Erratum: Phys. Rev. D 86, 099904 (2012)].
- [19] C. Aidala et al. Single-spin asymmetry of J/ψ production in $p+p$, $p+Al$, and $p+Au$ collisions with transversely polarized proton beams at $\sqrt{s_{NN}} = 200$ GeV. *Phys. Rev. D*, 98(1):012006, 2018, 1805.01491.
- [20] C. Aidala et al. Cross section and transverse single-spin asymmetry of muons from open heavy-flavor decays in polarized $p+p$ collisions at $\sqrt{s} = 200$ GeV. *Phys. Rev. D*, 95(11):112001, 2017, 1703.09333.
- [21] C. Adolph et al. First measurement of the Sivers asymmetry for gluons using SIDIS data. *Phys. Lett. B*, 772:854–864, 2017, 1701.02453.
- [22] Adam Szabelski. The gluon Sivers asymmetry measurements at COMPASS. *PoS*, DIS2016:219, 2016.
- [23] Vincenzo Barone, Alessandro Drago, and Philip G. Ratcliffe. Transverse polarisation of quarks in hadrons. *Phys. Rept.*, 359:1–168, 2002, hep-ph/0104283.
- [24] C. Hadjidakis et al. A Fixed-Target Programme at the LHC: Physics Case and Projected Performances for Heavy-Ion, Hadron, Spin and Astroparticle Studies. 7 2018, 1807.00603.
- [25] C.A. Aidala et al. The LHCSpin Project. pages 204–207, 2020, 1901.08002.
- [26] A. Accardi et al. Electron Ion Collider: The Next QCD Frontier: Understanding the glue that binds us all. *Eur. Phys. J. A*, 52(9):268, 2016, 1212.1701.
- [27] Emanuele R. Nocera, Richard D. Ball, Stefano Forte, Giovanni Ridolfi, and Juan Rojo. A first unbiased global determination of polarized PDFs and their uncertainties. *Nucl. Phys.*, B887:276–308, 2014, 1406.5539.
- [28] Cristiano Brenner Mariotto, M. B. Gay Ducati, and G. Ingelman. Soft and hard QCD dynamics in hadroproduction of charmonium. *Eur. Phys. J.*, C23:527–538, 2002, hep-ph/0111379.
- [29] Run overview of the relativistic heavy ion collider <https://www.agsrcrhichome.bnl.gov/RHIC/Runs/>.
- [30] I. N. Meshkov. Luminosity of an Ion Collider. *Phys. Part. Nucl.*, 50(6):663–682, 2019.
- [31] P. A. Zyla et al. Review of Particle Physics. *PTEP*, 2020(8):083C01, 2020.
- [32] I. Abt et al. Production of the Charmonium States χ_{c1} and χ_{c2} in Proton Nucleus Interactions at $\sqrt{s} = 41.6$ -GeV. *Phys. Rev. D*, 79:012001, 2009, 0807.2167.

[33] Cheuk-Yin Wong and Hui Wang. Effects of parton intrinsic transverse momentum on photon production in hard scattering processes. *Phys. Rev. C*, 58:376–388, 1998, hep-ph/9802378.

[34] W. Vogelsang and M. R. Whalley. A Compilation of data on single and double prompt photon production in hadron hadron interactions. *J. Phys.*, G23:A1–A69, 1997.

[35] Patrick Aurenche, Michel Fontannaz, Jean-Philippe Guillet, Eric Pilon, and Monique Werlen. A New critical study of photon production in hadronic collisions. *Phys. Rev.*, D73:094007, 2006, hep-ph/0602133.

[36] T. Binoth, J.P. Guillet, E. Pilon, and M. Werlen. A Full next-to-leading order study of direct photon pair production in hadronic collisions. *Eur. Phys. J. C*, 16:311–330, 2000, hep-ph/9911340.

[37] L. Apanasevich et al. Evidence for parton k_T effects in high p_T particle production. *Phys. Rev. Lett.*, 81:2642–2645, 1998, hep-ex/9711017.

[38] E. Anassontzis et al. High p(t) Direct Photon Production in p p Collisions. *Z. Phys. C*, 13:277–289, 1982.

[39] J. Badier et al. Direct Photon Pair Production From Pions and Protons at 200-GeV/c. *Phys. Lett. B*, 164:184–188, 1985.

[40] Hung-Liang Lai, Marco Guzzi, Joey Huston, Zhao Li, Pavel M. Nadolsky, Jon Pumplin, and C.-P. Yuan. New parton distributions for collider physics. *Phys. Rev. D*, 82:074024, 2010, 1007.2241.

[41] Stanley J. Brodsky, Kelly Yu-Ju Chiu, Jean-Philippe Lansberg, and Nodoka Yamanaka. The gluon and charm content of the deuteron. *Phys. Lett. B*, 783:287–293, 2018, 1805.03173.

[42] I. Abt et al. Study of proton parton distribution functions at high x using ZEUS data. 3 2020, 2003.08742.

[43] Albert M Sirunyan et al. Measurement of double-differential cross sections for top quark pair production in pp collisions at $\sqrt{s} = 8$ TeV and impact on parton distribution functions. *Eur. Phys. J. C*, 77(7):459, 2017, 1703.01630.

[44] H. Abdolmaleki and A. Khorramian. Parton distribution functions and constraints on the intrinsic charm content of the proton using the Brodsky-Hoyer-Peterson-Saka approach. *Phys. Rev. D*, 99(11):116019, 2019, 1903.02583.

[45] C. Lourenco and H.K. Wohri. Heavy flavour hadro-production from fixed-target to collider energies. *Phys. Rept.*, 433:127–180, 2006, hep-ph/0609101.

[46] A. Accardi et al. A Critical Appraisal and Evaluation of Modern PDFs. *Eur. Phys. J. C*, 76(8):471, 2016, 1603.08906.

[47] G.A. Alves et al. Forward cross-sections for production of D^+ , D^0 , $D(s)$, D^*+ and Λ_c in 250-GeV π^\pm , K^\pm , and p - nucleon interactions. *Phys. Rev. Lett.*, 77:2388–2391, 1996. [Erratum: Phys.Rev.Lett. 81, 1537 (1998)].

[48] George F. Sterman. Summation of Large Corrections to Short Distance Hadronic Cross-Sections. *Nucl. Phys. B*, 281:310–364, 1987.

[49] S. Catani and L. Trentadue. Resummation of the QCD Perturbative Series for Hard Processes. *Nucl. Phys. B*, 327:323–352, 1989.

- [50] Harry Contopanagos, Eric Laenen, and George F. Sterman. Sudakov factorization and resummation. *Nucl. Phys. B*, 484:303–330, 1997, hep-ph/9604313.
- [51] Nikolaos Kidonakis, Gianluca Oderda, and George F. Sterman. Evolution of color exchange in QCD hard scattering. *Nucl. Phys. B*, 531:365–402, 1998, hep-ph/9803241.
- [52] N.Y. Ivanov. Perturbative stability of the QCD predictions for single spin asymmetry in heavy quark photoproduction. *Nucl. Phys. B*, 615:266–284, 2001, hep-ph/0104301.
- [53] Stefano Catani, Michelangelo L. Mangano, Paolo Nason, and Luca Trentadue. The Resummation of soft gluons in hadronic collisions. *Nucl. Phys. B*, 478:273–310, 1996, hep-ph/9604351.
- [54] Edmond L. Berger and Harry Contopanagos. The Perturbative resummed series for top quark production in hadron reactions. *Phys. Rev. D*, 54:3085–3113, 1996, hep-ph/9603326.
- [55] Nikolaos Kidonakis. High order corrections and subleading logarithms for top quark production. *Phys. Rev. D*, 64:014009, 2001, hep-ph/0010002.
- [56] Stefano Forte, Giovanni Ridolfi, Joan Rojo, and Maria Ubiali. Borel resummation of soft gluon radiation and higher twists. *Phys. Lett. B*, 635:313–319, 2006, hep-ph/0601048.
- [57] S.J. Brodsky, P. Hoyer, C. Peterson, and N. Sakai. The Intrinsic Charm of the Proton. *Phys. Lett. B*, 93:451–455, 1980.
- [58] Stanley J. Brodsky, C. Peterson, and N. Sakai. Intrinsic Heavy Quark States. *Phys. Rev. D*, 23:2745, 1981.
- [59] L.N. Ananikyan and N.Ya. Ivanov. Azimuthal Asymmetries in DIS as a Probe of Intrinsic Charm Content of the Proton. *Nucl. Phys. B*, 762:256–283, 2007, hep-ph/0701076.
- [60] John Collins. *Foundations of perturbative QCD*, volume 32. Cambridge University Press, 11 2013.
- [61] Miguel G. Echevarria, Tomas Kasemets, Piet J. Mulders, and Cristian Pisano. QCD evolution of (un)polarized gluon TMDPDFs and the Higgs q_T -distribution. *JHEP*, 07:158, 2015, 1502.05354. [Erratum: JHEP 05, 073 (2017)].
- [62] Miguel G. Echevarria. Proper TMD factorization for quarkonia production: $pp \rightarrow \eta_{c,b}$ as a study case. *JHEP*, 10:144, 2019, 1907.06494.
- [63] Sean Fleming, Yiannis Makris, and Thomas Mehen. An effective field theory approach to quarkonium at small transverse momentum. *JHEP*, 04:122, 2020, 1910.03586.
- [64] P.J. Mulders and J. Rodrigues. Transverse momentum dependence in gluon distribution and fragmentation functions. *Phys. Rev. D*, 63:094021, 2001, hep-ph/0009343.
- [65] Daniel Boer, Stanley J. Brodsky, Piet J. Mulders, and Cristian Pisano. Direct Probes of Linearly Polarized Gluons inside Unpolarized Hadrons. *Phys. Rev. Lett.*, 106:132001, 2011, 1011.4225.
- [66] Cristian Pisano, Daniel Boer, Stanley J. Brodsky, Maarten G.A. Buffing, and Piet J. Mulders. Linear polarization of gluons and photons in unpolarized collider experiments. *JHEP*, 10:024, 2013, 1307.3417.
- [67] A.V. Efremov, N.Ya. Ivanov, and O.V. Teryaev. QCD predictions for the azimuthal asymmetry in charm leptoproduction for the COMPASS kinematics. *Phys. Lett. B*, 772:283–289, 2017, 1706.03125.

[68] N. Ya Ivanov, A.V. Efremov, and O.V. Teryaev. How to measure the linear polarization of gluons in unpolarized proton using the heavy-quark pair production. *EPJ Web Conf.*, 204:02006, 2019, 1812.00393.

[69] A.V. Efremov, N. Ya Ivanov, and O.V. Teryaev. The ratio $R = d\sigma_L/d\sigma_T$ in heavy-quark pair lepto-production as a probe of linearly polarized gluons in unpolarized proton. *Phys. Lett. B*, 780:303–307, 2018, 1801.03398.

[70] Daniel Boer and Cristian Pisano. Polarized gluon studies with charmonium and bottomonium at LHCb and AFTER. *Phys. Rev. D*, 86:094007, 2012, 1208.3642.

[71] Jian-Wei Qiu, Marc Schlegel, and Werner Vogelsang. Probing Gluonic Spin-Orbit Correlations in Photon Pair Production. *Phys. Rev. Lett.*, 107:062001, 2011, 1103.3861.

[72] Jean-Philippe Lansberg, Cristian Pisano, Florent Scarpa, and Marc Schlegel. Pinning down the linearly-polarised gluons inside unpolarised protons using quarkonium-pair production at the LHC. *Phys. Lett. B*, 784:217–222, 2018, 1710.01684. [Erratum: *Phys.Lett.B* 791, 420–421 (2019)].

[73] Geoffrey T. Bodwin, Eric Braaten, and G.Peter Lepage. Rigorous QCD analysis of inclusive annihilation and production of heavy quarkonium. *Phys. Rev. D*, 51:1125–1171, 1995, hep-ph/9407339. [Erratum: *Phys.Rev.D* 55, 5853 (1997)].

[74] Vernon D. Barger, Wai-Yee Keung, and R.J.N. Phillips. On psi and Upsilon Production via Gluons. *Phys. Lett. B*, 91:253–258, 1980.

[75] Vernon D. Barger, Wai-Yee Keung, and R.J.N. Phillips. Hadroproduction of ψ and Υ . *Z. Phys. C*, 6:169, 1980.

[76] R. Gavai, D. Kharzeev, H. Satz, G.A. Schuler, K. Sridhar, and R. Vogt. Quarkonium production in hadronic collisions. *Int. J. Mod. Phys. A*, 10:3043–3070, 1995, hep-ph/9502270.

[77] Yan-Qing Ma and Ramona Vogt. Quarkonium Production in an Improved Color Evaporation Model. *Phys. Rev. D*, 94(11):114029, 2016, 1609.06042.

[78] N. Brambilla et al. Heavy Quarkonium: Progress, Puzzles, and Opportunities. *Eur. Phys. J. C*, 71:1534, 2011, 1010.5827.

[79] Jean-Philippe Lansberg. New Observables in Inclusive Production of Quarkonia. 3 2019, 1903.09185.

[80] Mathias Butenschoen and Bernd A. Kniehl. J/psi polarization at Tevatron and LHC: Nonrelativistic-QCD factorization at the crossroads. *Phys. Rev. Lett.*, 108:172002, 2012, 1201.1872.

[81] Mathias Butenschoen and Bernd A. Kniehl. Next-to-leading-order tests of NRQCD factorization with J/ψ yield and polarization. *Mod. Phys. Lett. A*, 28:1350027, 2013, 1212.2037.

[82] Mathias Butenschoen, Zhi-Guo He, and Bernd A. Kniehl. η_c production at the LHC challenges nonrelativistic-QCD factorization. *Phys. Rev. Lett.*, 114(9):092004, 2015, 1411.5287.

[83] Li-Ping Sun, Hao Han, and Kuang-Ta Chao. Impact of J/ψ pair production at the LHC and predictions in nonrelativistic QCD. *Phys. Rev. D*, 94(7):074033, 2016, 1404.4042.

- [84] Zhi-Guo He, Bernd A. Kniehl, Maxim A. Nefedov, and Vladimir A. Saleev. Double Prompt J/ψ Hadroproduction in the Parton Reggeization Approach with High-Energy Resummation. *Phys. Rev. Lett.*, 123(16):162002, 2019, 1906.08979.
- [85] Jean-Philippe Lansberg, Hua-Sheng Shao, Nodoka Yamanaka, Yu-Jie Zhang, and Camille Noûs. Complete NLO QCD study of single- and double-quarkonium hadroproduction in the colour-evaporation model at the Tevatron and the LHC. 4 2020, 2004.14345.
- [86] Zhong-Bo Kang, Jian-Wei Qiu, and George Sterman. Heavy quarkonium production and polarization. *Phys. Rev. Lett.*, 108:102002, 2012, 1109.1520.
- [87] Yan-Qing Ma and Kuang-Ta Chao. New factorization theory for heavy quarkonium production and decay. *Phys. Rev. D*, 100(9):094007, 2019, 1703.08402.
- [88] Rong Li, Yu Feng, and Yan-Qing Ma. Exclusive quarkonium production or decay in soft gluon factorization. *JHEP*, 05:009, 2020, 1911.05886.
- [89] An-Ping Chen and Yan-Qing Ma. Theory for quarkonium: from NRQCD factorization to soft gluon factorization. 5 2020, 2005.08786.
- [90] Mathias Butenschoen and Bernd A. Kniehl. Reconciling J/ψ production at HERA, RHIC, Tevatron, and LHC with NRQCD factorization at next-to-leading order. *Phys. Rev. Lett.*, 106:022003, 2011, 1009.5662.
- [91] Mathias Butenschoen and Bernd A. Kniehl. World data of J/ψ production consolidate NRQCD factorization at NLO. *Phys. Rev. D*, 84:051501, 2011, 1105.0820.
- [92] Anton V. Karpishkov, Maxim A. Nefedov, and Vladimir A. Saleev. $B\bar{B}$ angular correlations at the LHC in parton Reggeization approach merged with higher-order matrix elements. *Phys. Rev. D*, 96(9):096019, 2017, 1707.04068.
- [93] V.A. Saleev, M.A. Nefedov, and A.V. Shipilova. Prompt J/ψ production in the Regge limit of QCD: From Tevatron to LHC. *Phys. Rev. D*, 85:074013, 2012, 1201.3464.
- [94] A.V. Karpishkov, M.A. Nefedov, and V.A. Saleev. Spectra and polarizations of prompt J/ψ at the NICA within collinear parton model and parton Reggeization approach. *J. Phys. Conf. Ser.*, 1435(1):012015, 2020.
- [95] Vincent Cheung and Ramona Vogt. Production and polarization of prompt J/ψ in the improved color evaporation model using the k_T -factorization approach. *Phys. Rev. D*, 98(11):114029, 2018, 1808.02909.
- [96] A. Airapetian et al. First measurement of the tensor structure function $b(1)$ of the deuteron. *Phys. Rev. Lett.*, 95:242001, 2005, hep-ex/0506018.
- [97] M. Harvey. On the Fractional Parentage Expansions of Color Singlet Six Quark States in a Cluster Model. *Nucl. Phys. A*, 352:301, 1981. [Erratum: Nucl.Phys.A 481, 834 (1988)].
- [98] Gerald A. Miller. Pionic and Hidden-Color, Six-Quark Contributions to the Deuteron $b1$ Structure Function. *Phys. Rev. C*, 89(4):045203, 2014, 1311.4561.
- [99] Paul Hoyer and D.P. Roy. The Intrinsic gluon component of the nucleon. *Phys. Lett. B*, 410:63–66, 1997, hep-ph/9705273.

[100] Heikki Mäntysaari and Björn Schenke. Accessing the gluonic structure of light nuclei at a future electron-ion collider. *Phys. Rev. C*, 101(1):015203, 2020, 1910.03297.

[101] Frank Winter, William Detmold, Arjun S. Gambhir, Kostas Orginos, Martin J. Savage, Phiala E. Shanahan, and Michael L. Wagman. First lattice QCD study of the gluonic structure of light nuclei. *Phys. Rev. D*, 96(9):094512, 2017, 1709.00395.

[102] J. Ashman et al. An Investigation of the Spin Structure of the Proton in Deep Inelastic Scattering of Polarized Muons on Polarized Protons. *Nucl. Phys. B*, 328:1, 1989.

[103] D. L. Adams et al. Measurement of the double spin asymmetry A-LL for inclusive multi gamma pair production with 200-GeV/c polarized proton beam and polarized proton target. *Phys. Lett.*, B336:269–274, 1994.

[104] A. Airapetian et al. Leading-Order Determination of the Gluon Polarization from high-p(T) Hadron Electroproduction. *JHEP*, 08:130, 2010, 1002.3921.

[105] B. Adeva et al. Spin asymmetries for events with high p(T) hadrons in DIS and an evaluation of the gluon polarization. *Phys. Rev.*, D70:012002, 2004, hep-ex/0402010.

[106] E. S. Ageev et al. Gluon polarization in the nucleon from quasi-real photoproduction of high-p(T) hadron pairs. *Phys. Lett.*, B633:25–32, 2006, hep-ex/0511028.

[107] M. Alekseev et al. Gluon polarisation in the nucleon and longitudinal double spin asymmetries from open charm muoproduction. *Phys. Lett.*, B676:31–38, 2009, 0904.3209.

[108] C. Adolph et al. Leading order determination of the gluon polarisation from DIS events with high- p_T hadron pairs. *Phys. Lett.*, B718:922–930, 2013, 1202.4064.

[109] C. Adolph et al. Leading and Next-to-Leading Order Gluon Polarization in the Nucleon and Longitudinal Double Spin Asymmetries from Open Charm Muoproduction. *Phys. Rev.*, D87(5):052018, 2013, 1211.6849.

[110] C. Adolph et al. Leading-order determination of the gluon polarisation from semi-inclusive deep inelastic scattering data. *Eur. Phys. J.*, C77(4):209, 2017, 1512.05053.

[111] A. Adare et al. Inclusive double-helicity asymmetries in neutral-pion and eta-meson production in $\vec{p} + \vec{p}$ collisions at $\sqrt{s} = 200$ GeV. *Phys. Rev.*, D90(1):012007, 2014, 1402.6296.

[112] A. Adare et al. The Polarized gluon contribution to the proton spin from the double helicity asymmetry in inclusive pi0 production in polarized p + p collisions at $\sqrt{s} = 200$ -GeV. *Phys. Rev. Lett.*, 103:012003, 2009, 0810.0694.

[113] A. Adare et al. Inclusive cross section and double helicity asymmetry for π^0 production in $p^+ p$ collisions at $\sqrt{s} = 62.4$ GeV. *Phys. Rev.*, D79:012003, 2009, 0810.0701.

[114] Jaroslav Adam et al. Longitudinal Double-Spin Asymmetries for π^0 s in the Forward Direction for 510 GeV Polarized pp Collisions. *Phys. Rev. D*, 98(3):032013, 2018, 1805.09745.

[115] U. A. Acharya et al. Measurement of charged pion double spin asymmetries at midrapidity in longitudinally polarized p + p collisions at $\sqrt{s} = 510$ GeV. *Phys. Rev. D*, 102(3):032001, 2020, 2004.02681.

[116] Pibero Djawotho. Gluon polarization and jet production at STAR. *Nuovo Cim.*, C036(05):35–38, 2013, 1303.0543.

- [117] L. Adamczyk et al. Measurement of the cross section and longitudinal double-spin asymmetry for di-jet production in polarized pp collisions at $\sqrt{s} = 200$ GeV. *Phys. Rev. D*, 95(7):071103, 2017, 1610.06616.
- [118] Jaroslav Adam et al. Longitudinal double-spin asymmetries for dijet production at intermediate pseudorapidity in polarized pp collisions at $\sqrt{s} = 200$ GeV. *Phys. Rev. D*, 98(3):032011, 2018, 1805.09742.
- [119] A. Adare et al. Double Spin Asymmetry of Electrons from Heavy Flavor Decays in $p + p$ Collisions at $\sqrt{s} = 200$ GeV. *Phys. Rev.*, D87(1):012011, 2013, 1209.3278.
- [120] A. Adare et al. Measurements of double-helicity asymmetries in inclusive J/ψ production in longitudinally polarized $p + p$ collisions at $\sqrt{s} = 510$ GeV. *Phys. Rev.*, D94(11):112008, 2016, 1606.01815.
- [121] Elliot Leader, Alexander V. Sidorov, and Dimiter B. Stamenov. New analysis concerning the strange quark polarization puzzle. *Phys. Rev.*, D91(5):054017, 2015, 1410.1657.
- [122] Daniel de Florian, Rodolfo Sassot, Marco Stratmann, and Werner Vogelsang. Evidence for polarization of gluons in the proton. *Phys. Rev. Lett.*, 113(1):012001, 2014, 1404.4293.
- [123] Daniel De Florian, Gonzalo Agustín Lucero, Rodolfo Sassot, Marco Stratmann, and Werner Vogelsang. Monte Carlo sampling variant of the DSSV14 set of helicity parton densities. *Phys. Rev.*, D100(11):114027, 2019, 1902.10548.
- [124] J. J. Ethier, N. Sato, and W. Melnitchouk. First simultaneous extraction of spin-dependent parton distributions and fragmentation functions from a global QCD analysis. *Phys. Rev. Lett.*, 119(13):132001, 2017, 1705.05889.
- [125] Jacob J. Ethier and Emanuele R. Nocera. Parton Distributions in Nucleons and Nuclei. *Ann. Rev. Nucl. Part. Sci.*, (70):1–34, 2020, 2001.07722.
- [126] Daniel de Florian, Rodolfo Sassot, Marco Stratmann, and Werner Vogelsang. Global Analysis of Helicity Parton Densities and Their Uncertainties. *Phys. Rev. Lett.*, 101:072001, 2008, 0804.0422.
- [127] C. Aidala, G. Bunce, and et al. Research plan for spin physics at RHIC., 2005.
- [128] M. Anselmino, E. Andreeva, V. Korotkov, F. Murgia, W. D. Nowak, S. Nurushev, O. Teryaev, and A. Tkabladze. On the physics potential of polarized nucleon-nucleon collisions at HERA. In *Future physics at HERA. Proceedings, Workshop, Hamburg, Germany, September 25, 1995-May 31, 1996. Vol. 1, 2*, 1996, hep-ph/9608393.
- [129] Elliot Leader. Spin in particle physics. *Cambridge University Press*, 2011.
- [130] Yu Feng and Hong-Fei Zhang. Double longitudinal-spin asymmetries in J/ψ production at RHIC. *JHEP*, 11:136, 2018, 1809.04894.
- [131] Werner Vogelsang. Prompt photon production in polarized hadron collisions. In *Deep inelastic scattering. Proceedings, 8th International Workshop, DIS 2000, Liverpool, UK, April 25-30, 2000*, pages 253–254, 2000, hep-ph/0006199.
- [132] L. E. Gordon and W. Vogelsang. Inclusive prompt photon production in polarized $p p$ collisions at HERA-N(polarized). *Phys. Lett.*, B387:629–636, 1996, hep-ph/9607442.

[133] L. E. Gordon. Constraints on Delta G from prompt photon plus jet production at HERA-N (polarized). *Phys. Lett.*, B406:184–192, 1997, hep-ph/9609403.

[134] Qing-hua Xu and Zuo-tang Liang. Probing gluon helicity distribution and quark transversity through hyperon polarization in singly polarized pp collisions. *Phys. Rev.*, D70:034015, 2004, hep-ph/0406119.

[135] A.V. Efremov and O.V. Teryaev. On Spin Effects in Quantum Chromodynamics. *Sov. J. Nucl. Phys.*, 36:140, 1982.

[136] A.V. Efremov and O.V. Teryaev. QCD Asymmetry and Polarized Hadron Structure Functions. *Phys. Lett. B*, 150:383, 1985.

[137] Jian-wei Qiu and George F. Sterman. Single transverse spin asymmetries. *Phys. Rev. Lett.*, 67:2264–2267, 1991.

[138] A. Efremov, V. Korotkiian, and O. Teryaev. The twist - three single spin asymmetries of pion production. *Phys. Lett. B*, 348:577–581, 1995.

[139] Dennis W. Sivers. Single Spin Production Asymmetries from the Hard Scattering of Point-Like Constituents. *Phys. Rev. D*, 41:83, 1990.

[140] Daniël Boer, Cédric Lorcé, Cristian Pisano, and Jian Zhou. The gluon Sivers distribution: status and future prospects. *Adv. High Energy Phys.*, 2015:371396, 2015, 1504.04332.

[141] U. D'Alesio, F. Murgia, and C. Pisano. Towards a first estimate of the gluon Sivers function from A_N data in pp collisions at RHIC. *JHEP*, 09:119, 2015, 1506.03078.

[142] M. Anselmino, M. Boglione, U. D'Alesio, A. Kotzinian, F. Murgia, and A. Prokudin. Extracting the Sivers function from polarized SIDIS data and making predictions. *Phys. Rev. D*, 72:094007, 2005, hep-ph/0507181. [Erratum: Phys. Rev. D 72, 099903 (2005)].

[143] M. Anselmino, M. Boglione, U. D'Alesio, A. Kotzinian, S. Melis, F. Murgia, A. Prokudin, and C. Turk. Sivers Effect for Pion and Kaon Production in Semi-Inclusive Deep Inelastic Scattering. *Eur. Phys. J. A*, 39:89–100, 2009, 0805.2677.

[144] S. Kretzer. Fragmentation functions from flavor inclusive and flavor tagged e+ e- annihilations. *Phys. Rev. D*, 62:054001, 2000, hep-ph/0003177.

[145] Daniel de Florian, Rodolfo Sassot, and Marco Stratmann. Global analysis of fragmentation functions for pions and kaons and their uncertainties. *Phys. Rev. D*, 75:114010, 2007, hep-ph/0703242.

[146] Rohini M. Godbole, Abhiram Kaushik, Anuradha Misra, Vaibhav Rawoot, and Bipin Sonawane. Transverse single spin asymmetry in $p + p^\uparrow \rightarrow J/\psi + X$. *Phys. Rev. D*, 96(9):096025, 2017, 1703.01991.

[147] M. Anselmino, M. Boglione, U. D'Alesio, E. Leader, and F. Murgia. Accessing Sivers gluon distribution via transverse single spin asymmetries in p(transv. polarized) $p \rightarrow D X$ processes at RHIC. *Phys. Rev. D*, 70:074025, 2004, hep-ph/0407100.

[148] Yuji Koike and Shinsuke Yoshida. Probing the three-gluon correlation functions by the single spin asymmetry in $p^\uparrow p \rightarrow DX$. *Phys. Rev. D*, 84:014026, 2011, 1104.3943.

[149] Zhong-Bo Kang, Jian-Wei Qiu, Werner Vogelsang, and Feng Yuan. Accessing tri-gluon correlations in the nucleon via the single spin asymmetry in open charm production. *Phys. Rev.*, D78:114013, 2008, 0810.3333.

[150] Rohini M. Godbole, Abhiram Kaushik, and Anuradha Misra. Transverse single spin asymmetry in $p + p^\uparrow \rightarrow D^+ X$. *Phys. Rev.*, D94(11):114022, 2016, 1606.01818.

[151] N. Hammon, B. Ehrnsperger, and A. Schaefer. Single-transverse spin asymmetry in prompt photon production. *J. Phys.*, G24:991–1001, 1998.

[152] Koichi Kanazawa and Yuji Koike. Single transverse-spin asymmetry for direct-photon and single-jet productions at RHIC. *Phys. Lett.*, B720:161–165, 2013, 1212.3071.

[153] U. A. Acharya et al. Probing gluon spin-momentum correlations in transversely polarized protons through midrapidity isolated direct photons in $p^\uparrow + p$ collisions at $\sqrt{s} = 200$ GeV. 2021 2102.13585.

[154] Daniel Boer and Werner Vogelsang. Asymmetric jet correlations in p p uparrow scattering. *Phys. Rev.*, D69:094025, 2004, hep-ph/0312320.

[155] Umberto D’Alesio, Francesco Murgia, Cristian Pisano, and Pieter Taels. Probing the gluon Sivers function in $p^\uparrow p \rightarrow J/\psi X$ and $p^\uparrow p \rightarrow DX$. *Phys. Rev. D*, 96(3):036011, 2017, 1705.04169.

[156] Umberto D’Alesio, Francesco Murgia, Cristian Pisano, and Sangem Rajesh. Single-spin asymmetries in $p^\uparrow p \rightarrow J/\psi + X$ within a TMD approach: role of the color octet mechanism. *Eur. Phys. J. C*, 79(12):1029, 2019, 1910.09640.

[157] D. L. Adams et al. Measurement of single spin asymmetry for direct photon production in p p collisions at 200-GeV/c. *Phys. Lett.*, B345:569–575, 1995.

[158] S. Kumano and Qin-Tao Song. Gluon transversity in polarized proton-deuteron Drell-Yan process. *Phys. Rev. D*, 101(5):054011, 2020, 1910.12523.

[159] Jacques Soffer, Marco Stratmann, and Werner Vogelsang. Accessing transversity in double-spin asymmetries at the BNL-RHIC. *Phys. Rev. D*, 65:114024, 2002, hep-ph/0204058.

[160] A. Mukherjee, M. Stratmann, and W. Vogelsang. Next-to-leading order QCD corrections to A(TT) for prompt photon production. *Phys. Rev. D*, 67:114006, 2003, hep-ph/0303226.

[161] R.L. Jaffe and Aneesh Manohar. Nuclear gluonometry. *Phys. Lett. B*, 223:218–224, 1989.

[162] Oleg Teryaev. Shear forces and tensor polarization. *PoS*, DIS2019:240, 2019.

[163] Pervez Hoodbhoy, R.L. Jaffe, and Aneesh Manohar. Novel Effects in Deep Inelastic Scattering from Spin 1 Hadrons. *Nucl. Phys. B*, 312:571–588, 1989.

[164] F.E. Close and S. Kumano. A sum rule for the spin dependent structure function $b-1(x)$ for spin one hadrons. *Phys. Rev. D*, 42:2377–2379, 1990.

[165] A.V. Efremov and O.V. Teryaev. On high p_T vector mesons spin alignment. *Sov. J. Nucl. Phys.*, 36:557, 1982.

[166] A.V. Efremov and O.V. Teryaev. On the oscillations of the tensor spin structure function. In *International Symposium: Dubna Deuteron 93*, 1994, hep-ph/9910555.

[167] O.V. Teryaev. Nucleon spin and orbital structure: 20 years later. *Mod. Phys. Lett. A*, 24:2831–2837, 2009.

[168] O.V. Teryaev. Spin structure of nucleon and equivalence principle. 4 1999, hep-ph/9904376.

[169] O.V. Teryaev. Sources of time reversal odd spin asymmetries in QCD. *Czech. J. Phys.*, 53:47–58A, 2003, hep-ph/0306301.

[170] O.V. Teryaev. Equivalence principle and partition of angular momenta in the nucleon. *AIP Conf. Proc.*, 915(1):260–263, 2007, hep-ph/0612205.

[171] O.V. Teryaev. Gravitational form factors and nucleon spin structure. *Front. Phys. (Beijing)*, 11(5):111207, 2016.

[172] George Y. Prokhorov, Oleg V. Teryaev, and Valentin I. Zakharov. Unruh effect for fermions from the Zubarev density operator. *Phys. Rev. D*, 99(7):071901, 2019, 1903.09697.

[173] Maxim V. Polyakov and Hyeon-Dong Son. Nucleon gravitational form factors from instantons: forces between quark and gluon subsystems. *JHEP*, 09:156, 2018, 1808.00155.

[174] S. Kumano and Qin-Tao Song. Spin asymmetry for proton-deuteron Drell-Yan process with tensor-polarized deuteron. In *22nd International Symposium on Spin Physics*, 2 2017, 1702.01477.

[175] A. Arbuzov et al. On the physics potential to study the gluon content of proton and deuteron at NICA SPD. *Prog. Part. Nucl. Phys.*, 119:103858, 2021, 2011.15005.

[176] D. L. Adams et al. Comparison of spin asymmetries and cross-sections in π^0 production by 200 GeV polarized anti-protons and protons. *Phys. Lett.*, B261:201–206, 1991.

[177] D. L. Adams et al. Analyzing power in inclusive π^+ and π^- production at high $x(F)$ with a 200-GeV polarized proton beam. *Phys. Lett.*, B264:462–466, 1991.

[178] A. Bravar et al. Single spin asymmetries in inclusive charged pion production by transversely polarized anti-protons. *Phys. Rev. Lett.*, 77:2626–2629, 1996.

[179] D.L. Adams et al. Measurement of single spin asymmetry in eta meson production in p (polarized) p and anti-p (polarized) p interactions in the beam fragmentation region at 200-GeV/c. *Nucl. Phys. B*, 510:3–11, 1998.

[180] Steven Heppelmann. Measurement of Transverse Single Spin Asymmetry A(N) in Eta Mass Region at Large Feynman X(F) with the STAR Forward Pion Detector. In *18th International Conference on Particles and Nuclei*, pages 273–275, 5 2009, 0905.2840.

[181] I. Arsene et al. Single Transverse Spin Asymmetries of Identified Charged Hadrons in Polarized p+p Collisions at $s^{**}(1/2) = 62.4$ -GeV. *Phys. Rev. Lett.*, 101:042001, 2008, 0801.1078.

[182] B.I. Abelev et al. Forward Neutral Pion Transverse Single Spin Asymmetries in p+p Collisions at $s^{**}(1/2) = 200$ -GeV. *Phys. Rev. Lett.*, 101:222001, 2008, 0801.2990.

[183] S.S. Adler et al. Measurement of transverse single-spin asymmetries for mid-rapidity production of neutral pions and charged hadrons in polarized p+p collisions at $s^{**}(1/2) = 200$ -GeV. *Phys. Rev. Lett.*, 95:202001, 2005, hep-ex/0507073.

[184] J. Adams et al. Cross-sections and transverse single spin asymmetries in forward neutral pion production from proton collisions at $s^{**}(1/2) = 200$ -GeV. *Phys. Rev. Lett.*, 92:171801, 2004, hep-ex/0310058.

[185] Justin Cammarota, Leonard Gamberg, Zhong-Bo Kang, Joshua A. Miller, Daniel Pitonyak, Alexei Prokudin, Ted C. Rogers, and Nobuo Sato. Origin of single transverse-spin asymmetries in high-energy collisions. *Phys. Rev. D*, 102(5):054002, 2020, 2002.08384.

- [186] Prokudin A., private communication.
- [187] M. Aghasyan et al. First measurement of transverse-spin-dependent azimuthal asymmetries in the Drell-Yan process. *Phys. Rev. Lett.*, 119(11):112002, 2017, 1704.00488.
- [188] Bakur Parsamyan. Transversely polarized Drell-Yan measurements at COMPASS. *PoS*, DIS2019:195, 2019, 1908.01727.
- [189] C. Brown et al. Letter of Intent for a Drell-Yan Experiment with a Polarized Proton Target. 8 2014.
- [190] Andrew Chen et al. Probing nucleon spin structures with polarized Drell-Yan in the Fermilab SpinQuest experiment. *PoS*, SPIN2018:164, 2019, 1901.09994.
- [191] J. C. Collins, A. V. Efremov, K. Goeke, S. Menzel, A. Metz, and P. Schweitzer. Sivers effect in semi-inclusive deeply inelastic scattering. *Phys. Rev.*, D73:014021, 2006, hep-ph/0509076.
- [192] A. Airapetian et al. Measurement of Azimuthal Asymmetries With Respect To Both Beam Charge and Transverse Target Polarization in Exclusive Electroproduction of Real Photons. *JHEP*, 06:066, 2008, 0802.2499.
- [193] M.G. Alexeev et al. Measurement of the cross section for hard exclusive π^0 muoproduction on the proton. *Phys. Lett. B*, 805:135454, 2020, 1903.12030.
- [194] R. Akhunzyanov et al. Transverse extension of partons in the proton probed in the sea-quark range by measuring the DVCS cross section. *Phys. Lett. B*, 793:188–194, 2019, 1802.02739.
- [195] K. Park et al. Hard exclusive pion electroproduction at backward angles with CLAS. *Phys. Lett. B*, 780:340–345, 2018, 1711.08486.
- [196] S. V. Goloskokov and P. Kroll. The Longitudinal cross-section of vector meson electroproduction. *Eur. Phys. J.*, C50:829–842, 2007, hep-ph/0611290.
- [197] S. V. Goloskokov and P. Kroll. The Role of the quark and gluon GPDs in hard vector-meson electroproduction. *Eur. Phys. J.*, C53:367–384, 2008, 0708.3569.
- [198] Yoshikazu Hagiwara, Yoshitaka Hatta, Roman Pasechnik, Marek Tasevsky, and Oleg Teryaev. Accessing the gluon Wigner distribution in ultraperipheral pA collisions. *Phys. Rev.*, D96(3):034009, 2017, 1706.01765.
- [199] O. V. Teryaev. Analytic properties of hard exclusive amplitudes. In *11th International Conference on Elastic and Diffractive Scattering: Towards High Energy Frontiers: The 20th Anniversary of the Blois Workshops, 17th Rencontre de Blois (EDS 05) Chateau de Blois, Blois, France, May 15-20, 2005*, 2005, hep-ph/0510031.
- [200] V. Goloskokov, P. Kroll, and O. Teryaev. Lepton-pair production in hard exclusive hadron-hadron collisions. arXiv:2008.13594, 8 2020, 2008.13594.
- [201] A.V. Efremov. Polarization in High p_T and Cumulative Hadron Production. *Sov. J. Nucl. Phys.*, 28:83, 1978.
- [202] A.V. Efremov, L. Mankiewicz, and N.A. Tornqvist. Jet handedness as a measure of quark and gluon polarization. *Phys. Lett. B*, 284:394–400, 1992.
- [203] A. Efremov and L. Tkatchev. Jet handedness correlation in hadronic Z^0 -decay. *AIP Conf. Proc.*, 343:821–833, 1995.

- [204] John C. Collins. Fragmentation of transversely polarized quarks probed in transverse momentum distributions. *Nucl. Phys. B*, 396:161–182, 1993, hep-ph/9208213.
- [205] R.L. Jaffe, Xue-min Jin, and Jian Tang. Interference fragmentation functions and the nucleon’s transversity. *Phys. Rev. Lett.*, 80:1166–1169, 1998, hep-ph/9709322.
- [206] Alessandro Bacchetta, Aurore Courtoy, and Marco Radici. First glances at the transversity parton distribution through dihadron fragmentation functions. *Phys. Rev. Lett.*, 107:012001, 2011, 1104.3855.
- [207] Bo-Qiang Ma, Ivan Schmidt, Jacques Soffer, and Jian-Jun Yang. Helicity and transversity distributions of nucleon and Lambda - hyperon from Lambda fragmentation. *Phys. Rev. D*, 64:014017, 2001, hep-ph/0103136. [Erratum: Phys.Rev.D 64, 099901 (2001)].
- [208] A. Schafer, L. Szymanowski, and O.V. Teryaev. Tensor polarization of vector mesons from quark and gluon fragmentation. *Phys. Lett. B*, 464:94–100, 1999, hep-ph/9906471.
- [209] Peter L. Cho, Mark B. Wise, and Sandip P. Trivedi. Gluon fragmentation into polarized charmonium. *Phys. Rev. D*, 51:2039–2043, 1995, hep-ph/9408352.
- [210] M. Alekseev et al. Measurement of the Longitudinal Spin Transfer to Lambda and Anti-Lambda Hyperons in Polarised Muon DIS. *Eur. Phys. J. C*, 64:171–179, 2009, 0907.0388.
- [211] Andrea Moretti. Transversity and Λ polarization at COMPASS. *PoS*, SPIN2018:138, 2018, 1901.01735.
- [212] A. Airapetian et al. Transverse Polarization of Lambda and anti-Lambda Hyperons in Quasireal Photoproduction. *Phys. Rev. D*, 76:092008, 2007, 0704.3133.
- [213] M.R. Adams et al. Lambda and anti-lambda polarization from deep inelastic muon scattering. *Eur. Phys. J. C*, 17:263–267, 2000, hep-ex/9911004.
- [214] A. Bravar et al. Analyzing power measurement in inclusive Lambda0 production with a 200-GeV/c polarized proton beam. *Phys. Rev. Lett.*, 75:3073–3077, 1995.
- [215] A. Bravar et al. Spin transfer in inclusive Lambda0 production by transversely polarized protons at 200-GeV/c. *Phys. Rev. Lett.*, 78:4003–4006, 1997.
- [216] B.I. Abelev et al. Longitudinal Spin Transfer to Lambda and anti-Lambda Hyperons in Polarized Proton-Proton Collisions at $s^{**}(1/2) = 200\text{-GeV}$. *Phys. Rev. D*, 80:111102, 2009, 0910.1428.
- [217] Ran Han. The polarization of anti-Lambda in $s^{**}(1/2) = 200\text{-GeV}$ polarized proton-proton collision. *AIP Conf. Proc.*, 915(1):432–435, 2007.
- [218] G. Bunce et al. Lambda0 Hyperon Polarization in Inclusive Production by 300-GeV Protons on Beryllium. *Phys. Rev. Lett.*, 36:1113–1116, 1976.
- [219] The MultiPurpose Detector – MPD. Conceptual Design Report, 2016.
- [220] Exploring strongly interacting matter at high densities - NICA White Paper, EPJA, 2016.
- [221] MPD web site <http://mpd.jinr.ru>.
- [222] J.V. Allaby et al. Structure in the angular distribution of high energy proton-proton scattering. *Phys. Lett. B*, 28:67–71, 1968.

[223] C. W. Akerlof, R. H. Hieber, A. D. Krisch, K. W. Edwards, L. G. Ratner, and K. Ruddick. Elastic Proton-Proton Scattering at 90-degrees and Structure within the Proton. *Phys. Rev.*, 159:1138–1149, 1967.

[224] Martin L. Perl, Jack Cox, Michael J. Longo, and M. Kreisler. Neutron-proton elastic scattering from 2-GeV/c to 7-GeV/c. *Phys. Rev. D*, 1:1857, 1970.

[225] J.L. Stone, J.P. Chanowski, H. Richard Gustafson, M.J. Longo, and S.W. Gray. Large Angle Neutron-Proton Elastic Scattering from 5-GeV/c to 12-GeV/c. *Nucl. Phys. B*, 143:1–39, 1978.

[226] D. G. Crabb et al. Spin Dependence of High p -Transverse **2 Elastic p p Scattering. *Phys. Rev. Lett.*, 41:1257, 1978.

[227] E. A. Crosbie et al. Energy Dependence of Spin Spin Effects in p p Elastic Scattering at 90-Degrees Center-Of-Mass. *Phys. Rev.*, D23:600, 1981.

[228] G.R. Court et al. Energy Dependence of Spin Effects in p (Polarized) p (Polarized) $\rightarrow pp$. *Phys. Rev. Lett.*, 57:507, 1986.

[229] Misak M Sargsian. Nucleon - Nucleon Interactions at Short Distances. 3 2014, 1403.0678.

[230] Stanley J. Brodsky, Carl E. Carlson, and Harry J. Lipkin. Spin Effects in Large Transverse Momentum Exclusive Scattering Processes. *Phys. Rev. D*, 20:2278–2289, 1979.

[231] Glennys R. Farrar, Steven A. Gottlieb, Dennis W. Sivers, and Gerald H. Thomas. Constituent Description of n n Elastic Scattering Observables at Large Angles. *Phys. Rev. D*, 20:202, 1979.

[232] A.H. Mueller. Proceedings of 17th rencontre de Moriond, Moriond, 1982 Van (Editions Frontieres, Gif-sur-Yvette, France, 1982) Vol. I p.13.

[233] S.J. Brodsky. Proceedings. of the 13th Int. Symposium on Multiparticle Dynamics, W. Kittel, W. Metzger and A. Stergiou (eds.) Singapore 1982,) p.963.

[234] I. Mardor et al. Nuclear transparency in large momentum transfer quasielastic scattering. *Phys. Rev. Lett.*, 81:5085–5088, 1998.

[235] J. Aclander et al. Nuclear transparency in 90 degree c.m. quasielastic $A(p,2p)$ reactions. *Phys. Rev. C*, 70:015208, 2004, nucl-ex/0405025.

[236] Stanley J. Brodsky and G.F. de Teramond. Spin Correlations, QCD Color Transparency and Heavy Quark Thresholds in Proton Proton Scattering. *Phys. Rev. Lett.*, 60:1924, 1988.

[237] D. Bhetuwal et al. Ruling out color transparency in quasi-elastic $^{12}C(e,e'p)$ up to Q^2 of 14.2 $(\text{GeV}/c)^2$. 11 2020, 2011.00703.

[238] John P. Ralston and Benard Pire. Oscillatory Scale Breaking and the Chromo - Coulomb Phase Shift. *Phys. Rev. Lett.*, 49:1605, 1982.

[239] Michail P. Rekalo and Egle Tomasi-Gustafsson. Threshold J/ψ production in nucleon-nucleon collisions. *New J. Phys.*, 4:68, 2002, nucl-th/0204066.

[240] R.A. Arndt, W.J. Briscoe, I.I. Strakovsky, and R.L. Workman. Updated analysis of NN elastic scattering to 3-GeV. *Phys. Rev. C*, 76:025209, 2007, 0706.2195.

[241] M. Sawamoto and S. Wakaizumi. Analysis of elastic p - p scattering at 6-GeV/c with spin orbit and spin spin coupling eikonal. *Prog. Theor. Phys.*, 62:563–565, 1979.

[242] O.V. Selyugin and O.V. Teryaev. Generalized Parton Distributions and Description of Electromagnetic and Graviton form factors of nucleon. *Phys. Rev. D*, 79:033003, 2009, 0901.1786.

[243] A. Sibirtsev, J. Haidenbauer, H.-W. Hammer, S. Krewald, and U.-G. Meissner. Proton-proton scattering above 3 GeV/c. *Eur. Phys. J. A*, 45:357–372, 2010, 0911.4637.

[244] William P. Ford and J.W. Van Orden. Regge model for nucleon-nucleon spin-dependent amplitudes. *Phys. Rev. C*, 87(1):014004, 2013, 1210.2648.

[245] M.N. Platonova and V.I. Kukulin. Refined Glauber model versus Faddeev calculations and experimental data for pd spin observables. *Phys. Rev. C*, 81:014004, 2010, 1612.08694. [Erratum: Phys. Rev. C 94, 069902 (2016)].

[246] A.A. Temerbayev and Yu.N. Uzikov. Spin observables in proton-deuteron scattering and T-invariance test. *Phys. Atom. Nucl.*, 78(1):35–42, 2015.

[247] D. Mchedlishvili et al. Deuteron analysing powers in deuteron–proton elastic scattering at 1.2 and 2.27 GeV. *Nucl. Phys. A*, 977:14–22, 2018, 1805.05778.

[248] Maria N. Platonova and Vladimir I. Kukulin. Theoretical study of spin observables in pd elastic scattering at energies $T_p = 800\text{--}1000$ MeV. *Eur. Phys. J. A*, 56(5):132, 2020, 1910.05722.

[249] Yu. Uzikov, J. Haidenbauer, A Bazarova, and A. Temerbayev. Spin observables of proton-deuteron elastic scattering at SPD NICA energies within the Glauber model and pN amplitudes Talk at NUCLEUS-2020, (11-17 October, 2020; S-Petersburg, Russia) . Submitted to PEPAN. 11 2020, 2011.04304.

[250] Gerald G. Ohlsen. Polarization transfer and spin correlation experiments in nuclear physics. *Rept. Prog. Phys.*, 35:717–801, 1972.

[251] Yu. Uzikov and C. Wilkin. The analysing powers in proton-deuteron elastic scattering. *Phys. Lett. B*, 793:224–226, 2019, 1902.03596.

[252] Yu. N. Uzikov and A.A. Temerbayev. Null-test signal for T -invariance violation in pd scattering. *Phys. Rev. C*, 92(1):014002, 2015, 1506.08303.

[253] Yu. N. Uzikov and J. Haidenbauer. Polarized proton-deuteron scattering as a test of time-reversal invariance. *Phys. Rev. C*, 94(3):035501, 2016, 1607.04409.

[254] O.V. Selyugin. Gravitation form-factors and spin asymmetries in hadron elastic scattering. 8 2010, 1008.1323.

[255] G. Goggi, M. Cavalli-Sforza, C. Conta, M. Fraternali, G.C. Mantovani, F. Pastore, and G. Alberi. Inelastic Intermediate States in Proton - Deuteron and Deuteron-deuteron Elastic Collisions at the {ISR}. *Nucl. Phys. B*, 149:381–412, 1979.

[256] U. Amaldi and Klaus R. Schubert. Impact Parameter Interpretation of Proton Proton Scattering from a Critical Review of All ISR Data. *Nucl. Phys. B*, 166:301–320, 1980.

[257] A.A. Anselm and V.N. Gribov. Zero pion mass limit in interactions at very high-energies. *Phys. Lett. B*, 40:487–490, 1972.

[258] V.A. Khoze, A.D. Martin, and M.G. Ryskin. t dependence of the slope of the high energy elastic pp cross section. *J. Phys. G*, 42(2):025003, 2015, 1410.0508.

[259] László Jenkovszky, István Szanyi, and Chung-I Tan. Shape of Proton and the Pion Cloud. *Eur. Phys. J. A*, 54(7):116, 2018, 1710.10594.

[260] O.V. Selyugin. New feature in the differential cross sections at 13 TeV measured at the LHC. *Phys. Lett. B*, 797:134870, 2019, 1903.04976.

[261] O.V. Selyugin. Anomaly in the differential cross sections at 13 TeV. 9 2020, 2009.10129.

[262] V.A. Baskov, O.D. Dalkarov, A.I. L'vov, and V.V. Polyanskiy. Studying periphery of the nucleon in diffractive scattering at SPD. Talk at NUCLEUS-2020, (11-17 October, 2020; S-Petersburg, Russia) . Submitted to PEPAN. 2020.

[263] V.V. Abramov. Phenomenology of single-spin effects in hadron production at high energies. *Phys. Atom. Nucl.*, 72:1872–1888, 2009.

[264] L. Frankfurt, E. Piasetsky, M. Sargsian, and M. Strikman. Probing short range nucleon correlations in high-energy hard quasielastic p d reactions. *Phys. Rev. C*, 51:890–900, 1995, nucl-th/9405003.

[265] L.L. Frankfurt, E. Piasetzky, M.M. Sargsian, and M.I. Strikman. On the possibility to study color transparency in the large momentum transfer exclusive d (p, 2 p) n reaction. *Phys. Rev. C*, 56:2752–2766, 1997, hep-ph/9607395.

[266] L.L. Frankfurt, M.M. Sargsian, and M.I. Strikman. Feynman graphs and Gribov-Glauber approach to high-energy knockout processes. *Phys. Rev. C*, 56:1124–1137, 1997, nucl-th/9603018.

[267] G.R. Farrar, H. Liu, L.L. Frankfurt, and M.I. Strikman. Transparency in Nuclear Quasiexclusive Processes with Large Momentum Transfer. *Phys. Rev. Lett.*, 61:686–689, 1988.

[268] L.L. Frankfurt and M.I. Strikman. Hard Nuclear Processes and Microscopic Nuclear Structure. *Phys. Rept.*, 160:235–427, 1988.

[269] Carlos G. Granados and Misak M. Sargsian. Quark Structure of the Nucleon and Angular Asymmetry of Proton-Neutron Hard Elastic Scattering. *Phys. Rev. Lett.*, 103:212001, 2009, 0907.2269.

[270] L. Frankfurt, T.S.H. Lee, G.A. Miller, and M. Strikman. Chiral transparency. *Phys. Rev. C*, 55:909–916, 1997, nucl-th/9608059.

[271] Leonid Frankfurt, Misak Sargsian, and Mark Strikman. Recent observation of short range nucleon correlations in nuclei and their implications for the structure of nuclei and neutron stars. *Int. J. Mod. Phys. A*, 23:2991–3055, 2008, 0806.4412.

[272] O. Hen, G.A. Miller, E. Piasetzky, and L.B. Weinstein. Nucleon-Nucleon Correlations, Short-lived Excitations, and the Quarks Within. *Rev. Mod. Phys.*, 89(4):045002, 2017, 1611.09748.

[273] V.A. Matveev, R.M. Muradian, and A.N. Tavkhelidze. Automodellism in the large - angle elastic scattering and structure of hadrons. *Lett. Nuovo Cim.*, 7:719–723, 1973.

[274] Stanley J. Brodsky and Glennys R. Farrar. Scaling Laws at Large Transverse Momentum. *Phys. Rev. Lett.*, 31:1153–1156, 1973.

[275] G. Bizard et al. Experimental study and baryonic exchange interpretation of the reaction H-2 (D, N) HE-3 in the intermediate-energy region. *Phys. Rev. C*, 22:1632–1637, 1980.

[276] Yu.N. Uzikov. Indication of asymptotic scaling in the reactions dd → p 3-H, dd → n 3-He and pd → pd. *JETP Lett.*, 81:303–306, 2005, hep-ph/0503185.

[277] A.A. Terekhin, V.P. Ladygin, Yu.V. Gurchin, A.Yu. Isupov, A.K. Kurilkin, P.K. Kurilkin, N.B. Ladygina, S.M. Piyadin, S.G. Reznikov, and A.N. Khrenov. Differential Cross Section for Elastic Deuteron–Proton Scattering at the Energy of 700 MeV per Nucleon. *Phys. Atom. Nucl.*, 80(6):1061–1072, 2017.

[278] A.A. Terekhin et al. The differential cross section in deuteron-proton elastic scattering at 500, 750 and 900 MeV/nucleon. *Eur. Phys. J. A*, 55(8):129, 2019.

[279] Yu. N. Uzikov. Search for scaling onset in exclusive reactions with the lightest nuclei. *Eur. Phys. J. A*, 52(8):243, 2016, 1601.05280.

[280] P.K. Kurilkin et al. Measurement of the vector and tensor analyzing powers for dp- elastic scattering at 880 MeV. *Phys. Lett. B*, 715:61–65, 2012, 1207.3509.

[281] P.K. Kurilkin et al. Investigation of the angular dependence of the analyzing powers in the deuteron-proton elastic scattering at the nuclotron. *Phys. Part. Nucl. Lett.*, 8:1081–1083, 2011.

[282] V.P. Ladygin et al. Tensor analyzing power $A(yy)$ in deuteron inclusive breakup on hydrogen and carbon at 9-GeV/c and large proton transverse momenta. *Phys. Lett. B*, 629:60–67, 2005.

[283] S.V. Afanasiev et al. *Phys. Lett. B*, 434:21–25, 1998.

[284] R. Vogt. J/ψ production and suppression. *Phys. Rept.*, 310:197–260, 1999.

[285] F. Maltoni et al. Analysis of charmonium production at fixed-target experiments in the NRQCD approach. *Phys. Lett.*, B638:202–208, 2006, hep-ph/0601203.

[286] S.J. Brodsky, E. Chudakov, P. Hoyer, and J.M. Laget. Photoproduction of charm near threshold. *Phys. Lett. B*, 498:23–28, 2001, hep-ph/0010343.

[287] N.S. Craigie. Lepton and Photon Production in Hadron Collisions. *Phys. Rept.*, 47:1–108, 1978.

[288] Yu.M. Antipov, V.A. Bessubov, N.P. Budanov, Yu.B. Bushnin, S.P. Denisov, Yu.P. Gorin, A.A. Lebedev, A.A. Lednev, Yu.M. Mikhailov, A.I. Petrukhin, S.A. Polovnikov, V.N. Roinishvili, V.S. Selesnev, V.I. Sergienko, D.A. Stoyanova, A.N. Sytin, Ya.A. Vazdik, and F.A. Yotch. j/ψ particle production by 70 gev/c protons. *Physics Letters B*, 60(3):309 – 312, 1976.

[289] C. Lourenço and H.K. Wöhri. Heavy-flavour hadro-production from fixed-target to collider energies. *Physics Reports*, 433(3):127–180, Oct 2006.

[290] E. A. Kuraev, E. S. Kokoulin, and E. Tomasi-Gustafsson. Hard light meson production in (anti)proton-hadron collisions and charge-exchange reactions. *Phys. Part. Nucl. Lett.*, 12(1):1–7, 2015, 1306.5169.

[291] Anar Rustamov. Inclusive meson production in 3.5-GeV p p collisions studied with the HADES spectrometer. *AIP Conf. Proc.*, 1257(1):736–740, 2010.

[292] M.G. Albrow et al. Inclusive ρ^0 Production in pp Collisions at the CERN ISR. *Nucl. Phys. B*, 155:39–51, 1979.

[293] Michail P. Rekalo and Egle Tomasi-Gustafsson. Threshold open charm production in nucleon-nucleon collisions. *Eur. Phys. J.*, A16:575–581, 2003, nucl-th/0210029.

[294] A. Sibirtsev and W. Cassing. Rho meson production and decay in proton nucleus collisions. *Nucl. Phys. A*, 629:717–738, 1998, nucl-th/9712009.

- [295] V. Blobel et al. Observation of Vector Meson Production in Inclusive p p Reactions. *Phys. Lett. B*, 48:73–76, 1974.
- [296] V.N. Baier, Victor S. Fadin, and Valery A. Khoze. Quasireal electron method in high-energy quantum electrodynamics. *Nucl. Phys. B*, 65:381–396, 1973.
- [297] Edward V. Shuryak. Two Scales and Phase Transitions in Quantum Chromodynamics. *Phys. Lett. B*, 107:103–105, 1981.
- [298] Aneesh Manohar and Howard Georgi. Chiral Quarks and the Nonrelativistic Quark Model. *Nucl. Phys. B*, 234:189–212, 1984.
- [299] V.I. Komarov. On the possibility of revealing the transition of a baryon pair state to a six-quark confinement state. *Phys. Part. Nucl. Lett.*, 15(1):69–75, 2018, 1704.06161.
- [300] Vladimir Komarov, Bota Baimurzinova, Ainur Kunsafina, and Dmitry Tsirkov. Centrality criteria of inelastic nucleon-nucleon collisions. 1 2020, 2001.09960.
- [301] Amand Faessler, V.I. Kukulin, and M.A. Shikhalev. Description of intermediate- and short-range NN nuclear force within a covariant effective field theory. *Annals Phys.*, 320:71–107, 2005, nucl-th/0505026.
- [302] T. Hatsuda and T. Kunihiro. Possible critical phenomena associated with the chiral symmetry breaking. *Phys. Lett. B*, 145:7–10, 1984.
- [303] D. Blaschke, Yu.L. Kalinovsky, A.E. Radzhabov, and M.K. Volkov. Scalar sigma meson at a finite temperature in a nonlocal quark model. *Phys. Part. Nucl. Lett.*, 3:327–330, 2006.
- [304] A. Aduszkiewicz et al. Proton-Proton Interactions and Onset of Deconfinement. *Phys. Rev. C*, 102(1):011901, 2020, 1912.10871.
- [305] Bo Andersson, G. Gustafson, G. Ingelman, and T. Sjostrand. Parton Fragmentation and String Dynamics. *Phys. Rept.*, 97:31–145, 1983.
- [306] H. Garcilazo and A. Valcarce. Strangeness -2 Hypertriton. *Phys. Rev. Lett.*, 110(1):012503, 2013, 1212.1369.
- [307] Avraham Gal. Comment on recent Strangeness -2 predictions. *Phys. Rev. Lett.*, 110:179201, 2013, 1301.1241.
- [308] H. Garcilazo and A. Valcarce. Reply to "Comment on Strangeness -2 hypertriton". *Phys. Rev. Lett.*, 110:179202, 2013, 1304.3552.
- [309] I.N. Filikhin and A. Gal. Faddeev-Yakubovsky search for (Lambda-Lambda) H-4. *Phys. Rev. Lett.*, 89:172502, 2002, nucl-th/0209003.
- [310] H. Nemura, Y. Akaishi, and Khin Swe Myint. Stochastic variational search for H-4(Lambda Lambda). *Phys. Rev. C*, 67:051001, 2003, nucl-th/0211082.
- [311] H. Garcilazo and A. Valcarce. Nonexistence of a Λ nn bound state. *Phys. Rev. C*, 89(5):057001, 2014, 1507.08061.
- [312] E. Hiyama, S. Ohnishi, B.F. Gibson, and Th. A. Rijken. Three-body structure of the nn Λ system with Λ N – Σ N coupling. *Phys. Rev. C*, 89(6):061302, 2014, 1405.2365.

[313] Jean-Marc Richard, Qian Wang, and Qiang Zhao. Lightest neutral hypernuclei with strangeness -1 and -2 . *Phys. Rev. C*, 91(1):014003, 2015, 1404.3473.

[314] Jean-Marc Richard, Qian Wang, and Qiang Zhao. Possibility of a new neutral hypernucleus $_{\Lambda\Lambda}^4n = (n, n, \Lambda, \Lambda)$. *J. Phys. Conf. Ser.*, 569(1):012079, 2014, 1408.1323.

[315] Thomas A. Rijken, M.M. Nagels, and Yasuo Yamamoto. Baryon-baryon interactions: Nijmegen extended-soft-core models. *Prog. Theor. Phys. Suppl.*, 185:14–71, 2010.

[316] H. Polinder, J. Haidenbauer, and U.-G. Meissner. Strangeness $S = -2$ baryon-baryon interactions using chiral effective field theory. *Phys. Lett. B*, 653:29–37, 2007, 0705.3753.

[317] J. Haidenbauer, S. Petschauer, N. Kaiser, U.-G. Meissner, A. Nogga, and W. Weise. Hyperon-nucleon interaction at next-to-leading order in chiral effective field theory. *Nucl. Phys. A*, 915:24–58, 2013, 1304.5339.

[318] J. Haidenbauer, Ulf-G. Meißner, and S. Petschauer. Strangeness $S = -2$ baryon–baryon interaction at next-to-leading order in chiral effective field theory. *Nucl. Phys. A*, 954:273–293, 2016, 1511.05859.

[319] Shreyasi Acharya et al. Study of the Λ - Λ interaction with femtoscopy correlations in pp and p-Pb collisions at the LHC. *Phys. Lett. B*, 797:134822, 2019, 1905.07209.

[320] D. Lonardoni, S. Gandolfi, and F. Pederiva. Effects of the two-body and three-body hyperon-nucleon interactions in Λ -hypernuclei. *Phys. Rev. C*, 87:041303, 2013, 1301.7472.

[321] A.V. Efremov. Quark-parton picture of the cumulative production. *Fiz. Elem. Chast. Atom. Yadra*, 13:613–634, 1982.

[322] Alexander Andrianov, Vladimir Andrianov, and Domenec Espriu. Chiral Imbalance in QCD and its consequences. *EPJ Web Conf.*, 125:01009, 2016.

[323] A.M. et al. Baldin. The Observation of High Energy Pions in Interactions of Relativistic Deuterons with Nuclei. *AIP Conf. Proc.*, 2:131–139, 1971.

[324] A.M. Baldin, N. Giordanescu, L.K. Ivanova, N.S. Moroz, A.A. Povtoreiko, V.B. Radomanov, V.S. Stavinsky, and V.N. Zubarev. An Experimental Investigation of Cumulative Meson Production. *Sov. J. Nucl. Phys.*, 20:629–634, 1975.

[325] A.V. Efremov, A.B. Kaidalov, V.T. Kim, G.I. Lykasov, and N.V. Slavin. Cumulative Hadron Production in Quark Models of Flucton Fragmentation. *Sov. J. Nucl. Phys.*, 47:868, 1988.

[326] V.T. Kim. QCD Evolution of Nuclear Structure Functions at Large X: EMC Effect and Cumulative Processes. *Phys. Part. Nucl. Lett.*, 15(4):384–386, 2018.

[327] S.V. Boyarinov et al. Production of Cumulative K^- Mesons on Protons at 10- $\{\text{GeV}\}$ Energy. *Sov. J. Nucl. Phys.*, 50:996–1000, 1989.

[328] S.V. Boyarinov et al. The Cumulative production of anti-protons by 10 GeV protons bombarding nuclear targets. *Sov. J. Nucl. Phys.*, 54:71–74, 1991.

[329] A.V. Efremov, V.T. Kim, and G.I. Lykasov. Hard Hadron - Nucleus Processes and Multi - Quark Configurations in Nuclei. *Sov. J. Nucl. Phys.*, 44:151, 1986.

[330] M. Braun and V. Vechernin. Nuclear structure functions and particle production in the cumulative region in the parton model. *Nucl. Phys. B*, 427:614–640, 1994.

- [331] Mauro Anselmino, Enrico Predazzi, Svante Ekelin, Sverker Fredriksson, and D.B. Lichtenberg. Diquarks. *Rev. Mod. Phys.*, 65:1199–1234, 1993.
- [332] A. Breakstone et al. A Diquark Scattering Model for High p_T Proton Production in pp Collisions at the {ISR}. *Z. Phys. C*, 28:335, 1985.
- [333] V.T. Kim. Diquarks as a Source of Large p_T Baryons in Hard Nucleon Collisions. *JINR-E2-87-75 (1987) Dubna*.
- [334] V.T. Kim. Diquarks and Dynamics of Large p_T Baryon Production. *Mod. Phys. Lett. A*, 3:909–916, 1988.
- [335] Victor t. Kim, Andrey A. Shavrin, and Andrey V. Zelenov. Diquark Dynamics in Large p_T Baryon Production. *Phys. Part. Nucl. Lett.*, to appear.
- [336] A.V. Efremov and V.T. Kim. Diquarks Role in Large p_T Deuteron and H-dihyperon Production in hard nucleon Collisions. *JINR-E2-87-74 (1987) Dubna*.
- [337] Ya. I. Azimov. Unexpected Mesons X, Y, Z, ... (tetraquarks? hadron molecules? ...). 2 2015, 1502.01279.
- [338] M.Yu. Barabanov, A.S. Vodopyanov, and S.L. Olsen. New research of charmonium over $D\bar{D}$ threshold using the antiproton beam with momentum ranging from 1 to 15 GeV/c. *Phys. Atom. Nucl.*, 77:126–130, 2014.
- [339] M.Yu. Barabanov, A.S. Vodopyanov, A.I. Zinchenko, and S.L. Olsen. Perspective Study of Charmonium and Exotics above the $D\bar{D}$ Threshold. *Phys. Atom. Nucl.*, 79(1):126–129, 2016.
- [340] Robert L. Jaffe and Frank Wilczek. Diquarks and exotic spectroscopy. *Phys. Rev. Lett.*, 91:232003, 2003, hep-ph/0307341.
- [341] Jennifer Rittenhouse West, Stanley J. Brodsky, Guy F. de Teramond, Alfred S. Goldhaber, and Ivan Schmidt. QCD Hidden-Color Hexa-diquark in the Central Core of Nuclei. 4 2020, 2004.14659.
- [342] Stanley J. Brodsky, I.A. Schmidt, and G.F. de Teramond. Nuclear bound quarkonium. *Phys. Rev. Lett.*, 64:1011, 1990.
- [343] S.J. Brodsky, A.H. Hoang, Johann H. Kuhn, and T. Teubner. Angular distributions of massive quarks and leptons close to threshold. *Phys. Lett. B*, 359:355–361, 1995, hep-ph/9508274.
- [344] K. Tsushima, D.H. Lu, G. Krein, and A.W. Thomas. J/Ψ -nuclear bound states. *Phys. Rev. C*, 83:065208, 2011, 1103.5516.
- [345] Stanley J. Brodsky. Novel QCD physics at NICA. *Eur. Phys. J. A*, 52(8):220, 2016.
- [346] Roel Aaij et al. Observation of $J/\psi p$ Resonances Consistent with Pentaquark States in $\Lambda_b^0 \rightarrow J/\psi K^- p$ Decays. *Phys. Rev. Lett.*, 115:072001, 2015, 1507.03414.
- [347] Roel Aaij et al. Observation of a narrow pentaquark state, $P_c(4312)^+$, and of two-peak structure of the $P_c(4450)^+$. *Phys. Rev. Lett.*, 122(22):222001, 2019, 1904.03947.
- [348] Rinaldo Baldini, Simone Pacetti, Adriano Zallo, and Antonino Zichichi. Unexpected features of $e^+ e^- \rightarrow p$ anti- p and $e^+ e^- \rightarrow \Lambda$ anti- Λ cross sections near threshold. *Eur. Phys. J. A*, 39:315–321, 2009, 0711.1725.

[349] Rinaldo Baldini Ferroli, Simone Pacetti, and Adriano Zallo. Time-like baryon form factors near threshold: Status and perspectives. *Nucl. Phys. B Proc. Suppl.*, 219-220:32–38, 2011.

[350] P. A. R. Ade et al. Planck 2013 Results. I. Overview of Products and Scientific Results. *Astronomy & Astrophysics*, 571:A1, 2014.

[351] Debasish Majumdar. *Dark Matter: An Introduction*. CRC Press, Aug 2014.

[352] Oliver Buchmueller, Caterina Doglioni, and Lian-Tao Wang. Search for Dark Matter at Colliders. *Nature Physics*, 13(3):217–223, Mar 2017.

[353] M. Aguilar et al. First Result from the Alpha Magnetic Spectrometer on the International Space Station: Precision Measurement of the Positron Fraction in Primary Cosmic Rays of 0.5–350 GeV. *Physical Review Letters*, 110(14), Apr 2013.

[354] M. Aguilar et al. Antiproton Flux, Antiproton-to-Proton Flux Ratio, and Properties of Elementary Particle Fluxes in Primary Cosmic Rays Measured with the Alpha Magnetic Spectrometer on the International Space Station. *Physical Review Letters*, 117(9), Aug 2016.

[355] Gaëlle Giesen, Mathieu Boudaud, Yoann Génolini, Vivian Poulin, Marco Cirelli, Pierre Salati, and Pasquale D. Serpico. AMS-02 Antiprotons, At Last! Secondary Astrophysical Component and Immediate Implications for Dark Matter. *Journal of Cosmology and Astroparticle Physics*, 2015(09):023–023, Sep 2015.

[356] Mattia di Mauro, Fiorenza Donato, Andreas Goudelis, and Pasquale Dario Serpico. New Evaluation of the Antiproton Production Cross Section for Cosmic Ray Studies. *Physical Review D*, 90(8), Oct 2014.

[357] Fiorenza Donato, Michael Korsmeier, and Mattia Di Mauro. Prescriptions on Antiproton Cross Section Data for Precise Theoretical Antiproton Flux Predictions. *Physical Review D*, 96(4), Aug 2017.

[358] A. Guskov and R. El-Kholy. On the Possibility to Study Antiproton Production at the SPD Detector at NICA Collider for Dark Matter Search in Astrophysical Experiments. *Physics of Particles and Nuclei Letters*, 16(3):216–223, may 2019.

[359] V. Alexakhin, A. Guskov, Z. Hayman, R. El-Kholy, and A. Tkachenko. On the Study of Antiprotons Yield in Hadronic Collisions at NICA SPD, 2020, 2008.04136.

[360] A. D. Kovalenko, Yu. N. Filatov, A. M. Kondratenko, M. A. Kondratenko, and V. A. Mikhaylov. Polarized deuterons and protons at NICA@JINR. *Physics of Particles and Nuclei*, 45(1):325–326, Jan 2014.

[361] Yu. N. Filatov, A. M. Kondratenko, M. A. Kondratenko, Ya. S. Derbenev, and V. S. Morozov. Transparent Spin Method for Spin Control of Hadron Beams in Colliders. *Phys. Rev. Lett.*, 124(19):194801, 2020, 2003.11469.

[362] A. D. Kovalenko, A. V. Butenko, V. A. Mikhaylov, M. A. Kondratenko, A. M. Kondratenko, and Yu N. Filatov. Spin Transparency Mode in the NICA Collider with Solenoid Siberian Snakes for Proton and Deuteron Beam. *J. Phys. Conf. Ser.*, 938(1):012025, 2018.

[363] Y. N. Filatov, A. M. Kondratenko, M. A. Kondratenko, Y. S. Derbenev, V. S. Morozov, and A. D. Kovalenko. Spin response function technique in spin-transparent synchrotrons. *Eur. Phys. J. C*, 80(8):778, 2020.

[364] A. Kovalenko, N. Agapov, Yu. Filatov, Kekelidze V., Lednický R., Meshkov I., Mikhaylov V., Sidorin A., Sorin A., and Trubnikov G. The NICA Facility in polarized proton operation mode. *IPAC11, San Sebastian, Spain, 4-9 Sept, TUPZ004, pp. 1804-1806*, 2011.

[365] A. Bazilevsky and W. Fischer. Impact of 3D polarization profiles on spin-dependent measurements in colliding beam experiments. *Phys. Part. Nucl.*, 45:257–259, 2014.

[366] Yu.N. Filatov, A.D. Kovalenko, A.V. Butenko, E.M. Syresin, V.A. Mikhaylov, S.S. Shimanskiy, A.M. Kondratenko, and M.A. Kondratenko. Spin Transparency Mode in the NICA Collider. *EPJ Web Conf.*, 204, 2019.

[367] A.M. Kondratenko, M.A. Kondratenko, A.D. Kovalenko, A.V. Butenko, S.S. Shimanskiy, E.M. Syresin, S.V. Vinogradov, and Y.N. Filatov. Kinematics of proton and deuteron beam polarization in the transparent spin mode of the NICA collider. *Journal of Physics: Conference Series*, 1435(1), 2020.

[368] Yu.N. Filatov, A.D. Kovalenko, A.M. Kondratenko, M.A. Kondratenko, and V.A. Mikhaylov. Proton And Deuteron Polarization Control In NICA Collider Using Small Solenoids. *XV Workshop on HESP DSPIN 2013 Proceedings, Dubna*, pages 351–354, 2013.

[369] A.D. Kovalenko, A.V. Butenko, V.D. Kekelidze, V.A. Mikhaylov, A.M. Kondratenko, M.A. Kondratenko, and Yu.N. Filatov. Ion polarization control in the MPD and SPD detectors of the NICA collider. *6th International Particle Accelerator Conference, IPAC 2015*, pages 2031–2033, 2015.

[370] Y.S. Derbenev, Y.N. Filatov, A.M. Kondratenko, M.A. Kondratenko, and V.S. Morozov. Siberian snakes, figure-8 and spin transparency techniques for high precision experiments with polarized hadron beams in colliders. *Symmetry*, 13(3):1–26, 2021.

[371] A.V. Butenko, A.D. Kovalenko, V.A. Mikhaylov, A.M. Kondratenko, M.A. Kondratenko, and Yu.N. Filatov. Solenoid Siberian snake without compensation of betatron oscillation coupling in NUCLOTRON@JINR. *IPAC 2014: Proceedings of the 5th International Particle Accelerator Conference*, pages 1162–1164, 2014.

[372] A. D. Kovalenko, A. V. Butenko, V. D. Kekelidze, V. A. Mikhaylov, A. M. Kondratenko, M. A. Kondratenko, and Yu. N. Filatov. NICA Facility in Polarized Proton and Deuteron Mode. *International Journal of Modern Physics: Conference Series*, 40:1660096, 2016, <https://doi.org/10.1142/S201019451660096X>.

[373] A.D. Kovalenko, A.V. Butenko, V.D. Kekelidze, V.A. Mikhaylov, M.A. Kondratenko, A.M. Kondratenko, and Y.N. Filatov. Orbital parameters of proton and deuteron beams in the NICA collider with solenoid Siberian snakes. *Journal of Physics: Conference Series*, 678(1), 2016.

[374] A D Kovalenko, A V Butenko, V D Kekelidze, V A Mikhaylov, M A Kondratenko, A M Kondratenko, and Yu N Filatov. Numerical calculation of ion polarization in the NICA collider. *Journal of Physics: Conference Series*, 678(1):012023, 2016.

[375] Ya. S. Derbenev, Kondratenko A. M., Kondratenko M. A., Morozov V. S., and Filatov Yu. N. Spin-Flipping Systems For Storage Rings. *Proceedings of XIV Advanced Research Workshop on High Energy Spin Physics (DSPIN-11), Dubna*, pp.377-384, 2011.

[376] I.B. Issinsky, A.D. Kovalenko, V.A. Mikhaylov, A.M. Kondratenko, and Yu.N. Filatov. Polarized Deuterons Acceleration in Nuclotron. *Proceedings of III Int. Symposium “Dubna Deuteron-95”, Dubna*, pages 169–176, 1995.

[377] N.I. Golubeva, I.B. Issinskii, A.M. Kondratenko, M.A. Kondratenko, V.A. Mikhailov, and E.A. Strokovskii. Study of Depolarization of Deuteron and Proton Beams in the Nuclotron Rings. *Preprint P9-2002-289, JINR, Dubna, (in Russian)*, 2002.

[378] S. Vokal, A.D. Kovalenko, A.M. Kondratenko, M.A. Kondratenko, V.A. Mikhailov, Yu.N. Filatov, and S.S. Shimanskii. Program of polarization studies and capabilities of accelerating polarized proton and light nuclear beams at the nuclotron of the joint institute for nuclear research. *Physics of Particles and Nuclei Letters*, 6(1):48–58, 2009.

[379] Yu. N. Filatov, A. D. Kovalenko, A. V. Butenko, A. M. Kondratenko, M. A. Kondratenko, and V. A. Mikhaylov. Polarized proton beam acceleration at the Nuclotron with the use of the solenoid Siberian Snake. *Physics of Particles and Nuclei*, 45(1):262–264, Jan 2014.

[380] Yu. Filatov et al. Orbital Parameters of Proton Beam in Nuclotron with Solenoid Siberian Snake. *Proceedings of XV Advanced Research Workshop on High Energy Spin Physics (DSPIN-13)*, pages 371–374, 2013.

[381] Yu.N. Filatov, A.V. Butenko, A.D. Kovalenko, V.A. Mikhaylov, A.M. Kondratenko, and M.A. Kondratenko. Acceleration of Polarized Proton and Deuteron Beams in Nuclotron at JINR. (8):2349–2351, May 2017.

[382] A D Kovalenko, A V Butenko, V A Mikhaylov, M A Kondratenko, A M Kondratenko, and Yu N Filatov. Acceleration of Polarized Protons up to 3.4 GeV/c in the Nuclotron at JINR. *Journal of Physics: Conference Series*, 938(1):012018, 2017.

[383] Kovalenko A.D., Perepelkin E.E., Superconducting Magnetic System of the SPD setup at NICA, EUCAS2019, Glasgow, 2019.

[384] B Abelev et al. Technical Design Report for the Upgrade of the ALICE Inner Tracking System. *J. Phys. G*, 41:087002, 2014.

[385] Luciano Musa. Letter of Intent for an ALICE ITS Upgrade in LS3. Technical Report CERN-LHCC-2019-018. LHCC-I-034, CERN, Geneva, Dec 2019.

[386] A. Sergi. NA62 Spectrometer: A Low Mass Straw Tracker. *Phys. Procedia*, 37:530–534, 2012.

[387] H. Nishiguchi et al. Development of an extremely thin-wall straw tracker operational in vacuum – The COMET straw tracker system. *Nucl. Instrum. Meth. A*, 845:269–272, 2017.

[388] M. Anelli et al. A facility to Search for Hidden Particles (SHiP) at the CERN SPS. 4 2015, 1504.04956.

[389] MyeongJae Lee. The Straw-tube Tracker for the Mu2e Experiment. *Nucl. Part. Phys. Proc.*, 273-275:2530–2532, 2016.

[390] V.N. Bychkov et al. Construction and manufacture of large size straw-chambers of the COMPASS spectrometer tracking system. *Part. Nucl. Lett.*, 111:64–73, 2002.

[391] K. Platzer, W. Dunnweber, N. Dedek, M. Faessler, R. Geyer, C. Ilgner, V. Peshekhonov, and H. Wellenstein. Mapping the large area straw detectors of the COMPASS experiment with X-rays. *IEEE Trans. Nucl. Sci.*, 52:793–798, 2005.

[392] V.Yu. Volkov, P.V. Volkov, T.L. Enik, G.D. Kekelidze, V.A. Kramarenko, V.M. Lysan, D.V. Peshekhonov, A.A. Solin, and A.V. Solin. Straw Chambers for the NA64 Experiment. *Phys. Part. Nucl. Lett.*, 16(6):847–858, 2019.

- [393] E. Abat et al. The ATLAS TRT barrel detector. *JINST*, 3:P02014, 2008.
- [394] E. Abat et al. The ATLAS TRT end-cap detectors. *JINST*, 3:P10003, 2008.
- [395] E. Abat et al. The ATLAS Transition Radiation Tracker (TRT) proportional drift tube: Design and performance. *JINST*, 3:P02013, 2008.
- [396] P. Gianotti et al. The Straw Tube Trackers of the PANDA Experiment. In *3rd International Conference on Advancements in Nuclear Instrumentation Measurement Methods and their Applications*, 2013, 1307.4537.
- [397] L. Glonti, T. Enik, V. Kekelidze, A. Kolesnikov, D. Madigozhin, N. Molokanova, S. Movchan, Yu Potrebenikov, and S. Shkarovskiy. Longitudinal tension and mechanical stability of a pressurized straw tube. *Instruments*, 2(4):27, 2018, 1810.04843.
- [398] R. Acciarri et al. Long-Baseline Neutrino Facility (LBNF) and Deep Underground Neutrino Experiment (DUNE). 2016, 1601.02984.
- [399] IHEP page <http://exwww.ihep.su/scint/mold/product.htm>.
- [400] Kuraray page <http://kuraraypsf.jp/psf/ws.html>.
- [401] Hamamatsu web page <https://www.hamamatsu.com/eu/en/product/optical-sensors/mppc/index.html>.
- [402] HVsys web page <http://hvsys.ru>.
- [403] AFI Electronics web page <https://afi.jinr.ru/ADC64>.
- [404] V. M. Abazov, G. D. Alexeev, Yu. I. Davydov, V. L. Malyshev, V. V. Tokmenin, and A. A. Piskun. Comparative analysis of the performance characteristics of mini-drift tubes with different design. *Instruments and Experimental Techniques*, 53(3):356–361, May 2010.
- [405] V. M. Abazov, G. D. Alexeev, Yu. I. Davydov, V. L. Malyshev, A. A. Piskun, and V. V. Tokmenin. Coordinate accuracy of mini-drift tubes in detection of an induced signal. *Instruments and Experimental Techniques*, 53(5):648–652, Sep 2010.
- [406] PANDA Collaboration. Technical Design Report for the: PANDA Muon System (AntiProton Annihilations at Darmstadt). Strong Interaction Studies with Antiprotons <https://panda.gsi.de/publication/re-tdr-2012-003>. September 2012.
- [407] V. M. Abazov et al. The Muon system of the run II D0 detector. *Nucl. Instrum. Meth.*, A552:372–398, 2005, physics/0503151.
- [408] P. Abbon et al. The COMPASS experiment at CERN. *Nucl. Instrum. Meth.*, A577:455–518, 2007, hep-ex/0703049.
- [409] G. D. Alekseev, M. A. Baturitsky, O. V. Dvornikov, A. I. Khokhlov, V. A. Mikhailov, I. A. Odnokloubov, and V. V. Tokmenin. The eight-channel ASIC bipolar transresistance amplifier D0M AMPL-8.3. *Nucl. Instrum. Meth.*, A462:494–505, 2001.
- [410] G.D Alexeev, M.A Baturitsky, O.V Dvornikov, V.A Mikhailov, I.A Odnokloubov, and V.V Tokmenin. The eight-channel fast comparator IC. *Nucl. Instrum. Meth.*, A423(1):157 – 162, 1999.

- [411] G. D. Alekseev, M. A. Baturitsky, O. V. Dvornikov, A. I. Khokhlov, V. A. Mikhailov, I. A. Odnokloubov, A. A. Shishkin, V. V. Tokmenin, and S. F. Zhirikov. The D0 forward angle muon system front-end electronics design. *Nucl. Instrum. Meth.*, A473:269–282, 2001.
- [412] G.D. Alekseev, A. Maggiora, and N.I. Zhuravlev. Digital Front-end Electronics for COMPASS Muon-Wall 1 Detector. *JINR Preprint*, E13-2005-37, 2005.
- [413] V.A. Babkin et al. MPD NICA, Technical Design Report of the Time of Flight System (TOF). 11 2018.
- [414] A.N. Akindinov et al. Latest results on the performance of the multigap resistive plate chamber used for the ALICE TOF. *Nucl. Instrum. Meth. A*, 533:74–78, 2004.
- [415] V. Ammosov et al. The HARP resistive plate chambers: Characteristics and physics performance. *Nucl. Instrum. Meth. A*, 602:639–643, 2009.
- [416] The STAR TOF Collaboration, Proposal for a Large Area Time of Flight System for STAR, 2004.
- [417] J. Velkovska et. al., Multi-gap Resistive Plate Chambers: Time-of-Flight system of the PHENIX high-pT Detector. Conceptual Design Report.
- [418] A.Golovin et. al., Technical Design Report of the Time of Flight System (TOF-700) BM@N, 2017.
- [419] N.A. Kuzmin, E.A. Ladygin, V.P. Ladygin, Yu.P. Petukhov, S.Ya. Sychkov, A.A. Semak, M.N. Ukhanov, and E.A. Usenko. High-rate glass MRPC for fixed target experiments at Nuclotron. *Nucl. Instrum. Meth. A*, 916:190–194, 2019, 1811.08637.
- [420] A. Akindinov et al. RPC with low-resistive phosphate glass electrodes as a candidate for the CBM TOF. *Nucl. Instrum. Meth.*, A572:676–681, 2007, physics/0612083.
- [421] V. Ammosov et al. Performance of RPC with low-resistive silicate glass electrodes exposed to an intense continuous electron beam. *Nucl. Instrum. Meth.*, A576:331–336, 2007.
- [422] Y. Haddad, G. Grenier, I. Laktineh, N. Lumb, and S. Cauwenbergh. High Rate Resistive Plate Chamber for LHC detector upgrades. *Nucl. Instrum. Meth.*, A718:424–426, 2013, 1211.5698.
- [423] A. Akindinov et al. Radiation-hard ceramic Resistive Plate Chambers for forward TOF and T0 systems. *Nucl. Instrum. Meth.*, A875:203, 2017.
- [424] Jing-Bo Wang et al. Development of multi-gap resistive plate chambers with low-resistive silicate glass electrodes for operation at high particle fluxes and large transported charges. *Nucl. Instrum. Meth. A*, 621:151–156, 2010.
- [425] D. Gonzalez-Diaz, D. Belver, A. Blanco, R. Ferreira-Marques, P. Fonte, J.A. Garzon, L. Lopes, A. Mangiarotti, and J. Marin. The effect of temperature on the rate capability of glass timing RPCs. *Nucl. Instrum. Meth. A*, 555:72–79, 2005.
- [426] A. Aliche, G. Cara Romeo, D. Hatzifotiadou, G. Valenti, M.C.S. Williams, Jinsook Kim, Y. Sun, D. Yakorev, and A. Zichichi. Aging and rate effects of the Multigap RPC studied at the Gamma Irradiation Facility at CERN. *Nucl. Instrum. Meth. A*, 579:979–988, 2007.
- [427] V. A. Gapienko, O. P. Gavrilchuk, A. A. Golovin, A. A. Semak, S. Ya. Sychkov, Yu. M. Sviridov, E. A. Usenko, and M. N. Ukhanov. Studying the counting rate capability of a glass multigap resistive plate chamber at an increased operating temperature. *Instrum. Exp. Tech.*, 56:265–270, 2013. [Prib. Tekh. Eksp. 2013, no. 3, 21(2013)].

[428] V.V. Ammosov, O.P. Gavrilchuk, V.A. Gapienko, V.G. Zaets, N.A. Kuzmin, Yu.M. Sviridov, A.A. Semak, S.Ya. Sychkov, E.A. Usenko, and A.I. Yukaev. Time resolution of a 6-gap resistive plate chamber with strip readout. *Prib. Tekh. Eksp.*, 2010(2):20–24, 2010.

[429] B. Singh et al. Technical Design Report for the: Strong Interaction Studies with Antiprotons. 7 2018.

[430] Miki Nishimura et al. Pixelated Positron Timing Counter with SiPM-readout Scintillator for MEG II experiment. *PoS*, PhotoDet2015:011.

[431] V.V. Anashin et al. PEPAN v.44, (2013) 1263 (in Russian).

[432] I.V. Ovtin et al. "Aerogel Cherenkov Counters of the KEDR Detector", CERN-BINP Workshop for Young Scientists in e^+e^- Colliders 2016, Geneva; CERN-Proceedings-2017-001 (CERN, Geneva, 2017).

[433] A. Abashian et al. The Belle Detector. *Nucl. Instrum. Meth. A*, 479:117–232, 2002.

[434] A.E. Antropov et al. Sector multipad prototype of the FMD-MCP detector for ALICE. *Nucl. Instrum. Meth. A*, 419:654–659, 1998.

[435] A.A. Baldin, G.A. Feofilov, P. Har'yuzov, and F.F. Valiev. Fast beam-beam collisions monitor for experiments at NICA. *Nucl. Instrum. Meth. A*, 958:162154, 2020.

[436] M. Bondila et al. Results of in-beam tests of an MCP-based vacuum sector prototype of the T0/centrality detector for ALICE. *Nucl. Instrum. Meth.*, A478:220–224, 2002.

[437] Hamamatsu S12572-010P Datasheet.

[438] A.V. Tishevsky et al., talk at ICAPP2020, submitted to J.Phys.:Conf.Ser.

[439] A. Adare et al. Inclusive cross section and single transverse spin asymmetry for very forward neutron production in polarized p+p collisions at s=200 GeV. *Phys. Rev.*, D88(3):032006, 2013, 1209.3283.

[440] C. Adloff et al. Construction and Commissioning of the CALICE Analog Hadron Calorimeter Prototype. *JINST*, 5:P05004, 2010, 1003.2662.

[441] I. G Alekseev et al. RHIC pC CNI polarimeter: Experimental setup and physics results. *AIP Conf. Proc.*, 675:812–816, 2003. [,812(2003)].

[442] S. Trentalange. talk "STAR Spin Analysis Update", 2004, 2003.

[443] C. E. Allgower et al. Measurement of analyzing powers of pi+ and pi- produced on a hydrogen and a carbon target with a 22-GeV/c incident polarized proton beam. *Phys. Rev.*, D65:092008, 2002.

[444] B. Z. Kopeliovich, I. K. Potashnikova, Ivan Schmidt, and J. Soffer. Single transverse spin asymmetry of forward neutrons. *Phys. Rev.*, D84:114012, 2011, 1109.2500.

[445] Clemens Adler, Alexei Denisov, Edmundo Garcia, Michael J. Murray, Herbert Strobele, and Sebastian N. White. The RHIC zero degree calorimeter. *Nucl. Instrum. Meth.*, A470:488–499, 2001, nucl-ex/0008005.

[446] B.M. Michelson. Event-Driven Architecture Overview. Patricia Seybold Group / Business-Driven ArchitectureSM, February 2, pp. 1–8 (2006).

- [447] Etschberger, K. IXXAT Automation GmbH. Controller Area Network (CAN) Basics, Protocols, Chips and Applications. IXXAT Press, 2001. ISBN3-00-007376-0.
- [448] J. Chaize, A. Götz, W. Klotz, J. Meyer, M. Perez, E. Taurel, and P. Verdier,. TANGO, 8th International Conference on Accelerator & Large Experimental Physics Control Systems, 2001, San Jose, California (JACoW, 2001).
- [449] E.V. Gorbachev, V.A. Andreev, A.E. Kirichenko, D.V. Monakhov, S.V. Romanov, T.V. Rukoyatkin, G.S. Sedykh, and V.I. Volkov. The Nuclotron and Nica control system development status. *Phys. Part. Nucl. Lett.*, 13(5):573–578, 2016.
- [450] WinCC-OA: Introduction for Newcomers <https://lhcb-online.web.cern.ch/ecs/PVSSIntro.htm>.
- [451] H Boterenbrood, H J Burckhart, J Cook, V Filimonov, Björn I Hallgren, and F Varela. Vertical Slice of the ATLAS Detector Control System. 2001.
- [452] Dominik Steffen et al. Overview and Future Developments of the intelligent, FPGA-based DAQ (iDAQ) of COMPASS. *PoS, ICHEP2016*:912, 2016.
- [453] M. Bodlak, V. Frolov, V. Jary, S. Huber, I. Konorov, D. Levit, J. Novy, R. Salac, and M. Virius. Development of new data acquisition system for compass experiment. *Nuclear and Particle Physics Proceedings*, 273-275:976 – 981, 2016. 37th International Conference on High Energy Physics (ICHEP).
- [454] I. Konorov. Data Acquisition System for the Spin Physics Detector, 2018.
- [455] I. Konorov. COMPASS Front-End, Trigger and DAQ Workshop, CERN 02–03 March 2020, <https://indico.cern.ch/event/863068/>.
- [456] B.M. Veit. COMPASS Front-End, Trigger and DAQ Workshop, CERN 02–03 March 2020, <https://indico.cern.ch/event/863068/>.
- [457] S. Huber. COMPASS Front-End, Trigger and DAQ Workshop, CERN 02–03 March 2020, <https://indico.cern.ch/event/863068/>.
- [458] V. Frolov. COMPASS Front-End, Trigger and DAQ Workshop, CERN 02–03 March 2020, <https://indico.cern.ch/event/863068/>.
- [459] M. Kavatsyuk, E. Guliyev, P.J.J. Lemmens, H. Löhner, and G. Tambave. VHDL implementation of feature-extraction algorithm for the PANDA electromagnetic calorimeter. In *2010 IEEE Nuclear Science Symposium, Medical Imaging Conference, and 17th Room Temperature Semiconductor Detectors Workshop*, pages 785–788, 2010.
- [460] M. Ziembicki. Workshop FEETDAQ2019, Munchen 11–13 Feb 2019, <https://indico.cern.ch/event/783347>.
- [461] M. Suchenek. Workshop FEETDAQ2019, Munchen 11–13 Feb 2019, <https://indico.cern.ch/event/783347>.
- [462] I. Konorov. Workshop FEETDAQ2019, Munchen 11–13 Feb 2019, <https://indico.cern.ch/event/783347>.
- [463] C. Ghabrous Larrea, K. Harder, D. Newbold, D. Sankey, A. Rose, A. Thea, and T. Williams. IPbus: a flexible Ethernet-based control system for xTCA hardware. *JINST*, 10(02):C02019, 2015.

- [464] Dominic Gaisbauer, Yunpeng Bai, Stefan Huber, Igor Konorov, Dymitro Levit, Stephan Paul, and Dominik Steffen. Unified communication framework. In *20th IEEE-NPSS Real Time Conference*, 2016.
- [465] J Serrano, P Alvarez, M Cattin, E Garcia Cota, J Lewis, P Moreira, T Wlostowski, G Gaderer, P Loschmidt, J Dedic, R Bär, T Fleck, M Kreider, C Prados, and S Rauch. The White Rabbit Project. Technical Report CERN-ATS-2009-096, CERN, Geneva, Nov 2009.
- [466] White Rabbit project repository, <https://ohwr.org/project/white-rabbit>.
- [467] I. Konorov, L Schmitt, and B. Grube. Compass tcs documentation, compass note, date: 20 june 2001.
- [468] Ph. Abbon et al. The COMPASS Setup for Physics with Hadron Beams. *Nucl. Instrum. Meth. A*, 779:69–115, 2015, 1410.1797.
- [469] Dmitriy Baranov, Sergey Mitsyn, Pavel Goncharov, and Gennady Ososkov. The Particle Track Reconstruction based on deep Neural networks. *EPJ Web Conf.*, 214:06018, 2019, 1812.03859.
- [470] G. Ososkov et al. Tracking on the BESIII CGEM inner detector using deep learning. *Computer Research and Modeling*, 10:1–24, 20.
- [471] Fernando Barreiro Megino et al. PanDA: Evolution and Recent Trends in LHC Computing. *Procedia Comput. Sci.*, 66:439–447, 2015.
- [472] F. Stagni, A. Tsaregorodtsev, L. Arrabito, A. Sailer, T. Hara, and X. Zhang. DIRAC in Large Particle Physics Experiments. *J. Phys. Conf. Ser.*, 898(9):092020, 2017.
- [473] M. Barisits, T. Beermann, F. Berghaus, et al. Rucio: Scientific data management. *Comput. Softw. Big Sci.*, 3:11, 2019.
- [474] Akos Frohner, Jean-Philippe Baud, Rosa Maria Garcia Rioja, Gilbert Grosdidier, Remi Mollon, David Smith, and Paolo Tedesco. Data management in EGEE. *J. Phys. Conf. Ser.*, 219:062012, 2010.
- [475] M. Al-Turany, D. Bertini, R. Karabowicz, D. Kresan, P. Malzacher, T. Stockmanns, and F. Uhlig. The FairRoot framework. *J. Phys. Conf. Ser.*, 396:022001, 2012.
- [476] Torbjörn Sjostrand, Stefan Ask, Jesper R. Christiansen, Richard Corke, Nishita Desai, Philip Ilten, Stephen Mrenna, Stefan Prestel, Christine O. Rasmussen, and Peter Z. Skands. An Introduction to PYTHIA 8.2. *Comput. Phys. Commun.*, 191:159–177, 2015, 1410.3012.
- [477] Bo Andersson, G. Gustafson, and B. Nilsson-Almqvist. A Model for Low p(t) Hadronic Reactions, with Generalizations to Hadron - Nucleus and Nucleus-Nucleus Collisions. *Nucl. Phys. B*, 281:289–309, 1987.
- [478] Bo Nilsson-Almqvist and Evert Stenlund. Interactions Between Hadrons and Nuclei: The Lund Monte Carlo, Fritiof Version 1.6. *Comput. Phys. Commun.*, 43:387, 1987.
- [479] S.A. Bass et al. Microscopic models for ultrarelativistic heavy ion collisions. *Prog. Part. Nucl. Phys.*, 41:255–369, 1998, nucl-th/9803035.
- [480] M. Bleicher et al. Relativistic hadron hadron collisions in the ultrarelativistic quantum molecular dynamics model. *J. Phys. G*, 25:1859–1896, 1999, hep-ph/9909407.

- [481] S. Agostinelli et al. GEANT4—a simulation toolkit. *Nucl. Instrum. Meth. A*, 506:250–303, 2003.
- [482] John Allison et al. Geant4 developments and applications. *IEEE Trans. Nucl. Sci.*, 53:270, 2006.
- [483] J. Allison et al. Recent developments in Geant4. *Nucl. Instrum. Meth. A*, 835:186–225, 2016.
- [484] Johannes Rauch and Tobias Schlüter. GENFIT — a Generic Track-Fitting Toolkit. *J. Phys. Conf. Ser.*, 608(1):012042, 2015, 1410.3698.
- [485] S. Gorbunov and I. Kisel. Reconstruction of decayed particles based on the kalman filter. Technical Report CBM-SOFT-note-2007-003, CBM Collaboration, 2007.
- [486] M. Al-Turany et al. ALFA: The new ALICE-FAIR software framework. *J. Phys. Conf. Ser.*, 664(7):072001, 2015.
- [487] Key4HEP software <https://key4hep.github.io/key4hep-doc/index.html>.
- [488] Offline Framework for the SPD experiment <https://git.jinr.ru/nica/spdroot>.
- [489] Kalman, Rudolph Emil. A New Approach to Linear Filtering and Prediction Problems. *Transactions of the ASME-Journal of Basic Engineering*, 82(Series D):35–45, 1960.
- [490] Milton Abramowitz and Irene A. Stegun. *Handbook of Mathematical Functions with Formulas, Graphs, and Mathematical Tables*. Dover, New York, ninth dover printing, tenth gpo printing edition, 1964.
- [491] J. Myrheim and L. Bugge. A fast Runge-Kutta method for fitting tracks in a magnetic field. *Nucl. Instrum. Meth.*, 160:43–48, 1979.
- [492] L. Bugge and J. Myrheim. Tracking and track fitting. *Nucl. Instrum. Meth.*, 179:365–381, 1981.
- [493] C Adolph et al. Search for exclusive photoproduction of $Z_c^\pm(3900)$ at COMPASS. *Phys. Lett. B*, 742:330–334, 2015, 1407.6186.
- [494] J. Badier et al. Experimental J/psi Hadronic Production from 150-GeV/c to 280-GeV/c. *Z. Phys.*, C20:101, 1983.
- [495] Ayuso, Catherine. Nuclear modification of J/Psi and Drell-Yan production at the E906/SeaQuest experiment. United States: N. p., 2020. Web. doi:10.2172/1637630.
- [496] Jaroslav Adam et al. Determination of the event collision time with the ALICE detector at the LHC. *Eur. Phys. J. Plus*, 132(2):99, 2017, 1610.03055.
- [497] Anton Karpishkov, Vladimir Saleev, and Maxim Nefedov. Estimates for the single-spin asymmetries in $p^\uparrow p \rightarrow J/\psi X$ process at PHENIX RHIC and SPD NICA. 8 2020, 2008.07232.
- [498] J. Badier et al. $\psi\psi$ Production and Limits on Beauty Meson Production From 400- $\{\text{GeV}\}/c$ Protons. pages 401–408, 1985.
- [499] M. Nefedov et al. η_c production at SPD NICA. The 9-th SPD Physics and MC meeting, 28.10.2020.
- [500] P. Aurenche, R. Baier, and M. Fontannaz. Prompt Photon Production at Colliders. *Phys. Rev.*, D42:1440–1449, 1990.
- [501] M. Bonesini et al. High Transverse Momentum π^0 Production by π^- and π^+ on Protons at 280- GeV/c . *Z. Phys.*, C37:39–50, 1987.

- [502] M. Bonesini et al. Production of High Transverse Momentum Prompt Photons and Neutral Pions in Proton Proton Interactions at 280-GeV/c. *Z. Phys.*, C38:371, 1988.
- [503] J. Antille et al. A Measurement of the Inclusive π^0 and η Production Cross-sections at High p_T in $p\bar{p}$ and pp Collisions at $\sqrt{s} = 24.3$ -{GeV}. *Phys. Lett. B*, 194:568, 1987.
- [504] A. Rymbekova. Study of the Polarized Gluon Structure of a Proton via Prompt-Photon Production in the SPD Experiment at the NICA Collider. *Ukr. J. Phys.*, 64(7):631–634, 2019.
- [505] A. Adare et al. Cross section and transverse single-spin asymmetry of η mesons in $p^\uparrow + p$ collisions at $\sqrt{s} = 200$ GeV at forward rapidity. *Phys. Rev. D*, 90(7):072008, 2014, 1406.3541.
- [506] Meshkov, I. N., Trubnikov, G. V. and others. NICA Technical Design Report, Dubna, (2015). 2015.
- [507] A. N. Sissakian, A. S. Sorin, V. D. Kekelidze, et al. The MultiPurpose Detector – MPD to study Heavy Ion Collisions at NICA (Conceptual Design Report), Dubna, (2014). 2014.
- [508] A. A. Baldin, I. G. Voloshina, E. E. Perepelkin, R. V. Polyakova, N. S. Rossiyskaya, T. V. Shavrina, and I. P. Yudin. Numerical simulation of the field distribution produced by the SP-40 magnet of the MARUSYA setup and comparison of simulation results with experimental data. *Technical Physics*, 52 (2007) 1397-1406, 52(11):1397–1406, 2007.
- [509] A. A. Baldin et al. Measurement of the spatial magnetic field distribution of MARUSYA spectrometer. *JINR Preprint P13-2006-67*, 2006.
- [510] A. A. Baldin et al. Magnet for Marusya Experiment. *Phys. Part. Nucl. Lett.*, 7(1 (157)), 2010.
- [511] A. A. Baldin. Polarization Studies at MARUSYA Setup. *Proceedings of International Workshop "Relativistic Nuclear Physics from Hundreds MeV to TeV*, (2008), 1998.
- [512] A. A. Baldin et al. Experimental Study of Asymmetries in Inclusive π^+ , p, d Spectra in Interaction of Polarized Protons and Deuterons with Carbon Targets at MARUSYA Setup. *JINR Preprint P1-2007-180*, 2007.
- [513] Holger Höltermann et al. Light Ion Linear Accelerator up to 7 AMeV for NICA. In *26th Russian Particle Accelerator Conference*, page WECAMH02, 2018.